Expériences interdisciplinaires d'interaction particule-matière

D. Dauvergne

N° d'ordre 38-2006
LYCEN – T 2006-14

Habilitation à Diriger des Recherches

présentée devant

l'Université Claude Bernard Lyon-I

par

Denis DAUVERGNE

Expériences interdisciplinaires d'interaction particule-matière

Soutenue le 13 juillet 2006
devant la Commission d'Examen

Jury :
Monsieur ILLE Bernard, Directeur de Recherches CNRS – Université Claude Bernard – LYON 1 (président)
Monsieur BOUFFARD Serge, Ingénieur de Recherches – CIRIL – CAEN (rapporteur)
Monsieur INDELICATO Paul, Directeur de Recherches CNRS – Université Pierre et Marie CURIE- PARIS (rapporteur)
Monsieur MEOT Vincent, Physicien CEA – CEA DAM – BRUYERES-LE-CHATEL (rapporteur)
Monsieur COHEN Camille, directeur de Recherches CNRS – INSP – PARIS
Madame HANNACHI Fazia, Directrice de Recherches CNRS – CENBG - GRADIGNAN
Monsieur POIZAT Jean-Claude, Professeur Emérite – Université Claude Bernard LYON 1

Sommaire

Préambule

Ce mémoire a été rédigé en vue de l'obtention de l'habilitation à diriger des recherches auprès de l'Université Lyon 1. Pour ce faire, j'ai réalisé la synthèse de mes travaux de recherches depuis que j'ai commencé celles-ci lors de mon arrivée dans le groupe des Collisions Atomiques dans les Solides de l'Institut de Physique Nucléaire de Lyon. Durant toute cette période j'ai eu la chance de pouvoir mener ces travaux qui présentent une certaine unité, et qui se prêtent donc assez facilement à cette synthèse.

Je n'ai pas cherché à rédiger une thèse, dans la mesure où de nombreux pans de ces recherches ont été publiés dans des articles entièrement reproduits dans ce mémoire. Le lecteur pourra donc lire celui-ci à plusieurs niveaux. La lecture approfondie des articles reproduits permettra de rentrer pleinement dans le sujet de l'interaction ion-cristal. La lecture des commentaires originaux permet, quant à elle, de recevoir mes analyses assez personnelles sur les différents travaux réalisés.

J'ai également voulu ajouter de-ci, de-là quelques élucubrations spéculatives qui montrent que, en ayant travaillé sur une thématique pendant tout ce temps, on peut avoir des idées originales que l'on aimerait continuer à développer. C'est le rôle du chercheur.

Ce mémoire comporte trois chapitres très déséquilibrés. Le premier, de loin le plus important, décrit nos expériences basées sur les échanges de charge et le dépôt d'énergie par des ions lourds en condition de canalisation. Le second est consacré aux mesures de temps de fission nucléaire, en particulier aux expériences de blocage cristallin. Le dernier chapitre porte sur la mesure de la photoionisation par création de paires électron-positon.

Les travaux présentés sont de nature essentiellement expérimentale, avec l'appui de simulations. Je rapporte essentiellement sur les travaux pour lesquels j'ai eu une contribution importante. Toutefois, ceux-ci ont toujours été entrepris au sein de collaborations, et je me dois de rendre hommage à mes collaborateurs qui, à différents niveaux, ont permis leur réalisation. Je ne ferai pas de remerciements individuels, mais je préciserai que j'ai eu cette chance de pouvoir travailler avec des scientifiques pour lesquels la compréhension de la Physique était la motivation majeure. Cette qualité nous a permis de ne pas nous enfermer dans une monoculture, et d'aborder des sujets très pluridisciplinaires.

J'ai également puisé sans vergogne dans les résultats des travaux de thèse de deux étudiants de notre groupe, Frédéric BARRUÉ et Etienne TESTA. Si j'ai participé activement à leur encadrement et à l'orientation de leurs recherches, c'est eux qui ont réalisé le travail approfondi que je présente à plusieurs reprises.

1 Echange de charge et perte d'énergie par des ions lourds en condition de canalisation dans un cristal

L'article "Heavy ion channeling : principles and applications" [Cohen 04] servira d'introduction générale sur la canalisation d'ions lourds rapides dans des cristaux. Il a été co-rédigé avec Camille Cohen pour les actes de l'école d'été Tracks 03, organisée en septembre 2003 à Mühlhausen, en Allemagne. A l'occasion de cette école, j'ai eu l'opportunité de faire le cours correspondant, à un public de niveau doctoral et post-doctoral.
La première partie présente les généralités sur les effets de canalisation et de blocage de particules rapides dans une cible cristalline. Elle est donc bien adaptée à l'introduction générale de ce chapitre.
La seconde partie est orientée vers la localisation d'impuretés en surface et dans le volume de cristaux, ainsi qu'à la localisation de réactions de fission nucléaire par blocage. Nous reviendrons sur ce dernier point dans le chapitre suivant de ce mémoire.
La troisième partie présente de façon générale l'intérêt de la canalisation d'ions lourds pour la perte d'énergie et les échanges de charge. Certains résultats ont été obtenus par notre collaboration, et, pour les expériences auxquelles j'ai contribué, des développements seront présentés dans ce chapitre.

Dans le domaine des vitesses élevées (très au-delà de la vitesse de Bohr) mais pas très relativistes, je classerai les processus d'échange de charges en trois catégories, en raison de leur importance :

- tout d'abord, les processus dominant dans les collisions ion-atome en général : ce sont des processus faisant intervenir les potentiels coulombiens écrantés du projectile et de la cible atomique. C'est le cas de la capture dite mécanique (MEC, pour Mechanical Electron Capture), ou non-radiative, dans laquelle le recul du noyau cible intervient nécessairement pour satisfaire à la conservation de l'énergie et de l'impulsion. C'est aussi le cas de l'ionisation par impact sur les noyaux écrantés de la cible (NII, pour Nuclear Impact Ionization). La canalisation d'ions lourds permet d'étudier la variation, voire l'extinction, de ces processus en fonction de l'énergie transverse, donc du paramètre d'impact.
- Ensuite, les processus résultant de l'interaction ion-électron (indépendamment –ou presque- du noyau atomique auquel l'électron est lié). Dans le cas de la capture d'un électron, la conservation de l'énergie et de l'impulsion peut être satisfaite par l'émission d'un photon pour la capture électronique radiative (REC, pour Radiative Electron Capture), qui est le processus inverse de l'effet photoélectrique. A défaut d'un troisième corps mis en jeu, le processus de capture doit être résonnant, comme c'est le cas pour la capture résonnante diélectronique (ou RTE, pour Resonant Transfer and Ionization) qui est le processus inverse de l'émission Auger. L'ionisation par impact sur un électron cible (EII, pour Electron Impact ionization) fait intervenir des états finals dans le continuum des états libres, et n'est donc pas résonnante, mais présente un seuil en énergie cinétique de l'électron cible dans le référentiel du centre de masse.

Ces derniers processus sont en général dominés par ceux du premier type, d'un facteur au moins égal à Z_{cible}. En condition de canalisation, pour lesquelles les collisions à petit paramètre d'impact avec les noyaux cible sont supprimées, ce sont les processus dominant l'échange de charge. Des études avec une forte statistique permettent d'extraire une information originale sur le gaz d'électrons (densités locales, profils Compton).

- Enfin, on rajoutera une sous-catégorie des processus du second type, qui sont les processus d'interaction ion-électron très exotiques, pour lesquels la section efficace est très petite, très inférieure au barn, comme la capture résonnante triélectronique (RT2E, pour Resonant Transfer and Double Ionization) qui met en jeu des corrélations à trois électrons, ou la capture résonnante par excitation nucléaire NEEC (Nuclear Excitation by Electron Capture) qui est le processus inverse de la conversion interne. La canalisation d'ions lourds peut permettre la mise en évidence de tels processus en fournissant une cible « épaisse » d'électrons (typiquement plus de 10^{20} e^-/cm^2).

La figure 1 ci-dessous illustre les différents modes d'échange de charge résultant de l'interaction ion-électron, au moyen de diagrammes des transitions en énergie dans le référentiel de l'ion : un électron de la cible cristalline (dont on néglige l'énergie de liaison, et qu'on suppose au repos dans le laboratoire) possède une énergie cinétique $E_e = (\gamma - 1) m_e c^2$, où γ est le facteur de Lorentz, et m_e la masse de l'électron.

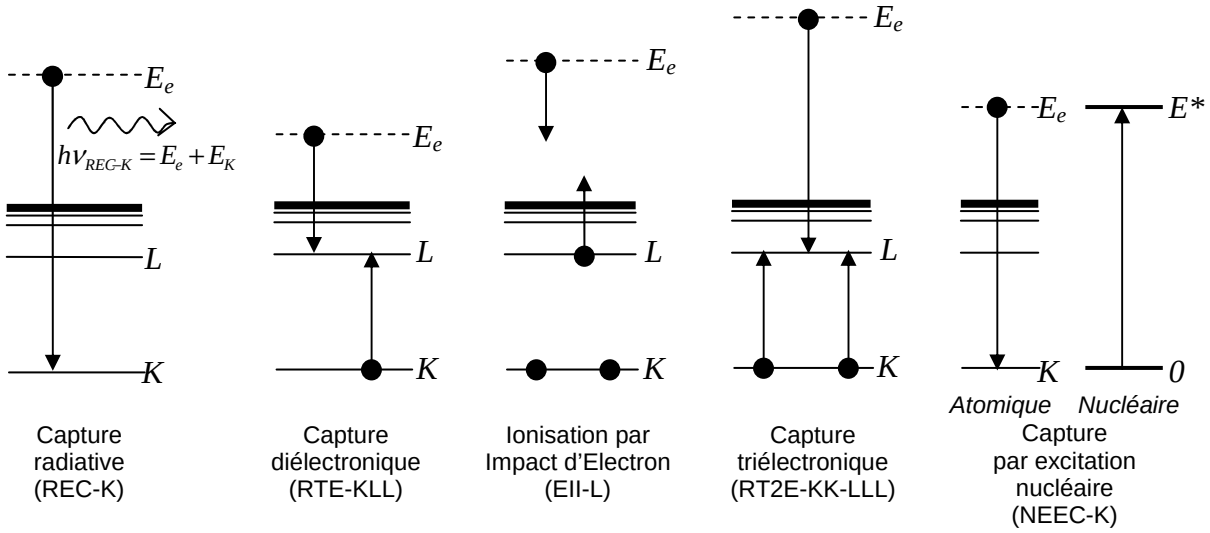

***Figure 1** : Description schématique des transitions en énergie correspondant aux différents modes d'échange de charge par interaction ion-électron, observables en condition de canalisation d'ions lourds. Les niveaux d'énergie sont ceux du projectile ionique (atomique et nucléaire dans le cas de la NEEC).*

Une description détaillée des échanges de charge par des ions lourds rapides a été présentée dans ma thèse [Dauvergne 93], et reprise avec un éclairage nouveau dans celle d'Etienne Testa récemment [Testa 05], au sein de notre groupe de recherche.

Dans ce chapitre nous ferons la synthèse de travaux effectués par notre collaboration sur ces différents processus dans l'ordre inverse de celui ci-dessus, c'est-à-dire en commençant par les processus à faible section efficace, afin de rompre avec l'ordonnancement habituel…

Nous verrons que, en plus de l'étude de ces processus d'échange de charge pour eux-mêmes, d'autres informations originales peuvent être extraites de ces expériences.

- Le mélange intra-couche influence considérablement la durée de vie d'états métastables peuplés par capture ou ionisation dans un solide, même pour des ions canalisés.
- Pour des ions fortement chargés à relativement faible vitesse, la polarisation du gaz d'électrons du cristal est telle qu'on peut mesurer un déplacement du niveau du continuum des états libres de l'ion, au moyen de l'énergie des photons de REC.

- Les ions subissant des collisions rasantes sur les rangées d'atomes sont soumis à un régime particulier pour les échanges de charge : la fréquence des collisions est telle que des électrons capturés dans des états excités n'ont pas le temps de décroître vers des états stables. C'est l'effet de superdensité, associé à une très forte perte d'énergie, car la densité électronique locale est très élevée au voisinage des rangées cristallines.
- L'influence de l'excitation résonnante cohérente, qui n'est pas corrélée au premier ordre à cet effet de superdensité, sera discutée.

Nous verrons enfin quelques aspects spécifiques du dépôt d'énergie par des ions lourds canalisés.

- Nous avons étudié, en fonction de l'énergie transverse des ions canalisés, les corrélations entre émission électronique par les surfaces d'un cristal, la perte d'énergie et les échanges de charge. Dans le cas des ions subissant l'effet de superdensité près des rangées d'atomes au voisinage de la surface d'entrée, le rendement d'émission électronique est très élevé, et, pour un cristal mince, la perte d'énergie intégrée sur toute l'épaisseur de cible est très supérieure à la normale. A l'opposé, les ions de faible énergie transverse sont caractérisés par un faible rendement d'émission électronique, associé à une faible perte d'énergie et à un gel des états de charge.
- L'utilisation des ions très lourds hydrogénoïdes ralentis en dessous de 20 MeV/u au GSI permet de faire des études originales sur le ralentissement de ces ions en canalisation ; en effet, le gel de leur état de charge, autorisé par les grands paramètres d'impact et par la faible densité électronique rencontrée, conduit à une perte d'énergie par collisions distantes qui peut excéder la perte d'énergie hors canalisation, pour laquelle les ions ont une charge à l'équilibre beaucoup plus faible.

Nous conclurons ce chapitre par les perspectives offertes par l'étude en cours de l'émission ionique en condition de canalisation, qui devrait apporter une information nouvelle sur la dynamique de l'endommagement sous impact d'ions lourds.

1-1 La canalisation d'ions lourds rapides dans des cristaux. Principes généraux et applications typiques

L'article ci-dessous correspond à la référence [Cohen 2004].

Available online at www.sciencedirect.com
SCIENCE DIRECT®
Nuclear Instruments and Methods in Physics Research B 225 (2004) 40–71
NIM B
Beam Interactions with Materials & Atoms
www.elsevier.com/locate/nimb

High energy ion channeling. Principles and typical applications

C. Cohen [a], D. Dauvergne [b,*]

[a] GPS, Universités Paris VI–Paris VII, 2, place Jussieu, 75251 Paris Cedex 05, France
[b] IPNL-CNRS/IN2P3, Université Lyon I, 4 rue E.Fermi, 69622 Villeurbanne Cedex 69622, France

Received 13 January 2004; received in revised form 9 March 2004

Abstract

The paper presents a review on selected aspects of high-energy ion channeling. Ion trajectories and fluxes are obtained in the frame of the 'continuum model', in which atomic strings or planes are considered as uniformly charged objects. Computer simulations treating the consecutive binary collisions are also presented. Some typical applications are described, which take mostly benefit of the development of a highly non-uniform ion flux strongly peaked far from the heart of target atoms. These applications concern of course particle–matter interactions through, for instance, refined studies of the impact parameter dependence of energy loss and of charge exchange processes. They also concern material and surface science or nuclear physics, through lattice location measurements.

PACS: 61.85.+p; 34.70.+e
Keywords: Channeling; Blocking; Energy loss; Charge exchange

1. Introduction

When a beam of swift ions enters a single crystal along a major crystallographic planar or axial direction, one observes a spectacular reduction of the yield associated to events that imply close nuclear encounters (nuclear reaction, large angle elastic scattering, formation of core-shell electron vacancies on target atoms and corresponding X-ray emission...). All these effects are characteristic of a phenomenon called Channeling, discovered and explained 40 years ago [1]. Channeling is the direct consequence of the fact that, in the particular beam-crystal geometry described above, the ions experience strongly correlated binary collisions with target atoms. These collisions focus the beam far from the atomic strings or planes of the crystal. Thus, the uniform flux associated to an ion beam impinging a crystal surface becomes progressively highly non-uniform as the ions penetrate in the bulk, with a pronounced maximum at the center of the 'channels' delimited by the atomic rows or planes. We will briefly show in Section 2 how one can very precisely calculate ion trajectories and fluxes in

* Corresponding author. Tel.: +33-4-72-44-62-57; fax: +33-4-72-43-12-43.
E-mail address: d.dauvergne@ipnl.in2p3.fr (D. Dauvergne).

0168-583X/$ - see front matter © 2004 Elsevier B.V. All rights reserved.
doi:10.1016/j.nimb.2004.03.017

crystals. The knowledge of the ion's flux can be exploited in many ways, illustrated in Section 3. First one can determine the crystallographic location of a given population of nuclei inside a crystal by studying the associated yield of close nuclear encounter events. Such studies are beneficial in material science for the localization of impurity lattice sites, of defects, of surface atom relaxation, of strains in epitaxial layer growth... [2]. But they are also beneficial in nuclear physics when determining the pathlength before fragmentation of nuclei that have first been excited by violent collisions at regular crystal lattice sites and thus the lifetime of these nuclei [3–5]. The second interesting feature of the non-uniform flux of channeled ions is that it permits to study specifically the interaction, at given impact parameter, of these ions with target electrons and particularly with loosely bound valence or conduction electrons. When the projectile is much faster than the electrons of the medium, one can use a crystal as a very dense quasi-free electron gas target and study charge exchange processes. Such studies, presented in Section 4, concern electron impact ionization or excitation (EII or EIE) [6,7], radiative electron capture (REC) [8] (that is the reverse of the photoelectric effect), resonant transfer and excitation (RTE) [9] (the reverse of the Auger effect), or nuclear excitation by electron capture (NEEC, the reverse of internal conversion). One can also study in detail the impact parameter dependence of ion energy loss and determine the contribution of local and non-local interactions in this process [7,10–12]. Finally, we will show in Section 5 that one can also exploit the fact that the correlated binary collisions of channeled ions with target atoms are quasi-periodic in time: this may induce resonant coherent excitation, populating excited atomic or nuclear levels [13–16].

2. Ion trajectories and fluxes in channeling geometry

2.1. Shadow behind an atom

Let us consider the situation represented in Fig. 1. A uniform flux of ions impinges on the first of a pair of atoms, the incident beam direction

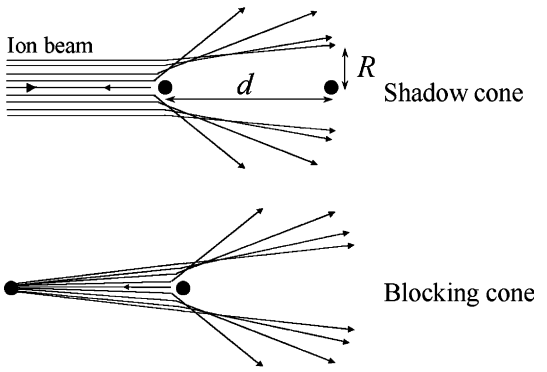

Fig. 1. Formation of a shadow cone and of a blocking cone.

being parallel to the axis joining the two atoms. Each ion is repelled by the screened Coulomb potential generated by the first atom, the smaller the impact parameter the stronger the deflection. The result is the formation of a shadow cone of radius R at the level of the second atom. Roughly (and strictly in the case of a Coulomb potential), R is proportional to $(Z_1Z_2d/E)^{1/2}$, where Z_1 and Z_2 are, respectively, the atomic numbers of the ions and of the atom, d the distance between the pair of atoms and E the ion energy. A typical order of magnitude is $R = 0.1$ Å for $E = 0.1$ MeV/u and $d = 3$ Å, i.e. a typical interatomic distance. Thus, if the two atoms are on the fixed positions shown in Fig. 1, there will be no close nuclear encounter on the second one. Assume now that the relative positions of the two atoms, perpendicularly to the mean axis, may fluctuate with a standard variation ρ. It can then be demonstrated that the close encounter yield on the second atom is only a function of the ratio ρ/R. In the following we will choose to normalize these yields to the ones corresponding to a uniform ion flux.

Let us now consider an ion beam entering a crystal parallel to low index atomic rows with a uniform impact parameter distribution. One can use Monte Carlo simulations to calculate ion trajectories resulting from a sequence of binary collisions characterized by a realistic screened Coulomb potential. In such simulations, the instantaneous positions of the crystal atoms, with respect to their mean site, that are sampled by a given ion are determined through the thermal

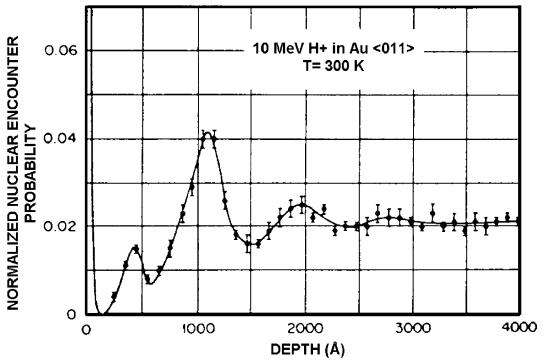

Fig. 2. Normalized close nuclear encounter probability as a function of penetration depth for a 10 MeV proton beam entering an Au crystal, parallel to a $\langle 0\,1\,1\rangle$ direction. This probability is obtained by Monte-Carlo simulations of sequences of binary collisions. The data are from [17].

vibration laws. Once a set of trajectories is calculated, the ion fluxes and thus the close nuclear encounter yields can be readily obtained. We present in Fig. 2, from [17], the result of a Monte-Carlo simulation providing the close nuclear encounter yield, as a function of penetration depth, for 10 MeV protons entering a gold crystal parallel to a $\langle 0\,1\,1\rangle$ direction. After some marked oscillations, this yield becomes independent of penetration depth and levels around 2%. At the very surface, the yield corresponds to the uniform entrance flux and is thus equal to 1. We will show in Section 3 how the very strong first peak yield can be used to provide information on the surface structure of crystals. As an example, we also show in Fig. 3 the calculated variation with the penetration depth of the ion flux at distances larger than $r_{\min} = 1.2$ Å from any atomic string when a beam of 10 MeV protons enters a silicon crystal along the $\langle 1\,1\,0\rangle$ direction. The normalization is made with respect to a uniform ion flux. One can see in the figure a marked flux peaking effect far from atomic strings: after some oscillations this flux stabilizes at a value around 2. The latter value is of course determined by the chosen cut-off $r_{\min}$.

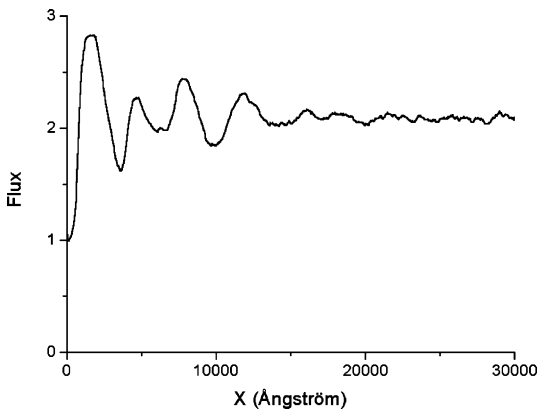

Fig. 3. Normalized ion flux variation with penetration depth at distances larger than 1.2 Å from atomic strings for a 10 MeV proton beam entering an Si crystal, parallel to a $\langle 0\,1\,1\rangle$ direction. This flux is obtained by Monte-Carlo simulations of sequences of binary collisions.

2.2. Averaged continuum potentials, transverse energy conservation

Rather quantitative assessments can be made when introducing reasonable approximations in order to replace the numerical calculations presented above by an analytical description of the channeling phenomena. The discrete series of binary collisions with atoms can be approximated by a continuous interaction between a projectile and uniformly charged strings or planes. In this frame, simple physical quantities that govern the behavior of the projectile population in the crystal are introduced and general trends can be predicted with the help of statistical physics.

Calling V the screened Coulomb ion-atom potential and z the penetration depth, the axial continuum potential $U(r)$ at the distance r from a string is

$$U(r) = \frac{2}{d}\int_0^\infty V[(r^2+z^2)^{1/2}]\,\mathrm{d}z, \tag{1}$$

where d is the inter-atomic spacing.

The planar potential $Y(y)$ at distance y from a plane is given by

$$Y(y) = Nd_{\mathrm{p}}\int_0^\infty 2\pi r V\left[\left(y^2+r^2\right)^{1/2}\right]\mathrm{d}r, \tag{2}$$

where d_{p} is the distance between two adjacent atomic planes.

In what follows we shall restrict ourselves to the description of axial channeling. We show in Fig. 4 from [12] the axial potential map in a plane perpendicular to the $\langle 1\,1\,0\rangle$ axis of a silicon crystal.

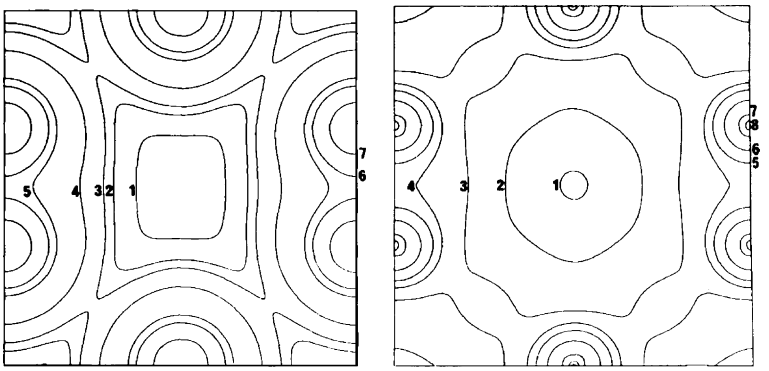

Fig. 4. (a) Potential map per unit charge in the plane transverse to a ⟨1 1 0⟩ direction in Si. This potential is averaged along ⟨1 1 0⟩. The values corresponding to the isocontours are (in eV) 1: 0.5, 2: 1.5, 3: 2.25, 4: 5, 5: 15, 6: 21, 7: 50. (b) Electron density map in the same transverse plane. This density is also averaged along ⟨1 1 0⟩. The values corresponding to the isocontours are (in electron Å^{-3}) 1: 0.032, 2: 0.1, 3: 0.24, 4: 0.5, 5: 1.0, 6: 3.0, 7: 10.0, 8: 30.0. From [12].

This map has been obtained by summing the axial potentials, given by relation (1), corresponding to the six rows represented in the figure and by setting to zero the value of the potential at the channel center. The motion of ions of kinetic energy E in the transverse plane is characterized by the conservation of the 'transverse energy' $E_\perp$. The latter is determined by the entrance conditions and, in the small angle approximation, is given by

$$E_\perp = QU(r) + E\Phi^2 = QU(r_i) + E\Phi_i^2. \tag{3}$$

In relation (3), relativistic corrections are neglected. Φ is the angle between the ion's trajectory and the atomic string at position r, while Φ_i and r_i are respectively the entrance angle and impact parameter. In this paper, we are interested in swift ions, that are most of the time highly stripped and can thus be assimilated to point charges $Q = Z_1 - n$, n being the number of core electrons, bound close to the ion's nuclei. Unless specified, we will use $Q = Z_1$ in the following. Relation (3) allows one to calculate the ion trajectories.

It is worthwhile to discuss the validity of the approximations that have been introduced in the present subsection. If one considers a set of binary collisions, $E_\perp$ changes abruptly at each collision, because the angle Φ changes at a fixed distance from the string. Then, between two collisions, this change is somewhat compensated because the potential component of $E_\perp$ changes continuously, as does the distance of the ion to the string, while the angle Φ is constant. A good check of the continuum approximation is to test up to what extent this compensation does conserve $E_\perp$. For this purpose, one may calculate the value of $E_\perp$ at the half-way plane between the $(i-1)$th and the ith atom of a string, using the continuum potential. The continuum approximation holds if the binary collision with the ith atom does not induce a significant change of $E_\perp$ calculated at the half-way plane between the ith and the $(i+1)$th atom of the string. The result is that $E_\perp$ is conserved at the first-order and thus the continuum model represents a good approximation as far as the minimum distance of approach to a string remains larger than $r_{\text{lim}} = (b_o \cdot d)^{1/2}/2$. Here, b_o is the collision diameter associated to the Coulomb potential, which is inversely proportional to the square of the ion velocity. Thus, as could be expected, the smaller the interatomic distance and the larger the ion velocity, the more accurate the continuum model.

Of course, the instantaneous positions of the crystal atoms in the transverse plane scatter around their mean values along the strings. The corresponding distribution is characterized by the two-dimensional rms. thermal vibration amplitude ρ. This weakens the correlation between successive binary collisions and induces incoherent multiple scattering which, in the average, increases $E_\perp$. Such a process, called dechanneling, becomes very important when the ions can approach the strings

at distances of the order of ρ, i.e. when their transverse energy is large. However, even ions with a low initial $E_\perp$ experience incoherent multiple scattering by collisions on target electrons. Thus, their transverse energy also increases on the average, but much more slowly.

It is convenient (but somewhat arbitrary) to set a limit to the transverse energy, $E_{\perp\mathrm{lim}}$, above which an ion cannot be considered as channeled. One can decide, for instance, that this is the case for ions that can approach strings at distances smaller than ρ and thus experience close nuclear encounter events. With this definition, one has $E_{\perp\mathrm{lim}} = Z_1 U(\rho)$. It can be seen in Fig. 4 that when a uniform ion flux impinges on a crystal surface, most of the ions get a potential energy much smaller than $U(\rho)$. Then, roughly, they will reach a transverse energy above $E_{\perp\mathrm{lim}}$ if the beam entrance direction makes an angle Φ_i with the string greater than a critical value Ψ_C given by

$$E\Psi_\mathrm{C}^2 = Z_1 U(\rho). \tag{4}$$

Ψ_C is called the channeling critical angle. Its value depends of course on the choice of the screened interatomic potential. A good estimate has been provided by Lindhard [1] for axial channeling:

$$\Psi_\mathrm{C} = (2Z_1 Z_2 e^2/Ed)^{1/2}. \tag{5}$$

2.3. Ion flux at statistical equilibrium

The knowledge of the particle trajectories provides the determination of the ion flux $P(\vec{r}, z)$ at any point of the crystal. In fact, as already indicated in Section 1, one can clearly see in Fig. 2 that after some penetration depth the close nuclear encounter yield, and thus the ion flux near strings, becomes independent of depth. This is also true far away from the strings, as seen on Fig. 3 and, more generally, at any point of the transverse plane. This feature reflects the establishment of a statistical equilibrium where all the available configurations in the transverse phase space of an ion of given $E_\perp$ are equiprobable. The incoherent multiple scattering events described in Section 2.2 accelerate significantly the establishment of equilibrium. The latter is reached while the $E_\perp$ distribution is still only marginally affected by multiple scattering. Let us call $P_\infty(r|E_\perp)$ the contribution of ions of transverse energy $E_\perp$ to the flux at statistical equilibrium, at distance r from an atomic string. It can be shown that

$$P_\infty(r|E_\perp) = \begin{cases} 2\pi r/A(E_\perp) & \text{for} \quad U(r) < U(r_{E\perp}), \\ 0 & \text{for} \quad U(r) > U(r_{E\perp}). \end{cases} \tag{6}$$

Expression (6) is fully valid only close enough to atomic strings, i.e. in regions where equipotential lines are circular. $A(E_\perp)$ is the available area of the transverse space for the ion considered and $r_{E_\perp}$ its minimum distance of approach to the strings. One can associate to each string a unit cell in the transverse plane, centered on the string and with a radius r_0 given by

$$\pi r_0^2 = 1/Nd. \tag{7}$$

The overall flux $P_\infty(r)$ at statistical equilibrium is then obtained by integrating over all transverse energies, each $E_\perp$ being affected with a weight given by the transverse energy distribution $g(E_\perp)$:

$$P_\infty(r) = \int_0^\infty g(E_\perp) P_\infty(r|\bar{E}_\perp)\,\mathrm{d}E_\perp. \tag{8}$$

For a beam entering parallel to a string, the integration of relation (8) leads to the very simple result

$$P_\infty(r, \Phi_i = 0) = (2r/r_0^2)\ln(r_0^2/(r_0^2 - r^2)). \tag{9}$$

2.4. Blocking: rule of reversibility

Let us first consider a beam of ions (Z_1, E) entering a crystal with a uniform distribution of entrance impact parameters, and with an entrance angle distribution characterized by a mean value Φ, with respect to a given crystallographic direction, and by a spread of rms. $\Delta\Phi$. The corresponding flux distribution at a point $(\vec{r}, z)$ in the crystal is noted $P_\mathrm{in}(\vec{r}, z, \Phi, \Delta\Phi)$. Let us now consider an isotropic emission of the very same ions (Z_1, E) from the very same point of the crystal, $(\vec{r}, z)$ and call $P_\mathrm{out}(\vec{r}, z, \Phi, \Delta\Phi)$ the flux of ions emerging from the crystal observed by a detector placed at an angle Φ, with an aperture corresponding to an angular spread of rms. $\Delta\Phi$. It can be demonstrated, using the Liouville theorem, that

$$P_{\text{in}}(\vec{r}, z, \Phi, \Delta\Phi) = P_{\text{out}}(\vec{r}, z, \Phi, \Delta\Phi). \quad (10)$$

Let us call $\chi_{\text{in}}(\Phi)$, or channeling yield, the close nuclear encounter yield on any population of atoms of given spatial distribution inside the crystal for a beam entering with the angle Φ. The consequence of relation (10) is that, whatever $\Phi, \chi_{\text{in}}(\Phi)$ is equal to the yield $\chi_{\text{out}}(\Phi)$ of ions leaving the crystal along Φ after being emitted by the very same atom population. $\chi_{\text{out}}(\Phi)$ is called the blocking yield. The equality between channeling and blocking yields is well verified experimentally [18]. The blocking effect is schematized in Fig. 1: the scattering by an atom generates a 'blocking cone' in the initially isotropic angular distribution. The blocking cone axis is along the axis of the atomic pair.

We show in Fig. 5 a typical blocking pattern registered on a position sensitive detector [5]. A 24 MeV/u ^{238}U beam was transmitted through a 6 μm thick Si crystal. The incident angle was set a few degrees off the ⟨1 1 0⟩ crystal axis and the detector was placed in order to intercept the ions that were elastically scattered in the vicinity of the ⟨1 1 0⟩ direction. The darker the pattern, the larger the number of ions intercepted. The central bright spot of the pattern corresponds to the intersection of the ⟨1 1 0⟩ direction by the detector plane, and, obviously, the emission yield in this direction is very weak. One also observes weak emission along the lines that correspond to the intersection of crystallographic planes with the detector plane. The inset represents the one-dimensional blocking pattern integrated over the azimuth angles and centered along the axial direction. The emission yield $\chi(\Phi = 0)$ is very small, around 3%. We will show in Section 3 that the blocking effect is used to bring valuable and specific information in surface physics, concerning surface lattice sites. We will also show that it is a very powerful tool for the determination of the lifetime of excited nuclei before fragmentation.

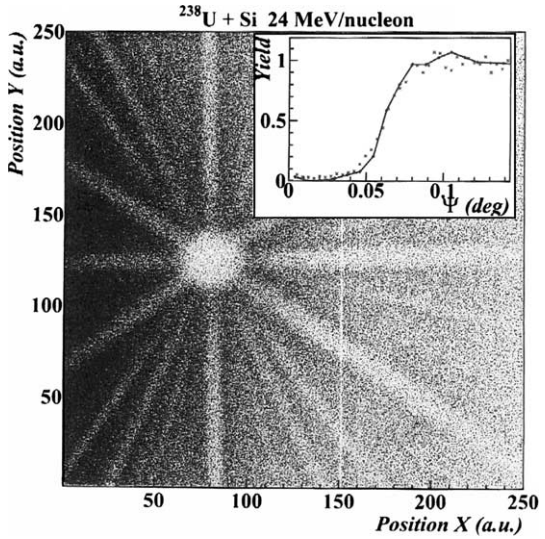

Fig. 5. Blocking pattern in the vicinity of a ⟨1 1 0⟩ direction of Si. This pattern corresponds to the angular distribution of 24 MeV/u U ions after elastic scattering on crystal atoms. The inset represents the axial blocking dip after averaging over the azimuth. From [5].

Recently, a departure from the reversibility rule has been observed when heavy ions, around 1 MeV/u with an initially isotropic distribution are transmitted through thin crystals [19]. This effect that can, at least partially, be attributed to charge exchange processes will be discussed in Section 4.

2.5. Validity of a classical description for high energy ion channeling

The criterion of validity for a classical description of a binary collision between particles depends on the interaction potential. The problem has been analyzed in detail by Bohr [20]. For a Coulomb potential, a classical description holds if the wavelength ƛ associated to a particle with a velocity equal to the relative velocity v between collision partners and with a mass equal to the reduced mass, $\mu = M_1M_2/(M_1 + M_2)$, is small at the scale of the collision diameter: $b_0 = 2Z_1Z_2e^2/\mu v^2$. Calling $v_0 = e^2/\hbar$ the Bohr velocity, this implies that the so-called 'Bohr parameter' κ must obey the following relation:

$$\kappa = b_0/ƛ = 2Z_1Z_2v_0/v > 1. \quad (11)$$

In channeling, one deals with the ion motion in the transverse plane. In the frame of the continuum approximation, one must then ask whether the collision of an ion with maximum transverse velocity $v_{\perp C} = v\Psi_C$ with a continuous string can be treated classically. The first observation is that, as

the critical angle Ψ_C is inversely proportional to v, the condition searched should be independent of the longitudinal ion velocity. This is indeed the case. With some realistic approximations concerning the axial potential given by relation (1), it can be shown that the transverse motion of a charged particle of mass M_1 can be described classically as long as

$$(M_1/m_e)^{1/2} \gg 1, \tag{12}$$

m_e being the electron mass. This relation is thus obviously fulfilled for ions. Thus, in the frame of the continuum model, ion channeling can always be treated classically, which is not the case for electron channeling.

It is also important to check up to what extent the spreading of the ion-wave packet induced by successive collisions could affect the validity of the continuum model. This is a tough question. Let us call a the screening radius associated to the screened interatomic potential V. It can be shown that, as long as the critical angle remains smaller than about a/d (a value around 10^{-1} rad), the wave-packet associated to the ion retains its width during its collision with a string. This is the case for swift ions above typically 100 keV/u. In such a situation, it can also be shown that $E_\perp$ fluctuations can be neglected. The continuum approximation and the $E_\perp$ conservation are thus not affected by quantum fluctuations for high-energy ions.

3. Determination of lattice sites: applications to material science and nuclear physics

3.1. Material science

3.1.1. Lattice location of impurities

Consider an ion beam entering a crystal with an incident direction characterized by an angle Φ. We have shown in Section 2 how the non-uniform ion flux in channels, and, consequently, the yield $\chi(\Phi)$ of close nuclear encounter with any population of atoms inside a crystal could be calculated. Conversely, it is possible to determine the lattice sites occupied by a population of atoms inside a crystal by studying the corresponding close nuclear encounter yields $\chi(\Phi)$. Practically, one attempts to fit the values $\chi(\Phi)$ measured experimentally in the vicinity of various crystallographic directions, with yields calculated assuming various distributions of occupied sites. This is illustrated in Fig. 6, from [21]. The aim of the experiment was to determine the location of deuterium atoms implanted in a bcc tungsten crystal. The implanted deuterium was characterized via the $D(^3He, p)^4$ He nuclear reaction. The angular dependence of the yield associated to this reaction, in the vicinity of the $\langle 1\,0\,0\rangle$ direction, clearly shows that the implanted atoms occupy tetrahedral sites.

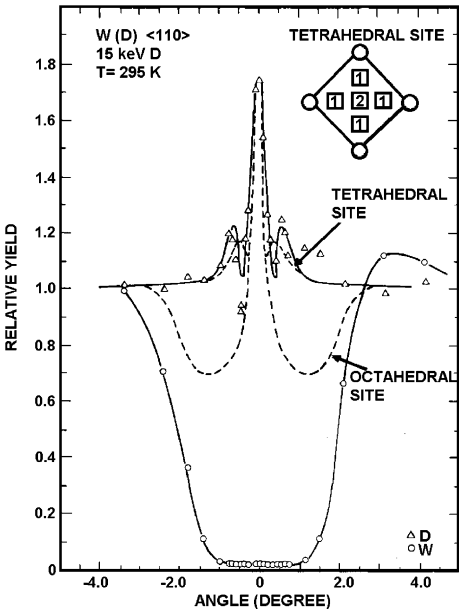

Fig. 6. Close nuclear encounter yield as a function of the tilting angle of a ^{3}He beam with respect to the $\langle 1\,0\,0\rangle$ direction of a W crystal. (○) backscattering yield on W atoms; (△) proton yield from the D (^{3}He,p)^{4}He reaction on implanted deuterium. Two numerical simulations of this latter yield are also represented assuming that D atoms occupy either octahedral sites (dotted line) or tetrahedral sites (full line). The comparison with experimental results shows that the D atoms occupy the tetrahedral sites. The data are from [21].

3.1.2. Heteroepitaxy

Another interesting example is the determination of lattice strains when thin layers of a species A are epitaxially grown on the top of a crystalline substrate of a species B. The strains result from the

lattice mismatch between the meshes of A and B. If the mismatch is not too strong, and if the layer A is not too thick, atoms A will be located in registry with atoms B. If, for instance, the lattice parameter of A, a_A, is larger than a_B, layer A will then be compressed in the plane parallel to the substrate surface and, in compensation, it will experience a tensile strain perpendicularly to this plane. The corresponding tetragonal distortion can be determined in channeling experiments. Assume cubic meshes and a (0 0 1) surface orientation. The result of the tetragonal distortion is that the $\langle 0\,1\,1\rangle$ axes of A and B are not exactly parallel. The corresponding angular shift can be evidenced when comparing channeling dips, $\chi(\Phi)$ in the vicinity of the $\langle 0\,1\,1\rangle$ direction corresponding to close nuclear encounter on A and B atoms, respectively. A typical example, from [22], is shown in Fig. 7. It corresponds to the growth of an Fe layer (of bcc structure) on the top of a (0 0 1) GaAs substrate (of diamond structure). One has $2a_{Fe}/a_{GaAs} = 1.015$. As a consequence, the Fe layer is compressed in the (0 0 1) plane. This is well evidenced when comparing the position of the minima corresponding to the channeling angular scans associated respectively to Fe and to GaAs, in the vicinity of the $\langle 0\,1\,1\rangle$ direction. When the sample is heated above 450 °C, Fe reacts with GaAs and forms a three-atomic compound, FeGaAs, in the interface region. The position of the minimum of the channeling angular scan, across $\langle 0\,1\,1\rangle$, associated to the non-reacted part of the deposit in the surface region (pure Fe) is also compared in Fig. 7 to that of the substrate. This comparison clearly shows that the presence of the reacted layer at the interface reverses the strain experienced in the (0 0 1) plane by the Fe film, from compressive to tensile.

3.1.3. Surface studies

Channeling experiments also provide very interesting information on the structure of the very surface of crystals. As an example, Fig. 8, from [2], shows the comparison between two energy spectra

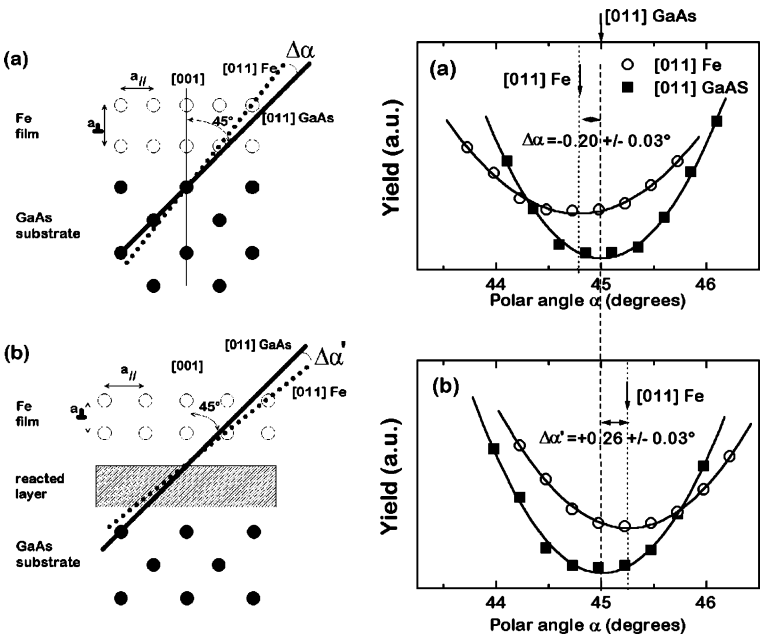

Fig. 7. Angular scans across the [0 1 1] axis 45° off the (0 0 1) surface plane of a GaAs crystal, corresponding to the backscattering of 1 MeV ^{4}He ions: (a) the comparison between the scans corresponding to the substrate and to an as-deposited Fe layer demonstrates that the latter is under compressive strain in the (0 0 1) plane. (b) after heating at 450 °C, an interfacial FeGaAs forms, and the remaining Fe surface film is now under tensile strain in the (0 0 1) plane. From [22].

of backscattered ions, obtained with a 2 MeV ^{4}He beam incident on a W crystal. The first one corresponds to a 'random' orientation of the beam far from any major crystallographic direction. For the second spectrum, the beam was aligned along a $\langle 1\,0\,0\rangle$ axis. The energy scale in the abscissa can be related to a depth scale, via the energy loss of ions in the crystal: the highest energy corresponds to backscattering events at the crystal surface. It clearly appears in Fig. 8 that the backscattering yield in the bulk of the crystal is reduced by about two orders of magnitude in the axial channeling geometry. However, there is a marked peak yield in the corresponding spectrum, associated to backscattering events in the very near surface region. This 'surface peak' is related to the strong and narrow peak yield predicted, in the same region, by the Monte-Carlo simulations shown in Fig. 2. Its integral is related to the penetration depth required for the development of the shadow cone, and is usually expressed in 'number of atoms per row'. Let us call α_i the normalized backscattering yield on the ith atom of a row. As the entering ion flux is uniform, one has $\alpha_1 = 1$. As seen in Fig. 2, α_i decreases rapidly with i in the very near surface region, and thus, the sum $S = \Sigma_i \alpha_i$ converges rapidly. This sum is the integral of the surface peak expressed in number of atoms per row. Monte-Carlo simulations demonstrate that, for a perfect crystal, S is a unique function of the ratio ρ/R, ρ being the two-dimensional rms. amplitude of the atom thermal vibrations perpendicularly to the strings, and R the radius of the shadow cone, as illustrated in Fig. 1. The relation between S and ρ/R is represented in Fig. 9, from [23], which shows the result of many simulations performed on various ion-crystal couples. Practically, for ions between 0.1 and 1 MeV/u, the ratio ρ/R is of the order of 1 and S is thus of the order of 2 (see Fig. 9). Consequently, its value is mainly related to the shadowing efficiency of surface atoms on subsurface atoms. It then provides direct information on the lattice location of surface atoms. We now give some illustrations of surface studies.

Fig. 10, from [24], represents the evolution of S as a function of temperature T, in a Pb crystal with a (1 0 1) surface. As ρ varies roughly like $T^{1/2}$, S is

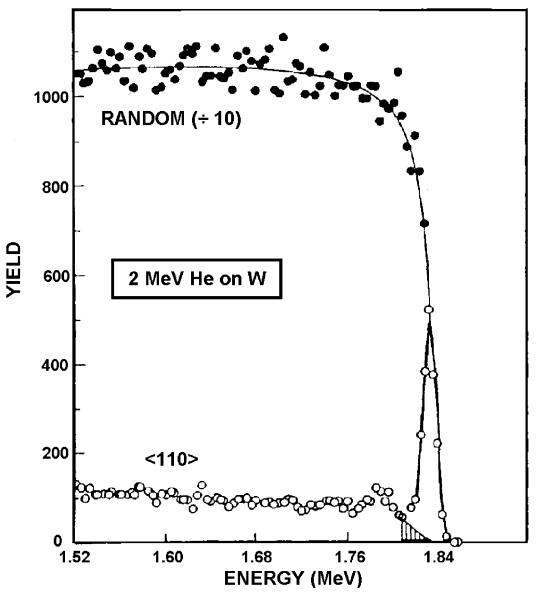

Fig. 8. Random (●) and $\langle 1\,0\,0\rangle$ aligned (○) backscattering spectra obtained with a 2 MeV ^{4}He beam sent on a W crystal. Note the surface peak at the high energy edge of the aligned spectrum. The data are from [2].

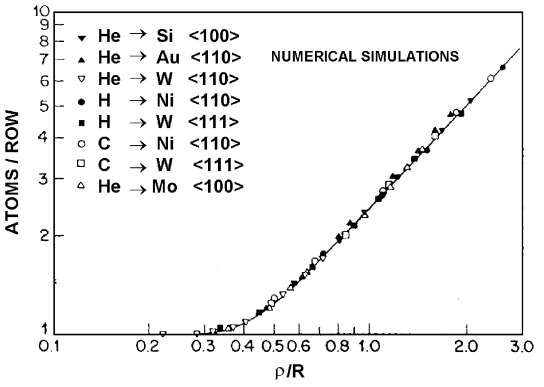

Fig. 9. Calculation by numerical simulations, for various ion-target combinations, of the surface peak area, expressed in number of atoms per row. This area is represented as a function of the ratio between the two-dimensional rms thermal vibration amplitude ρ and the radius R of the shadow cone at the level of the second atom of the atomic string considered. The data are from [23].

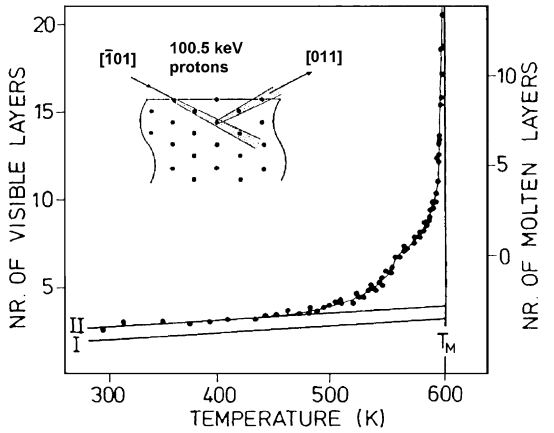

Fig. 10. (●) Integral of the surface peak as a function of temperature measured for the backscattering of a 100 keV proton beam incident along the [1 0 1] axis of a Pb crystal with (1 0 1) surface. The backscattered ions are detected along the [0 1 1] direction. The full lines correspond to numerical simulations assuming the absence of any surface disordering. (Simulation I) surface atom thermal vibration amplitude equal to that of bulk atoms and (simulation II) Adjustment of thermal vibration amplitude of surface atoms in order to fit the experimental results below 450 K. The data are from [24].

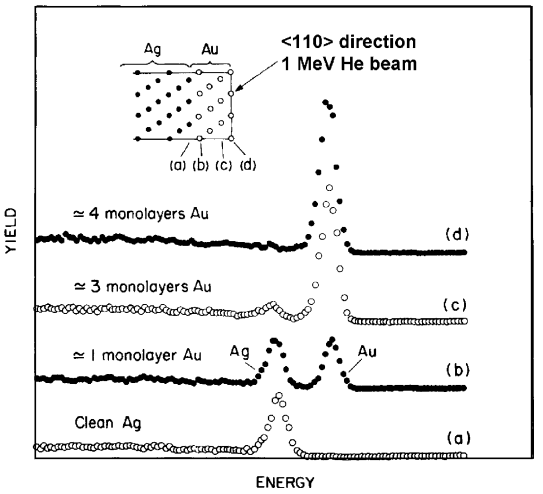

Fig. 11. Backscattering spectra for 1 MeV ^{4}He ions incident along the [1 1 0] axis of (a) a clean Ag (1 1 1) surface and of Au-covered surfaces (b)–(d). The Ag surface peak decreases due to shadowing by Au atoms. The data are from [2].

expected to increase with T. The full line I represents the simulated variation of S assuming that surface atoms vibrate like bulk atoms. The full line II is the result of simulations in which the vibrations of surface atoms are larger (by about 50%) than those of bulk atoms. Up to 450 K, this line fits very well the experimental results, represented by the points in the figure. Thus these measurements provide a precise determination of the surface thermal vibration amplitude. But the most striking observation is the strong and increasing discrepancy between the simulated and measured values of S above 450 K, i.e. well below the temperature of the first-order phase transition leading to bulk melting (600 K). The effect is reversible in T. The very high values of S measured above 450 K demonstrate the establishment of a strong surface disordering, thermally activated. The authors have been able to study the depth over which such a disorder extends, as a function of temperature, and have assigned these results to surface premelting.

Information can also be reached on the very first steps of epitaxy, as illustrated in Fig. 11 from [2]. The authors have deposited increasing quantities of Au, from 0 to 4 monolayers on top of an Ag crystal (Ag and Au have the same mesh and the same lattice parameter). The figure represents backscattering spectra registered in axial alignment geometry at various steps of the deposit. One clearly sees the gold peak appearing in the high-energy part of the spectra, the integral of which saturates when the deposited quantity exceeds three monolayers. In the mean time, the Ag surface peak weakens continuously and disappears when the Au deposit exceeds three monolayers. This behavior demonstrates: (i) that the deposition proceeds via a layer by layer growth mode (no Au islanding). (ii) That the deposited Au forms a good single crystal. (iii) That the Au crystal is in perfect epitaxy with the Ag substrate, which leads to the shadowing of the Ag atoms by Au atoms and thus to the disappearance of the Ag surface peak.

We now present an illustration related to surface relaxation. One consequence of the discontinuity corresponding to the surface is that the lattice sites of the surface atoms differ from those of bulk atoms. For symmetry reasons this corre-

sponds to a coherent displacement, i.e. to an expansion or a contraction of the first interplanar distances. These relaxations can be measured by channeling in the very same way than the tetragonal distortions s case of the Fe/GaAs system. However, in the present case, this distortion concerns the surface atoms of the substrate instead of deposits. One can then perform angular scans across an axis not perpendicular to the crystal surface and compare the angular position of the minima corresponding respectively to the bulk yield (unstrained region) and to the surface peak yield (strained region). This provides a measurement of the surface relaxation. We show in Fig. 12 from [25] an even more sophisticated illustration of this type of studies, performed on a Cu crystal, the surface orientation of which, $(4,1,0)$, makes a small angle with respect to the (1 0 0) plane. Such a surface (called 'vicinal') self-organizes in (1 0 0) terraces of equal length separated by periodic steps of $\langle 0\,0\,1\rangle$ orientation. As surface atoms relax with respect to regular bulk lattice sites, one expects that step edge atoms should relax with respect to other surface atom lattice sites. This is clearly evidenced in the angular blocking scans shown in Fig. 12. These scans were performed across the $\langle 0\,1\,1\rangle$ axis contained in the plane of the terrace, by moving a tightly collimated detector perpendicularly to this plane. Of course, the minimum of the bulk yield corresponds to a detection angle of 90°, i.e. when the detector is along the axis. But the angular positions of the blocking scans corresponding to the surface peak are different, as seen on the figure. Roughly, these positions are related to the direction along which the edge atoms shadow the other surface atoms. They provide thus the edge atom relaxation. One sees on Fig. 12 that for a bare Cu surface this relaxation is a contraction towards the crystal bulk below the surface plane, while, when the Cu surface is covered by one monolayer of oxygen, the relaxation becomes an expansion above the surface plane.

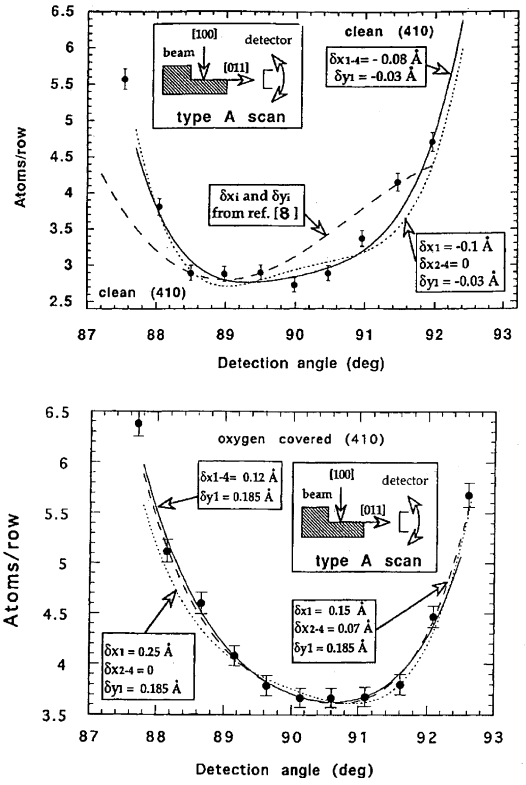

Fig. 12. Evidence for step edge relaxation, perpendicularly to the terraces, on $(4,1,0)$ Cu. The surface peak blocking dips corresponding to backscattering, in the vicinity of the [0 1 1] axis in the terrace's plane, of 200 keV ^{4}He ions sent parallel to [1 0 0], are asymmetrical. (Upper part) Clean surface; evidence for step edge contraction; (Lower part) oxygen covered surface; evidence for step edge expansion. (●) Experimental results. (Lines) Monte-Carlo simulations with various hypotheses on the relaxation. From [25].

3.1.4. Characterization of defects

We have just seen that detailed information can be brought on the sites occupied by surface or step edge atoms by studying the behavior of the surface peak, for instance by means of backscattering spectra. One can also use backscattering experiments in channeling geometry to determine the displacements from regular lattice sites of bulk atoms, i.e. to study lattice defects. This is well illustrated in Fig. 13, from [26]. A nickel single crystal was implanted, in its near surface region, by Sb ions (the implantation energy was 80 keV, corresponding to a range of 250 Å). Fig. 13 shows various backscattering spectra, corresponding to different implantation fluences, in which the probing beam (2 MeV ^{4}He ions) was aligned with a $\langle 1\,1\,0\rangle$ crystallographic direction. It also shows two

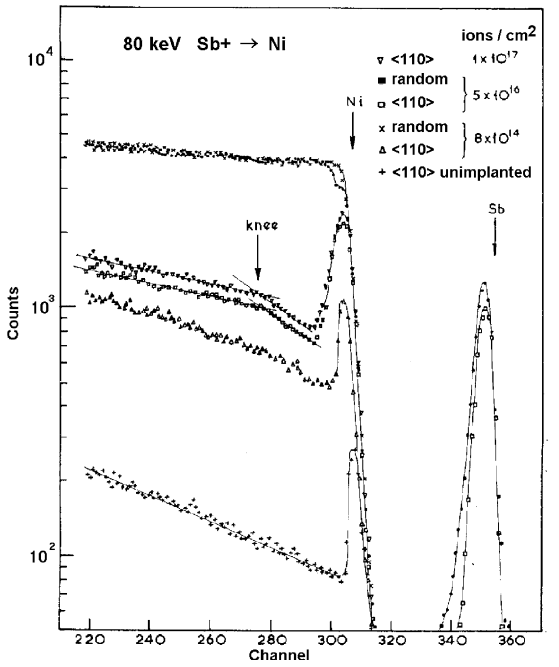

Fig. 13. Random and aligned backscattering spectra from a 2 MeV ^{4}He helium beam on a (1 1 0)Ni crystal, for increasing fluence of 80 keV Sb^+ ion implantation, inducing crystal damage. From [26].

random backscattering spectra, corresponding respectively to a low and a high implantation dose. In Fig. 13, the higher the channel number the greater the energy of the backscattered ions. The high-energy peak corresponds to backscattering on Sb atoms, and the lower energy plateau to backscattering on Ni atoms. On this plateau, the lower the energy, the deeper the depth at which a backscattering event took place. In the random spectrum corresponding to a high implantation fluence, one observes a lowering of the high-energy part of the Ni plateau, corresponding to backscattering events on Ni atoms in the shallow region were Sb was implanted. This is related to the change of composition in this region. But the most interesting observation is the very strong influence of implantation on the aligned spectra. When the implantation fluence increases, one can notice the development and broadening of a peak of scattering yield on Ni atoms in the implantation zone. In the same time, there is a strong increase of the backscattering yield corresponding to the deeper part of the sample. One also observes a region just after the peak, in which the slope of the Ni plateau is stronger than at greater depths. All these behaviors are related to the implantation-induced displacement of Ni atoms from regular sites, along the path of the implanted species. These displacements have two main consequences on the interaction of the aligned ^{4}He probing beam with the crystal. First, the displaced Ni atoms are no more located in regions of the transverse plane where the ^{4}He ion flux is low. Thus, the backscattering yield on Ni increases in the near surface region corresponding to the implanted ion path; this is the origin of the backscattering yield peak observed. But one must also consider that there is an angular spread of the incoming ^{4}He beam when crossing this perturbed crystal region. As a consequence the transverse energy distribution associated to the beam is shifted towards larger $E_\perp$ values, which in turn increases the backscattering yield on Ni atoms even if they occupy regular lattice sites. This explains the increase of this yield, when compared to the one corresponding to an unimplanted crystal, even in deep regions where no defects are present. This 'dechanneling effect' can be clearly seen in the region of the Ni plateau with high slope, behind the backscattering yield peak. In the corresponding depth interval, the fast increase of the backscattering level is more due to dechanneling than to direct encounter with displaced Ni atoms. In order to extract properly the depth distribution of the concentration of displaced atoms, one must then subtract properly the contribution of dechanneling, for instance behind the backscattering yield peaks of Fig. 13. Of course one must take into account the fact that this contribution steadily increases during the penetration of the probing beam in the perturbed region. The evaluation of the dechanneling rate is not easy as it depends strongly on the nature of the defects. For instance, the dechanneling induced by point defects is due to incoherent multiple scattering and one can show that dechanneling is in this case a decreasing function of the probing ion velocity. On the contrary, extended defects like dislocations induce a somewhat coherent beam bending, and, in this case, the dechanneling efficiency increases with the probing ion velocity. Finally, in order to

check precisely the positions occupied by the displaced atoms, one must determine the close encounter yields along various crystalline directions, and, ideally, fit these yields through numerical simulations. The study of defects by ion channeling can then provide precise and quantitative information, but it is a difficult task.

3.2. Nuclear Physics: fission time measurements

These measurements are based on the fact that channeling and blocking yields $\chi(\Phi)$ corresponding to a given population of scattering or emitting centers crucially depend on the sites occupied by this population, with respect to regular lattice sites. To illustrate this feature, we show in Fig. 14, from [27], three channeling dips, performed with the same incoming beam, across the $\langle 1\,1\,1\rangle$ axis of a W crystal. The first one corresponds to backscattering events, the second to tungsten L-X-ray production and the third to the emission of M-X-rays. The first two dips are nearly identical. Both of them imply collisions with W atoms at impact parameters much smaller than ρ, the 2-D rms. vibration amplitude of W atoms (the L-shell of W is well localized at this scale). On the contrary, for the M-shell, vacancies can already be produced at impact parameters somewhat larger than ρ. They may then originate from ions of transverse energy smaller than $Z_1U(\rho)$. The consequence is that the associated dip is narrower and that the minimum yield is significantly larger than in the first two cases. Of course, due to the reversibility principle, the same conclusions hold for blocking: the lower the potential energy associated to the position of the emitting centers, the narrower and the less pronounced the dips. The analysis of such dips and, if necessary, their fit by simulations, should then provide the positions of the emitting centers.

This is the basis of the fission time measurements. Excited nuclei, decaying mostly by fission, are produced in a crystal by collision of energetic ions with crystal atoms (the incident ion beam is sent along a random direction in order not to extinct the collision probability). These excited nuclei recoil along a given direction with a velocity that can be determined by the kinematics of the collision. After a certain path, related to their lifetime and velocity, fission may occur and the charged fragments will be emitted isotropically in the frame of the excited nuclei. These fragments will be submitted to the blocking effect to an extent that

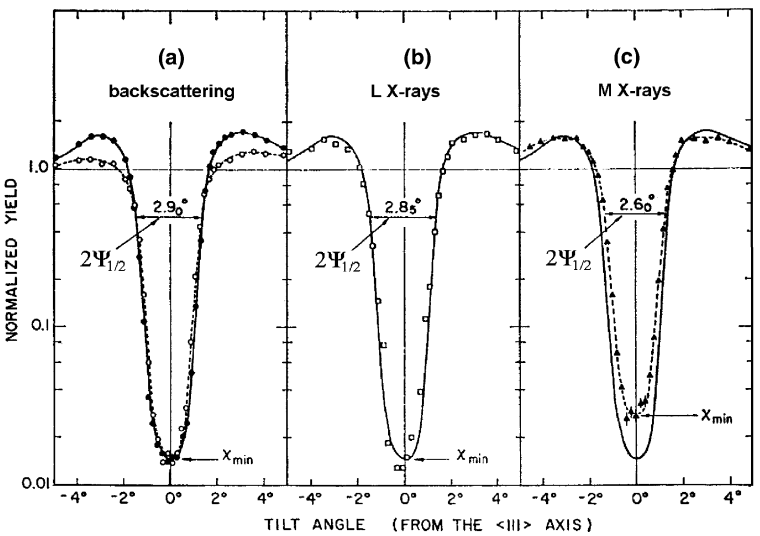

Fig. 14. Comparison of three angular scans across the [1 1 1] axis of a W crystal, with 1.4 MeV ^{4}He incident ions: (a) backscattering events from two depth windows respectively centered around 1200 and 5000 Å; (b) L-shell X-rays yield and (c) comparison of backscattering and M-shell X-rays yields. The data are from [27].

depends on the location, with respect to lattice sites, from which they are emitted (see the first paragraph of the present subsection). The analysis of the blocking dips appearing on position-sensitive fragment detectors should then provide the distribution of the time elapsed between the collision and the fission events. The shape of the dips and the associated minimum yields vary continuously when the emission point of the fragments is located at distances from atomic strings between 0.1 Å (typical order of magnitude of ρ) to a few Å (typical interatomic distances). The range of times that can then be reached will depend on the recoil direction and velocity. Practically the accessible time window is between a few 10^{-19} and 10^{-16} s.

The fissile excited nuclei that we are considering are complex dynamical systems. The time dependence of the fission probability depends on the interplay between cooling down (via evaporation of neutrons or of light charged particles and γ emission) and deformation towards the saddle point at which the fission process becomes irreversible. The velocity of the deformation is limited by the nuclear viscosity, which in turn depends on the time-decreasing nucleus temperature. Fission time measurements are thus expected to provide information on nuclear dissipation. The shape and extension of fission time distributions also depend strongly on the evolution with the residual excitation energy of the activation energies associated respectively to particle evaporation and to fission. The values reached by these activation energies at low residual excitation energy will determine the probability of fission events with long associated times. Such events are expected to occur for highly fissile nuclei.

One can then expect that the distribution of fission time should have complex shapes departing from a simple exponential decay characterized by a single decrement. In such a situation, the characterization of the distributions by only a mean 'lifetime' is obviously insufficient. The existence of a very low tail extending towards very long times will drastically affect the mean lifetime without changing significantly the shape of the body of the distribution.

An interesting feature of lifetime measurements via the study of blocking yields is that the latter depend very much on the shape of the lifetime distribution and not only on mean values. This is clearly demonstrated in Fig. 15 from [28] which represents the simulation of blocking dips in the vicinity of the $\langle 1\,1\,0\rangle$ axis of a thin Si crystal for $Z = 41$ fission fragments generated by a 29 MeV/u Pb beam incident on the crystal 5° off the axis direction. In the simulations various mean lifetimes τ and various distribution shapes were assumed. For exponential shapes the blocking effect is maximum for $\tau \leqslant 3 \times 10^{-19}$ s. The blocking dip is already significantly narrower for $\tau = 10^{-18}$ s, the blocking effect is highly reduced for $\tau = 10^{-17}$ s and disappears above $\tau = 10^{-16}$ s. But the most striking effect displayed on Fig. 15 is the very strong difference between the blocking dip associated to an exponential decay characterized by $\tau = 10^{-17}$ s and the one associated to a two-component distribution of the same mean lifetime. The latter is the weighted sum of two exponential decays, the first one (97%) with $\tau_1 = 10^{-19}$ s, and the second one (3%) with $\tau_2 = 3 \times 10^{-16}$ s. The weighted sum of τ_1 and τ_2 provides a value $\langle\tau\rangle = 10^{-17}$ s. The lifetime associated to this distribution is thus fully dominated by the small component with long lifetime, but, of course, the blocking dip is mainly determined by the strong component with the short lifetime. It is thus much closer to the dip with an exponential decay

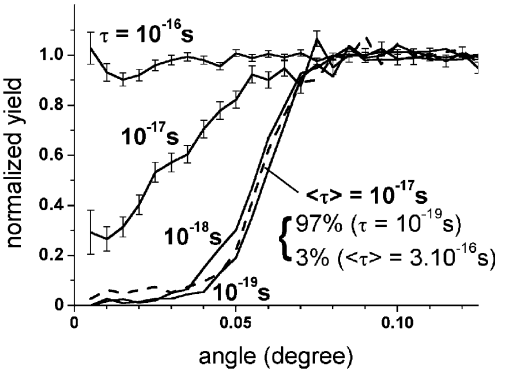

Fig. 15. Simulation of blocking dips, across the [1 1 0] axis of an Si crystal, for $Z = 41$ fission fragments originating from 29 MeV/u Pb nuclei incident 5° off the axis. Various fission time distributions are used. (Solid lines) Simple exponential decays with various decrements and (dashed line) two-component time distribution (see text). From [28].

characterized by a decrement of 10^{-19} s than to the one with a decrement of 10^{-17} s. However, the influence on the dip of the weak component with a low lifetime is detectable if the experimental statistics is appropriate.

In fact, one of the major findings of blocking measurements is the unambiguous evidence that very long lifetime components ($\tau > 10^{-17}$ s) frequently exist in the fission time distributions [4,5,28,29]. This is in no way an artifact related to the technique, as there are systems for which blocking experiments clearly show that there is no long lifetime [30]. Other techniques devoted to the measurement of fission times, such as the study of pre-scission emission multiplicity [31] are unable to reveal such components. However, in order to determine up to what extent the filling of the blocking dips is related to the existence of a long lifetime component, one must also search for all other possible contributions to this filling. This can be done in principle by registering blocking dips for ions produced in the very same crystal without any long lifetime component. This is the case of ions elastically scattered, giving rise to the blocking dip shown in Fig. 5. For such ions some filling of the dips may arise from the existence of crystal defects, but it can also be partially due to incoherent multiple scattering that may re-orient the trajectory of an ion parallel to crystallographic directions. This effect, called 'feeding-in' is the reverse of the dechanneling effect mentioned in Section 2. There is still another source of feeding-in that is specific of fission fragments and thus does not affect the blocking dips of elastically scattered ions. This source is the post-fragmentation neutron emission. The efficiency of such an emission is maximal if it takes place when the fragment is far from strings or planes, i.e. if mostly all its transverse energy is kinetic. In such a situation the trajectory re-orientation induced by neutron emission may, for given emission directions, reduce the transverse energy of the fragment. The influence of post-fragmentation neutron emission is thus not only related to the mean number of emitted neutrons and to their energy distribution, but also to the time distribution of the emission. All these features can be predicted theoretically in a quite reliable way, and thus the effect of post-fragmentation neutron emission can be rather well accounted for.

Moreover, collisions between energetic ions and crystal atoms produce a wide variety of excited nuclei, with a wide range of excitation energies. These nuclei may fragment in a more or less symmetrical way. In order to extract interpretable data, one has to determine the lifetime distribution associated to a given type of fragmentation, from a given excited nucleus, with a given initial excitation energy. This has been achieved for instance in [5], devoted to the study of the fission of uranium-like nuclei. Those were produced by collision of ions from a ^{238}U beam of 24 MeV/u with the nuclei of a Si crystal. The two fragments, A and B, produced after a collision were detected in coincidence, and their atomic numbers determined, using position-sensitive telescopes. For neutron rich nuclei like uranium, the charged particle evaporation is negligible and thus $Z_A + Z_B$ is the atomic number of the excited nucleus before fragmentation. Only events such that $Z_A + Z_B = 92 \pm 5$ were selected, and they thus arise from uranium-like excited nuclei. The initial excitation energy was determined by measuring, event by event, the neutron multiplicity, using a high efficiency 4π neutron detector inside which the goniometer supporting the Si crystal was placed. We show in Fig. 16, from [5], the blocking dips associated to various ranges of neutron multiplicity, i.e. to various ranges of initial excitation energies. It clearly appears that the dips corresponding to low multiplicities, i.e. to low initial excitation energies, are the most filled. However, the width of the dips appears to remain rather constant, whatever the filling is. This behavior can only be interpreted by assuming that there is a two-component lifetime distribution with, respectively, a very short ($<3\times10^{-19}$ s) and a very long ($>3\times10^{-17}$ s) associated mean value. For high neutron multiplicities, i.e. strong initial excitation energies, the weight X of the component with long mean lifetime is negligible. This weight continuously increases when the initial excitation energy decreases, and may reach 30–40% for neutron multiplicities smaller than 4, which correspond to initial excitation energies smaller than 50 MeV.

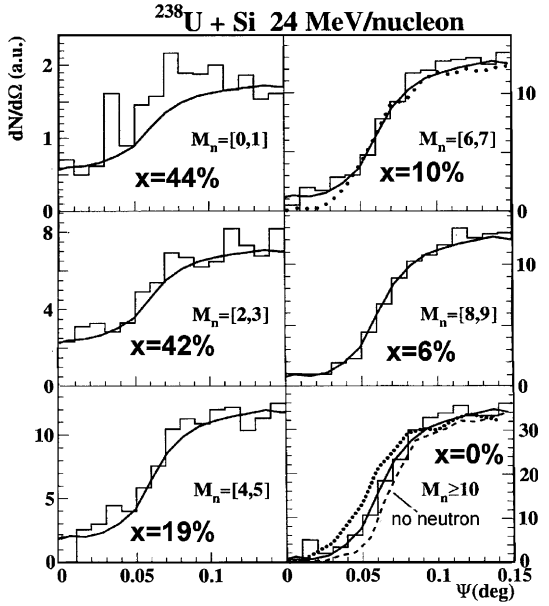

Fig. 16. Blocking dips, across the [1 1 0] axis of a Si crystal, for fission fragments originating from U like nuclei after collision of 24 MeV/u ^{238}U, with target nuclei. The full lines correspond to fits performed assuming a two-component time distribution (see text). The dotted lines correspond to the best fits obtained assuming exponential time distributions. In the fits the influence of post-scission neutron emission is taken into account. The various dips correspond to various total neutron multiplicities M_n, and thus to various initial excitation energies. From [5].

To conclude, fission time measurements by the blocking technique bring specific information on long lifetime components. They also allow an analysis of the shapes of the time distributions.

4. Energy loss and charge exchange in channeling geometry: interaction with a dense, non-uniform electron gas

We will first present general considerations on energy loss and charge exchange processes in Sections 4.1 and 4.2, respectively. The experimental results that are presented in Sections 4.3 and 4.4 often correspond to the 'high velocity regime' in which the ions velocity is significantly larger than the mean orbital velocity of target or projectile electrons. In such a situation the ions are nearly fully stripped and can be considered as point charges. This is, however, not the case for the results presented in Sections 4.3.4 and 4.4; here the ions are in the 'intermediate velocity regime', heavy ions may carry many electrons, not always highly localized in the nucleus vicinity, and charge changing cross-sections are high.

4.1. Energy loss

4.1.1. General considerations and theoretical approaches

The slowing down of ions in crystals is strongly affected by channeling effects. The energy loss distribution $g(\Delta E)$ of an initially monokinetic ion beam transmitted through a crystal in channeling geometry is much broader than after transmission along a random direction. The mean energy loss is generally significantly smaller in channeling; the lower edge of $g(\Delta E)$ corresponds to losses that can be less than one half of the mean random loss, and the upper edge to losses that can be nearly twice the mean random loss. This is illustrated in Fig. 17 that shows the energy distributions of a Pb ion beam, with an initial energy of 29 MeV/u, after crossing a thin Si crystal, respectively along a random and a $\langle 1\,1\,0\rangle$ axial orientation. In this figure, the energy losses in channeling geometry are normalized to the mean random loss, after taking into account a correction factor related to the

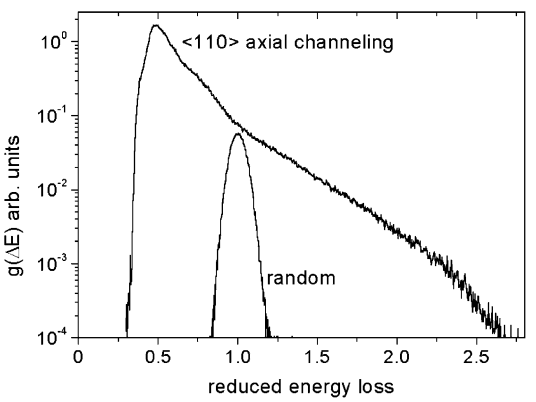

Fig. 17. Energy loss distributions obtained with 29 MeV/u incident Pb^{56+} ions transmitted through 1.1 μm of Si. $\langle 1\,1\,0\rangle$ axial and random crystal orientations. The energy loss is normalized to the random energy loss value, and corrected from a Q^2 dependence (see text). The integrals are not normalized.

different charge states at the crystal exit (see Section 4.3.2). The very broad distribution observed in the axial case is related to the fact that ions with different $E_\perp$ explore different accessible transverse areas ($AE_\perp$). Thus they sample different impact parameter distributions and electronic densities. The analysis of $g(\Delta E)$ can then provide information on the stopping power $S(E,r)$ at various distances r from the crystal axes or planes.

In order to interpret such data, an impact parameter description of the energy loss processes is required. In what follows, we will consider separately the contribution of rather localized and tightly bound core-shell target electrons and of the delocalized valence or conduction target electron gas. We will also suppose that ions can be described as point charges of fixed value Qe. Effects related to deviations from this behavior will be mentioned at the end of this subsection.

In what concerns the interaction with core target electrons, various impact parameter treatments, at different levels of approximation, are available. However, most of these treatments have restricted domains of applicability. These restrictions are related to the value taken by the Bohr parameter $\kappa = 2Qv_o/v$ characterizing the interaction of an ion of velocity v with an electron at rest.

If one has: (i) $\kappa > 1$ and (ii) $v > v_e$, where v_e is the orbital velocity of the target electron considered, a classical description of the slowing-down process can be used. In the corresponding theory, proposed by Bohr [20], target electrons are considered as classical oscillators. In random media the stopping power is then given by

$$\frac{dE}{dx} = \frac{4\pi Q^2 e^4}{m_e v^2} N Z_2 \ln \frac{b_{max}}{b_{min}} = \frac{4\pi Q^2 e^4}{m_e v^2} N Z_2 \ln \frac{1.123 m_e v^3}{Qe^2 \langle\omega\rangle}, \quad (13)$$

where N is the atomic density, $b_{max} = 1.123v/\langle\omega\rangle$ is a mean adiabatic cut-off (for $b > b_{max}$ the collision time exceeds the mean orbital period) and $b_{min} = b_o/2 = Qe^2/m_e v^2$. The mean frequency $\langle\omega\rangle$ is defined by $Z_2 \ln(\langle\omega\rangle) = \sum_f f_f \ln(\omega_f)$, where f_f are the dipole oscillator strengths and ω_f the frequencies associated to transitions between the atom ground state and well defined final states indexed by f.

If $\kappa < 1$, i.e. at high ion velocities and/or low Q values, a perturbation quantum treatment is well adapted. In random media, it leads to the well-known Bethe stopping power [32]:

$$\frac{dE}{dx} = \frac{4\pi Q^2 e^4}{m_e v^2} N Z_2 \left[\ln \frac{2 m_e v^2}{\hbar\langle\omega\rangle} + \ln \gamma^2 - \beta^2 \right], \quad (14)$$

where $\beta = v/c$, $\gamma = (1-\beta^2)^{-1/2}$. $\hbar\langle\omega\rangle = I$ is the mean logarithmic excitation energy per electron associated to the mean frequency $\langle\omega\rangle$ already defined. Surveys of stopping power for fast ions can be found in [33,34] and references therein. For practical use, the energy loss, the straggling (in energy and angular), the range of ions in matter, as well as effects related to collision cascades over a wide range of energy can be computed in 'random media' by simulation codes like SRIM [35].

Recently, Schiwietz and Grande [36] have used the non-perturbative Bloch theory [37] to propose an approximate and simple impact parameter description that is valid in the whole range of impact parameters with respect to electrons, and that applies for any κ value. The Bloch stopping formula tends asymptotically towards the Bohr formula (13) and the Bethe formula (14) for respectively great and small κ values. In a first step, Schiwietz and Grande calculate the energy transfer $T(b_e)$ to a bound electron at impact parameter b_e. They find

$$T(b_e) = T_{sudden}(b_e) \times h(v,\kappa,b_e) \times \sum_f f_f g\left(\frac{b_e \omega_f}{v}\right), \quad (15)$$

where $T_{sudden} = 2Q^2 e^4/m_e v^2 b_e^2$ is the energy transfer to a free electron when neglecting the electron recoil (momentum approximation). The summation, weighted by the dipole-oscillator strengths f_f, is performed over all the final states reached by transitions, with frequencies ω_f, that imply the considered electron. The functions h and g are explicitly given in [36]. The function h tends towards 1 when b_e becomes larger than the shell radius b_{shell} of the bound target electron. For $b_e < b_{shell}$, the function h decreases rapidly, compensating the divergence of T_{sudden} when $b_e \to 0$.

This divergence, without physical meaning, is related to the fact that the momentum approximation does not hold for collisions with small b_e at the scale of b_0 or of the wavelength associated to an electron of velocity v. The function g, the expression of which is already derived in [38], depends only on the ratio between b_e and the adiabatic impact parameter cut off v/ω_f. It accounts for the binding of the target electron. At impact parameters greater than v/ω_f the target electron adjusts more and more adiabatically to the slow varying external field, and the function g tends asymptotically towards 0. For impact parameters smaller than $0.5v/\omega_f, g$ is practically equal to 1.

The next step of the calculation in [36] is to extract the energy transfer $T_{at}(b)$ in a collision with an atom at impact parameter b. The authors show that one has simply

$$T_{at}(b) = \int d\vec{r}\, T(b_e)\rho_e(\vec{r}), \tag{16}$$

where $\rho_e(\vec{r})$ is the electronic density at point $\vec{r}$ with respect to the target nucleus. The integral in Eq. (16) is calculated numerically.

In the same way, one can calculate the contribution of core target electrons to the energy loss of a channeled ion, at a given point of the transverse plane, considering the core electrons associated to the strings delimiting an axial channel (see Fig. 4). Such a calculation has been performed in the frame of the classical oscillator approximation (case of swift heavy ions with $\kappa > 1$) in [39], and a similar analysis is available in [7]. In both papers the target was a Si crystal and only well-channeled ions were considered. The accessible transverse space of these ions was outside the shell radius of the target core-electrons and thus the value of the function h in relation (15) was equal to 1.

The authors of [7,39] have also evaluated the contribution to slowing down due to the valence or conduction electrons, of mean density $\bar{\rho}_g$. This quasi-free Fermi gas can be characterized by the plasma frequency

$$\omega_p = (4\pi\bar{\rho}_g e^2/m_e)^{1/2}. \tag{17}$$

ω_p is of the order of 10 eV, and, for swift ions, the associated adiabatic cut-off parameter v/ω_p is very large, much higher than the radius r_0 of a unit cell in the transverse plane. In such a situation the treatment used for the evaluation of the core electron contribution cannot be applied. It would concern a much too large number of electrons and, moreover, at large distances from the ion, one cannot anymore describe the slowing down in terms of individual binary collisions. Then, in [7,39] the authors have divided the energy losses in two fractions, corresponding respectively to close and distant collisions. The first part is due to energy transfers to the valence electrons inside the unit shell radius, inside the channel where the ion lies. The corresponding energy loss was obtained by integration, over the impact parameters with respect to the ions, of transfers T_{sudden} to free electrons, with a weight given by the local electron density. The contribution of more distant collisions, at impact parameters greater than r_0 (the radius of the unit cell, in the transverse plane, that is associated to a string of atoms) was obtained via relation (13) in which b_{min} was replaced by r_0 and b_{max} by the adiabatic cut-off impact parameter corresponding to a frequency $\langle\omega\rangle = \omega_p$.

We now come back to the assimilation of the ions to point charges. This assimilation becomes questionable when the shell radius of the electrons that remain attached to the ion are no more small at the scale of the impact parameters involved in the collisions leading to the slowing down. This is an important effect at moderate velocities. Usually, the ion size is taken into account by introducing an effective charge Z_1^* instead of the real charge Q in expressions giving energy transfers or stopping powers, like the relations (13)–(15). The problem of the screening of non-fully stripped projectiles has been recently addressed in [40,41]. We will see in Section 4.2 that, at a given velocity, the mean charge-state of channeled ions may markedly differ from the equilibrium charge-state in random media. This must of course be taken into account when analyzing energy losses in channeling.

We finally address the question of energy loss fluctuations ('energy straggling'). Energy loss is a stochastic process. Let us consider an ion with a given charge-state Q. As already pointed out, the energy loss of this ion can be divided in two parts. The first one arises from distant collisions; it can

be considered as a continuous slowing down, and its contribution to energy straggling can be neglected. The second one, related to individual binary collisions is usually the main cause of energy straggling. In a binary collision model, the number of energy transfer events for a given path δx in matter is a random variable, and so is the energy transferred in each collision. Thus there is an energy loss distribution, the mean value of which defines the stopping power S through $\langle \delta E \rangle = S\delta x$. If the width of this distribution is large with respect to the maximum energy transfer in one single interaction, the distribution tends towards a gaussian, the width of which is associated to a variance $\delta\Omega^2$. In random media, the upper limit of $\delta\Omega^2$ has been estimated by Bohr [20]. It applies to ions of velocity larger than the orbital velocity of all target electrons. Introducing corrective factors due to relativistic effects one gets the relation

$$\delta\Omega^2 = 4\pi Q^2 e^4 \rho_e \delta x \gamma^2 X = \delta\Omega_B^2 \gamma^2 X, \tag{18}$$

where $\delta\Omega_B^2$ is the non-relativistic Bohr result, γ the Lorentz factor and X a correction factor due to the departure from the Rutherford scattering law at relativistic energies [34].

For lower ion energies two effects should be considered. First, as seen above, there is a definite lowering of energy transfers to tightly bound electrons, which can be taken into account by introducing a reduced value of ρ_e in relation (18). This effect, that tends to lower $\delta\Omega^2$, is somewhat compensated by effects related to charge exchange, that plays a major role for heavy ions at high and intermediate velocities. The mean charge-state of such ions in matter fluctuates around a mean value, which has two consequences on energy loss processes. First, to each charge value is associated a given stopping power value (see relations (13) and (14)). Second, any charge exchange process involves an energy transfer. For these two reasons, the charge state fluctuations introduce energy loss fluctuations that have been recently shown to be dominant, when compared to the values obtained by relation (18), for slightly relativistic heavy ions in low Z targets [42].

We now come to the case of channeled ions. We have seen that, in channeling geometry, the very broad energy loss distribution is associated to the transverse energy distribution: it does in no way reflect the energy loss fluctuations of a given ion. Such fluctuations are reflected in the energy loss distribution of ions of given $E_\perp$. We consider here the case where these ions have a long enough path to explore uniformly their available accessible transverse space $A(E_\perp)$. The variation of energy losses that may occur along the ion trajectories during this exploration will be considered in the next subsection. We have seen that the energy straggling given by relation (18) is due to close collisions. In order to estimate its value for a well-channeled ion with low $E_\perp$, one must then introduce in relation (18) a value of ρ_e equal to the mean electron density sampled by this ion in its accessible transverse space $A(E_\perp)$. As ρ_e is much smaller than the average electron density in the solid, the value of $\delta\Omega^2$ is strongly reduced. Also, we will see in Section 4.2 that the dominant charge exchange processes take place in the vicinity of nuclei, and are thus suppressed for well channeled ions that are confined near channel centers. As a consequence, these ions will also be less submitted to energy loss fluctuations in connection with charge exchange. The general conclusion is thus that ions with low and well-defined $E_\perp$ experience energy loss fluctuations much lower than random ions.

4.1.2. Impact parameter dependence of stopping rate: measurements

The first systematic study of the variation of energy loss with the transverse energy $E_\perp$, and thus the accessible transverse space $A(E_\perp)$ of an ion has been achieved by Datz et al. [10], in planar channeling experiments. Planar channeled ions oscillate between two adjacent atomic planes. The planar potential is non-harmonic, and thus the wavelength associated to the oscillations depends on the oscillation amplitude, which, of course, increases with $E_\perp$. This feature was used in [10] in transmission type experiments through thin gold crystals. The incident beam was sent parallel to the (1 1 1) plane. A very collimated detector was used to receive only the ions leaving the crystal precisely along the incident direction and to analyze their energy. These ions have necessarily undergone an

integer number n_i of half-oscillations inside the planar channel. To each value of n_i corresponds a distinct and narrow $E_\perp$ window. The registered energy loss spectrum thus consists in distinct peaks, the positions of which provide the stopping rate values associated to the set of selected $E_{\perp i}$. These values are averaged over a half-oscillation, i.e. over the accessible $A(E_{\perp i})$. Inside this area, the local energy loss rate may vary considerably, in connection with the local variations of the electronic density, especially if the ion has a high $E_\perp$. The experiments of [10] can provide estimates of the local value of the stopping power, at given distance from an atomic plane, when comparing the losses suffered by ions having respectively undergone n_i and $n_{(i+1)}$ half-oscillations. This comparison gives the stopping rate in the region between $A(E_{\perp i})$ and $A(E_{\perp(i+1)})$.

A measurement of the local stopping rate very close to atomic strings has been performed by Vickridge et al. [43]. In this work, the excitation curve (yield as a function of incident beam energy) of the very narrow and quasi-isolated resonance of the nuclear reaction ^{27}Al(p, γ)^{28}Si has been registered, by scanning the proton beam around the resonance energy (992 keV), in random and axial alignment geometry on an Al crystal. In channeling, only the ions entering the crystal at distances from the strings of the order of the thermal vibration amplitude of the Al atoms (about 0.1 Å), can induce the reaction. Moreover, the reaction can take place only near the surface, in the small fraction Δx of the ion's path during which they remain at such small distances from the strings, i.e. before the shadow cone radius becomes too large. The thick Al crystal thus behaves as a thin target and the excitation curve consists in a narrow peak. The integral of the peak is fixed by the value of Δx. However, at given integral, the height and width of this peak are determined by the local stopping power, i.e. by the number of atomic collisions required to loose an energy amount equal to the resonance width. The higher the stopping rate, the smaller the peak height and the larger the peak width. For the 1 MeV protons used in [43] it was found that the local electronic stopping very close to the strings was an order of magnitude larger than the random stopping.

In Section 4.4, we will give examples of stopping rate measurements for ions remaining at very large impact parameters from atomic strings, of the order of r_0 (hyperchanneled ions).

4.2. Charge exchange

Let us first start this section with some semantical notions, in order to clarify the various processes that will be discussed therein.

Ion ionization may occur by impact on a target nucleus (Nuclear Impact Ionization, NII) or on a target electron (Electron Impact Ionization, EII). At high energies, ionization cross-sections roughly scale as the square of the target charge and thus NII cross-sections are generally much higher than EII ones, except for very light targets. This is also true for inner-shell excitation of the projectile (Nuclear Impact Excitation, NIE, and Electron Impact Excitation, EIE).

At high velocity, electron transfer from a target atom into a bound state of a projectile ion restricts to a three-body process. Energy and momentum conservation may involve the recoil of the target atom. We will refer to this process as the Mechanical Electron Capture (MEC). Alternatively, the excess energy and momentum corresponding to the electron capture can be carried out by a photon. This process is called radiative recombination when the initial state corresponds to a free electron, and Radiative Electron Capture (REC) for an initially bound electron. Radiative recombination is the time reverse process of the photoelectric effect. In a third mechanism, electron capture can be resonant when the energy of the transition between the initial and final state of the electron matches the energy of an electronic excitation of the ion. This resonant capture process is called Dielectronic Recombination (DR) for an initially free electron and Resonant Transfer and Excitation (RTE) for a bound target electron. Dielectronic recombination is the time reverse of the Auger emission. RTE and DR can occur only at given resonant projectile energies, and for given initial electronic configurations (in particular it is forbidden for bare ions).

NII and MEC are generally the dominant charge exchange processes between a swift heavy

ion and an atomic target (except for highly relativistic ions, and/or very low Z_2 values of the target atoms). As ions penetrate inside a target, their electronic configurations evolve until ionization and capture probabilities level, leading to charge equilibrium after penetration through a given target thickness. Fluctuations in the balance between capture and loss events lead to a charge state distribution around the equilibrium charge. At equilibrium, the occupancy of an electronic shell with principal quantum number n is mainly characterized by the adiabaticity parameter $\eta_n = v_{ion}/v_n$, v_n being the average electron velocity in a projectile bound state, and v_{ion} the ion velocity. As predicted by Bohr, if $\eta_n < 1$, the n-shell is filled, and if $\eta_n > 1$, it is empty. To a lesser extent the equilibrium charge depends also on the atomic number of the target atoms.

NII and MEC involve the interaction of the projectile with the screened nuclear target Coulomb field, and are restricted to impact parameters of the order of the orbital radius of the electron in the bound state of the projectile.

As a consequence, for fast ions in channeling conditions, NII and MEC will be strongly suppressed because the non-uniform flux distribution inside the crystal favors large impact parameters. Also, this non-uniform flux allows one to study the impact parameter dependence of NII and MEC. This can be done over an impact parameter range extending from the rms. amplitude of the target atom thermal vibrations up to the maximum distance of approach to atomic strings or planes at which these processes may occur. In particular, studying MEC as a function of impact parameter is particularly attractive at low values of η_n, as we will see below.

Then, for well-channeled ions, ionization will occur through electron impact and capture will require the emission of a photon (REC), except at suitable energies for which the resonant RTE processes is allowed. As illustrated by the electron density map in Fig. 4(b), ions with the lowest transverse energies sense only very low electron densities. For instance, hyperchanneled ions (e.g. those that are confined inside equipotential 3 of Fig. 4(a)) sample in the average a density of $\sim$0.1 e Å^{-3}, which is 7 times smaller than the mean electron density in silicon. Moreover, this density arises only from quasi-free electrons of the valence or conduction bands. They will be characterized by a much narrower momentum distribution (Compton profile) than core electrons, located close to the atomic strings (typically inside contour 5 of Fig. 4(b)).

One can act on the electron density sensed by channeled ions by varying their associated transverse energy distribution. This can be done by slightly tilting the crystal, by angle $\delta\Psi < \psi_C$, thus by introducing a small misalignment between the crystal axis and the beam incidence. If the initial incidence was parallel to the axis, this misalignment will induce an increase by $E\delta\Psi^2$ of the transverse energy of channeled ions, that will enlarge their accessible transverse space, and accordingly the 'electron target thickness'. One can see in Fig. 4(b), when comparing contours close to the channel center and close to the atomic strings, that a tilt angle smaller than the channeling critical angle can lead to an enhancement by about one order of magnitude of the electron target thickness sampled by the best channeled ions.

We will now illustrate how this ability of channeled ions to experience a dense, non uniform electron target, can lead to original results on charge exchange

4.3. Combined energy loss and charge exchange measurements

The effect of channeling on the charge state distribution at the exit of a crystal target is the most dramatic when incident ions are very far from the charge at equilibrium. In this situation, one can access to exclusive information on ion-matter interaction, as we will see now.

4.3.1. $E_\perp$ selection: measurement of EII cross-sections and of hyperchanneled ions stopping

Fig. 18 presents the charge state distributions $F(Q_{out})$ obtained with 27 MeV/u Xe^{35+} incident ions (i.e. with 19 electrons) on a 20.7 μm thick silicon crystal target [12]. In this experiment, $\eta_L = 1.2$, and the charge at equilibrium in random conditions corresponds to a partly empty L-shell, as illustrated by the charge distribution $F_R(Q_{out})$

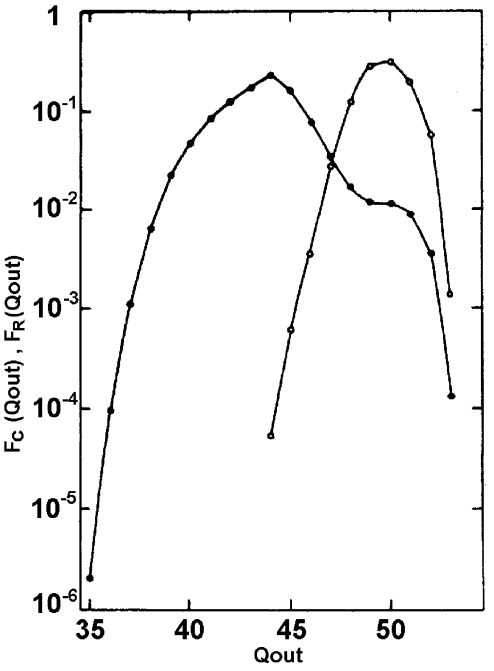

Fig. 18. Emerging charge state distributions of 27 MeV/u incident Xe^{35+} ions transmitted through 20.7 μm of Si: (Open circles) random conditions $F_R(Q_{out})$; (full circles) ⟨1 1 0⟩ alignment $F_C(Q_{out})$. From [12].

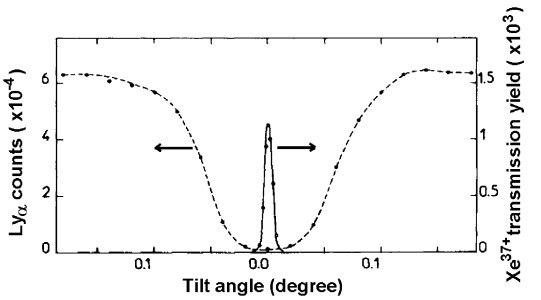

Fig. 19. Tilt angle dependence of $F_C(Q_{out} = 37)$ and Ly_α yield, in the vicinity of the ⟨1 1 0⟩ direction of a 20.7 μm Si crystal, for incident Xe^{35+} at 27 MeV/u. From [12].

associated to ions having crossed the crystal upon a random orientation. This charge distribution is centered around $Q_{out} = 50$, i.e. is far from the incident charge state. For ⟨1 1 0⟩ axial alignment, the charge state distribution $F_C(Q_{out})$ ranges from $Q_{out} = 35$ up to $Q_{out} = 53$. Actually, this distribution reflects the transverse energy distribution of channeled ions: ions with a high transverse energy experience all impact parameters, and their charge at the exit is close to the random equilibrium charge. For such ions, as well as for a random orientation, the balance between NII and MEC determines the charge distribution. On the other side, ions with the lowest transverse energy experience regions where the electronic density is very small. However, one can observe only a very small fraction of ions frozen in their initial charge state. This means that, even for channeled ions, for which NII is forbidden, ionization events by electron impact may occur. In Fig. 19 is shown the dependence of $F_C(Q_{out} = 37)$ (nearly frozen ions) on the crystal orientation relative to the axial direction. As a comparison the Ly_α yield is also shown. Ly_α emission results from K-shell excitation or ionization, which is only possible by nuclear impact (the kinetic energy is below the threshold for K-shell EII). Thus the Ly_α dip reflects the close collision extinction dip. It can be deduced from Fig. 19 that the critical transverse energy to emerge with $Q_{out} = 37$ is 5.6×10^{-3} times smaller than the critical channeling transverse energy given by Eqs. (4) and (5). Thus these ions are hyperchanneled. With the help of simulations, the mean transverse energy corresponding to each emerging charge state was determined, together with the mean sampled electron density. These correspondences are shown in Fig. 20. The EII cross-sections were evaluated for each charge state, as well as the impact parameter dependence of energy loss. For the best-channeled ions, the latter was found to be only slightly dependent on the local electron density. In other words, the energy loss at large distance from the atomic strings is dominated by distant collisions with the valence electron gas.

4.3.2. Emission of target electrons

Information on the impact parameter dependence of target ionization has been obtained recently by our collaboration group, in a similar study with 29 MeV/u Pb^{56+} ions incident on a thin silicon crystal (1.1 μm). Again the exit charge-state was used to discriminate over ions with different transverse energies. The energy loss was measured with a high resolution and the secondary electron

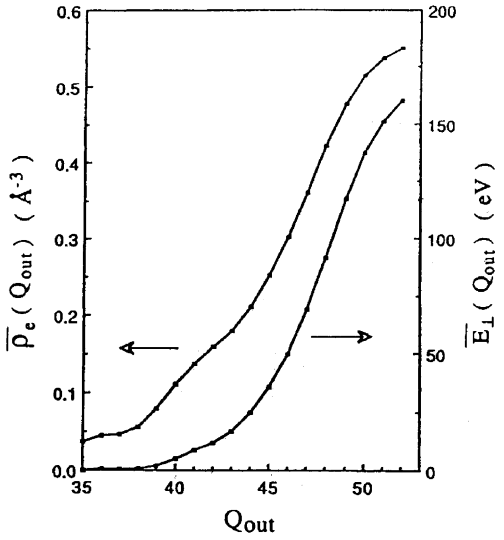

Fig. 20. Average transverse energy (per unit charge), and mean sampled electron density, as a function of emerging charge Q_{out}, for incident Xe^{35+} at 27 MeV/u sent on a 30.7 thick silicon crystal along the $\langle 1\,1\,0\rangle$ axis. From [12].

emission from both entrance and exit target surfaces for each ion impact was measured (electron multiplicities). As in the previous example, for $\langle 1\,1\,0\rangle$ axial orientation the charge state distribution at emergence, shown in Fig. 21, is very broad, reflecting the transverse energy distribution. It ranges from $Q_{out} = 56$ up to $Q_{out} = 78$, whereas the random charge distribution is centered around $Q_{out} = 69$. Fig. 22 shows various electron multiplicity distributions from entrance and exit target surfaces, together with energy loss distributions. These distributions correspond to different emerging charge states associated respectively to well channeled ions frozen in their initial charge state ($Q_{out} = 56$, Fig. 22(a)), and poorly channeled ions ($Q_{out} = 72$, Fig. 22(b)) in axial channeling conditions. The distributions obtained for random incidence, and corresponding to $Q_{out} = 72$ are also displayed in Fig. 22(b). As already mentioned in Section 4.1, we show in this figure reduced energy loss values ΔE_{red}, in units of mean random loss ΔE_R, with a first-order correction accounting for the mean ion charge state in the target: $\Delta E_{red} = \Delta E(Q_{out}) \times (2\langle Q\rangle_R^2/(Q_{in}^2 + Q_{out}^2)/\Delta E_R$, where $\langle Q\rangle_R$ is the mean random charge state inside the target and $Q_{in} = 56$. Well-channeled frozen ions emerge from the crystal with a mean reduced energy loss of about 0.5. From Fig. 21 they represent typically half of the total beam. In the energy loss distribution corresponding to the $\langle 1\,1\,0\rangle$ orientation, one can select the ions having lost the minimal energy (see the inset on the top left of

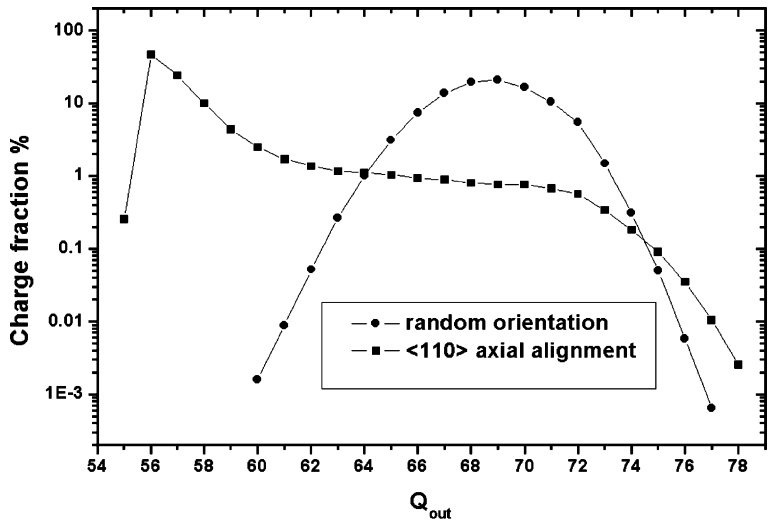

Fig. 21. Emerging charge state distributions for 29 MeV/u incident Pb^{56+} ions transmitted through 1.1 μm of Si in $\langle 1\,1\,0\rangle$ axial and random conditions.

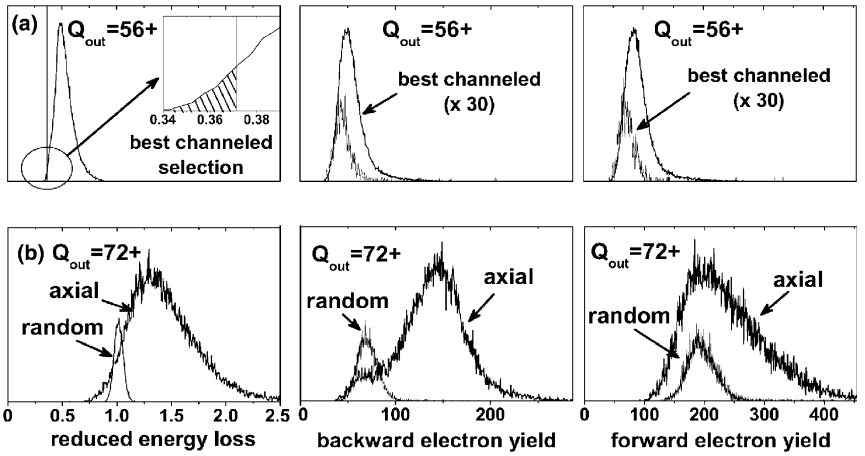

Fig. 22. Energy loss distributions, backward and forward electron multiplicity distributions obtained with 29 MeV/u incident Pb^{56+} ions transmitted through 1.1 μm of Si: (a) ⟨1 1 0⟩ axially channeled ions emerging with $Q_{out} = 56$. The inset in the first plot shows the selection of ions with the lowest energy loss. The electron multiplicity distributions corresponding to this selection are shown. (b) ions emerging with $Q_{out} = 72$, ⟨1 1 0⟩ and random conditions. The energy loss is normalized to the random energy loss value, and corrected from a Q^2 dependence (see text). The integrals of both multiplicity distributions and energy spectra are not normalized.

Fig. 22(a)). This very small fraction (about 0.5% of the total beam) has a reduced energy loss lower than 0.37. These ions are hyperchanneled. For poorly channeled ions (Fig. 22(b)), the situation is completely different: such ions enter close to the atomic strings and thus their energy loss is strongly enhanced close to the entrance. Once the atomic string repels them, their energy loss rate is reduced, until they approach again another string. As the crystal is thin, statistical equilibrium is not fully established at the exit. In the ion path, the number of close collisions with strings, during which the energy loss rate is very high, is small (typically between 1 and 4). It may exhibit strong relative variations when comparing the trajectories of two ions with very similar $E_\perp$. The resulting energy spectrum is very broad, and its mean value is much higher than the random loss. One can see in Fig. 22(b) that the maximum reduced losses measured extend up to 2.5. Although the target thickness is much larger than the path needed to reach the center of the channel for ions entering close to a string (about 2000 Å), high transverse energy ions may experience very large integrated electron densities.

Electrons collected from the surfaces are mainly low energy secondary electrons. The corresponding electron yield is correlated to energy loss, as illustrated in Fig. 22 for both backward and forward emissions. The backward yield for the best channeled 56+ ions is attenuated by a factor 0.6 with respect to the random yield. The same behavior is observed for the forward emission yield of these ions. In this latter case, as in random geometry the ions emerge with a higher charge-state than the frozen 56+ well-channeled ions, the comparison can be done after correction for the Q^2 dependence on the ion-electron collision cross-sections. The local electron density sampled by a hyperchanneled ion in the ⟨1 1 0⟩ axis is less than 15% of the average electron density of silicon, a reduction much stronger than the attenuation of the electron multiplicity for these ions. The attenuation of energy loss, which is due mainly to the extinction of close collisions near the channel center, is also much more pronounced. This shows that distant collisions are the main source for secondary electron emission by hyperchanneled projectiles.

For poorly channeled ions, one observes an enhancement by a factor of 2 of the backward electron multiplicity compared to random conditions. The maximum of the forward electron yield distribution is the same as in random condition,

with a tail extending towards large values. Ions with a high transverse energy may leave the crystal at any position in the transverse space, as in random conditions. Some ions may undergo close collisions along a string in the vicinity of the exit, which leads to the tail observed towards high forward electron multiplicities.

To conclude, electron multiplicities can be used to identify clearly the entrance impact parameter of channeled ions. It was deduced from these experiments that the forward electron multiplicities are not only the result of ionization events near the crystal exit, but may also arise from highly ionizing events, in relation with glancing collisions with strings, much deeper in the crystal. Thus the forward electron yield carries less information about the conditions of emergence than backward emission does about entrance conditions.

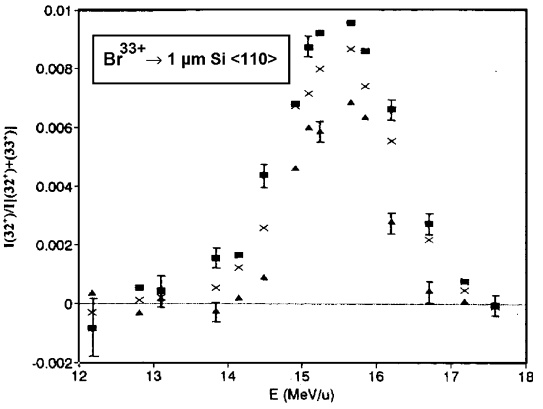

Fig. 23. Background subtracted charge state fraction $F_C(Q_{out} = 32)/(F_C(Q_{out} = 33) + F_C(Q_{out} = 32))$ as a function of the incident energy of Br^{33+} ions channeled in a 1 μm thick Si crystal, for three energy loss ranges, in units of the random energy loss: (squares) 0.55–0.62; (crosses) 0.48–0.55; (triangles) 0.41–0.48. The data are from [39].

4.3.3. Local longitudinal momentum distribution of target electrons

Local target-electron momentum distribution can also be inferred from charge exchange measurements in channeling. For KLL Dielectronic Recombination for instance, the resonance condition is (non relativistic) $((m_e/M_{ion})\vec{p}_{ion} - \vec{p}_e)^2/2m_e = E_K - 2E_L$, where $\vec{p}_{ion}$ and $\vec{p}_e$ are respectively the ion and electron momenta in the laboratory frame, E_K the initial K-shell binding energy, and E_L the L-shell binding energy in the final state. Thus the DR resonance profile is broadened by the longitudinal momentum distribution of the electron to be captured. Andersen et al. [39] have shown that the KLL DR resonance profile depends on the energy loss rate of channeled Br^{33+} ions in a 1 μm thick ⟨1 1 0⟩ Si crystal. Fig. 23 shows their data for the capture rate as a function of incident ion energy, for three adjacent energy loss windows, ranging between 0.41 and 0.62 times the random energy loss rate. Such ions sense mainly valence electrons of silicon. Both amplitude and width of the resonance are found to vary with the energy loss. The amplitude is directly proportional to the electron density, whereas the width depends on the electron Compton profile. Assuming that valence electrons behave locally like a Fermi electron gas, energy loss rates, DR amplitudes and the evolution of the resonance width could be reproduced quantitatively.

A detailed analysis of the target electron Compton profile was made by Andriamonje et al. [8], by observing REC photons. In the same way than a DR resonance is broadened, the energy of REC photons is spread by the longitudinal target electron momentum distribution. In the projectile frame, a target electron has a kinetic energy E_c, and the energy of a photon associated to the capture of an electron of initial binding energy E_i and longitudinal momentum p_z into the n-shell of the projectile is

$$h\nu_{n\text{-REC}} = E_c + E_n - \gamma E_i - \beta\gamma p_z c, \tag{19}$$

where E_n is the binding energy of the n-shell. Fig. 24 shows two X-ray spectra obtained with 60 MeV/u bare krypton ions incident on a 37 μm thick silicon crystal. K- and L-REC peaks are observed for both random and ⟨1 1 0⟩ axial orientation conditions. At such a high energy, the mean charge-state at equilibrium corresponds to bare ions, so that REC was observable for both random and channeling conditions in this experiment. For a random orientation, all target electrons of silicon contribute with the same weight to REC. The calculated contributions from core electrons (K- and L-shells of silicon) and valence electrons, that

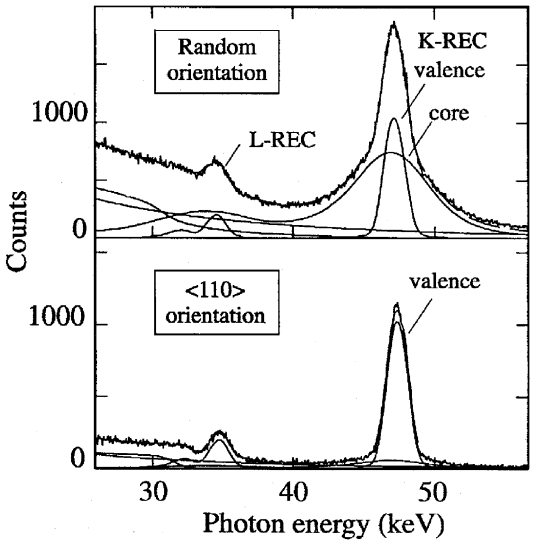

Fig. 24. X-ray spectra recorded at 90° in the laboratory for 60 MeV/u Kr^{36+} ions incident on a 37 μm thick silicon crystal. The spectra are normalized to the same number of incident ions. The solid lines show the calculated contributions of REC from valence and core electrons, and Bremsstrahlung. From [8].

have a narrower Compton profile, are drawn on the spectra. For ⟨1 1 0⟩ axial orientation, the core electron contribution drops down by one order of magnitude, whereas the valence electron contribution is only slightly reduced. By varying the crystal tilt angle from axial to random orientation, the authors of [8] could follow and interpret the evolution of both components. In particular impact parameter dependent Compton profiles for core electrons were required to reproduce the shape of the REC peaks at small tilting angles, i.e. when the ion flux distributions are non-uniform. Such a local information is not available by other techniques investigating Compton profiles, because they integrate uniformly over all impact parameters.

4.3.4. Deceleration of highly charged ions

We have seen that channeled ions have a reduced probability to undergo charge exchange, due, first, to their large impact parameters relative to the target nuclei and, second, to the reduced electron density far from the atomic planes and rows. One may use this property to decelerate highly charged ions (for instance bare or hydrogenic uranium ions) down to low energies where they are very far from charge equilibrium in random conditions, although the capture cross-sections increase dramatically with decreasing energy. The idea is that the very high charge of those slow ions may lead to extremely high energy-loss rates, despite the very low electron density encountered. There are three main limitations for deceleration of ions frozen in a high charge-state. The first one is related to the increase of transverse energy due to electronic multiple scattering (dechanneling). The second one is the increasing MEC probability at very large impact parameters: capture into highly excited states occurs when the projectile velocity is of the same order than the corresponding orbital velocity. The last limitation is due to the high probability of capture by REC in very thick targets: even if the electron density is very low at the center of a crystal channel, one must account for the strong increase of REC cross-sections at low energies. We now discuss the extent of these limitations.

Concerning the first point, the mean increase $\Delta E_\perp$ of transverse energy due to the scattering of channeled ions on target electrons can be estimated as a function of the total energy loss ΔE:

$$\Delta E_\perp = \frac{1}{2}\frac{m_e}{M_{ion}}\Delta E. \tag{20}$$

The factor 1/2 in Eq. (20) accounts for the fact that only close ion-electron collisions contribute to angular scattering. However, this close collision contribution drops down severely for very well channeled ions. As already stated in Section 4.3.1 when discussing the results of [12], the energy loss of hyperchanneled ions is essentially due to distant collisions, which do not lead to appreciable angular deflections. Thus Eq. (20) may overestimate considerably the increase of transverse energy for hyperchanneled ions. Note also, but this is a second-order effect, that for a given accessible transverse space, the reduction of the overall ion energy counteracts the spreading of the angular distribution ($\Psi_{max} = (E_\perp/E)^{1/2}$).

About the second point, channeled ions may avoid MEC as far as the Rydberg ion formed by a capture into a highly excited state has a much

smaller size than that of the crystal channel (i.e. the radius should not exceed 0.5 Å). In such a situation MEC is avoided for a well-channeled ion (remaining near the channel center) as there is no possible contribution of the target nucleus to an electron capture. Using the hydrogenic atom model of Bohr, one finds that the orbital velocity for a shell radius of 0.5 Å in a uranium atom is roughly $10v_0$. (it corresponds to a principal quantum number $n = 10$). This is the velocity of a uranium ion at 2.5 MeV/u. It is then hopeless to slow-down a H-like uranium ion in a crystal below this energy, but it is certainly worthwhile to try to obtain hydrogenic uranium ions at such low energies. One is also helped in this task by the fact that, even for well-channeled ions, electrons captured in highly-excited states have a strong probability to be lost through EII. Classical Transport Monte Carlo simulations have been undertaken recently by Grüner et al. [44] in the MeV/u energy region, that describe this competition between capture and ionization as a function of impact parameter in this intermediate velocity regime. We will come back on this point in the next section.

For the third point, concerning the probability of REC by hyperchanneled ions, a theoretical estimate is easier. REC cross-sections have maximum values for capture into the lower n states of the projectile, and thus REC can be treated as a local process. Actually, REC cross-sections are limited to less than 10^4 barns per electron for very heavy ions in the energy range described above (more than 2.5 MeV/u). Then, the survival probability for well channeled ions, sampling electron densities of about 0.1 e^-Å^{-3}, is non zero up to lengths of a few ten microns. This allows to decelerate considerably highly charged ions.

A first attempt has been performed at GSI with 20 MeV/u U^{91+} ions extracted from the ESR storage ring [45]. After a path length of 11 μm of silicon (⟨1 1 0⟩ alignment) nearly 30% of the incident ions remained frozen in their incident charge, and their energy loss was 4% of the initial energy, whereas the random energy loss rate was 5%. Starting from this result, Fig. 25 shows how the energy loss rate should evolve with energy for well-channeled U^{91+} ions. Since these ions do not capture electrons, the energy loss rate should continue

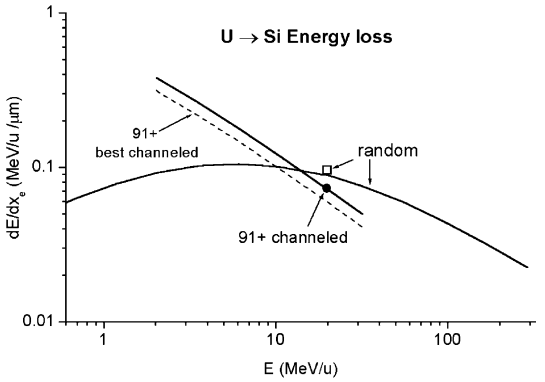

Fig. 25. Expected evolution of the energy loss for channeled U^{91+} ions in the ⟨1 1 0⟩ axis of silicon. The experimental data (circle: most probable energy loss in channeling, square: loss for random orientation) are taken from [45]. The random energy loss curve corresponds to SRIM calculations [38]. The dashed curve corresponds to the loss experienced by the best channeled ions.

to grow up like $1/v^2$ with decreasing energies. Below 15 MeV/u, we arrive at the paradoxical situation where channeled ions loose more energy than unchanneled ions, in relation with the Q^2 dependence of the stopping power. A recent and unpublished study with a thicker crystal and a lower incident energy confirmed this effect.

4.4. Breaking the reversibility rule: transverse cooling and heating

Recently, Assmann et al. [19] reported a violation of the channeling-blocking reversibility rule described in Section 2. This rule predicts in particular that an initially uniform angular distribution of ions should retain its uniformity when the ions cross a crystal. The authors of [19] have sent various beams, with uniform distributions over an angular range very large at the scale of channeling critical angles, on various crystals, and they observed strong anisotropies in the emerging beam. In some cases an enhancement of the angular distribution can be observed along crystallographic axes or planes (transverse cooling), in other cases transverse heating leads to a depopulation in these directions. Both heating and cooling phenomena depend on the ion velocity, on the projectile and target nuclear charges, and on the

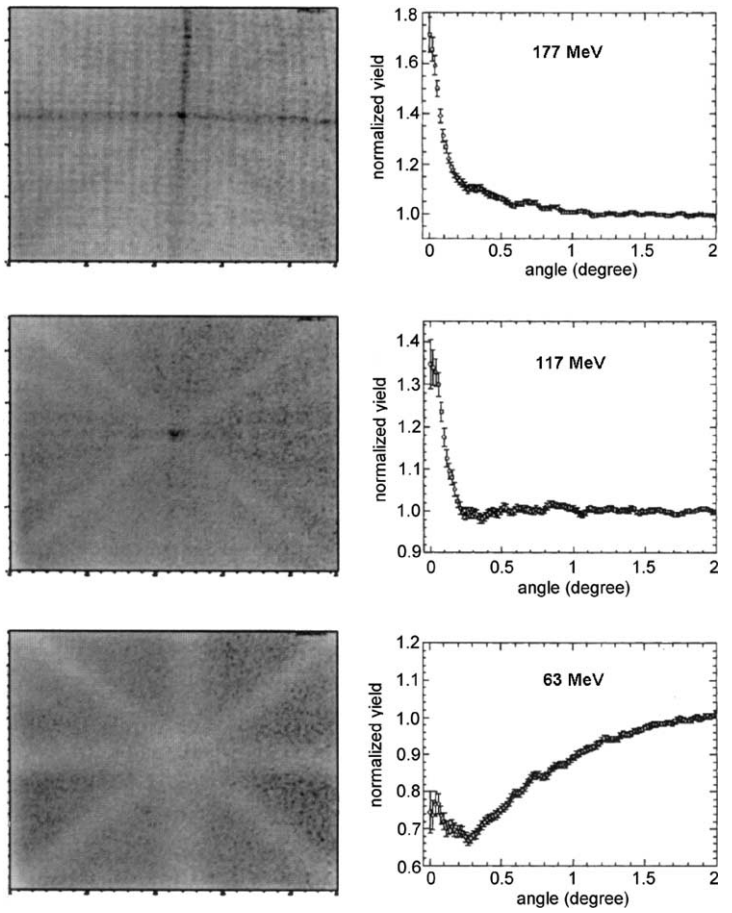

Fig. 26. Flux distributions for Y ions transmitted through a 3.4 μm thick silicon crystal, for various energies (at emergence); (right part) circular averaged distributions around the ⟨1 0 0⟩ axis. The incident ion energy decreases from the upper part (showing a cooling effect) to the lower part (showing a heating effect) of the figure. The data are taken from [46].

considered crystallographic direction. In particular, cooling to heating transitions occur when the energy of the beam of a given species decreases. Fig. 26 illustrates such a situation for Y ions transmitted through a 3.4 μm thick Si crystal [46]. The authors proposed that the dependence of charge exchange with impact parameter could explain the phenomenon, at least partially. Consider, for instance, an ion of charge Q and transverse energy $E_{\perp}$, given by Eq. (3). Its transverse motion is governed by a string potential per unit charge $U(r)$, which is a decreasing function of r. If a charge-changing event (single electron capture or loss) occurs at distance r, the transverse energy of the ion varies by $\pm U(r)$, and, in the mean time, the potential barrier associated to dechanneling varies by $\pm U(r_{\min}), r_{\min}$ being a typical minimum distance of approach to atomic strings or rows of the order of ρ. As $U(r_{\min}) \geqslant U(r)$, an electron loss leads to transverse cooling, while an electron capture leads to transverse heating. When charge equilibrium is reached the same number of ionizations and captures occur in the average. Let us then consider the situation of an ion experiencing a cycle consisting of an equal number n of capture and loss events. As the charge of the ion is conserved after the cycle, so is the potential barrier $Q \cdot U(r_{\min})$. Let us now call, respectively, r_{C} and r_{L} the average radii

associated to a capture and a loss event. The cycle will induce a change of the transverse energy of the ion whose absolute value is equal to $n(U(r_L) - U(r_C))$. Thus, if $r_C < r_L$, the cycle will induce transverse cooling and, conversely, if $r_C > r_L$, it will induce transverse heating. The overall heating or cooling efficiency is high if r_C and r_I differ significantly, and, of course, if the charge-changing cross-sections are large, which is the case for heavy ions at intermediate velocities. A few additional remarks are needed:

– In the experiments where cooling or heating patterns have been observed [19,44,46], charge exchange cross-sections are huge, and capture and loss processes take place at large impact parameters. In particular, capture occurs into excited states of the projectile, which may lead to a delayed auto-ionization, at large distance from the strings or planes. This could explain that cooling is more persistent along the major axial directions.

– A full theoretical description of the phenomenon has been undertaken [44] by means of n-body Classical Transport Monte Carlo, which leads to encouraging results.

5. Resonant coherent excitation

Okorokov [47] predicted in 1965 that channeled particles should be sensitive to the periodicity of the charge distribution along crystallographic directions, i.e. to harmonics of the string potential, $U(\vec{r}, z)$, the variation of which with z is now considered. The zero-order continuum potential is obtained after averaging, through Eq. (1), over all the atoms of a string. Higher order terms correspond to the maxima of the Fourier transform of $U(\vec{r}, z)$. Resonant Coherent Excitation (RCE) can occur when an excitation frequency $\Delta E/h$ of the projectile matches a harmonic of the collision frequency along an atomic string:

$$\frac{\Delta E}{h} = k\gamma\frac{v}{d}, \tag{21}$$

where v is the projectile velocity, d the interatomic spacing along the propagation direction, γ the Lorenz factor and k a positive integer. In other words, RCE is the resonant absorption (or emission) by the projectile of a momentum corresponding to the reciprocal lattice vector $G_k = k2\pi\hbar/d$.

Under planar channeling conditions, one may adjust the excitation frequency by varying the angle θ relative to the atomic strings belonging to the plane [49]. For instance in the case of the (1 0 0) plane of a fcc crystal, Eq. (21) becomes

$$\frac{\Delta E}{h} = \gamma\frac{v}{d_{\langle 1\,0\,0\rangle}}(k\cos\theta + l\sin\theta), \tag{22}$$

where $d_{\langle 1\,0\,0\rangle}$ is the interatomic distance along a $\langle 1\,0\,0\rangle$ string, θ the angle between the trajectory and the $\langle 1\,0\,0\rangle$ axial direction and k, l are positive integers.

The first observation of atomic RCE has been reported by Datz et al. in [48] and [13]. The authors measured the ionization probability as a function of incident energy for axially channeled H-like, low Z ions ($Z = 4$–9). When the incidence energy matches one of the harmonic resonance defined by Eq. (21) for $n = 1$ to $n = 2$ electronic excitation, the frozen H-like fraction of emerging ions drops down, in connection with the higher ionization probability of the $n = 2$ states. During these experiments, energy shifts and broadening of resonances compared to vacuum energy transitions have been observed, and interpreted in terms of influence of the static crystal field and of the wake field, the latter corresponding to the polarization of the electron gas in the vicinity of the moving charge. Further complementary studies have been performed since then. Datz et al. did observe atomic RCE through the radiative decay of the excited state [14]. Komaki et al. have extended these measurements to higher Z ions at higher energies [15]. By recording simultaneously the energy loss, they could obtain detailed information on the Stark splitting of the $n = 2$ state of Ar^{17+} ions as a function of the impact parameter in planar channeling conditions. Actually, the static transverse electric field sampled by an ion in the vicinity of an atomic plane (or row) is responsible for this Stark splitting. The stronger the electric field, the stronger the splitting. Low transverse energy ions, which can be selected through the weak energy loss they experience, are confined in regions where the transverse field is small, and the

resonance energy is thus closer to its value in non-perturbed condition. On the opposite, ions with the highest transverse energy, which can be selected through the strong energy loss they experience, have an accessible transverse space extending nearly all over the channels. They can thus undergo RCE both close to the channel walls, with a high efficiency, in regions where the Stark splitting is strong, and at larger distances, with lower efficiency, in regions where the Stark splitting is weak. The consequence is that the energy width of the resonance is significantly broadened for these ions.

Note that not only the RCE probability is enhanced close to the strings or planes, but also the ionization of the excited ion, which makes the quantitative evaluation of the RCE process not straightforward. Also, as RCE takes place preferentially close to atomic strings, the influence of target atoms thermal vibrations cannot be ignored, as it is done for instance in relation (1) where all the atoms are assumed to be perfectly aligned along a string. The potential $U(\vec{r},z)$ is thus a random function, with a given taking for each ion. Such takings can be calculated by summing the contribution to $U(\vec{r},z)$, of the individual atoms of a string placed at random distances from regular lattice sites, according to the thermal vibration amplitude distribution. These fluctuations tend to lower the value of the coherence length associated to an RCE resonance, and thus contribute to a broadening and a weakening of the resonance.

So far, nuclear RCE has not been observed, but theoretical descriptions and predictions on this effect are available [16].

6. Concluding remarks

We have tried to show that the understanding of ion motion in crystals raises important questions related to ion–matter interactions. The introduction of the continuum model by Lindhard [1] has allowed a description of channeling phenomena at a high level of generality. It has in particular permitted to benefit of powerful concepts originating from statistical physics. Setting the limits of the continuum description, in connection with atomic periodicity along crystallographic directions or with non correlated or poorly correlated scattering events, was also a task of fundamental importance. Once understood, channeling effects provide, in turn, unique opportunities for refined studies of ion–matter interaction. These opportunities are mostly related to the very non-uniform ion flux that develops inside crystals in aligned geometry. This feature can be taken into benefit in order to determine precisely the impact parameter dependence of various processes. As moreover the ion flux is focused far from atomic strings or planes, one can study very specific aspects of ion–electron interactions without being perturbed by the interactions with target nuclei. We have given a few examples of such studies in Section 4. Of course, many other studies would have deserved a detailed description. In particular, we have not shown how one could also take into benefit the absence of interactions with target nuclei to study unexplored events, with extremely low associated cross-sections. Let us only mention in this domain the study of the resonant trielectronic recombination, a process in which the capture of an electron promotes two other electrons, already bound, into excited states. Channeling measurements have allowed to set for the cross-section of such a process a lower limit two orders of magnitude weaker than previously reported during ion-gas experiments [50]. In the same spirit, channeling experiments are planned in order to evidence a process called nuclear excitation by electron capture and to determine its cross-section. This effect, resonant with the ion beam energy, in which the capture of an electron in an atomic shell leads to nuclear excitation, is the reverse of internal conversion [51].

We have also illustrated applications of channeling for lattice site determination, and shown that these applications could interest domains as different as material science and nuclear physics. In what concerns material and surface science many other and very powerful techniques are available. X-rays or electron diffraction for instance take benefit of the very high amount of information that can be derived from measurements in reciprocal space. Scanning tunnel or atomic force microscopy may provide atomic resolution and allow to study objects of very small lateral

dimension. The specificity of channeling measurements is related to two main features. First, these measurements probably present the highest sensitivity to atomic displacements (down to 10^{-2} Å). Second, they illustrate in a quite straightforward way the presence of effects implying coherent atomic displacements, such as lattice strain or surface relaxation. However, even if these effects are easily detectable, the refined analysis of the measurements requires some effort (computer simulation are often needed) and a real knowledge and understanding of channeling.

Another application that would have deserved presentation is the ability to deflect high-energy beams using bent crystals. The bending is such that the change in the crystalline orientation is kept significantly smaller than the channeling critical angle over a length corresponding to the oscillation of an ion in a channel. Then, ions may remain channeled and guided by the continuum potential. Experiments have been performed at CERN with light [52] and heavy ions [53] in the relativistic energy range (above 100 GeV/nucleon). These experiments have shown that, after transmission through a bent crystal, a few cm long, a large fraction of the incident beam (10–50%) could exit, with negligible angular divergence, having been deflected by a few mrad. Dechanneling by crystalline defects, induced by crystal bending, is mainly responsible for the relatively low transmission factors. Bent crystals are now routinely used to deflect charged particle beams in high-energy accelerators.

Acknowledgements

We would like to thank all authors who allowed us to reproduce their data. A. L'Hoir and J.-C. Poizat are gratefully thanked for their very helpful criticisms and suggestions.

References

[1] J. Lindhard, Mat. Fys. Medd. Dan. Vid. Selsk. 34 (14) (1965).
[2] L.C. Feldman, J.W. Mayer, S.T. Picraux, Material Analysis by Ion Channeling, Academic Press, New York, 1982.
[3] A.F. Tulinov, Dokl. Akad. Nauk. SSSR 162 (1965) 546; A.F. Tulinov, Sov. Phys.-Dokl. 10 (1965) 463.
[4] J.S. Forster, I.V. Mitchell, J.U. Andersen, A.S. Jensen, E. Laegsgaard, W.M. Gibson, K. Reichelt, Nucl. Phys. A 464 (1987) 497.
[5] F. Goldenbaum, M. Morjean, J. Galin, E. Liénard, B. Lott, Y. Périer, M. Chevallier, D. Dauvergne, R. Kirsch, J.C. Poizat, J. Remillieux, C. Cohen, A. L'Hoir, G. Prévot, D. Schmaus, J. Dural, M. Toulemonde, D. Jacquet, Phys. Rev. Lett. 82 (2000) 5012.
[6] S. Andriamonje, R. Anne, N.V. de Castro Faria, M. Chevallier, C. Cohen, J. Dural, M.J. Gaillard, R. Genre, M. Hage-Ali, R. Kirsch, A. L'Hoir, B. Farizon-Mazuy, J. Mory, J. Moulin, J.C. Poizat, Y. Quéré, J. Remillieux, D. Schmaus, M. Toulemonde, Phys. Rev. Lett. 63 (1989) 1930.
[7] D. Dauvergne, C. Scheidenberger, A. L'Hoir, J.-U. Andersen, S. Andriamonje, C. Bockstiegel, M. Chevallier, C. Cohen, N. Cue, S. Czajkowski, J.-S. Forster, H. Geissel, H. Irnich, T. Kandler, R. Kirsch, A. Magel, P.-H. Mokler, G. Munzenberg, F. Nickel, Yu.L. Pivovarov, J.-C. Poizat, M.-F. Politis, J. Remillieux, D. Schmaus, Th. Stohlker, T. Suzuki, M. Toulemonde, Phys. Rev. A 59 (1999) 2813.
[8] S. Andriamonje, M. Chevallier, C. Cohen, N. Cue, D. Dauvergne, J. Dural, F. Fujimoto, R. Kirsch, A. L'hoir, J.C. Poizat, Y. Quéré, J. Remillieux, C. Rohl, H. Rothard, J.P. Rozet, D. Schmaus, M. Toulemonde, D. Vernhet, Phys. Rev. A 54 (1996) 1404.
[9] S. Andriamonje, M. Chevallier, C. Cohen, N. Cue, D. Dauvergne, J. Dural, R. Genre, Y. Girard, R. Kirsch, A. L'Hoir, J.C. Poizat, Y. Quéré, J. Remillieux, D. Schmaus, M. Toulemonde, Phys. Lett. A 164 (1992) 184.
[10] S. Datz, C.D. Moak, T.S. Noggle, B.R. Appleton, H.O. Lutz, Phys. Rev. 179 (1969) 315.
[11] M.T. Robinson, Phys. Rev. 179 (1969) 327.
[12] A. L'Hoir, S. Andriamonje, R. Anne, N.V. de Castro Faria, M. Chevallier, C. Cohen, J. Dural, M.J. Gaillard, R. Genre, M. Hage-Ali, B. Farizon-Mazuy, J. Mory, J. Moulin, J.C. Poizat, Y. Quéré, J. Remillieux, D. Schmaus, M. Toulemonde, Nucl. Instr. and Meth. B 48 (1990) 145.
[13] C.D. Moak, S. Datz, O.H. Crawford, H.F. Krause, P.F. Dittner, J. Gomez Del Campo, J.A. Biggerstaff, P.D. Miller, P. Hvelplund, H. Knudsen, Phys. Rev. A 19 (1979) 977.
[14] S. Datz, P.F. Dittner, H.F. Krause, C.R. Vane, O.H. Crawford, J.S. Forster, G.S. Ball, W.G. Davies, J.S. Geiger, Nucl. Instr. and Meth. 100 (1995) 272.
[15] K. Komaki, T. Azuma, T. Ito, Y. Takabayashi, Y. Yamazaki, M. Sano, M. Torikoshi, A. Kitagawa, E. Takada, T. Murakami, Nucl. Instr. and Meth. 146 (1998) 19.
[16] Yu.L. Pivovarov, H. Geissel, Yu.M. Filimonov, O.E. Krivosheev, C. Scheidenberger, Nucl. Instr. and Meth. B 119 (1996) 283.
[17] J.H. Barrett, Phys. Rev. B 3 (1971) 1527.
[18] E. Bögh, J.L. Whitton, Phys. Rev. Lett. 19 (1967) 553.

[19] W. Assmann, H. Huber, S.A. Karamian, F. Grüner, H.D. Miesques, J.U. Andersen, M. Posselt, B. Schmidt, Phys. Rev. Lett. 83 (1999) 1759.
[20] N. Bohr, K. Dan Vidensk Selsk. Mat.-Fys. Medd. 18 (8) (1948).
[21] S.T. Picraux, F.L. Vook, Ion implantation in semiconductors, in: S. Namba, Plenum, New York, 1975, p. 355.
[22] C. Lallaizon, B. Lépine, S. Ababou, A. Guivarc'h, S. Députier, F. Abel, C. Cohen, J. Appl. Phys. 86 (1999) 5515.
[23] I. Stensgaard, L.C. Feldman, P.J. Silverman, Surf. Sci. 77 (1978) 513.
[24] J.W.M. Frenken, J.F. Van der Veen, Phys. Rev. Lett. 54 (1985) 134.
[25] C. Cohen, A. L'Hoir, J. Moulin, D. Schmaus, M. Sotto, J.L. Domange, J.C. Bouillard, Surf. Sci. 339 (1995) 41.
[26] Z.Y.A. Al-Tamimi, W.A. Grant, G. Carter, Nucl. Instr. and Meth. 209 (1983) 363.
[27] J.A. Davies, L. Eriksson, N.G.E. Johansson, I.V. Mitchell, Phys. Rev. 181 (1969) 548.
[28] F. Barrué, S. Basnary, A. Chbihi, M. Chevallier, C. Cohen, D. Dauvergne, H. Ellmer, J. Frankland, D. Jacquet, R. Kirsch, P. Lautesse, A. L'Hoir, M. Morjean, J.C. Poizat, C. Ray, M. Toulemonde, Nucl. Instr. and Meth. B 193 (2002) 852.
[29] J.U. Andersen, A.S. Jensen, K. Jørgensen, E. Loesgaard, K.O. Nielsen, J.S. Forster, I.V. Mitchell, D. Ward, W.M. Gibson, J.J. Cuomo, K. Dan. Vidensk. Selsk. Mat. Fys. Medd. 40 (1980) 7.
[30] S.A. Karamian, J.S. Forster, J.U. Andersen, W. Assmann, C. Broude, J. Chevallier, J.S. Geiger, F. Grüner, V.A. Khodyrev, F. Malaguti, A. Uguzzoni, Eur. Phys. J. A 17 (2003) 49.
[31] D.J. Hinde, Nucl. Phys. A 553 (1993) 255c.
[32] H. Bethe, Z. Phys. 76 (1930) 293.
[33] S.P. Ahlen, Rev. Mod. Phys. 52 (1980) 121.
[34] J. Lindhard, A.H. Sørensen, Phys. Rev. A 53 (1996) 2443.
[35] J.F. Ziegler, J.P. Biersack, U. Littmark, The Stopping and Range of Ions in Solids, Pergamon Press, New York, 1985.
[36] G. Schiwietz, P.L. Grande, Nucl. Instr. and Meth. B 153 (1999) 1.
[37] F. Bloch, Ann. Phys. 16 (1933) 285.
[38] J.D. Jackson, Classical Electrodynamics, Wiley, New York, 1975.
[39] J.U. Andersen, J. Chevallier, G.C. Ball, W.G. Davies, J.S. Forster, J.S. Geiger, J.A. Davies, H. Geissel, E.P. Kanter, Phys. Rev. A 54 (1996) 624.
[40] G. De M. Azevedo, P.L. Grande, G. Schiwietz, Nucl. Instr. and Meth. B 164–165 (2000) 203.
[41] P. Sigmund, A. Schinner, Phys. Rev. Lett. 86 (2001) 1486.
[42] H. Weick, H. Geissel, C. Scheidenberger, F. Attallah, D. Cortina, M. Hausmann, G. Münzenberg, T. Radon, H. Schatz, K. Schmidt, J. Stadlmann, K. Sümmerer, M. Winkler, Phys. Rev. Lett. 85 (2000) 2725.
[43] I. Vickridge, A. L'Hoir, J. Gylai, C. Cohen, F. Abel, Europhys. Lett. 13 (1990) 635.
[44] F. Grüner, W. Assmann, F. Bell, M. Schubert, J.U. Andersen, S. Karamian, A. Bergmaier, G. Dollinger, L. Görgens, W. Günther, M. Toulemonde, Phys. Rev. B 68 (2003) 174104.
[45] D. Dauvergne, A. Bräuning-Demian, F. Bosch, H. Bräuning, M. Chevallier, C. Cohen, A. Gumberidze, A. L'Hoir, R. Kirsch, C. Kozhuharov, D. Liesen, P.-H. Mokler, J.-C. Poizat, C. Ray, Th. Stohlker, M. Tarisien, E. Testa, S. Toleikis, M. Toulemonde, Nucl. Instr. and Meth. B 205 (2003) 773.
[46] F. Grüner, M. Schubert, W. Assmann, F. Bell, S. Karamian, J.U. Andersen, Nucl. Instr. and Meth. B 193 (2002) 165.
[47] V.V. Okorokov, Pisma Zh. Eksp. Teor. Fiz. 2 (1965) 175; V.V. Okorokov, JETP Lett. 2 (1965) 111.
[48] S. Datz, C.D. Moak, O.H. Crawford, H.F. Krause, P.F. Dittner, J. GomezDelCampo, J.A. Biggerstaff, P.D. Miller, P. Hvelplund, H. Knudsen, Phys. Rev. Lett. 40 (1978) 843.
[49] S. Datz, C.D. Moak, O.H. Crawford, H.F. Krause, P.D. Miller, P.F. Dittner, J. Gomez Del Campo, J.A. Biggerstaff, H. Knudsen, P. Hvelplund, Nucl. Instr. and Meth. 107 (1980) 15.
[50] M. Chevallier, C. Cohen, N. Cue, D. Dauvergne, J. Dural, P. Gangnan, R. Kirsch, A. L'Hoir, D. Lelièvre, J.F. Libin, P.H. Mokler, J.C. Poizat, H.T. Prinz, J.M. Ramillon, J. Remillieux, P. Roussel-Chomaz, J.P. Rozet, F. Sanuy, D. Schmaus, C. Stephan, M. Toulemonde, D. Vernhet, A. Warczak, Phys. Rev. A 61 (2000) 22742.
[51] N. Cue, J.-C. Poizat, J. Remillieux, Euro. Phys. Lett. 8 (1989) 19.
[52] S.P. Møller, T. Worm, M. Clément, N. Doble, K. Elsener, L. Gatignon, P. Grafström, E. Uggerhøj, M. Hage-Ali, P. Siffert, Nucl. Instr. and Meth. B 84 (1994) 434.
[53] G. Arduini, C. Biino, M. Clément, K. Cornelis, N. Doble, K. Elsener, G. Ferioli, G. Fidecaro, L. Gatignon, P. Grafström, M. Gyr, W. Herr, J. Klem, U. Mikkelsen, E. Weisse, S.P. Møller, E. Uggerhøj, A. Taratin, A. Freund, P. Keppler, J. Major, Phys. Rev. Lett. 79 (1997) 4182.

1-2 Recherche de processus rares d'interaction ion-électron – Le cristal comme cible épaisse d'électrons.

Le principe de ces expériences est relativement simple : les ions bien canalisés subissent principalement des collisions proches avec les électrons de valence ou de conduction du cristal. Pour le silicium par exemple, la valeur moyenne de la densité électronique du gaz de valence est de 0,2 $e^-/Å^3$. Un cristal de 10 µm permet ainsi d'obtenir une « épaisseur » d'électrons de l'ordre de 2.10^{20} e^-/cm^2. Pour comparaison, un jet gazeux fournit une cible d'environ 10^{13} e^-/cm^2.
Les faisceaux disponibles au GANIL dans une émittance réduite adaptée à la canalisation sont au maximum de 10^6 à 10^7 ions/s sur un impact de 2 à 3 mm^2. Pour adopter le langage des physiciens des particules, cela représente une sensibilité de l'ordre de 1 $\mu barn^{-1}$ par heure de faisceau. Une irradiation de 10h permet donc de produire un événement dont la section efficace est de 0,1 µbarn. Ces chiffres sont très indicatifs, il faut prendre en compte la sévérité éventuelle avec laquelle ont veut supprimer les collisions proches sur les noyaux, qui est couplée avec les conditions de faisceau et d'alignement du cristal. De plus l'efficacité de détection du processus considéré doit être rajoutée. De façon très générale, j'ai considéré une durée d'irradiation de 10h, qui correspond en pratique à un temps raisonnable de prise de données utile pour les temps de faisceaux alloués par les comités d'expériences. Cette durée peut bien sûr être supérieure, la limitation principale n'étant pas l'endommagement du cristal : en effet, nos expériences ont montré que la dégradation d'un cristal (mesurée par la variation du taux χ_{min} d'extinction des collisions proches sur les noyaux cible en canalisation) devient significative pour une fluence de quelques 10^{13} ions/cm^2 avec une incidence quelconque, avec les ions de plus fort dE/dx. Ce taux d'endommagement sera plus faible en conditions de canalisation, car il est en partie dû aux collisions élastiques sur les noyaux cible, et, de plus, le dépôt d'énergie électronique est réduit pour les ions canalisés. Par ailleurs, en pratique, il est aisé de changer de point d'impact si nécessaire.

De façon plus détaillée, on sait caractériser avec précision le gaz d'électrons cible rencontré par les ions canalisés. La figure 2 ci-dessous illustre cette caractérisation, au moyen du taux de capture radiative dans une cible, normalisé à une section efficace calculée.

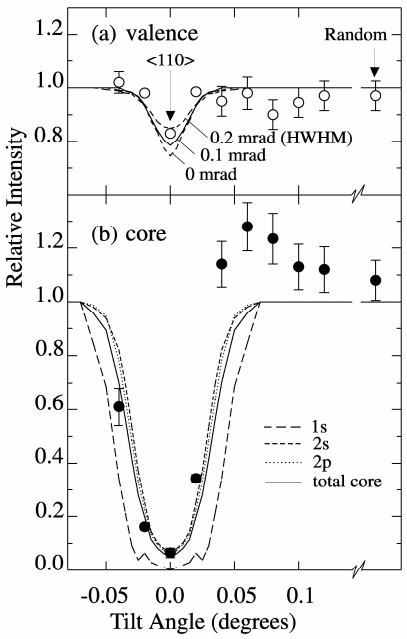

***Figure 2** : taux de capture radiative REC mesurés (points) et simulés (courbes), par des ions Kr^{36+} de 60 MeV/u, pour les différents électrons d'un cristal de silicium, en fonction de son orientation par rapport à la direction d'axe <110>. Les taux sont normalisés à une valeur calculée théorique pour une orientation quelconque du cristal. (a) capture des électrons de valence ; les simulations sont obtenues avec différentes valeurs de divergence angulaire de faisceau (b) capture des électrons de cœur, les simulations sont obtenues pour les différentes couches orbitales du silicium (avec la divergence angulaire 0,1mrad FWHM). D'après [Andriamonje 96].*

Le profil Compton (distribution en impulsion dans la direction de propagation du projectile) des électrons de cœur étant plus large que celui des électrons de valence, on peut séparer les contributions de ces deux populations à la capture REC, avec l'aide de simulations. Nous reviendrons plus en détail sur ce point dans la section I-3-2. Dans l'exemple donné figure 2, obtenu pour une expérience avec des ions incidents Kr^{36+} de 60 MeV/u en fonction de l'orientation par rapport à l'axe <110> d'un cristal de silicium de 37 µm, on a tenu compte de facteurs expérimentaux (divergence angulaire du faisceau, décanalisation dans le cristal relativement épais). Pour l'orientation axiale (angle nul) l'interaction avec les électrons de cœur du silicium est fortement diminuée par rapport à l'orientation quelconque (d'un facteur 0,06) ; la contribution résiduelle de ces électrons de cœur est due principalement aux électrons de la couche n=2. La contribution des électrons de valence, quant à elle, subit aussi une légère diminution pour l'orientation axiale, d'environ 15%, par rapport à la densité moyenne du gaz de valence dans le cristal.
Ces valeurs des contributions d'électrons de cœur et de valence varient en fonction de la distribution initiale de l'énergie transverse du faisceau dans le cristal, donc des conditions expérimentales. Mais cet exemple montre qu'on peut déterminer la densité électronique rencontrée par le faisceau au moyen d'une étude spécifique d'un processus dont la probabilité est proportionnelle à cette densité, comme la capture radiative.

Après ces remarques introductives d'ordre général, je présente ci-dessous deux études dans lesquelles notre collaboration s'est engagée. La première a porté sur la recherche de la capture résonnante triélectronique (RT2E), et la seconde sur la recherche de la capture résonnante électronique par excitation nucléaire (NEEC).

I-2-1 : Recherche de la capture résonnante triélectronique RT2E

Les résultats scientifiques de cette expériences sont décrits dans la référence ci-dessous : "Upper limit determination of resonant trielectronic recombination cross section for krypton using crystal channeling" [Chevallier 00].
Très brièvement, pour le lecteur qui ne souhaiterait pas lire cet article, nous avons cherché à observer la capture résonnante d'un électron en couche L, accompagnée de l'excitation simultanée des deux électrons K vers la couche L, d'un ion initialement hydrogénoïde Kr^{34+} (capture triélectronique, ou RT2E, dite KK-LLL en utilisant la terminologie des transitions Auger). Cette expérience consistait à observer, à l'énergie de la résonance et à deux énergies hors résonance, le rendement de coïncidences triples entre la détection des deux photons K_α de désexcitation de cet état dit « triplement excité » et la détection d'ions Kr^{33+}, transmis à travers un cristal aligné de 3,6 µm avec une perte d'énergie réduite, caractéristique d'un ion canalisé avec une faible énergie transverse. Cette expérience a été réalisée dans la voie SPEG du GANIL.
Au-delà de cette publication, cette expérience a constitué un engagement considérable de ma part, car je l'ai conçue et proposée au comité d'expérience du GANIL une première fois fin 1994. Dans le même temps j'interférais avec des théoriciens de structure atomique qui effectuaient des calculs de l'effet inverse, dit « double Auger » (émission de deux électrons avec cascade d'un 3^e électron vers le fondamental) [Marques 1998]. Leurs calculs ont été revus à la baisse après une erreur, ce qui nous a poussés à soumettre à nouveau l'expérience déjà acceptée car il nous fallait davantage de temps de faisceau et un dispositif différent pour la rendre réalisable. Etant données les très faibles sections efficaces attendues, le dispositif expérimental a été compliqué, et nous avons décidé d'effectuer des triples coïncidences, tout en détectant 100% du faisceau transmis dans les divers états de charge en sortie du cristal

cible afin de rejeter d'éventuelles coïncidences fortuites avec le faisceau pulsé, d'intensité 3.10^6 ions/s. J'ai dû concevoir tout le dispositif expérimental :

- détection sous grand angle solide des photons X au niveau de la cible : 25% de l'angle solide total étaient couverts par 3 détecteurs NaI(Tl) de grande surface, un 4^e détecteur Ge étant utilisé en plus pour avoir des spectres X de référence avec une meilleure résolution ;
- détection de tous les ions transmis dans divers états de charge à l'aide de scintillateurs. Certains de ces scintillateurs devaient être montés sur une table de translation afin de déplacer l'impact du faisceau, car ils vieillissaient sous irradiation. Nous avons fait une expérience test dédiée à la mesure du vieillissement d'un scintillateur plastique en fonction de la fluence (et du flux). Pour la détection des ions dans l'état de charge majoritaire, j'ai conçu un compteur capable de détecter des ions lourds un par un avec une efficacité de 100% à un taux de comptage de 2.10^6/s, tout en étant insensible à l'irradiation. Ce dispositif, décrit dans l'article ci-dessous, consistait en une feuille de cuivre posée sur un scintillateur plastique dopé au plomb, qui détectait la fluorescence K du cuivre (de l'ordre d'une centaine de photons K_α du cuivre étaient ainsi collectés par ion incident, ce qui compensait la faible luminosité du plastique scintillateur). Ce dispositif a bien fonctionné.
- La supervision des calculs d'optique du faisceau menés au GANIL : il fallait connaître les trajectoires (et leurs enveloppes) des ions de chaque état de charge afin de positionner les scintillateurs.
- L'électronique de détection, chargée de réaliser des coïncidences multiples avec une fenêtre en temps de moins de 80 ns.
- L'interaction avec le service technique du CIRIL, qui a dû accomplir un travail considérable pour adapter notre dispositif à des exigences qui ont évolué au cours du temps. Ce fut de plus la première expérience de canalisation dans SPEG.

De plus l'expérience avait été initialement programmée dans LISE avec un faisceau d'ions Nb, pour lesquels nous espérions différencier les raies K_α hypersatellites, ce qui aurait permis de signer sans ambiguïté la présence d'une double lacune K des projectiles (le premier photon, émis alors que la couche K est vide, a une énergie supérieure au second). Cette première expérience a malheureusement échoué, à cause de la difficulté de l'accélérateur à produire ces faisceaux de niobium suffisamment intenses mais stables dans l'émittance voulue. Les décharges à répétition au niveau de la source ont finalement conduit à l'incendie d'un des cyclotrons injecteurs, un certain 6 juin 96. Nous avons donc demandé à être reprogrammés, cette fois-ci dans SPEG avec un faisceau de krypton, en 1997.

Cette description ne relève peut-être pas vraiment d'un mémoire scientifique, mais elle a marqué le chercheur encore inexpérimenté que j'étais à l'époque.

De plus l'enjeu scientifique n'était sans doute pas à la mesure de la difficulté de cette expérience, surtout lorsqu'il était évalué dans le cadre de la politique scientifique de l'IN2P3, bien que nous ayons été soutenus par notre Institut pour la réaliser. En effet, l'observation d'un état triplement excité (à deux lacunes K) d'un ion Kr^{33+} et de ses modes de désexcitation présente certainement un intérêt fondamental en physique de la structure atomique, pour l'étude des corrélations multiples entre électrons. Cependant, la très faible probabilité de production de cet état pour un ion lourd comme le krypton montre qu'il joue un rôle négligeable dans les réarrangements électroniques. C'était sans illusions à ce sujet que nous avions exposé clairement les enjeux devant le comité d'expérience de physique non-nucléaire du GANIL. Ses membres ont estimé que l'expérience valait la peine d'être réalisée, c'est ce que nous avons fait.

Les résultats ont conduit à une valeur limite supérieure de la section efficace (environ 2mbarn par électron cible à la résonance), ce qui représentait une amélioration de deux ordres de

grandeur par rapport à une tentative d'un groupe de Michigan avec une cible gazeuse [Zaharakis 95]. Cependant nous avons été limités dans la sensibilité de l'expérience par la mauvaise qualité du cristal : celui-ci avait été aminci par attaque chimique, et l'épaisseur n'était pas du tout uniforme, de telle sorte qu'il y avait des parties très minces, correspondant probablement à des cônes d'attaque chimique autour de défauts. Une fraction des ions du faisceau – petite mais non négligeable - traversait ces régions amincies sans être canalisée. Il en résultait une perte d'énergie inférieure à la perte d'énergie des ions canalisés dans la partie de la cible d'épaisseur nominale. Le bruit de fond créé par ces particules était très supérieur au signal attendu du RT2E (ce bruit de fond correspondait à des événements décorrélés d'une capture et de deux excitations, lors de collisions avec les cœurs atomiques de la cible). L'utilisation d'un cristal de meilleure qualité aurait permis d'améliorer notre sensibilité d'un ordre de grandeur, et ainsi d'atteindre la limite de l'observation attendue du signal RT2E (voir figure 5 de l'article).
Depuis, la capture triélectronique KK-LLL a été mise en évidence sur des ions légers, et représente même une fraction appréciable de l'échange de charge [Schnell 03], ce qui montre que ce type de processus suscite un intérêt en physique atomique, même si ce n'est pas pour les ions lourds multichargés.

Cette expérience aura été extrêmement formatrice pour moi, et je suis très reconnaissant envers les physiciens beaucoup plus expérimentés de notre collaboration de m'avoir laissé conduire ce projet. Leur motivation était certainement ce souci de me faire acquérir ce savoir-faire.

Upper-limit determination of resonant trielectronic recombination cross-section for krypton using crystal channeling

M. Chevallier,[1] C. Cohen,[2] N. Cue,[3] D. Dauvergne,[1] J. Dural,[4] P. Gangnan,[5] R. Kirsch,[1] A. L'Hoir,[2] D. Lelièvre,[4] J.-F. Libin,[5] P. H. Mokler,[6] J.-C. Poizat,[1] H.-T. Prinz,[6] J.-M. Ramillon,[4] J. Remillieux,[1] P. Roussel-Chomaz,[5] J.-P. Rozet,[2] F. Sanuy,[1] D. Schmaus,[2] C. Stephan,[7] M. Toulemonde,[4] D. Vernhet,[2] and A. Warczak,[8]

[1]*Institut de Physique Nucléaire de Lyon and IN2P3, Université Claude Bernard Lyon-I, 43, Boulevard du 11 Novembre 1918, 69622 Villeurbanne Cedex, France*

[2]*Groupe de Physique des Solides, CNRS UMR 75-88, Universités Paris VII et Paris VI, 75251 Paris Cedex 05, France*

[3]*Department of Physics, The Hong Kong University of Sciences and Technology, Kowloon, Hong Kong*

[4]*CIRIL, UMR 11 CNRS-CEA, rue Claude Bloch, 14040 Caen Cedex, France*

[5]*GANIL, CEA/IN2P3, BP 5027, 14076 Caen Cedex 5, France*

[6]*Gesellschaft für Schwerionenforschung (GSI), D-64291 Darmstadt, Germany*

[7]*IPN Orsay and IN2P3, BP 1, 91406 Orsay Cedex, France*

[8]*Institut Fizyki, Uniwersytet Jagielloński, PL-30-059 Kraków, Poland*

(Received 2 July 1999; published 18 January 2000)

We used channeling through a thin crystal to get an estimate of the cross section of the resonant trielectronic capture by Kr^{34+} ions. *K* x-ray–*K* x-ray coincidence measurements were performed with a selection on the charge state and energy loss of transmitted ions. An upper limit of 1.9×10^{-27} cm^2 at the resonance is obtained, and this represents an improvement by two orders of magnitude with respect to previous ion-gas experiments. The possibility to reach the theoretical predictions experimentally is discussed.

PACS number(s): 34.80.Lx, 61.85.+p, 34.70.+e, 32.80.Hd

I. INTRODUCTION

Trielectronic recombination (TR) is a resonant electron capture process that may occur during heavy ion-electron collisions: the capture of an electron by an ion with at least two electrons in the initial state is accompanied by the simultaneous double electronic excitation of the ion. This process is due to a three-electron interaction that is analogous to dielectronic recombination (DR), in which electron capture is accompanied by a single excitation. Figure 1 presents these electronic transitions in the ion rest frame. Figure 1(a) illustrates the particular case of the *KK-LLL* resonant trielectronic recombination for a He-like ion: the energy gained during the capture into the $n=2$ state of an electron with the required kinetic energy in the ion frame is devoted to the $(1s^2\rightarrow 2\ell 2\ell')$ excitation of the two *K* electrons. This leads to an excited Li-like ion with its three electrons in the *L* shell (''triply'' excited). For sufficiently high *Z* ions, the radiative decay of this triply excited state by two successive *K* x-ray emissions dominates autoionization, and recombination effectively occurs. The analogy with DR is shown in Fig. 1(b) for the *K-LL* resonance, occurring at a lower electron kinetic energy.

Of course, resonant electron-capture processes similar to DR and TR can take place during ion-atom collisions. These processes are called respectively resonant transfer and excitation (RTE) and, following Zaharakis *et al.* [1], resonant transfer and double excitation (RT2E). RTE is the capture of an initially bound electron, and can lead either to autoionization (RTEA) or radiative stabilization (RTEX). An important feature of RTE (and RT2E), if one compares them to DR (and TR), is the broadening of the resonance due to the Compton profile of the electron to be captured, i.e., the longitudinal momentum distribution in the initial state. For the corresponding trielectronic process, we may use RT2E2A, RT2EAX, and RT2E2X to denote two-Auger, Auger +radiative, and double radiative decay of the intermediate state, respectively.

For low *Z* ions, the triply excited state formed during trielectronic recombination decays mostly by autoionization. This has been observed for the lightest ions: Schultz [2] reported on resonances above the ionization threshold produced during electron scattering or electron-impact ionization experiments that originate from the formation of $2\ell^2 2\ell'$ states of H^{2-} and He^- ions. More recently, Müller *et al.* [3] measured the cross sections for the resonant capture into $n=2$ triply excited states of Li atoms by means of very precise Li^+-electron crossed-beam experiments, by using the energy dependence of electron-impact ionization: with a resonance strength of about 10^{-20} cm^2 eV, this process (which keeps the ion charge constant) lowers the electron-impact ionization of Li^+ ions significantly (by less than 1%).

The time reversal process of the resonant capture during trielectronic recombination (trielectronic capture) is the three-electron Auger decay, also called the ''double'' Auger effect [DA, double deexcitation–single ionization; see Fig. 1(c)], that has been observed in ion-atom [4,5] and ion-surface [6,7] collision experiments. Excited light ions with a double *K* hole were produced [5–7], and the ratios *R* of DA to single Auger rates for such states were found to be around 3×10^{-4} for C and N ions [5,7]. Following the detailed balance principle, these ratios should be similar to the ratios of trielectronic capture over dielectronic capture cross sections.

Trielectronic capture—and DA—are of fundamental interest for the study of three-electron correlation in bound systems. Most of the theoretical works on DA have con-

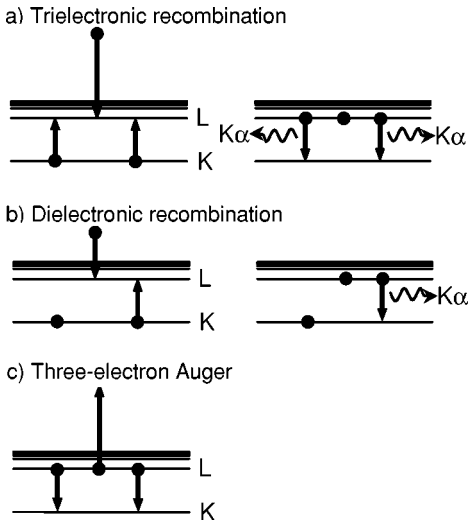

FIG. 1. Schematic representations of (a) *KK-LLL* trielectronic recombination (TR) for an initial ground-state He-like ion (b) *K-LL* dielectronic recombination (DR) for the same initial state (c) *KK-LLL* three-electron Auger (DA).

cerned low-Z ions [8,9]. Vaeck and Hansen [9] pointed out that, for double-K-hole nitrogen ions, the main contribution to DA comes from the shake-down mechanism accompanying a single autoionization, when at least one $2s$ electron is present in the initial state. A shake-down transition can take place because the initial $2s$ and the final $1s$ wave functions are not orthogonal. Their calculations show that R values depend more strongly on the number of $2s$ electrons than on the total number of L electrons. Thus ''real correlation'' effects (e.g., those involving only $2p$ electrons) lead to values of R much smaller than those involving initial $2s$ electrons (typically $\sim 10^{-6}$ and $\sim 10^{-4}$, respectively; this last number being in agreement with experimental results [7]). Marques *et al.* [10] used multiconfiguration Dirac-Fock (MCDF) calculations to estimate DA rates and the ratio R for higher Z systems ($Z=36,41,64$). They did not include the shake-down contribution, which was assumed to be small ($\sim 20\%$ of the total DA rate for krypton, and less for higher Z ions). Their final calculations provided a value of $R=2.786 \times 10^{-7}$ for triply excited Kr^{33+} (three electrons in the L shell). For the same ion Badnell [1,11] estimated a ratio $R \sim 10^{-6}$ by using a three-L-electron interaction through configuration mixing with a Breit-Pauli Hamiltonian.

For those high-Z ions, the experimental study of trielectronic recombination is more attractive than the study of DA, because the radiative decay of a double K hole dominates autoionization. Using an initial He-like ion in its ground state, the signature of the *KK-LLL* trielectronic recombination is a double K x-ray emission, along with the decrease of the ion charge by one unit.

One attempt to observe RT2E is reported by Zaharakis *et al.* in Ref. [1]. During Kr^{34+}-ion–H_2-gas collisions, they detected x rays in coincidence with Kr^{33+} transmitted ions at various incidence energies. Due to the low interaction rates in such experiments, they could only measure the energy dependence of the sum of the $L,M,\ldots$ REC cross sections ($\sim 10^{-23}$ cm^2), and no $K\alpha$ photon could be detected in coincidence. They gave an upper limit of the RT2E cross section of about 10^{-25} cm^2.

Crystal channeling provides a powerful technique for investigating such a low-cross-section process, because channeled ions interact mainly with a dense gas of quasifree electrons. In alignment conditions, ions acquire a transverse energy at the entrance of the crystal, according to their incidence angle and their position relative to the atomic rows or planes. Ions with a transverse energy (per unit charge) below the maximum value of the continuum string or planar crystal potential are known to be channeled and can access only a restricted part of the transverse space [12]. This results in the extinction of close collisions with target atomic cores, and the attendant reduction of ion-electron interactions, such as energy loss. One can then study ion-electron interaction processes that are hardly observable in classical ion-solid or ion-atom collisions, as was demonstrated in previous studies of radiative electron capture (REC) [13–15], electron-impact ionization and excitation (EII and EIE, respectively) [16–18], and resonant transfer and excitation [19–21]. A review of charge-exchange experiments in channeling conditions is given in Ref. [22]. The processes just mentioned have relatively high cross sections (more than 10 b), and thus are easily observable in channeling conditions. For instance, the impact-parameter dependence of REC line shapes was studied in detail [15], and the Compton profiles of silicon valence electrons were found to be very close to those of free electrons (Fermi gas) for the same local density. These Compton profiles are also responsible for the broadening of the RTE resonance profiles reported in Refs. [19–21]. The conditions for observing the very rare TR process in channeling conditions are more stringent than those discussed above. They are described in the following sections.

II. EXPERIMENT

A primary beam of 43.1-A MeV Kr^{31+} from the GANIL facility (Caen, France) was used in our study. The final beam on the target was obtained by means of degrading/stripping Al foils followed by a magnetic spectrometer for the selection of the charge (34+), the energy (37.1, 40.6, and 42.7 A MeV with $\Delta p/p=10^{-4}$), and the emittance ($\epsilon_x=\epsilon_y=0.15\pi$ mm mrad). The two extreme incidence energies are outside the *KK-LLL* resonance, whereas 40.6 A MeV is on the resonance. The beam, with a typical intensity of $(2-3)\times 10^6$ ions/s (within a 9.4-MHz HF pulsed structure) was sent to the Spectromètre à Perte d'Énergie pour le GANIL (SPEG) [23] beam line, and had a diameter of 1 mm on the target. A sketch of the experimental setup in the SPEG line is shown in Fig. 2. This beam line is equipped with a high-resolution spectrometer (8.1 mm on the focal plane corresponding to $\Delta p/p=10^{-3}$). The target was a 3.6-μm-thick Si crystal oriented along the $\langle 110 \rangle$ axial direction. A high efficiency for the detection of projectile K x-ray–K x-ray coincidences was achieved by means of three large NaI(Tl) detectors covering 25% of the total solid angle. These detectors were chosen for their large area and relatively high counting rate capabilities, despite their poor energy resolution. Two

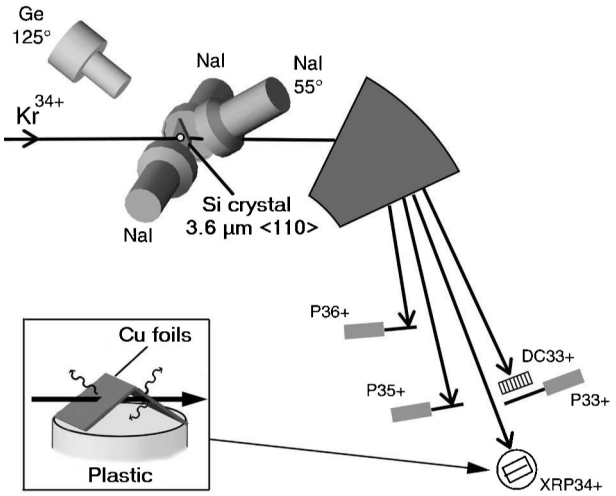

FIG. 2. A schematic of the experimental setup.

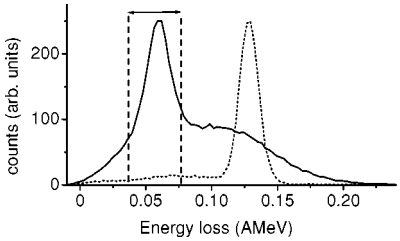

FIG. 3. Energy-loss distributions for axial (full line) and random (dashed line) crystal orientations. The energy-loss range (axial alignment) selected in the data analysis is indicated.

detectors were placed at 90° from the beam direction, and the third one at 55°. The K x-ray–K x-ray coincidence efficiency was $\epsilon_{KK}=3.7\pm0.4\%$ (assuming an isotropic emission in the projectile frame). An additional Ge detector at 125° with a much smaller solid angle was used for observing x rays with a better energy resolution. Transmitted ions were charge- and energy-analyzed by the last magnetic stage of the SPEG spectrometer. Down-charged 33+ ions were detected by a drift chamber (DC33+) for position information and a plastic scintillator (P33+) for triggering (see Fig. 2). The main trigger of the event-by-event acquisition (i.e., the trigger for possible TR events) was the detection of a 33+ ion in coincidence with two photons registered simultaneously in two NaI(Tl) detectors. Additional triggers [single events registered by the germanium, NaI(Tl) and DC33+ detectors] were used to observe single charge-exchange and excitation processes.

The fraction of accelerator-HF pulses containing more than one incident ion was not negligible. The probability of undue triggering (detection of three uncorrelated events) increases as the cube of the number of ions per pulse, and then the experimental background increases correspondingly. Thus we detected all the transmitted ions in such a way that we could select, off line, those events for which no 34+, 35+, or 36+ ion were detected within the same pulse as the 33+ ion. During preliminary tests, the plastic scintillators (type BC400) were found to detect up to $\sim10^8$ Kr ions per mm^2 in our energy range before the reduction of their efficiency by radiation damage became significant. In the present experiment the charge-state distribution in channeling conditions (slightly varying with the incident energy) is $F(36+)\leqslant1\%$, $F(35+)\simeq3.5\%$, $F(34+)\simeq95\%$, $F(33+)\leqslant1\%$, $F(32+)$ being negligible. The 36+ and 35+ ions were detected by plastic scintillators (P36+ and P35+ respectively; see Fig. 2). The location of the beam impact on these scintillators was changed when necessary. The detection of 34+ ions required a special arrangement because of its very-high-counting rate. The detector (XRP34+) was based on x-ray fluorescence. Copper radiator foils were placed on the top of a plastic scintillator (see the inset of Fig. 2). A very large number of simultaneous x rays were emitted inside the radiator (mainly Cu $K\alpha$ arising from Cu atom ionization). This led to a measurable signal in the large solid angle scintillator with a 100% efficiency.

III. RESULTS AND ANALYSIS

Channeled ions are characterized by their low-energy loss rate. Figure 3 presents two energy-loss distributions for transmitted 33+ ions as measured by the drift chamber at 37.1-A MeV incidence energy. One corresponds to a random crystal orientation and the other one is obtained in axial channeling conditions ($\langle110\rangle$ orientation). The width of the ''random'' distribution is dominated by energy straggling (the width of the direct beam is typically 50% narrower and is mainly due to the size of the beam spot on the target). A low-energy loss tail (extending down to 0) is due to etch pits in the crystal. These pits were formed during the chemical etching of the crystal. The spectrum obtained in alignment conditions has two distinct components: a narrow distribution, with a most probable energy loss roughly equal to half of the random energy loss, and a broader one, centered at a higher energy loss, that corresponds to unchanneled ions. In principle, making cuts in the energy-loss spectrum allows one to select ions with a given transverse energy inside the crystal channel. This transverse energy is related to the mean electronic density encountered inside the crystal channel (see, for instance, Refs. [22,21,17,15]). Our aim was initially to study RT2E as a function of the sampled electron density. The RT2E signal results from a triple coincidence of K x-ray–K x-ray–Kr^{33+} detection arising from a single collisional event. The background signals have the same signature but originate from three uncorrelated events during the ion's passage through the crystal, because K emission cannot result from a nonresonant capture by a He-like ion. Hence it is proportional to the cube of the number of target electrons. Then the ratio of the RT2E signal to the background rate varies as the inverse square of the electron target ''thickness.'' Unexpectedly this background was observed to increase for the lowest-energy losses. Two factors can account for this. First the total thickness of the amorphous layers (SiO_2) on the two surfaces of the crystal was measured to be 100 Å (equivalent Si thickness for the RBS technique used). Mechanical electron capture (MEC) and nuclear impact ionization (NIE) can occur in these layers, whatever the transverse energy of channeled ions is. Both MEC and NIE have much larger cross sections than REC and EIE, which are the

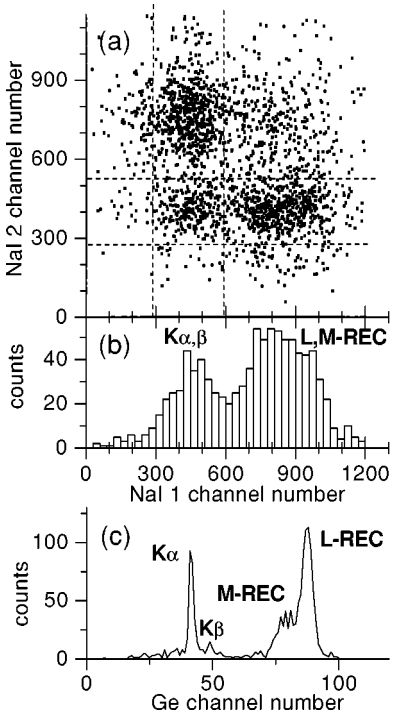

FIG. 4. (a) Scatter plot of the coincidence x-ray–x-ray distribution for two NaI(Tl) detectors (located at 90° from the beam direction), in coincidence with Kr^{33+} ions with the selected energy loss. (b) Histogram of the NaI1 events corresponding to the *K* x ray on NaI2 for the energy cut shown in (a). (c) Energy spectrum of the Ge detector (125°) for x rays in coincidence with Kr^{33+} ions.

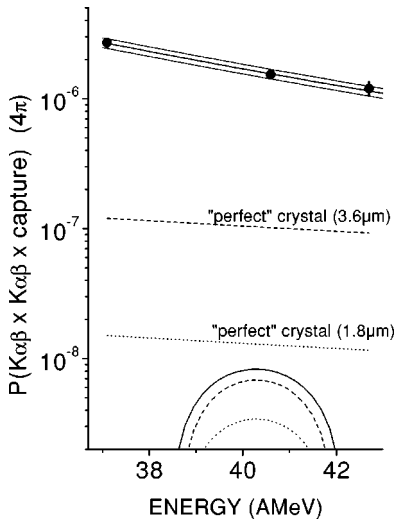

FIG. 5. Probability, for ions in the selected energy-loss range, of emitting two $K\alpha\beta$ photons and capturing one electron in the crystal. The lines are the result of a fit (weighted by the experimental error bars) with $\pm 2\sigma$ standard deviations. The lower solid curve is the expected RT2E resonance profile for channeled ions sampling a density of $0.2e^-$ Å^{-3}. Dashed curves: calculated background and resonance profiles for a ''perfect'' crystal (3.6 μm thick, sampled electron density: $0.15e^-$ Å^3). Dotted curves: the same, for a 1.8-μm-thick ''perfect'' crystal.

only processes likely to occur during ion-electron collisions in channeling. Second, the nonhomogeneity of the target thickness mentioned above can allow a small part of nonchanneled ions to lose very little energy in thinner parts of the target, even less than channeled ions sampling the full crystal thickness. Thus, we decided to optimize the fraction of real channeled ions by selecting particles having their energy loss between 0.45 and 0.6 times the normal energy loss (random orientation), as indicated by the two vertical lines in Fig. 3. No severe selection in transverse energy was made, and the mean sampled electron density was estimated to be equal to the total valence electron density in silicon, i.e., $0.2e^-$ Å^{-3}. This electron density was deduced with an accuracy of $\pm 20\%$ from the amplitude of L,M REC lines in the x-ray spectra, the cross sections of which are well known [24].

Sample x-ray spectra are presented in Fig. 4. In Fig. 4(a) we show one of the NaI(Tl)-NaI(Tl) two-dimensional x-ray coincidence spectra recorded at a beam energy of 37.1 *A* MeV, after selection of the 33+ ions as discussed above. Cuts were made in these spectra, as represented in Fig. 4(b) [histogram of the NaI1 events after selection of *K* x rays registered in NaI2, as shown in Fig. 4(a)]. Figures 4(b) and 4(c) allow the comparison between such a triple coincidence NaI(Tl) spectrum and a spectrum obtained with the Ge detector (in coincidence with 33+ ions). Due to a much better energy resolution of the Ge detector, one clearly sees $K\alpha,\beta$ components, and $L,M,\ldots$ REC lines at higher energies. A small bremsstrahlung contribution is also visible around the *K* x rays. The NaI(Tl) detectors are only able to resolve the *K* x-ray peak (that contains also some bremsstrahlung) and the REC peak. Note that the relative amplitudes between *K* x rays and REC on the two spectra are different because the observation angles are different and also because the NaI(Tl) spectrum is conditioned by the detection of a second *K* x ray.

IV. DISCUSSION

The probability for a channeled ion (actually, an ion selected in the energy-loss range defined above) to emit two *K* x rays in the full solid angle and to emerge from the crystal as 33+ is represented in Fig. 5 at the three incidence energies. The error bars are due to statistics. No evidence for a resonance is found at 40.6 *A* MeV. The solid line through the experimental points is the result from a fit of these data [with a function $P(E)=aE^{-6}$]. The power (-6) of the energy dependence, used in the fitting function, reflects the dominance of MEC and NIE over REC and EIE. Indeed, $P(\mathrm{MEC})$ varies with energy as $E^{-5.5}$, $P(L-\mathrm{REC})$ as $E^{-1.8}$, and $P(\mathrm{NIE})$ and $P(\mathrm{EIE})$ depend little on the incident energy [25]. This shows that crystal defects are the main source of background in this experiment: for a perfect crystal, one would have had only the background due to REC-EIE-EIE sequential events, with an energy dependence close to $E^{-1.8}$.

The lines above and below the best fit correspond to $\pm 2\sigma$ deviations of the fitting parameter *a*. From this fit one can extract an upper limit of the trielectronic recombination cross section per target electron at the resonance energy. With a 95% confidence level (based on statistics) we obtain $\sigma(\mathrm{RT2E}) < 1.9\times 10^{-27}$ cm^2. Systematic uncertainties of

30% on this value are due to the K x-ray–K x-ray coincidence absolute efficiency ($\sim\pm10\%$), the absolute dose determination ($\sim\pm20\%$, that comes from the photomultiplier background on the 34+ detector at high counting rates), and to the mean target electron density estimate ($\sim\pm20\%$).

The expected shape of the trielectronic recombination resonance is also shown in Fig. 5. We used here the Compton profile of a free-electron gas with a density $\rho_e=0.2e^-$ Å^{-3}, as we did in previous RTE studies [20]. The amplitude of the calculated resonance was deduced from the final calculations of Marques *et al.* [10]. These authors estimated the ratio R of DA over single Auger rates for LLL triply excited states to be 3×10^{-7} for Kr ions. This ratio is close to the ratio of trielectronic over dielectronic recombination rates, or for RT2E over RTE cross sections (using the same electron Compton profile). Badnell calculated the ratio of DA over single-electron Auger rates to be somewhat higher ($R\sim10^{-6}$ [1,11]), and also made calculations for RTE for Kr^{35+} ions incident on H_2 targets [26]. We can conclude from our experimental results that R is smaller than 5×10^{-6}. Considering reasonably that the sensitivity of the experiment reported in Ref. [1] is limited to $\sim10\%$ of the $(L+M)$-REC cross sections (from their error bars), i.e., to about 10^{-24} cm^2 per target electron, our results represent an improvement by more than two orders of magnitude for the upper limit of the trielectronic recombination cross section. However, using the same technique (triple coincidences in channeling conditions), one could increase the sensitivity of our experiment by more than one order of magnitude, and reach the range of the theoretical estimates, by the following considerations: results of calculations of the background probability resulting from pure ion-electron interaction (i.e., $L,M,\ldots$ REC–K-L EIE–K-L EIE) are given in Fig. 5 (dashed lines): they correspond to a ''perfect'' crystal, i.e., with an homogeneous thickness and without amorphous layers. Using such a crystal would allow one to select lower electron densities for well channeled ions (around $0.15e^-$ Å^{-3}, as we did in a previous REC experiment [15]). For the same crystal thickness this background is calculated to be below 10^{-7} at the resonance energy. Note that the corresponding calculated resonance profile is narrower, because both the width and the amplitude depend on the electron density. Since the probability of these three uncorrelated events varies as the cube of the target thickness, using a thinner crystal would certainly make the trielectronic recombination cross sections reachable: we present also in Fig. 5 the calculations for a 1.8-μm-thick ''perfect'' crystal (dotted line), for which the signal to background ratio would be enhanced by another factor of 4 as compared to the 3.6-μm-thick crystal. These last calculations correspond to the almost thinnest crystals that can realistically be used with our experimental setup (energy losses have to be resolved between channeled and unchanneled ions). We should mention at this point that the available theoretical estimates of DA rates at the time of our experimental run were higher by one order of magnitude than those published in Ref. [10]. For comparison, the same signal to background ratio would be obtained for a 1.8-μm-thick ''perfect'' crystal or for a 7.5-μg/cm^2 amorphous carbon target (the MEC-NIE-NIE background is considerably lower for low-Z targets). However, in the latter case, the RT2E rate would be lower by one order of magnitude, which would make the accumulation of statistics out of reach within reasonable beam times.

V. SUMMARY AND CONCLUSION

In summary, crystal channeling and triple coincidence measurements (K x-ray–K x-ray–e^- capture by a channeled ion) was used to estimate the KK-LLL trielectronic recombination cross section for He-like krypton ions. An upper limit is obtained that corresponds to an improvement by two orders of magnitude over that obtained in previous ion-gas experiments. The present result is compatible with theoretical predictions: the shake-down mechanism that provides the main contribution to double Auger rates for low-Z systems has a much smaller contribution at $Z=36$ (the shake-up, corresponding to trielectronic recombination, is not measurable here). The ''pure'' three-electron correlation contribution to DA (and TR) is more than one order of magnitude below the sensitivity of our experiment. The use of much better quality crystals could certainly help to observe this exotic electron capture mode.

ACKNOWLEDGMENTS

We would like to thank the GANIL and CIRIL staffs for their technical support, and J.-P. Marques, F. Parente, P. Indelicato, and N.R. Badnell for providing us the results of their calculations prior to their publication.

[1] K.E. Zaharakis, R.R. Haar, O. Woitke, M. Zhu, J.A. Tanis, and N.R. Badnell, Phys. Rev. A **52**, 2910 (1995).
[2] G.J. Schultz, Rev. Mod. Phys. **45**, 378 (1973).
[3] A. Müller, G. Hofmann, B. Weissbecker, M. Stenke, K. Tinschert, M. Wagner, and E. Salzborn, Phys. Rev. Lett. **63**, 758 (1989).
[4] V.V. Afrosimov, Yu.S. Gordeev, A.N. Zinov'ev, D.Kh. Rasulov, and A.P. Shergin, Pis'ma Zh. Eksp. Teor. Fiz. **21**, 539 (1975) [JETP Lett. **21**, 249 (1975)].
[5] V.V. Afrosimov, A.P. Ahmedov, Yu.S. Gordeev, A.N. Zinoviev, and A.P. Shergin, in *Proceedings of the Tenth ICPEAC, Paris*, 1977, edited by G. Watel (North-Holland, Amsterdam, 1977), p. 184.
[6] P. Moretto-Capelle, A. Bordenave-Montesquieu, P. Benoit-Cattin, S. Andriamonje, and H.J. Andrä, Z. Phys. D **21**, S347 (1991).
[7] L. Folkerts, J. Das, S.W. Bergsma, and R. Morgenstern, Phys. Lett. A **163**, 73 (1992).
[8] M.Y. Amusia and I.S. Lee, J. Phys. B **24**, 2617 (1991).
[9] N. Vaeck and J.E. Hansen, J. Phys. B **25**, 3613 (1992).
[10] J-P. Marques, F. Parente, P. Indelicato, and J.-P. Desclaux, J. Phys. B **31**, 2897 (1998).

[11] N. R. Badnell (private communication).
[12] J. Lindhard, Mat. Fys. Medd. K. Dan. Vidensk. Selsk. **34**, No. 14 (1965).
[13] B.R. Appleton, R.H. Ritchie, J.A. Biggersaff, T.S. Noggle, S. Datz, C.D. Moak, H. Verbeek, and V.N. Neelavathi, Phys. Rev. B **19**, 4347 (1979).
[14] S. Andriamonje, M. Chevallier, C. Cohen, J. Dural, M.J. Gaillard, R. Genre, M. Hage-Ali, R. Kirsch, A. L'Hoir, B. Mazuy, J. Mory, J. Moulin, J.C. Poizat, Y. Quéré, J. Remillieux, D. Schmaus, and M. Toulemonde, Phys. Rev. Lett. **59**, 2271 (1987).
[15] S. Andriamonje, M. Chevallier, C. Cohen, N. Cue, D. Dauvergne, J. Dural, R. Kirsch, A. L'Hoir, J.-C. Poizat, Y. Quéré, J. Remillieux, C. Röhl, J.-P. Rozet, D. Schmaus, M. Toulemonde, and D. Vernhet, Phys. Rev. A **54**, 1404 (1996).
[16] N. Claytor, B. Feinberg, H. Gould, C.E. Bemis, J. Gomez del Campo, C.A Ludemann, and C.R. Vane, Phys. Rev. Lett. **61**, 2081 (1988).
[17] A. L'Hoir, S. Andriamonje, R. Anne, N.V. De Castro Faria, M. Chevallier, C. Cohen, J. Dural, M.J. Gaillard, R. Genre, M. Hage-Ali, R. Kirsch, B. Farizon-Mazuy, J. Mory, J. Moulin, J.C. Poizat, Y. Quéré, J. Remillieux, D. Schmaus, and M. Toulemonde, Nucl. Instrum. Methods Phys. Res. B **48**, 45 (1990).
[18] D. Dauvergne, C. Scheidenberger, A. L'Hoir, J.U. Andersen, S. Andriamonje, C. Böckstiegel, M. Chevallier, C. Cohen, N. Cue, S. Czajkowski, J.S. Forster, H. Geissel, H. Irnich, T. Kandler, R. Kirsch, A. Magel, P.H. Mokler, G. Münzenberg, F. Nickel, Yu L. Pivovarov, J.-C. Poizat, M.-F. Politis, J. Remillieux, D. Schmaus, Th. Sthlker, T. Suzuki, and M. Toulemonde, Phys. Rev. A **59**, 2813 (1999).
[19] S. Datz, C.R. Vane, P.F. Dittner, J.P. Giese, J. Gomez Del Campo, N.L. Jones, H.F. Krause, P.D. Miller, M. Schulz, H. Schöne, and T.M. Rosseel, Phys. Rev. Lett. **63**, 742 (1989).
[20] S. Andriamonje, M. Chevallier, C. Cohen, N. Cue, D. Dauvergne, J. Dural, R. Genre, Y. Girard, R. Kirsch, A. L'Hoir, J.-C. Poizat, Y. Quéré, J. Remillieux, D. Schmaus, and M. Toulemonde, Phys. Lett. A **164**, 184 (1992).
[21] J.U. Andersen, J. Chevallier, G.C. Ball, W.G. Davies, J.S. Forster, J.S. Geiger, J.A. Davies, and H. Geissel, Phys. Rev. Lett. **70**, 750 (1993).
[22] H.F. Krause and S. Datz, in *Advances in Atomic, Molecular and Optical Physics*, edited by B. Bederson and H. Walther (Academic, New York, 1996), Vol. 37, p. 139.
[23] L. Bianchi, B. Fernandez, J. Gastebois, A. Gillibert, W. Mittig, and J. Barrette, Nucl. Instrum. Methods Phys. Res. A **276**, 509 (1989).
[24] M. Stobbe, Ann. Phys. (Leipzig) **7**, 661 (1930).
[25] J.P. Rozet, C. Stephan, and D. Vernhet, Nucl. Instrum. Methods Phys. Res. B **107**, 67 (1996).
[26] Th. Stöhlker, Ph.D. thesis, University of Giessen, Germany, 1991 (unpublished).

I-2-2 Capture électronique résonnante par excitation nucléaire NEEC

Ce processus est le processus inverse de la conversion interne nucléaire : un électron est capturé par un ion, et cette capture est accompagnée de l'excitation simultanée du noyau. L'électron incident doit donc avoir l'énergie nécessaire pour satisfaire la condition de résonance.
Le NEEC a été proposé pour la première fois par Goldanskii et Namiot [Goldanskii 76]. Des études de faisabilité ont ensuite été présentées par nos collaborateurs [Cue 89, Kimball 91].

La condition de la résonance s'écrit, pour un ion d'énergie cinétique E_R :

$$E_R = \left(E^* - E_n - \gamma E_i - \beta\gamma p_z c\right)\left(\frac{M_{ion}}{m_e} + 1 + \frac{E^* - E_n}{2m_e c^2}\right), \qquad (1)$$

où E^* est l'énergie de la transition nucléaire, E_n l'énergie de liaison de l'électron dans l'état final, E_i son énergie de liaison dans l'état initial, p_{ez} son impulsion longitudinale, et M_{ion} et m_e les masses respectives de l'ion dans l'état initial et de l'électron ; β et γ sont les facteurs cinématiques de Lorentz pour l'ion.
Si on considère un électron libre et au repos initialement, et si on néglige la masse de l'électron capturé par rapport à celle de l'ion, alors l'équation (1) se simplifie :

$$E_R \approx \frac{M_{ion}}{m_e}\left(E^* - E_n\right) \qquad (2)$$

La section efficace du NEEC est reliée au taux de conversion interne $\lambda^{IC}_{f\to i}$ d'une transition d'un état nucléaire excité f vers le fondamental i (de spins J_f et J_i respectivement) par la relation suivante, déduite du principe du bilan détaillé (règle d'or de Fermi) :

$$\sigma_{NEEC}(\varepsilon) = \frac{(2\pi\hbar)^2}{2m_e\varepsilon}\frac{2J_f+1}{2J_i+1}\Gamma^{IC}_{f\to i}\frac{\Gamma^{tot}}{(\varepsilon-\varepsilon_R)^2 + \left(\frac{\Gamma^{tot}}{2}\right)^2}, \qquad (3)$$

où $\Gamma^{IC}_{f\to i} = \lambda^{IC}_{f\to i}\hbar$, et Γ^{tot} est la largeur totale de l'état excité. Dans l'expression (3), ε est l'énergie de l'électron dans le référentiel de l'ion, et $\varepsilon_R = (m_e/M_{ion})E_R$ l'énergie cinétique correspondante pour la résonance NEEC.
Il faut noter que le dernier terme de l'équation (3) fait intervenir une forme de résonance de type Lorentzienne. Or les électrons d'une cible solide ou atomique ont une distribution en impulsion (le profil Compton, cf. le dernier terme de la 1ère parenthèse de l'équation (1)) qui élargit le profil de la fonction d'excitation lorsqu'on considère l'ion comme projectile, en cinématique inverse. En effet, pour des ions rapides, l'élargissement de la résonance par le profil Compton est bien plus important que la largeur intrinsèque de celle-ci.
Un calcul supposant une distribution de Fermi de vitesses d'un gaz d'électrons libres (d'énergie de Fermi E_F) conduit à la section efficace suivante à la résonance :

$$\sigma_{NEEC}(\varepsilon_R) = \frac{(\pi\hbar)^2}{m_e\sqrt{\varepsilon_R{}^3 E_F}}\frac{2J_f+1}{2J_i+1}\Gamma^{IC}_{f\to i}. \qquad (4)$$

Le NEEC peut jouer un rôle significatif dans le peuplement d'états nucléaires excités dans les plasmas chauds. De plus il suscite un intérêt certain comme moyen de peupler ou dépeupler des états isomériques. Le processus analogue d'excitation nucléaire par transition entre états atomiques liés (Nuclear Excitation by Electronic Transition) a fait l'objet de travaux intensifs au cours des 30 dernières années [Gemmell 02].

Certes, on nous objectera que, la théorie faisant intervenir des éléments de matrice de transitions nucléaires connues, l'observation du NEEC ne devrait pas apporter beaucoup de surprises. De plus les faibles sections efficaces (20 µbarn par e^- cible dans le cas décrit ci-dessus) limitent considérablement le champ d'applications de ce processus. Toutefois, sa mise en évidence demeure un objectif à caractère fondamental, et il est évident que ce processus doit être observé.

L'équation (4) montre que la section efficace de NEEC est d'autant plus grande que le taux de conversion interne est élevé, ce qui ne facilite pas son observation en tant que processus de capture électronique, car l'ion ne change pas de charge s'il perd son électron, et le NEEC n'est pas facilement identifiable par rapport à une diffusion élastique ion-électron si la conversion interne est rapide.
L'objectif initial de la proposition d'expérience NEEC au GSI (en 1989 !) était de tenter d'observer ce processus au moyen de la désexcitation gamma en vol d'un ion ayant capturé un électron. Un rendement radiatif élevé implique cependant un taux de conversion interne faible, et la section efficace attendue, de l'ordre du µbarn par électron cible, rend l'expérience irréalisable compte tenu des faisceaux disponibles au GSI (du point de vue de l'intensité dans l'émittance exigée pour une expérience de canalisation).
Une autre possibilité était d'utiliser des ions avec au moins une lacune K, et de capturer un électron en couche L, en étant sous le seuil de conversion interne pour la couche K ; par exemple, on peut capturer un électron en couche L d'un ion $^{238}U^{91+}$, en excitant la transition M1 de 45 keV à une énergie voisine de 24 MeV/u. L'électron retombe alors en couche K, ce qui bloque la conversion interne et permet de transporter le noyau excité sur de longues distances, car la durée de vie radiative est longue. Le passage cet ion sélectionné U^{90+} dans une seconde cible mince, avec signature d'un nouvel événement de capture électronique (par émission d'un photon REC ou d'une transition L), serait alors suivi d'une ré-ionisation par conversion interne, et donc d'un gel de l'état de charge héliumoïde. Cependant, une telle expérience n'est pas facile, car elle nécessite une double analyse magnétique, qui n'est pas disponible au GSI à basse énergie.
L'idée de nos collègues de Bruyères le Châtel d'observer la conversion interne retardée sur un noyau isomérique est donc *a priori* séduisante : Le noyau candidat est le ^{57}Fe, avec une transition à 14 keV (voir schéma figure 3). La durée de vie du niveau excité est de 79 ns pour un ion hydrogénoïde.

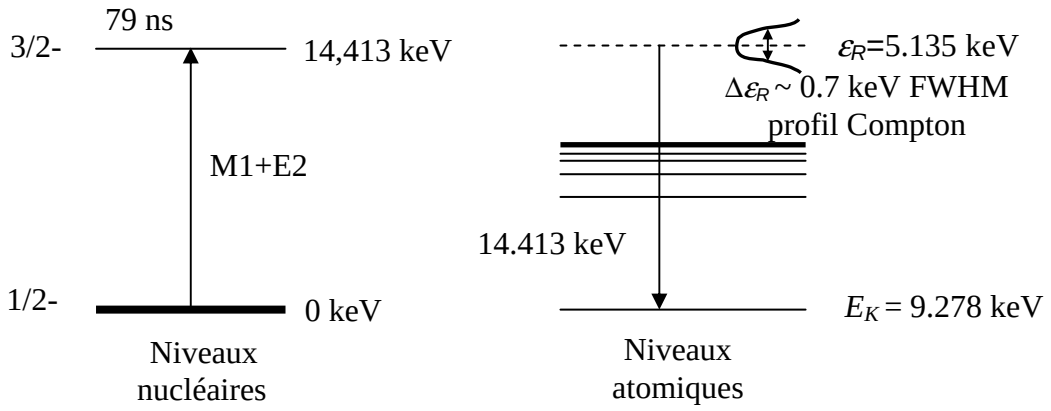

***Figure 3** : schéma de la transition NEEC sur un noyau $^{57}Fe^{26+}$. Le profil Compton correspond à l'élargissement calculé pour un gaz d'électrons libres de 0,2 e-/ Å^3.*

En utilisant des ions incidents Fe^{26+}, les ions 25+ ayant subi une capture NEEC sont sélectionnés à l'aide d'un premier dipôle dans la voie LISE du GANIL, puis perdre leur électron par conversion sur une section droite de 5,6 m, ce qui permet de sélectionner les ions 26+ transmis à travers un second dipôle. Le schéma de l'expérience est représenté figure 4, avec les taux de transmission attendus pour des ions canalisés. L'utilisation de deux faisceaux ^{56}Fe et ^{57}Fe doit permettre de signer, à l'énergie de la résonance $E_R = 9,4$ MeV/u, l'augmentation due au NEEC du nombre d'ions $^{57}Fe^{26+}$ transmis au plan focal image de LISE, par rapport aux isotopes A=56. Le bruit de fond principal attendu est causé par l'ionisation dans le gaz résiduel dans la section droite entre les deux dipôles. La probabilité qu'un ion canalisé fasse une capture REC dans le cristal, puis subisse une ionisation dans la section droite avec un vide moyen de 10^{-7} mbar, est estimée à 5.10^{-9} par ion, alors que la probabilité calculée de NEEC et de désexcitation par conversion interne entre les dipôles est de $1,9.10^{-9}$.

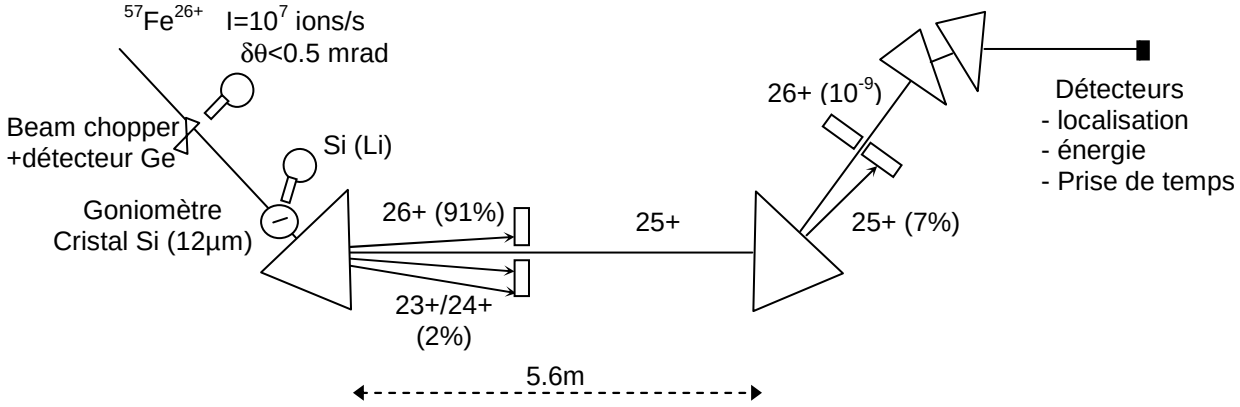

***Figure 4**: Schéma de principe de l'expérience NEEC pour des ions ^{57}Fe dans la voie LISE.*

L'expérience réalisée en septembre 2004 a malheureusement démontré que le vide moyen entre les deux dipôles était environ de 6.10^{-6} mbar lors de l'expérience. Des études sont actuellement en cours pour conclure à la possibilité ou non d'améliorer ce vide. Cela peut sembler surprenant, mais cette voie de faisceau a été considérablement contaminée depuis la création du GANIL, car elle sert à la production de faisceaux secondaires ; l'insertion de nouveau éléments, ou la modification d'éléments existants dans cette voie, pose de nombreux problèmes, en particulier en ce qui concerne la radioprotection. Le reste est l'affaire de la bonne volonté des personnes - voire des autorités - compétentes…

1-3 Etude détaillée de processus d'interaction ion-électron

Dans cette section, je reviendrais sur des expériences qui ont permis d'étudier en détail des processus résultant de l'interaction ion-électron, tels que la capture résonante diélectronique (ou RTE), la capture radiative REC, et l'ionisation par impact d'électrons EII.
Les études sur les deux premiers processus ont été menées durant ma thèse.

1-3-1 La capture résonante diélectronique.

Je ne m'appesantirai pas sur cette étude ancienne, et je renvoie le lecteur à la lecture de l'article [Andriamonje 92] ci-dessous. Mon mémoire de thèse retrace également l'analyse de cette expérience, réalisée en 1990, de façon très détaillée.
Pour situer cette étude dans le contexte d'alors, il y avait une controverse sur l'existence présumée d'un gaz d'électron ultra-froid au centre des canaux d'un cristal, suite à la parution d'un article sur l'observation du RTE en condition de canalisation dans un cristal d'or par A. Belkacem et al. [Belkacem 90]. Des résonances anormalement étroites avaient été mesurées par ces auteurs. Depuis, d'autres études, dont la nôtre, ont montré que ces résultats ne sont pas reproductibles.
Notre expérience n'était certes pas la plus sensible pour étudier la largeur du profil Compton des électrons d'un cristal, en particulier parce que la structure fine de la résonance KLL d'ions incidents Xe^{52+} ne permettait pas de caractériser cette largeur Compton. D'autre part, le cristal utilisé étant relativement épais, la perte d'énergie, et le réchauffement transverse associé pour les ions canalisés, ne permettaient pas la sélection d'ions hypercanalisés.
Cependant, si un gaz d'électrons ultra-froid était présent au centre des canaux d'un cristal de silicium, notre expérience l'aurait mis en évidence, grâce à l'analyse en forme et en amplitude de la fonction d'excitation, toutes deux caractéristiques de la densité électronique rencontrée.
Notre étude avait néanmoins le mérite d'être la première à mettre en évidence le processus RTE à la fois par les échanges de charge et par la détection des photons K_α. Ces deux mesures complémentaires et indépendantes étaient en relativement bon accord, et en accord avec des calculs obtenus à partir de taux de transition Auger publiés dans la littérature. Une meilleure prise en compte de la distribution angulaire de ces photons K_α (isotropes dans le référentiel du centre de masse, plutôt qu'en $\sin^2\theta_{lab}$), aurait parfait cet accord, car il aurait renormalisé la courbe d'excitation RTE-X par un facteur proche de 1,5. Il n'y avait pas de quoi publier un erratum. Depuis, d'autres expériences ont été consacrées au RTE, y compris en cible solide. J'ai eu l'opportunité de participer à l'une d'entre elles lors de mon séjour au GSI en 1993, avec des ions U^{90+} [Kandler 95]. En ce qui concerne la caractérisation du gaz d'électrons cible rencontré par des ions canalisés, une étude réalisée par Andersen et al. [Andersen 96] à Chalk River aura été plus précise que la nôtre, car ils ont utilisé un spectromètre à haute résolution, et réalisé l'expérience avec un cristal très mince, ce qui limite le réchauffement transverse. Ils ont donc pu, en utilisant un faisceau d'ions brome (Z=33), étudier finement la largeur du pic de résonance RTE-KLL en fonction de l'énergie transverse des ions canalisés. Ils n'ont pas conclu, eux non plus, à l'existence d'un gaz d'électrons ultra-froids dans le silicium.

Physics Letters A 164 (1992) 184–190
North-Holland

PHYSICS LETTERS A

RTE measurement with Xe^{52+} ions channeled in a Si crystal ☆

S. Andriamonje [1], M. Chevallier [2], C. Cohen [3], N. Cue [4], D. Dauvergne [2], J. Dural [5], R. Genre [2], Y. Girard [3], R. Kirsch [2], A. L'Hoir [3], J.C. Poizat [2], Y. Quéré [6], J. Remillieux [2], D. Schmaus [3] and M. Toulemonde [5]

[1] *Centre d'Etudes Nucléaires de Bordeaux–Gradignan and IN2P3, Le Haut-Vigneau, 33175 Gradignan Cedex, France*
[2] *Institut de Physique Nucléaire de Lyon and IN2P3, Université Claude Bernard Lyon I, 43 Boulevard du 11 Novembre 1918, 69622 Villeurbanne Cedex, France*
[3] *Groupe de Physique des Solides, Université Paris VII, 75251 Paris Cedex 05, France*
[4] *Department of Physics, The Hong Kong University of Science and Technology, Kowloon, Hong Kong*
[5] *Centre Interdisciplinaire de Recherche avec les Ions Lourds, 14040 Caen Cedex, France*
[6] *Laboratoire des Solides Irradiés, Ecole Polytechnique, 91128 Palaiseau Cedex, France*

Received 13 January 1992; revised manuscript received 10 February 1992; accepted for publication 12 February 1992
Communicated by B. Fricke

KLL resonant transfer and excitation (RTE) of 33–43 MeV/nucleon He-like Xe ions channeled along the ⟨110⟩ axis of a thin Si crystal has been investigated in measurements of charge state distributions and of the resulting X-ray production. The resonance peaks obtained by the two methods are quite similar. The charge state measurements show that RTE appears, for well channeled ions, to be rather independent of the electron density they sample. Resonance energy, width and intensity are compared with theoretical estimates.

1. Introduction

Resonant transfer and excitation (RTE) is a process in which the capture of a bound target electron by a projectile ion is accompanied by a simultaneous ion excitation [1]; the resonantly formed doubly excited state decays to a non-autoionizing state either by the Auger effect (RTEA, equivalent to an inelastic electron scattering) or by radiative emission (RTEX). RTEX is similar to dielectronic recombination (DR) occurring with free electrons and first discussed in the case of astrophysical plasmas [2]. In the RTE case, the resonance profile is broadened by the longitudinal momentum distribution – with respect to the beam direction – of the target electron to be captured. The electron capture accompanied by ion excitation is the time reversal of the Auger effect, a property which is used in the evaluation of RTE cross sections.

Experimentally, RTEX can be studied by X-ray or/ and by charge exchange measurements. Such experiments were performed during the last decade with light gas targets [1,3–5] and various projectile ions up to uranium.

Crystal channeling has also been recognized recently as an interesting tool for RTEX experimentation [6–8]. Indeed, channeled ions encounter mainly loosely bound electrons, so that target nuclei and tightly bound electrons are not involved in charge exchange, so that target nuclei and tightly bound electrons are not involved in charge exchange. Electron–ion interaction processes become predominant and thus directly observable. This is the case for radiative electron capture (REC) [9], electron impact ionization [10], and primary bremsstrahlung [11].

Two groups have performed RTE measurements in channeling conditions. Belkacem et al. [6] observed the KLL resonance with incident Ti^{19+} and Ti^{20+} ions channeled in a thin gold crystal and then energy- and charge-analyzed. They selected the best channeled particles, i.e., those which have the smallest energy lost. The resonance peak was found to be

☆ Work performed at GANIL (Caen, France).

surprisingly narrow, and at an energy slightly higher than expected. Datz et al. [7] studied the KLL resonances with Ca^{18+}, S^{15+}, and Ti^{20+} incident ions channeled in a silicon crystal by measuring X-ray emission. Using Ti^{20+} ions, they measured the K_α yield in coincidence with outcoming Ti^{19+} ions. The width of the resonance peak was found to be comparable to that obtained with a H_2 gas target, and they observed no shift in the resonance energy. They recently repeated their Ti measurements [8] with Ti^{20+} in a thin gold crystal, and were unable to reproduce the results of ref. [6]. In a recent paper, Feagin and Wanser [12] claim that the Compton profile of gold conduction electrons is significantly narrower than predicted by a simple free electron gas model, and thus suggested that the width of the resonance in aligned gold crystals could be as low as the value obtained in ref. [6].

The present paper describes a similar study of the KLL resonance, with heavier projectiles, He-like Xe ions, incident along the $\langle 110 \rangle$ direction of a Si crystal. In that case the KLL peak is separated from all other KL*n* resonances involving higher excited states. Two-electron projectiles (52+) have been used, because they could be produced with a large intensity around the resonance energy, and also because RTE rates are expected to be larger with He-like than with H-like projectiles. Moreover RTE rates could be readily determined from literature. The measurements were on the charge and energy analysis of the transmitted ions and projectile X-ray spectroscopy.

2. Experimental method

The experiment was performed at GANIL (Caen, France) in the LISE extension, a beam-line designed for the analysis of highly stripped ions (fig. 1). The incident energy was degraded by steps of 400–1200 keV/nucleon in aluminum foils (T1) of various thicknesses which could be tilted in the beam. A monokinetic and parallel beam of Xe^{52+} ions was then selected by a set of collimators and a magnetic spectrometer (B1 ,B2). The beam intensity at the target (T2) was between 2 and 5 nA. The effective target thickness was 21 μm, thin enough for the electron capture probability to be low for well channeled ions, and thick enough for the energy loss in the crystal to be readily measured. A three axis goniometer which moved with an accuracy of 0.1 mrad was used for crystal alignment. Ions emerging from the crystal were magnetically charge- and energy-analyzed (B4), and the ions with selected charge states were detected in a wire chamber (proportional gas counter). The overall detection energy resolution is about 20 keV/nucleon. Electronic noise on wires was a limitation for the measurement of low charge fractions. A hyperpure Ge detector, with an energy resolution of 300 eV at 20 keV, viewed the beam impact on the target at $\theta_{lab}=90°$. The radiative lifetimes of Xe-ion excited states formed by electron capture or collisional excitation are quite short, which means that the corresponding X-ray emission takes place when the projectile is still inside the crystal target. The absolute number of incident ions was measured using a beam chopper made of silver-coated blades, in which the emitted Ag-K_α X-rays were detected by a Si(Li) diode.

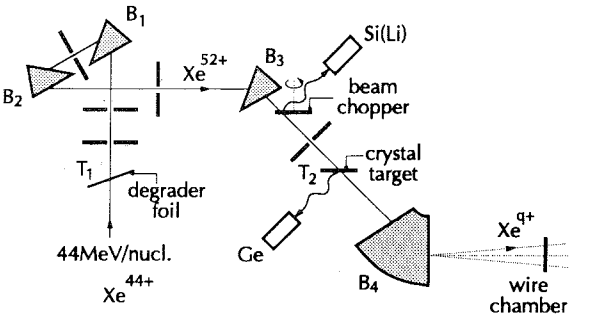

Fig. 1. Sketch of the experimental setup.

At each incident energy, determined by the degrader thickness, collimators were used to keep the beam emittance at 0.15π mm mrad in each transverse direction. Then we measured, at the target, the position of the beam spot in the horizontal plane and the incidence angle. It is remarkable that, when the beam energy was changed, the beam position and direction delivered by the accelerator were found to stay within 1.5 mm and 1 mrad, respectively. However, when necessary, the beam spot was readjusted at the center of the target, and at each energy the crystal was realigned by measuring the extinction yield of the Xe-K_α emission around the $\langle 110 \rangle$ direction; then the X-ray spectrum and the charge distribution were recorded. Charge distributions and X-

ray spectra were also measured for random orientation.

3. Results

For ⟨110⟩ alignment, charge state distributions of transmitted Xe ions are dominated by the "frozen" charge 52+. The 51+ component, due to one electron capture, has been found to be at most about 10% of the total beam. As the 50+ component has been found to be always less than 1%, the conditions for single capture are essentially fulfilled for channeled particles.

A typical wire chamber spectrum is given in fig. 2, which shows the energy distribution of 52+ and 51+ ions transmitted for axial incidence of 38.2 MeV/nucleon Xe^{52+} (on the top of the resonance, see below). Vertical arrows give the calculated "virtual" positions where direct beams of charges 52+ and 51+ would be detected and the positions of ions transmitted for a random crystal orientation. From the energy loss distribution, one deduces that most of these ions have been channeled, in spite of the fact that these two peaks contain the quasi-totality of unchanneled ions, which constitute about 3% of the transmitted beam and have a mean charge at emergence 51.5. The most probable energy loss is found to be about 0.4 times the "random" energy loss.

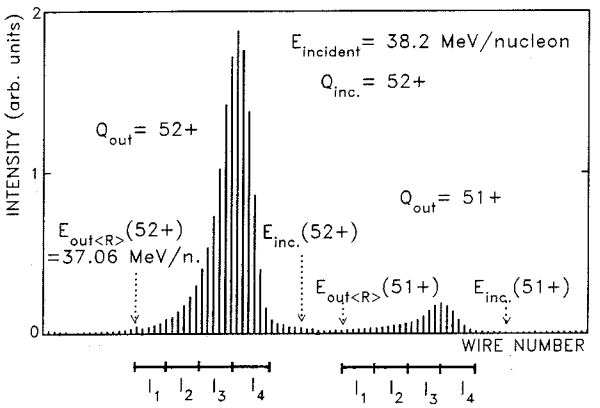

Fig. 2. Energy distribution in the wire chamber for 38.2 MeV/nucleon Xe^{52+} ions incident along the ⟨110⟩ axis, for two outcoming charge states, the "frozen" 52+ and the 51+. Vertical arrows represent the calculated energy positions of the virtual direct beam (E_{inc}) and emerging random beam ($E_{out}\langle R\rangle$) (see text). The intervals I_1–I_4 are defined in the text. The dispersion is here about 40 keV/nucleon per wire. The FWHM of the direct beam is less than two wires, and the FWHM of the histograms corresponding to random orientation is about five wires.

The energy loss of a channeled ion is known to be partly due to the local electron density it samples but has also a non-local component. Each component has its own dependence upon the transverse energy of the particle, that determines its accessible transverse space in the crystal. In order to select ions travelling through various target electron densities, we have divided the transmitted ions into groups I_1–I_4, according to their energy loss in the crystal (the width of each group being a fifth of the random energy loss). The energy dependence of electron capture has been studied for each group separately.

In fig. 3 we show the observed energy dependence of the ratio of charge fractions (50+51)/(50+51+52), which represents the electron capture probability by 52+ incident ions in the crystal. The energy groups I_3 and I_4 correspond to the best channeled ions: the ions belonging to I_4 have experienced between 0.2 and 0.4 times the random loss ΔE_R (between 0.4 and 0.6 times ΔE_R for I_3). The two KLL

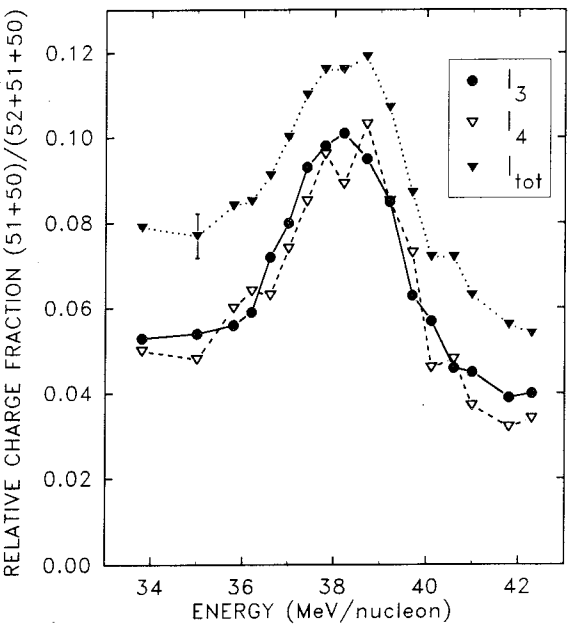

Fig. 3. Relative fractions of ions that have captured at least one electron after passing through the 21 μm Si crystal along the ⟨110⟩ axis, for various groups of energy losses.

RTE resonance peaks (I_3 and I_4) appear to be sitting on a continuum that decreases with energy and is due to radiative electron capture into the Xe L shell. At the resonance, the probabilities for resonant KLL RTE and for non-resonant L REC captures respectively, are about of the same magnitude. The peaks for the I_3 and I_4 groups seat on the same continuum and are quite similar in amplitude, shape and width, which is surprising since the target electron gas traversed by the channeled ions has different mean densities in the two cases. Results for unchanneled and poorly channeled ions (groups I_1 and I_2) are rather inconclusive. They are not shown here, because the continuum level due to mechanical capture of target core electrons is much larger and the resonance peak, hardly visible for the I_2 group, disappears for the I_1 group. Finally the curve labelled I_{tot} is the RTE resonance peak for all energy groups together. It will be compared to the RTE resonance peak observed by means of the Xe-K_α emission, which we discuss now.

The radiative decays of the doubly excited states produced in the RTE process lead to a K_α peak, which also contains a contribution from non-resonant formation of K shell vacancies in close encounters of unchanneled ions with Si atoms. Further, the observation of the energy dependence of the K_α yield is complicated by the fact that L REC and K_α photons have the same energy at the KLL RTE resonance. This is illustrated in fig. 4, where three X-ray spectra, corresponding to the same number of incident ions, obtained at incident energies below (a), at (b), and above (c) the resonance, can be compared.

In fig. 5 we show the energy dependence of the (L REC+K_α) photon yield at 90° (curve a). The RTE resonance appears nicely, sitting on the continuum formed by L REC photons and by K_α photons from deexcitation of unchanneled Xe ions in their close interaction with Si atom cores. Both components decrease monotonously when the incident energy increases. A subtraction of this continuum has been made and the absolute total RTEX yield (curve b) has been determined by using the angular distribution suggested by Bhalla [13],

$$W(\theta) \sim 1 - \tfrac{1}{2} P_2 \cos\theta ,$$

where $P_2 \cos\theta$ is the Legendre polynomial of order two (we assume here the dominance of dipolar transitions in the decay of these doubly excited states).

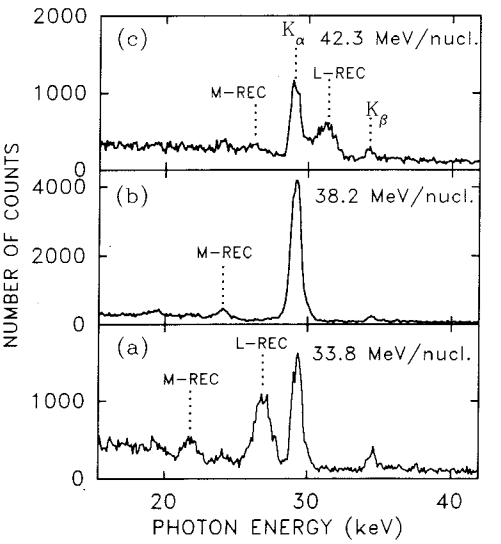

Fig. 4. Photon spectra in axial alignment, at various incident ion energies, observed at 90° to the beam, after normalization to the same number of incident ions. The energy 38.2 MeV/nucleon corresponds to the center of the resonance (notice the changes in the vertical scales).

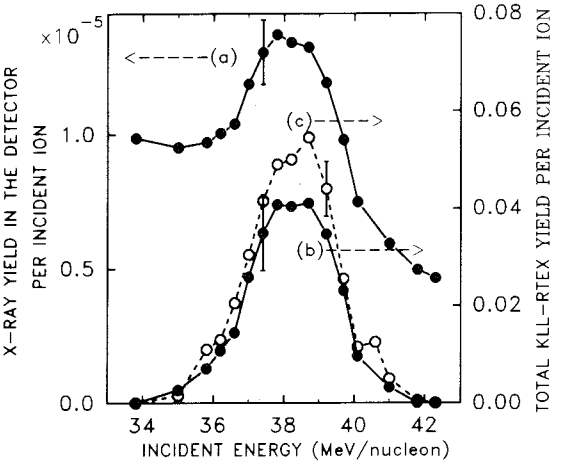

Fig. 5. (a) (K_α+L REC) photon yield in the Ge detector, located at 90° to the beam direction, after correction for counting dead time and beam-monitor efficiency (left scale). (b) Total KLL RTEX yield in the 4π solid angle (right scale). (c) RTE resonance peak obtained by charge analysis (right scale).

Moreover we also show the resonance peak (curve c), deduced from the charge state measurement, obtained after subtraction of the continuum in the curve I_{tot} of fig. 3.

4. Discussion of results

First of all we find a good agreement between the two methods used to observe the RTE resonance. As seen in fig. 5, the energy positions and widths are quite the same. The RTE yields agree within 25%, although several technical and physical reasons might have spoiled the agreement: absolute X-ray yields rely on accuracies of the incident beam intensity measurement (the uncertainty on the beam-chopper calibration is about 10%), the Ge detector solid angle and efficiency determinations (5%), and principally on the assumed angular distribution $W(\theta)$ of the K_α photons as discussed above (using an isotropic distribution would increase the experimentally deduced total rates by 20%). The probability of L-electron loss by the projectile in the crystal, which would affect more the charge state measurement than the K_α X-ray emission, is expected to be small (less than 10%), if one refers to previous channeling charge state measurements performed with Li-like Xe ions [14].

Next we compare our data with theoretical estimates. The DR rates of He-like ions calculated by Nilsen [15] were used, and then from these rates the DR cross sections were calculated following the integration method of McLaughlin and Hahn [16]. These cross sections are shown in fig. 6a after averaging over energy bins of 0.05 MeV/nucleon. One can see three groups of resonances, corresponding to the fine structure in j–j coupling of the intermediate doubly excited states (they are labelled according to their j–j values, e.g., $j_1=\frac{1}{2}$ $j_2=\frac{3}{2}$).

The energy loss of the ions in the crystal ($\simeq 0.5$ MeV/nucleon in our velocity range) broadens the resonances and shifts them to higher energies, as shown in fig. 6b, where the three groups of resonances are still visible.

In order to compare these predicted cross sections per target electron to the experimental RTE yield (figs. 5b and 5c), one has to multiply σ_{DR} by the mean electron density $\bar{\rho}$ and by the target thickness t. We must then estimate $\bar{\rho}$ which should depend on the transverse energy and thus be different for the groups I_3 and I_4. A detailed analysis of the relationship between transverse energy and energy loss has been performed in a similar experimental situation in ref. [10]. Applying this analysis to the present case, we deduce that ions from both I_3 and I_4 are restricted

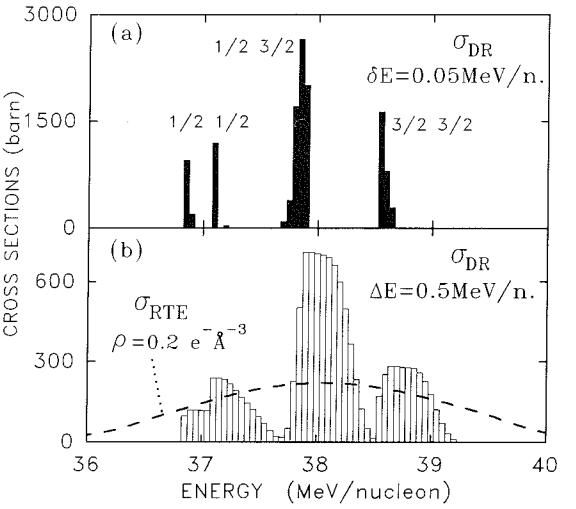

Fig. 6. Energy dependence of RTE cross sections calculated for an He-like Xe ion channeled along the ⟨110⟩ axis of a 21 μm thick Si crystal: (a) Dielectronic recombination cross section for a target electron at rest (δE is the integration energy bin). (b) The same as (a) after convolution with the ion energy loss profile in the crystal target for a total energy loss ΔE (histograms), and after convolution with the Compton profile of a free electron gas of density ρ (dashed curve).

in regions of the transverse plane where the density of L-shell Si electrons is negligible. The difference in the energy losses for the two groups arises mainly from the fact that ions from I_3, with higher transverse energy, can already significantly induce the ionization of L-shell Si electrons in rather large impact parameter collisions (0.55 Å from the atomic string, if the $\simeq 0.25$ Å extension of the Si L-shell is taken into account). Moreover, ions from group I_4 sample a density of Si valence electrons (0.15 e$^-$Å^{-3}) smaller than the ions from I_3 (0.20 e$^-$Å^{-3}). In regard of these different sampled densities the RTE measured yields I_3 and I_4 are found surprisingly close to each other (fig. 3) and then appear not to be proportional to the local electron density. We have thus decided to take for $\bar{\rho}$ the mean value for the valence electron gas ($\rho_{val}=0.2$ e$^-$Å^{-3}).

Taking this electron density leads to a calculated area of the RTE peak that is $\sim 50\%$ larger than the experimental value of fig. 5c. This slight disagreement between this prediction and the experiment could be due to an overestimate either of the DR rates given in ref. [15] or of the assumed electron density.

Another way of investigating the effective electron density involved in the RTE process is to study the width of the resonance. We used here the method proposed by Brandt [17], based on the impulse approximation, to take into account the target electron Compton profile. This would be straightforward for a free electron gas, for which the momentum distribution is uniform within the Fermi sphere of radius $p_F=\hbar(3\pi^2\bar{\rho})^{1/3}$. The corresponding resonance shape calculated for a Fermi gas of density $\bar{\rho}=\rho_{val}$ is shown in fig. 6b (dashed line). One can notice that the fine structure of the KLL resonance is now washed out, in agreement with our measurements. A quantitative comparison in shape is shown in fig. 7 between the experimental resonance observed with energy groups I_3+I_4 and the calculated curve of fig. 6b. These calculated values have to be multiplied by 0.63 in order to reproduce the experimental peak area. The calculated and experimental peak positions are in good agreement. Furthermore, the calculated curve is seen to reproduce well the width of the experimental resonance peak. In our opinion this agreement may be fortuitous, since axial channeling does not provide a totally free target electron gas. The interest of fig. 6b is then to give the lower limit of the resonance width, since the capture of valence electrons should lead to a wider RTE peak (if one excludes crystalline effects along the $\langle 110\rangle$ axis of Si of the type discussed in ref. [12] for the $\langle 110\rangle$ axis of gold crystals). We have to keep in mind that the resonance shape is here dominated by the fine structure (see fig. 6a) and thus is not very sensitive to small variations of the electron Compton profile. However, the present result excludes a Compton profile in Si as narrow as that found by Belkacem et al. [6] in a gold crystal (in our case the fine structure of the resonance should still be observable).

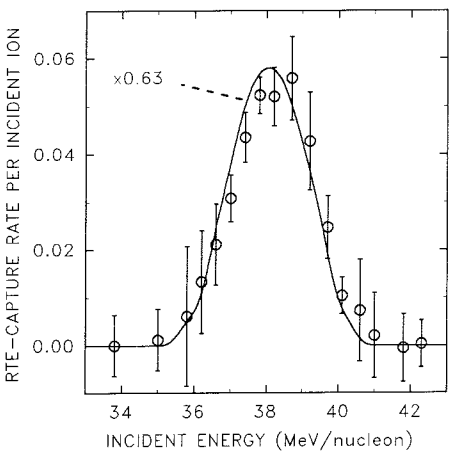

Fig. 7. Comparison between the experimental RTE yield for the channeled ions of the I_3+I_4 group (errors are due to electronic noise in the wire chamber) and the RTE yield calculated with an assumed electron density of 0.2 $e^-Å^{-3}$ (solid line) after normalization of total peak areas.

In fact a correct prediction of the resonance width should consider the exact momentum distribution of the valence electrons along the crystal axis. We are presently investigating this problem more completely.

It is also important to note that the continuum components of the capture yield for the groups I_3 and I_4, mostly due to the L REC process, do not seem to reflect the respective encountered electron densities (see fig. 3). This relative non-locality of both L REC and KLL RTE along channeling trajectories is quite intriguing and deserves to be studied further.

5. Conclusion

We have observed RTE in aligned crystals by two independent methods, X-ray emission and charge exchange, which lead nearly to the same results.

Our theoretical estimates reproduce the experimental RTE capture probability in channeling with an accuracy better than 50%. Moreover, we observed that resonant KLL RTE and non-resonant L REC captures are rather independent of the local electronic density near the center of the $\langle 110\rangle$ channel.

Finally our experiment with a Si crystal orientated along the $\langle 110\rangle$ axis does not reveal an anomalous energy and width for the resonance, as reported in ref. [6] for the $\langle 110\rangle$ gold channel. If these anomalous effects were in Si large as in Au our experiment would have shown them. Nevertheless, in our case, the width of the fine structure of doubly occupied L states in Xe^{51+}, together with the energy loss of the projectiles in the crystal, are not conclusive for a detailed study of electron Compton profiles along crystal channels. Further channeling experiments at GANIL will attempt to measure more accurately these Compton profiles.

Acknowledgement

We would like to thank the GANIL staff and particularly M. Bajard and D. Bibet for providing us a very high quality beam, allowing the first study at GANIL of excitation functions in channeling conditions. We also acknowledge the CIRIL staff for their help, and Drs. J. Désesquelles and J.P. Desclaux for helpful discussions about the structure of xenon ions. The supports of NATO under Research Grant CRG 890597 and of CNRS under GDR86 are gratefully acknowledged.

References

[1] J.A. Tanis, S.M. Shafroth, J.E. Willis, M. Clark, J. Swenson, E.N. Strait and J.R. Mowat, Phys. Rev. Lett. 47 (1981) 828.
[2] A. Burgess, Astrophys. J. 139 (1964) 776.
[3] J.A. Tanis, Nucl. Instrum. Meth. A 262 (1987) 52.
[4] P.H. Mokler and S. Reusch, Z. Phys. D 8 (1988) 393.
[5] W.G. Graham, K.H. Berkner, E.M. Bernstein, M.W. Clark, B. Feinberg, M.A. McMahan, T.J. Morgan, W. Rathbun, A.S. Schlachter and J.A.Tanis, Phys. Rev. Lett. 65 (1990) 2773.
[6] A. Belkacem, E.P. Kanter, K.E. Rehm, E.M. Bernstein, M.W. Clark, S.M. Ferguson, J.A. Tanis, K.H. Berkner and D. Schneider, Phys. Rev. Lett. 64 (1990) 380.
[7] S. Datz, C.R. Vane, P.F. Dittner, J.P. Giese, J. Gomez del Campo, N.L. Jones, H.F. Krause, P.D. Miller, M. Schulz, H. Schöne and T.M. Rosseel, Phys. Rev. Lett. 63 (1989) 742.
[8] P.F. Dittner, C.R. Vane, H.F. Krause, J. Gomez del Campo, N.L. Jones, P. Zeijlmans van Emmichoven, U. Bechtold and S. Datz, Bull. Am. Phys. Soc. 36 (1991) 1365.
[9] S. Andriamonje, M. Chevallier, C. Cohen, J. Dural, M.J. Gaillard, R. Genre, M. Hage-Ali, R. Kirsch, A. L'Hoir, B. Mazuy, J. Mory, J. Moulin, J.C. Poizat, J. Remillieux, D. Schmaus and M. Toulemonde, Phys. Rev. Lett. 59 (1987) 2271.
[10] A. L'Hoir, S. Andriamonje, R. Anne, N.V. De Castro Faria, M. Chevallier, C. Cohen, J. Dural, M.J. Gaillard, R. Genre, M. Hage-Ali, R. Kirsch, B. Farizon-Mazuy, J. Mory, J. Moulin, J.C. Poizat, Y. Quéré, J. Remillieux, D. Schmaus and M. Toulemonde, Nucl. Instrum. Methods B 48 (1990) 45.
[11] S. Andriamonje et al., to be published.
[12] J.M. Feagin and K.H. Wanser, Phys. Rev. A 44 (1991) 4228.
[13] C.P. Bhalla, Phys. Rev. Lett. 64 (1990) 1103
[14] J.C. Poizat, S. Andriamonje, R. Anne, N.V. De Castro Faria, M. Chevallier, C. Cohen, J. Dural, B. Farizon-Mazuy, M.J. Gaillard, R. Genre, M. Hage-Ali, R. Kirsch, A. L'Hoir, J. Mory, J. Moulin, Y. Quéré, J. Remillieux, D. Schmaus and M. Toulemonde, in: The physics of electronic and atomic collisions, eds. A. Dalgarno et al. (American Institute of Physics, 1990) p. 317.
[15] J. Nilsen, At. Data Nucl. Data Tables 38 (1988) 340.
[16] D.J. McLaughlin and Y. Hahn, Phys. Rev. A 29 (1982) 712.
[17] D. Brandt, Phys. Rev. A 27 (1983) 1314.

1-3-2 : la capture électronique radiative REC

Notre collaboration avait réalisé une première étude de la capture radiative par des ions Xe^{53+} en condition de canalisation [Andriamonje 87]. Cependant, l'intérêt suscité par l'étude des profils Compton des électrons dans un cristal au moyen du RTE nous a poussés à proposer une nouvelle expérience en 1992, lors de ma thèse. Dans cette expérience nous pouvions observer la capture radiative à la fois pour des ions canalisés et pour des ions non canalisés, en utilisant des ions accélérés à une vitesse telle que $\eta_K = v_{ion}/v_K > 1$, où v_K est la vitesse d'un électron K de l'ion, de telle sorte que l'état de charge majoritaire soit celui de l'ion complètement épluché. Nous nous posions également la question de la localité de ce processus : dépend-t-il de la densité électronique locale rencontrée par l'ion dans le solide, ou bien, à l'instar de la capture mécanique, ou de l'excitation-ionisation des atomes cible, responsable de la perte d'énergie, est-ce un processus à plus grande portée ? De plus, la polarisation du gaz d'électron par le champ électrique de l'ion très chargé modifie-t-elle significativement la densité électronique au voisinage de l'ion ?
L'étude à la fois de l'amplitude et de la largeur des raies de photons REC devait nous fournir cette information locale sur le gaz d'électron rencontré par les ions canalisés.
C'est pourquoi nous avons réalisé cette expérience à forte statistique (avec un cristal épais) et à haute résolution, en utilisant des détecteurs X de bonne résolution, et très collimatés, afin de réduire l'élargissement Doppler des photons détectés.
L'article ci-dessous [Andriamonje 96] constitue un travail de synthèse assez poussé de cette étude, avec notamment les résultats des simulations que j'ai réalisées. Ce travail d'analyse et d'interprétation a été long (l'article a été publié trois ans après l'expérience). Ceci est dû à la richesse des informations qu'on peut en extraire. En particulier, nous avons calculé les profils Compton dépendant du paramètre d'impact pour les électrons de cœur du silicium, par transformée de Fourrier partielle des fonctions d'ondes électroniques (équations 2 et 3 de l'article). Ces calculs ont été nécessaires pour obtenir un bon accord entre l'expérience et les simulations. Cette expérience a permis, pour la première fois, d'étudier la distribution en impulsion des électrons d'un atome en fonction du paramètre d'impact lors d'une collision. Cette information n'est pas accessible par les méthodes classiques d'étude du profil Compton par diffusion Compton ou par annihilation de positons. Seules des expériences d'analyse de recul simultané des électrons et de l'atome cible peuvent, dans le cas de collisions lentes avec des cibles gazeuses d'atomes ou de molécules légères, fournir une information similaire. Ces expériences RIMS (Recoil Ion Momentum Spectroscopy) ont été largement développées dans la dernière décennie.
Avec beaucoup de recul, cette expérience aurait pu être améliorée de deux façons différentes : la première, en utilisant un cristal plus mince : cela aurait diminué l'influence du réchauffement transverse des ions canalisés, et donc permis une étude plus précise du gaz d'électrons rencontré par les ions les mieux canalisés. La seconde amélioration aurait consisté en l'utilisation d'une acquisition événement par événement, avec un détecteur permettant de mesurer la perte d'énergie de chaque ion transmis pour chaque état de charge. Cette dernière amélioration a été faite par la suite dans nos expériences au GANIL, en utilisant le spectromètre SPEG, ou bien, si on reste dans la voie LISE, en mesurant le temps de vol sur quelques dizaines de mètres des ions transmis. Néanmoins, ces deux améliorations auraient conduit nécessairement à une diminution du taux de comptage, et donc à une plus faible statistique. On ne peut pas gagner sur tous les tableaux.

K-shell radiative electron capture with bare 60-MeV/u Kr ions channeled in a Si crystal: Experiments and simulations

S. Andriamonje,[1] M. Chevallier,[2] C. Cohen,[3] N. Cue,[4] D. Dauvergne,[2] J. Dural,[5] F. Fujimoto,[6] R. Kirsch,[2] A. L'Hoir,[3] J.-C. Poizat,[2] Y. Quéré,[6] J. Remillieux,[2] C. Röhl,[1] H. Rothard,[5] J. P. Rozet,[3] D. Schmaus,[3] M. Toulemonde,[5] and D. Vernhet[3]

[1]*Centre d'Etudes Nucléaires de Bordeaux-Gradignan and IN2P3, le Haut-Vigneau, 33175 Gradignan Cedex, France*

[2] *Institut de Physique Nucléaire de Lyon and IN2P3, Université Claude Bernard Lyon-I, 43, Bd du 11 Novembre 1918, 69622 Villeurbanne Cedex, France*

[3]*Groupe de Physique des Solides, CNRS URA 017, Université Paris VII et Paris VI, 75251 Paris Cedex 05, France*

[4]*Department of Physics, The Hong Kong University of Science and Technology, Kowloon, Hong Kong*

[5]*Centre Interdisciplinaire de Recherches avec les Ions Lourds, UMR 11 CNRS-CEA, rue Claude Bloch, 14040 Caen Cedex, France*

[6]*Laboratoire des Solides Irradiés, Ecole polytechnique, 91128 Palaiseau Cedex, France*

(Received 24 January 1996)

We have performed *K*-shell radiative electron capture (*K*-REC) measurements with bare 60.1-MeV/u incident krypton ions, both in channeling conditions and for random orientation of a 37-μm silicon crystal. The sampled electron densities are quite different in each case, which has an influence both on the shape and on the amplitude of the *K*-REC photon peak. We have developed simulations of the *K*-REC photon lines: for this we have determined the impact parameter distribution at statistical equilibrium for various beam incidence conditions (direction and angular spread) using the continuum potential model for channeled ions. Multiple scattering effects were included. The *K*-REC photon peak was calculated within the nonrelativistic dipole approximation, *K*-REC being assumed to be a purely local process. Solid state electron densities were used, and impact parameter dependent electron momentum distributions (Compton profiles) were calculated for $2s$ and $2p$ silicon electrons. A remarkable agreement is found between the spectra measured with very high statistics, and the calculated ones, which leads to the following results: (i) The dependence of the *K*-REC yield on the beam incidence angle is obtained separately for silicon core and valence electrons, which was never observed before. We find that the core electron contribution to REC is still significant for axial alignment, whereas it is generally neglected in the literature. (ii) Electron Compton profiles are found to vary significantly with impact parameter. (iii) The free electron gas model represents a fair approximation for the description of valence electron Compton profiles. (iv) The *K*-REC cross section is measured with an absolute accuracy better than 20%, and found to be close to the value calculated within the nonrelativistic dipole approximation. [S1050-2947(96)01808-2]

PACS number(s): 34.70.+e, 61.85.+p, 34.80.Lx

I. INTRODUCTION

Channeling of swift heavy ions in thin crystals can be used as a tool for suppressing the interaction between the projectile and the atomic cores of a solid target. Interaction with conduction and valence electrons of the crystal becomes observable, and even dominant. Thus channeling allows the observation of charge exchange processes between highly stripped heavy ions and quasifree electrons, i.e., processes which involve no recoil of the target atom: this is the case for radiative electron capture (REC) [1–3], in which electron capture is accompanied by the emission of a photon, resonant transfer and excitation (RTE) [4–7], in which the capture is accompanied by the resonant electronic excitation of the projectile, and electron impact ionization (EII) [8,9]. Moreover, through the study of such localized processes, channeling can be used to get more information about the local electronic structure in a crystal. Basically, an axially channeled ion can be viewed as a particle trapped in a two-dimensional potential, that is, the transverse potential, averaged along the atomic rows. Then the transverse energy of the ion inside the crystal determines the accessible transverse space for the trajectory, and thus the mean electron density sampled by the ion. As studied in detail by L'Hoir *et al.* [9], one can connect the energy loss rate and the charge state at emergence of a channeled ion to its transverse energy. However, since energy loss is not a purely local process [10], the determination of the densities of target electrons in various states sampled by channeled ions remains a major problem in the interpretation of experiments devoted to a charge exchange process in channeling conditions. If the process studied is also observable in random conditions (for which all electrons of the crystal may participate with the same probability), the comparison of random and aligned experiments should allow one to extract the specific contributions of each type of target electron.

The momentum distribution of electrons (Compton profile) reflects the dispersion of the kinetic energy of the target electrons. For instance, it is wider for *K*-shell electrons than for valence or conduction electrons. These distributions are connected to the electron wave functions and densities. Thus studies of charge exchange processes taking place at well

defined distances from atomic strings should provide additional information on the local electron density through the corresponding electron Compton profile, and then allow a more detailed confrontation of experiments with the theoretical description of electron structure in solids. Both RTE and REC are processes which imply large momentum transfer for the captured electron. They are then expected to be ''local'' processes, and thus, in principle, able to give information on local electron densities and Compton profiles. Compton profiles can be deduced from RTE through the study of resonance shapes, and from REC through the study of the photon line shapes. However, in RTE experiments—*KLL*-RTE especially [6,11,7]—the fine structure of the resonance is a limiting factor for a precise study of the line shape and thus of the Compton profile of the target electrons (except for the lightest and heaviest ions for which the resonance structure is either negligible or dominant with respect to the Compton profile). *K*-REC is a much more attractive case for the two following reasons: REC is a nonresonant process, which makes it easier to observe experimentally, and *K*-REC is monoenergetic. The *K*-REC shape has already been used for determining electron densities by Datz *et al.* [11] and by Miraglia *et al.* [12] in their interpretation of a previous experiment by Appleton *et al.* [1]. In these works the contribution of core electrons to the *K*-REC line shape could not be evaluated, in particular, because *K*-REC could not be observed in random conditions.

The aim of this work is the study of *K*-shell radiative capture by bare channeled ions. The *K*-REC line shape has been studied as a function of the crystal orientation, i.e., of the transverse energy distribution of the incident ions along the crystal axis. A few years ago, we had already observed *K*- and *L*-REC with hydrogenlike 25-MeV/u Xe^{53+} ions channeled in a Si crystal [2]. However, *K*-REC was not easily observable in random conditions, because the *K* shell of incident Xe^{53+} ions was rapidly filled up, mainly by nonradiative capture. Here we use 60.1-MeV/u Kr^{36+} ions incident on a thin silicon crystal. The transmitted ions are still mostly bare in random as well as in channeling conditions, which allows us to observe *K*-REC in both cases.

In Sec. II we describe the experimental setup that allows charge state and energy analysis of the transmitted ions, and detection of photons coming from the impact area. In Sec. III we present our experimental data, which include charge state distributions and high statistics x-ray energy spectra, and also an energy spectrum of photons detected in coincidence with well channeled ions. In Sec. IV we describe a simulation code that enables us to calculate both the amplitude and shape of the *K*-REC line. Compton profiles of silicon core electrons are calculated via a partial Fourier transform of the wave function as a function of the distance to the target atomic rows. Valence electrons are treated in a semiclassical way, as a nonuniform Fermi gas: electrons are considered as free electrons with exact solid state local densities. The confrontation of calculated and measured profiles is discussed in Sec. V. A fully exhaustive description of the *K*-REC line in terms of core and valence electron contributions is presented, and shows that silicon core electrons still contribute significantly in channeling conditions, and thus should not be neglected as is done in most channeling studies. We also show that the free electron model is a good approximation for valence electrons.

II. EXPERIMENT

The experiment was performed at the Grand Accelerateur National d'Ions Lourds (Caen, France), in the LISE beamline, designed for charge and energy analysis of highly stripped ions (Fig. 1). The beam transverse emittance was given to be isotropic with 0.1π mm mrad [half width at half maximum (HWHM)] projected along one direction, and the spot size on the target was at most equal to the spatial resolution of the multiwire chambers, which is 1 mm. Under these conditions, the beam intensity on the crystal was between 10 and 100 pA. The absolute number of incident ions was measured using a rotating beam chopper made of silver coated blades, from which the Ag $K\alpha$ x rays were detected by a Si(Li) diode. The crystal target was hold by a three-axis goniometer, which could be moved with an accuracy of 10^{-3} degrees. The effective crystal thickness was 37 μm, a thickness that ensures single collision conditions for radiative capture by channeled ions, and charge state equilibrium for a random orientation, and allows energy loss measurements. Two intrinsic Ge detectors viewed the crystal, at 90° and 125°. Vertical slits were placed in front of the detectors, in order to limit Doppler broadening. A Si(Li) detector was set at 90°, but, as a lead shield masked the crystal target, it could view only the radiative decay of long lifetime excited states. Ions emerging from the crystal were magnetically charge and energy analyzed. A multiwire proportional gas counter placed in the dispersive focal plane was used to measure charge state fractions and energy losses. The resolution of this spectrometer was $\Delta p/p = 5.5\times10^{-4}$. Upstream from this wire chamber, two vertical slits could select ions of given energy and charge state. These ions were sent onto an Al foil, where they produced secondary electrons that were detected by means of a channeltron. This signal could be used as a trigger for the 90° Ge detector.

III. RESULTS

In Fig. 2 we present transmitted ion charge state distributions obtained with Kr^{36+}, Kr^{35+}, and Kr^{33+} incident ions, respectively, under random and $\langle 110\rangle$ alignment conditions.

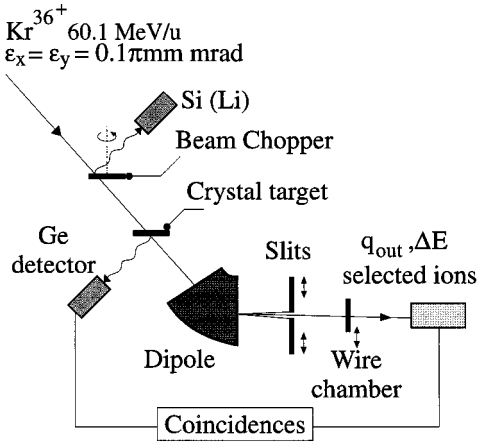

FIG. 1. Scheme of the experimental setup.

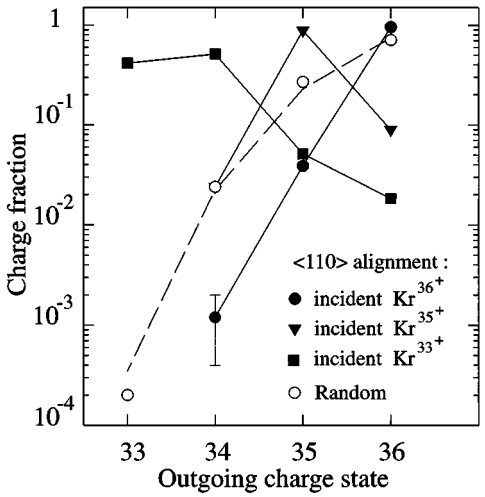

FIG. 2. Charge state distributions obtained for Kr^{q+} incident ions ($q=33,35,36$) at 60.1 MeV/u on a 37-μm Si crystal for alignment along the $\langle 110 \rangle$ direction. The dashed curve corresponds to a calculation for random orientation [13].

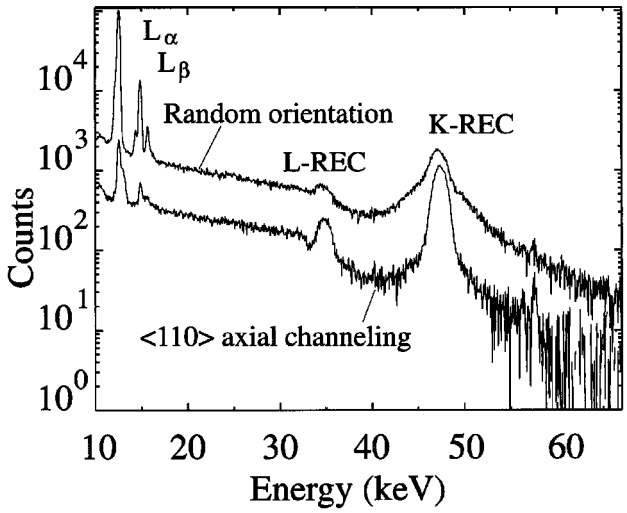

FIG. 3. Single spectra corresponding to all the photons detected at 90° for 60.1-MeV/u Kr^{36+} ions incident on a 37-μm silicon crystal.

For random orientation the three distributions are found to be identical, which means that charge state equilibrium is reached within the 37-μm-thick Si target, in good agreement with theoretical predictions [13]. Most of the emergent particles are bare ions (74%), which, as noted earlier, will allow one to study *K*-REC by fully stripped ions in random conditions also. Nevertheless, since only bare and H-like ions can induce *K*-REC (with probabilities in the ratio of 2:1), the *K*-REC cross section evaluation in random conditions will require the knowledge of the charge distribution averaged along the ion path in the target: for Kr^{36+} incident ions, the mean fraction values of Kr^{36+} and Kr^{35+} ions inside the target have been calculated to be 77% and 22%, respectively.

In channeling conditions, Fig. 2 shows that the charge distributions depend strongly on the incident charge state, which means that they are far from charge equilibrium. As Kr^{36+} and Kr^{35+} incident ions remain essentially frozen in their initial charge state, we are in a situation of single collision for both electron capture and loss. The electron capture probability is found to be about twice larger for bare ions than for H-like ions (4% and 2.5%, respectively). As mechanical capture occurs preferentially in states with quantum number $n \geq 2$, and as *K*-REC is by far the dominant radiative capture process, such a result confirms that capture by channeled ions is dominated by *K*-REC. The probability of capturing two electrons successively is quite small, and is represented by the 34+ fraction obtained for Kr^{36+} incident ions (about 10^{-3}, with a large experimental uncertainty in this particular case). Channeled Kr^{35+} ions may lose their electron by EII since the *K*-shell binding energy is lower than the maximum energy transfer in an electron-electron collision at this beam velocity: it happens to about 9% of them. For Kr^{33+} incident ions the charge distribution is dominated by EII, and only 40% of them stay frozen in their initial charge state: their probability for losing one electron is dominated by the *L*-electron loss. Moreover, as the probability for losing successively three electrons is very small for channeled ions, the 36+ fraction (2%) is fed essentially by the unchanneled part of the beam. As the 36+ fraction is largely dominant for random incidence, the above value of 2% is equal to the unchanneled fraction (or more exactly to the fraction of ions able to lose electrons in close ion-atom collisions), which reflects very good channeling conditions.

Let us consider now the x-ray emission by channeled Kr ions, which gives a deeper insight into their interaction with the crystal electrons. X-ray spectra were recorded for various crystal orientations around the $\langle 110 \rangle$ direction.

In Fig. 3 we present two energy spectra of photons detected at 90° from the Kr^{36+} beam direction, for random and $\langle 110 \rangle$ crystal orientation, respectively. They are normalized to the same number of incident Kr^{36+} ions, corrected for dead time, and the background from surrounding radioactivity has been subtracted. First of all, channeling conditions are seen to cause a general reduction of the various components of the random spectrum, which is made of peaks due to the Kr Lyman series and to the radiative electron capture, and also of a continuum due to primary and secondary bremsstrahlung.

The Lyman lines are quite strongly attenuated (much more than REC lines): the reason is that Lyman photons result mostly from deexcitation after nonradiative capture into ($n>1$) shells or after excitation of a *K*-shell electron, both events taking place in close collisions with Si crystal atoms: the L_α yield is measured to be 2.5% of the value obtained for random incidence, which is to be compared to the above 2% fraction deduced from charge state measurements. In fact, the L_α yield is slightly higher than 2% because some channeled ions may contribute to this yield by deexcitation after *L*-REC capture.

In opposition to Lyman emission, bremsstrahlung and REC photons result basically from the interaction of the projectile with target electrons, and the photon yields depend on the mean electron density experienced by the projectile.

Primary bremsstrahlung is the photon emission by a target electron accelerated in the Coulomb field of the charged projectile. The maximum photon energy is equal to the kinetic energy E_c in the projectile frame of a target electron at rest in the laboratory frame. Secondary electron bremsstrahlung

is a two-step process, in which a target electron is elastically scattered by the projectile, and then radiates part of its energy during slowing down in the target. The corresponding energy spectrum extends up to $\sim 4E_c$, since forward scattered electrons can be given twice the velocity of the projectile in the laboratory frame.

The attenuation of the bremsstrahlung yield in channeling conditions is measured to be 3.5, which corresponds to the ratio (14/4) of the total number of electrons per Si atom to the number of valence electrons.

The case of radiative electron capture is more interesting, and also more complex: not only are the K- and L-REC peak integrals lowered by channeling, but the line shapes are also strongly modified. In the following we will concentrate on the K-REC peak, which shows up the most distinctly against the continuum. It is clearly seen that for random crystal orientation the K-REC peak comprises broad wings that vanish almost completely in channeling conditions. For random incidence all types of target electrons may be captured, and the wings are due to the contribution of core electrons that present a broad Compton profile. In alignment conditions, channeled projectiles capture mainly valence electrons that present a much narrower Compton profile. Between these two extreme orientations ($\langle 110 \rangle$ axial channeling and random conditions) the body and wings of the K-REC peak evolve differently, as will be shown later. This means that a pertinent description of REC along the transition from channeling to random conditions requires a study of the peak shape, which reflects the various Compton profiles of the captured target electrons. Moreover, it has to be noted that not only the amplitude, but also the shape, of the broad contribution due to the capture of core electrons varies from random to channeling conditions. Since the impact parameter distribution inside the crystal is quite different in each case, this suggests that the Compton profile of core electrons in a given atomic shell may depend on the location where the capture occurs.

In order to study more accurately radiative electron capture by channeled ions, we have performed a coincidence measurement using incident Kr^{36+} ions. The x-ray detector was triggered by the detection of a Kr ion transmitted with the charge 35+ (resulting from one electron capture), and with a reduced energy loss. We have selected channeled 35+ ions that have lost less than half of the random energy loss value. They represent $(45 \pm 7)\%$ of the transmitted Kr^{35+} ions. The x-ray spectrum presented in Fig. 4 (along with the corresponding single spectrum, similar to that already shown in Fig. 3), is then uniquely due to channeled Kr ions that have captured one electron of the crystal by REC. Bremsstrahlung is largely washed out since only $\sim 2\%$ of the total transmitted beam is selected for triggering the coincidence. The REC peaks appear nicely (including M-REC), as well as L_α, L_β, and L_γ lines that result from deexcitation after radiative electron capture into the L, M, and N shells, respectively. In particular, L-REC and L_α peaks are found equal within 15% (after correction for detector efficiency). The small discrepancy (in favor of L-REC) is probably due to slight differences in angular distributions of L_α and L-REC photons. The comparison of the coincidence spectrum with the corresponding single spectrum yields the most important feature related to the K-REC peak: the vanishing

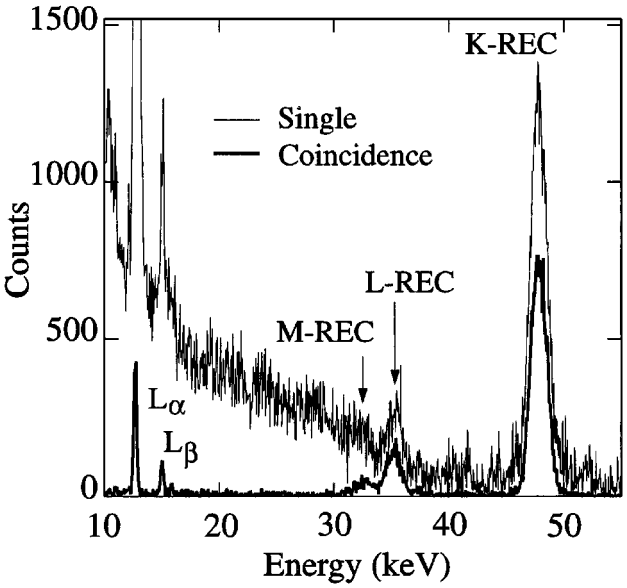

FIG. 4. Photon spectrum recorded at 90° for 60.1-MeV/u Kr^{36+} incident ions in coincidence with well channeled ions which have captured one electron inside the 37-μm silicon crystal aligned along the $\langle 110 \rangle$ axis. The corresponding single spectrum is also shown.

of the wings that are visible in the single spectrum, and that are due to the radiative capture of inner-shell target electrons by poorly or nonchanneled ions. The coincidence K-REC peak shows that well channeled ions can capture only electrons with a narrow Compton profile, i.e., valence electrons.

It is not easy to determine with precision the absolute mean energy of the K-REC peak: as the crystal was tilted by 35.2° when aligned along the $\langle 110 \rangle$ direction, a small variation of the beam spot position on the crystal caused a significant shift of the K-REC peak, due to the Doppler effect. Nevertheless, the comparison of the energies of K-REC peaks and L_α peaks (observed at 90° and 125°) indicates that, with respect to the theoretical energy [see below Eq. (4)], there is no shift of the K-REC peak greater than 50 eV. We observe a significant variation of the mean energy of the K-REC peak between random and channeling conditions which can be explained (due to the drastic decrease of K-REC cross section with increasing photon energy) by the cumulative effects of the reduced energy loss and of the narrowing of the target electron Compton profile.

Moreover, we have also obtained an x-ray spectrum (not shown) in coincidence with well channeled Kr^{34+} ions that have captured two electrons in the crystal. The 34+ fraction is very small for 36+ incident ions in channeling conditions (see Fig. 2). We found no evidence for double K-REC (double electron capture accompanied by emission of one photon), which would correspond to photons around 94 keV at 90° in the laboratory frame. This was expected because the probability, for a channeled ion, to undergo a close interaction with two valence electrons simultaneously is quite low, much smaller than during binary collisions with atoms, in which core electrons, more localized around the nucleus, can be captured.

Finally, as mentioned above, we also recorded spectra of delayed x-rays with a Si-Li detector that could detect (at

90°) only photons emitted downstream from the crystal target. These spectra were obtained in coincidence with transmitted Kr^{35+} and Kr^{34+} well channeled ions. The results of this study of delayed photons are published separately [14]. They show that intrashell excitation plays a major role in the evolution of metastable states of the $n=2$ levels in channeling conditions. A value of the cross section for $2s$-$2p$ mixing has been obtained.

IV. SIMULATIONS

As noted above we have performed Monte Carlo simulations, in order to reproduce the experimental K-REC peaks. First we establish the ion flux in the crystal, i.e., the impact parameter distribution of moving ions with respect to atomic strings, and then their corresponding encounter probability. On the other side, electron momentum distributions of target electrons to be captured are determined as a function of the impact parameter (i.e., of the place where the capture occurs). Finally, we discuss the K-REC cross sections that are needed to obtain absolute yields. Moreover, the comparison with experimental data requires one to substract the bremsstrahlung continuum, which is also discussed.

A. Distribution of transverse energy for channeled ions: Corresponding ion flux

An ion penetrating the crystal with an energy E is given a transverse energy $E_{T0}=E(\psi_0+\delta\psi)^2+V(\vec{r}_{0\perp})$ where ψ_0 is the mean angle between the beam direction and the crystallographic axis. $\vec{r}_{0\perp}$ and $\delta\psi$ are random variables which account, respectively, for the distribution of entrance positions (which is uniform) and entrance directions (which corresponds to the beam angular divergence around ψ_0). V is the continuum transverse potential. It was calculated in Ref. [9] in the case of the $\langle 110\rangle$ axis of Si. Near the atomic strings, we have taken into account the influence on V of the thermal vibrations of the crystal atoms (1D rms thermal vibration amplitude at room temperature, $u_1=0.077$ Å) by using the single string potential proposed in Ref. [15]. The beam angular divergence is supposed to be Gaussian in any transverse direction. Various values of the angular width were considered in the simulations, in order to check the value given by the accelerator staff (HWHM of the angular spread projected along one direction, 0.1 mrad).

We assumed that statistical equilibrium is reached in the 4D transverse phase space. As a consequence, a particle of given transverse energy E_T has a uniform probability to be at any point of the accessible transverse space, i.e., at any $\vec{r}_\perp$ where $V(\vec{r}_\perp)<E_T$ [16]. This is true only sufficiently far from the crystal entrance, since the incoming ions may keep a ''phase memory'' at the beginning of their path [17], over a characteristic path length Λ. In our case the crystal thickness ($t=37$ μm) is much greater than Λ (≈ 2.5 μm) and one may consider that statistical equilibrium prevails all along the crystal.

In Fig. 5 we present impact parameter distributions at statistical equilibrium $\Phi(b,\psi_0)$ inside the $\langle 110\rangle$ crystal channel for various mean incidence angles ψ_0. Here we define the impact parameter as the distance b to the closest atomic string. $\Phi(b,\psi_0)$ is normalized as $\int\Phi(b,\psi_0)db=1$.

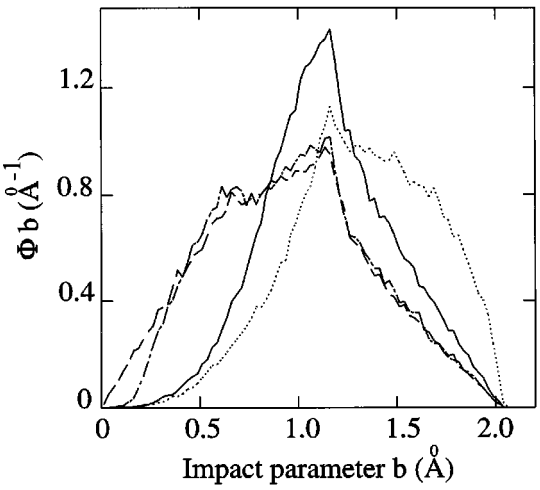

FIG. 5. Simulation of impact parameter distributions $\Phi(b,\psi_0)$ relative to the nearest atomic strings, obtained for different incident angles ψ_0. Dotted curve: $\psi_0=0$, no beam angular divergence and no multiple scattering. Dashed curve: random incidence. In the other curves one takes into account a beam angular divergence of 0.1 mrad (HWHM) and multiple scattering. Solid line: $\psi_0=0$. Dash-dotted curve: $\psi_0=0.03°$.

In the random incidence case, all positions in the transverse space are equiprobable. Then, for a single string (cylindrical geometry), the distribution $\Phi(b)$ increases linearly with b: $\Phi(b)=2b/b_0^2$, $0\leq b\leq b_0$, where b_0 is the radius of a unit cell in the transverse plane, associated with a single string [$\pi b_0^2=1/(Nd)$, where d is the interatomic distance along the $\langle 110\rangle$ strings and N is the number of Si atoms per unit volume]. The departure from this distribution above $b=0.7$ Å is simply due to multistring effects.

In the same figure, we show first the distribution $\Phi(b,\psi_0=0)$ corresponding to an incident beam parallel to the $\langle 110\rangle$ strings without any angular divergence. In this case the flux is strongly enhanced at large impact parameters, i.e., many ions are confined close to the center of the channel (hyperchanneling). Conversely, small impact parameters are strongly inhibited: channeled ions cannot approach the target atom cores.

The drawback of using a quite thick crystal is that multiple scattering, which tends to increase the transverse energy of a particle, is not negligible. Both electronic and nuclear contributions (the latter being significant only for large E_T values) are taken into account in our calculations. Particles entering the target with a transverse energy E_{T0} suffer, when traversing the crystal, a mean transverse energy increase ΔE_T induced by multiple scattering on target electrons and target nuclei. A good estimation of the contribution of target electrons to ΔE_T can be obtained, following Bonderup *et al.* [18], from the mean energy loss of these particles through the crystal. For instance, for ions with very small E_{T0} values, we find $\Delta E_T/Q=6$ eV (where Q is the projectile charge). For the contribution of target nuclei, we used the treatment proposed in Ref. [16] and developed in Ref. [19]. The probability of REC events is small enough to ensure the validity of the hypothesis of the single collision regime; consequently, the probability for a REC event to occur at given penetration depth z is uniform over $[0,t]$, where t is the

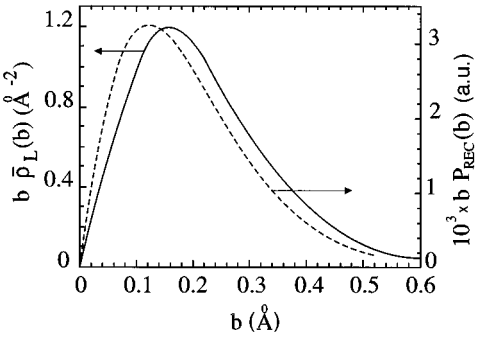

FIG. 6. Comparison between the K-REC yield $bP_{K\text{-REC}}(b)$, from Ref. [12] (dashed curve) for the capture of L Si electrons by 25-MeV/u Xe^{53+} ions at given impact parameter b to $b\overline{\rho_L}(b)$ (solid curve). $\overline{\rho_L}(b)$ is the mean L-electron density at b [see Eq. (1)].

target thickness. We have thus calculated the probability of a REC event for a particle entering the crystal with E_{T0} by considering that its transverse energy when the REC event may occur is $E_T = E_{T0} + \eta\overline{\Delta E_T}$, η being a random variable uniformly distributed over [0,1].

In Fig. 5 we show a distribution $\Phi(b,\psi_0=0)$ for which a realistic beam angular divergence is taken into account: we assume an isotropic Gaussian shape characterized by a width of 0.1 mrad HWHM when projected along one direction. Multiple scattering (before capture) is also taken into account in this calculation of $\Phi(b)$. Multiple scattering and incident beam angular divergence are seen to reduce hyperchanneling strongly. In the following, these effects will be included in the calculated distributions $\Phi(b)$ used in our simulations. We also show in Fig. 5 the distribution $\Phi(b,\psi_0)$ corresponding to a beam entering the crystal with $\psi_0=0.03°$ (the relativistic Lindhard critical angle for channeling [16] is $\psi_c=0.05°$ in our experimental conditions). The distribution is very close to the one corresponding to the random case, except for small impact parameters $b \leqslant 0.2$ Å .

B. Electron densities in the channel

In order to simulate REC events, we have assumed that interactions with target electrons are binary events that can be considered independently. We have then to describe the interaction between an ion of well defined position $\vec{r}_\perp$ in the transverse plane and a target electron with a well defined wave function. The classical description of the ion trajectories is justified, owing to their high mass and velocity. In such a situation, REC yields could be calculated within the impulse approximation, following the treatment of Ref. [12]. In fact, we use here a simpler approach assuming that the probability for a REC event to occur at $\vec{r}_\perp$ is proportional to the mean electron density $\overline{\rho(\vec{r}_\perp)}$ at this point of the transverse space, i.e., averaged along the ion trajectory:

$$\overline{\rho(\vec{r}_\perp)} = \frac{1}{d}\int_{-d/2}^{d/2} \rho(\vec{r}_\perp, z)\,dz \qquad (1)$$

where d is the interatomic distance along the $\langle 110\rangle$ string. In fact, such a hypothesis is supported by comparing the dependence of REC probability on impact parameter calculated in Ref. [12] for target Si electrons in various initial atomic

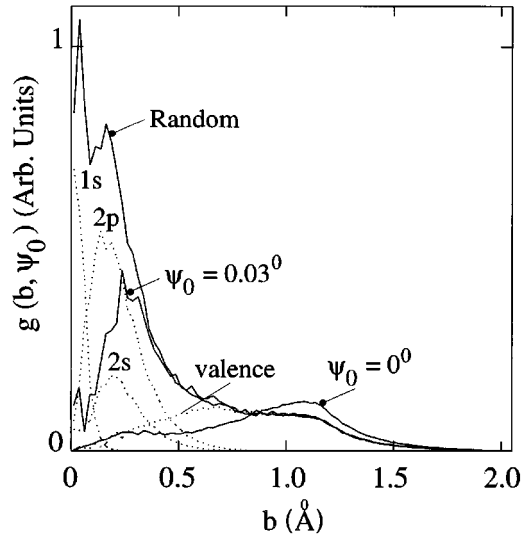

FIG. 7. Mean sampled electron density distribution $g(b,\psi_0)$ (solid lines) for three different incidence angles ψ_0. Mean electron densities $\overline{\rho_{st}}(b)$ (dotted lines).

quantum states (nlm) captured by high velocity Xe ions to the mean corresponding electronic density $\overline{\rho_{nlm}}(\vec{r}_\perp)$. The comparison is shown in Fig. 6 for the capture of L-shell Si electrons. In fact, taking into account the axial symmetry around a string, we compare $bP_{K\text{-REC}}(b)$ to $b\overline{\rho_L}(b)$ $[\overline{\rho_L}(b)=\overline{\rho_{2s}}(b)+\overline{\rho_{2p}}(b)]$. The shapes are nearly identical; the only difference consists in a small shift $\delta b = 0.03$ Å on the abscissa of the two curves. This shift is small when compared both to the extension of $b\overline{\rho_L}(b)$ and to the uncertainty in the impact parameter dependence of the channeled ion fluxes. We thus decided to neglect it.

The electron encounter probability of incident projectiles depends on the flux distribution $\Phi(b,\psi_0)$ and on the densities $\overline{\rho_{st}}(b)$ associated with given electronic states of silicon $(1s,2s,2p,\text{valence})$ averaged over z. In Fig. 7 we show the mean electron encounter probability $g(b,\psi_0)$, together with the various $\overline{\rho_{st}}(b)$, as a function of impact parameter b. The $g(b,\psi_0)$ values are obtained from products $\overline{\rho}(\vec{r}_\perp)\Phi(\vec{r}_\perp,\psi_0)$ in the Monte Carlo calculations, $\overline{\rho(\vec{r}_\perp)}$ being the total mean electronic density for $\vec{r}_\perp$. The three distributions $g(b)$ shown correspond to the three incident beam orientations (random, $\psi_0=0$, and $\psi_0=0.03°$) already considered in Fig. 5. For the random orientation, $g(b)$ is simply proportional to $\overline{\rho}(b)$. The densities $\overline{\rho_{st}}(b)$ were calculated from the atomic wave functions of Ref. [20] in the case of core electrons and, for valence electrons, using the Fourier coefficient of Ref. [21] obtained with nonlocal pseudopotentials.

The analysis of Fig. 7 provides information on the contribution to $g(b,\psi_0)$ of each electronic state. For $\psi_0=0$, the capture of valence electrons takes place preferentially at large distance from the target strings: more electrons are captured at $b>0.8$ Å than in the random case. However, the overall valence capture yield, i.e., the integral over b of the valence encounter probability, is lower than in the random case, for which the encounter can also occur at smaller b, i.e., in regions of higher valence electron densities. This is illustrated by the map of Fig. 8, which shows that the valence

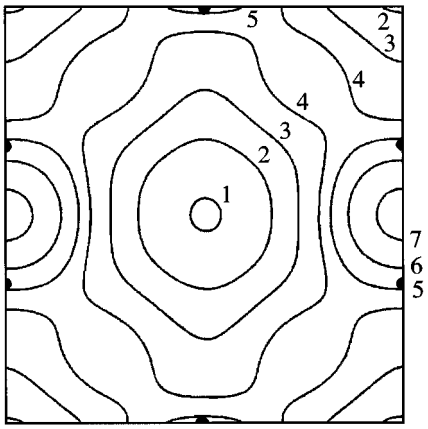

FIG. 8. Map of the mean valence electron density $\overline{\rho_{val}}(\vec{r}_\perp)$ averaged along z. Densities in electron per Å^3: 1, 0.032; 2, 0.08; 3, 0.15; 4, 0.225; 5, 0.275; 6, 0.35; 7, 0.45. The black circles represent the position of the $\langle 110 \rangle$ atomic strings.

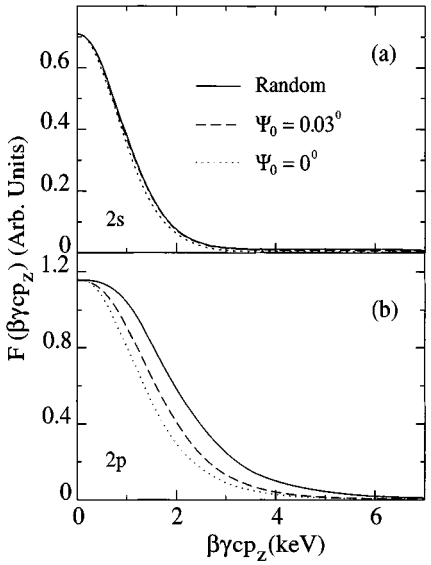

FIG. 9. Shape of the momentum distributions $F_{nl}(p_z;\psi_0)$ of $2s$ (a) and $2p$ (b) electrons captured for beams incident at various ψ_0. Solid line: random orientation; dashed line: $\psi_0 = 0.03°$; dotted line: $\psi_0 = 0$. Multiplying factors were applied to bring the curves together at $p_z = 0$. Electron momenta are converted into REC photon energies.

electron density is maximum between the closest strings: these electrons are the binding electrons of the crystal lattice. They cannot be captured by well channeled ions since the potential in this region is rather high (around 19 eV per unit charge), although much smaller than the critical transverse energy E_{TC} [$E_{TC}/Q = E\psi_c^2/Q \simeq V(b \simeq 0.15$ Å$)/Q = 110$ eV]. As a consequence, the overall valence electron encounter probability is smaller than in the random case only for tilt angles ψ_0 significantly smaller than ψ_c. One can see in Fig. 7 that, already for a tilt angle $\psi_0 = 0.03° = 0.6\psi_c$, there is no longer an effect.

Since small impact parameters are forbidden for channeled ions, their encounter probability with core $2s$ and $2p$ electrons which are rather localized near the nuclei is much smaller than in the random case. As the spatial extension of $\rho_{nlm}(b)$ is quite similar for these two states, the corresponding encounter probabilities are reduced by about the same amount in channeling. Of course the smaller the impact parameter the stronger this reduction. The reduction of the $1s$ electrons contribution is still stronger. At the intermediate tilt angle ($\psi_0 = 0.03°$), the encounter probability with $2s$ and $2p$ electrons increases markedly but is still much smaller than in the random case (note that $1s$ electrons are still almost entirely hidden). It must be pointed out that not only the overall encounter probability but also the variation of the local encounter probability with impact parameter depends strongly on ψ_0.

C. Momentum distribution of target electrons at a given impact parameter

The shape of the measured REC lines is mainly determined by the momentum distribution of the captured electrons. A calculation of this distribution requires the knowledge of the target electrons wave functions. We have considered separately the contribution of core and valence electrons. In Sec. IV B we have shown (see Fig. 6) that REC events take place at given $\vec{r}_\perp$ with a probability proportional to $\overline{\rho(\vec{r}_\perp)}$. We shall now assume that the shape of the REC peak of capture events taking place at $\vec{r}_\perp$ depends on the momentum distribution of the electrons at this point of the transverse space. For this purpose, we have used the electronic wave functions in a mixed representation $\Psi(\vec{r}_\perp, p_z) = \Psi(b, p_z)$ (we recall that b is the distance to the closest string for a particle at $\vec{r}_\perp$). We thus calculate the partial Fourier transform:

$$\Psi_{nlm}(b,p_z) = \frac{1}{\sqrt{2\pi\hbar}} \int_{-\infty}^{+\infty} \phi_{nl}(\sqrt{b^2+z^2}) Y_{lm}(\theta) e^{ip_z z/\hbar} dz \tag{2}$$

where $\tan\theta = b/z$, ϕ_{nl} is the radial atomic wave function, and Y_{lm} its angular part.

The probability density $|\Psi_{nlm}(b,p_z)|^2$ is the conditional momentum distribution $J_{nlm}(p_z|b) = J_{nl}(p_z|b)$ of a core electron at given b. This distribution is normalized through:

$$\int_0^{+\infty} 2\pi b db \int_{-\infty}^{+\infty} |\Psi_{nlm}(b,p_z)|^2 dp_z = 1. \tag{3}$$

From $J_{nl}(p_z|b)$ one may easily deduce the momentum distribution $J_{nl}(p_z|\vec{r}_\perp)$ in the channel. In our simulations we have determined the momentum distributions $F_{nl}(p_z, \psi_0)$ of electrons of a given state captured by incident ions, when the beam enters the crystal with an incident angle ψ_0. Such a distribution is obtained by averaging the distributions $J_{nl}(p_z|\vec{r}_\perp)$ with a weight $g_{nl}(\vec{r}_\perp, \psi_0) = \rho_{nl}(\vec{r}_\perp)\Phi(\vec{r}_\perp, \psi_0)$ [note that for random incidence, $\Phi(\vec{r}_\perp, \psi_0 \gg \psi_c)$ is constant].

In Fig. 9 we present the shapes of $F_{nl}(p_z, \psi_0)$ corresponding to $2s$ and $2p$ electrons for various ψ_0 values. The calculations were performed as in Fig. 7 for $\psi_0 = 0$, $\psi_0 = 0.03°$, and $\psi_0 \gg \psi_c$ (random). For convenience, the momentum values on the abscissa are converted to REC photon energy dispersion in the projectile frame [the p_z are multiplied by

$\beta\gamma c$, see Eq. (4) below]. For an easier comparison of shapes, the profiles are represented with the same maximum amplitude. There is a clear dependence on ψ_0 of the shape of the distributions corresponding to $2p$ electrons, which provide the major contribution to the total core Compton profile. Such an effect is much weaker on the distributions corresponding to $2s$ electrons. The general trend is that the momentum distribution of captured electrons is narrower in aligned than in random conditions. As the ion flux distribution for an aligned beam favors large b values, the effect observed can be understood in a classical picture, considering that target electrons of a given state have a lower mean kinetic energy at large b, where the potential energy is higher.

For $1s$ electrons of silicon, the spatial extension of the wave function is of the same order as the target atom thermal vibrations. Thus, even for a beam entering the crystal parallel to the $\langle 110 \rangle$ rows, the particles which can capture $1s$ electrons are those which approach very close to the strings. They experience strong multiple scattering, and they can rapidly be considered as unchanneled particles which sample the crystal uniformly. Thus we directly used the atomic Compton profile of $1s$ silicon electrons tabulated in Ref. [22], which is already averaged over b.

In principle, the calculation of the Compton profile associated with the capture of valence electrons should be performed in a similar way as for L silicon electrons. Unfortunately, we are dealing with an extremely large number of wave functions (Bloch waves). Moreover, these Bloch waves are obtained as linear combinations of plane waves; thus, Fourier transformation [Eq. (2)] raises very severe computational problems, related to the fact that the Fourier transform of a plane wave is a Dirac distribution. We then decided to use a semiclassical treatment based on a description of valence electrons as a nonuniform free electron gas. In such a description, the only relevant parameters are the density $\rho(\vec{r}_\perp,z)$ and the associated momentum distribution $J_F(p_z|\vec{r}_\perp,z)=\frac{1}{2}p_F(\vec{r}_\perp,z)$ with $-p_F(\vec{r}_\perp,z)\leqslant p_z\leqslant p_F(\vec{r}_\perp,z)$ and where $p_F(\vec{r}_\perp,z)=\hbar[3\pi^2\rho(\vec{r}_\perp,z)]^{1/3}$ is the Fermi momentum experienced by an ion along its trajectory. The density $\rho(\vec{r}_\perp,z)$ to be considered to calculate p_F is the total electron density $\rho_{val}(\vec{r}_\perp,z)+\rho_{core}(\vec{r}_\perp,z)$: a valence electron captured in regions where the core electron density ρ_{core} is significant has a momentum distribution which is broadened by these core electrons. Calculating the shape of the Compton profile associated with the capture of valence electrons within the framework of this semiclassical treatment is questionable; however, in aligned geometry, valence electrons are mostly captured in regions where ρ_{core} is negligible and $\rho(\vec{r}_\perp,z)$ varies rather smoothly with the coordinates, and it seems appropriate to use a free electron gas model. An interesting feature of the results of Ref. [12] is, as stated in Sec. IV B, that the range of the interactions leading to a REC event is very limited [a capture in $\vec{r}_\perp$ has a probability proportional to $\overline{\rho(\vec{r}_\perp)}$ to occur; see Fig. 6]. In our semiclassical treatment, it is thus natural to assume that REC is a local process, taking place at a well defined coordinate $(\vec{r}_\perp,z)$ with a probability proportional to $\rho(\vec{r}_\perp,z)$ and that the momentum distribution of the electron captured at this point is given by $J_F(p_z|\vec{r}_\perp,z)$.

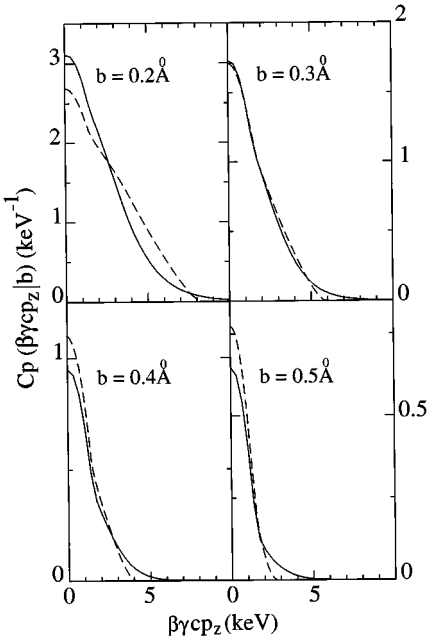

FIG. 10. Comparison of Compton profiles $C_{p_1}(p_z|b)$ (dashed lines) and $C_{p_2}(p_z|b)$ (solid lines) (see text) at various impact parameters b. Electron momenta are converted into REC photon energies.

We have checked the validity of the semiclassical treatment by applying it to both core and valence Si electrons, such a treatment being indeed much more doubtful for the former than for the latter. In this way we obtained Compton profiles $C_{p_1}(p_z|b)$ calculated by averaging $J_F(p_z|\vec{r}_\perp,z)$ over z with the weight $\rho(\vec{r}_\perp,z)$. They are compared in Fig. 10 to profiles $C_{p_2}(p_z|b)$ calculated by the quantum treatment through Eq. (2) for core electrons and semiclassically for valence electrons by averaging $J_F(p_z|\vec{r}_\perp,z)$ over z with the weight $\rho_{val}(\vec{r}_\perp,z)$. As in Fig. 9 the scaling factor $\beta\gamma c$ is used for p_z. At low impact parameters ($b\leqslant 0.3$ Å), i.e., in regions of high and strongly b-dependent electronic densities, the profiles $C_{p_1}(p_z|b)$ are markedly too broad and thus the semiclassical treatment is not appropriate. On the contrary, the agreement between the widths of $C_{p_1}(p_z|b)$ and $C_{p_2}(p_z|b)$ is fair for $b\geqslant 0.3$ Å (the discrepancy never exceeds 10%). However, a significant difference remains for large p_z values: the semiclassical treatment does not reproduce the wings predicted by the quantum treatment. Still, the comparison of $C_{p_1}(p_z|b)$ and $C_{p_2}(p_z|b)$ demonstrates that the semiclassical treatment applied to all target electrons provides already rather correct Compton profiles in regions where the overall electron density is not too high. It can thus be applied with confidence to the valence gas, for which, as indicated above, a full quantum treatment is out of reach.

The momentum distributions of valence electrons at point $\vec{r}_\perp$, $C_{p_{1\,val}}(p_z|\vec{r}_\perp)$, obtained from the semiclassical treatment, can be averaged over $\vec{r}_\perp$, leading to the distribution

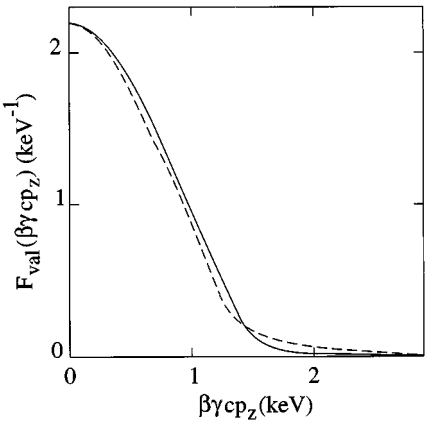

FIG. 11. Comparison of valence momentum distributions $F_{\text{val -random}}(p_z)$ uniformly averaged over the transverse space (uniform flux). Dotted line: $F_{\text{val -random}}(p_z)$ from Ref. [23]; solid line: $F_{\text{val -random}}(p_z)$ from a nonuniform Fermi gas description of valence electrons.

$F_{val}(p_z)$. If we attribute to each position $\vec{r}_\perp$ a weight proportional to $\overline{\rho_{val}}(\vec{r}_\perp)$, we simulate the Compton profile $F_{val\text{ -}and}(p_z)$ associated with a uniform ion flux in the crystal (random situation). Such a profile can be compared to the experimental determination performed in high resolution x-ray measurements [23]. The comparison is shown in Fig. 11. The agreement is satisfactory and confirms again the validity of the semiclassical approach that we have used.

D. Intensity and shape of the REC peak

After obtaining the longitudinal target electron momentum distribution, we determined the *K*-REC peak shape according to the following procedure. In the projectile frame, the relation between the energy $h\nu$ of the *K*-REC photon and the captured target electron momentum for a given position $\vec{r}_\perp$ in the channel is

$$h\nu = E_c + E_K - \gamma E_i - \beta\gamma c p_z \tag{4}$$

where E_K and E_i are, respectively, the final and initial binding energies of the electron, γ is the Lorentz factor, and $E_c=(\gamma-1)m_e c^2$ is the kinetic energy of an electron with the ion velocity v_{ion}.

We calculated the *K*-REC capture probability within the impulse approximation. We used the nonrelativistic dipole approximation [24]. For the radiative recombination of a free electron in the ion *K* shell, the cross section is

$$\sigma_{K\text{-REC}} = \frac{2^7\pi}{3}\frac{e^2}{m_e c^2}\frac{h}{m_e c}\frac{E_K^3}{h^2\nu^2(h\nu - E_K)} \times \exp\left(-\frac{4\zeta\tan^{-1}(1/\zeta)}{1-\exp(-2\pi\zeta)}\right) \tag{5}$$

where $\zeta=\sqrt{E_K/(h\nu-E_K)}$. In our experiment, the captured electrons are initially bound. As these binding energies are significantly smaller than E_c, we decided, however, to use Eq. (5). In this equation, $\sigma_{K\text{-REC}}$ can be considered as a function of the photon energy $h\nu$. As seen in Eq. (4), $h\nu$ depends on both the initial binding energy and the momentum of the electron. The influence of the initial state on $\sigma_{K\text{-REC}}$ was thus taken into account through these dependences.

$h\nu$ depends also (and mainly) on the ion kinetic energy E_c. This energy decreases quasilinearly inside the target. In order to fit the experimental *K*-REC peak we have thus taken into account in the calculations the mean energy loss $\overline{\Delta E}$ of the projectile inside the crystal, which differs from channeling to random conditions. As a REC event can take place at any penetration depth, this induces a decrease $-(m_e/M_{ion})\Delta E$ of $h\nu$ in expression (4), ranging quasiuniformly from zero to $-(m_e/M_{ion})\overline{\Delta E}$.

The REC peak was determined in the ion frame by a Monte Carlo simulation in the following way. For an incident ion indexed by i, a transverse energy E_{iT} is chosen, according to the distribution of incident impact parameters and angles, and according to the mean transverse energy increase induced by multiple scattering, ΔE_T. Then the $\vec{r}_{i\perp}$ position is sampled uniformly in the accessible transverse space. At this position an electron momentum p_z is chosen according to the corresponding distribution. For p_z, the distribution can correspond to either core or valence electrons with weights proportional to $\overline{\rho_{core}}(\vec{r}_{i\perp})$ and $\overline{\rho_{val}}(\vec{r}_{i\perp})$, respectively. We then calculated, via Eqs. (4) and (5), the photon energy $h\nu_i$ and the probability $P_i = \sigma_{K\text{-REC}}\overline{\rho(\vec{r}_{i\perp})}t$ (where t is the target thickness) for a *K*-REC event to occur. This procedure was iterated: the P_i values added at the corresponding abscissa $h\nu_i$ give the REC peak.

This calculation can be performed for any beam entrance conditions. It has been applied to various mean entrance angles ψ_0 with respect to the $\langle 110\rangle$ rows. It has also been used in the random incidence case for which all incident particles sample the whole transverse plane uniformly.

In order to simulate our experimental results, we have to determine the shape and intensity of the REC peak in the laboratory frame from the calculation performed above in the ion rest frame. We must then perform the Lorentz transform of the photon peak. We assumed a $\sin^2\theta_{lab}$ dependence of the angular distribution of the *K*-REC photons [25]. We also convoluted the photon peak with a distribution function resulting from the measured detector resolution and Doppler broadening associated with the detector collimator aperture. The combined contribution to the *K*-REC peak width of ion energy loss inside the crystal, Doppler effect, and detector resolution is quite small compared to the width of the Compton profile: for the valence electron contribution (i.e., with smallest momenta), the Compton profile width is still three times larger. Higher order REC (*L*-, and *M*-REC) lines were obtained in the same way as the *K*-REC line. The relative normalization factors of *L*- and *M*-REC with respect to *K*-REC were deduced from the coincidence spectrum of Fig. 4, where the various contributions are resolved without any background. We did not distinguish between the radiative capture into the separate $2s$, $2p_{1/2}$, and $2p_{3/2}$ sublevels; this separation causes an additional broadening ($\sim$80 eV) of the

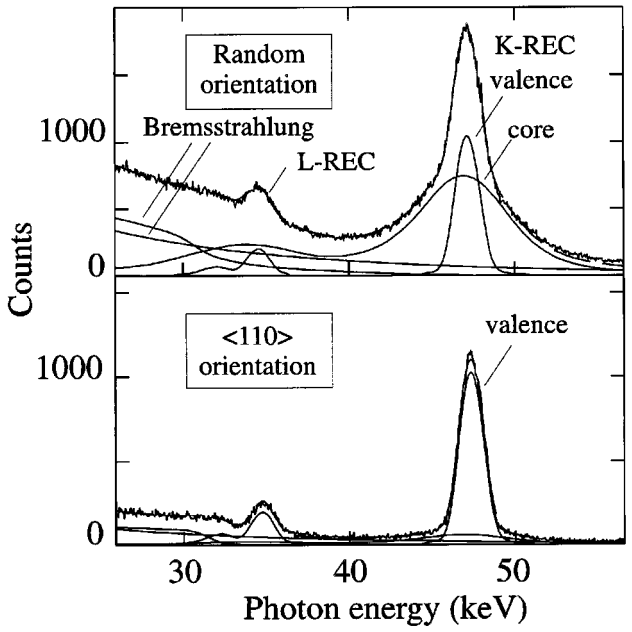

FIG. 12. Decomposition of the single x-ray spectra of Fig. 3. The dashed line represents the sum of the various simulated contributions.

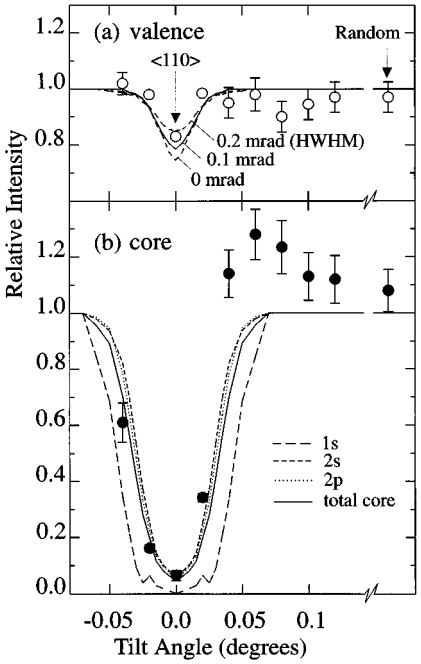

FIG. 13. Channeling dips for *K*-REC. (a) silicon valence electron contribution; the curves correspond to simulations for various beam angular divergences; (b) core electron contribution; the calculated dips corresponding to various states are represented; the beam angular divergence is 0.1 mrad HWHM. The calculated and experimental dips in (a) and (b) are normalized to the random *K*-REC calculated yield.

L-REC that is much smaller than the Compton profile, and thus negligible.

E. Calculation of the background induced by bremsstrahlung

In order to estimate with precision the background below the REC peaks to be subtracted, we have calculated for each spectrum the shape of the bremsstrahlung contribution. The primary bremsstrahlung (bremsstrahlung of a target electron in the field of the bare projectile) is obtained within the Sommerfeld-Maüe method (distorted wave–unscreened potential [26]). Then the theoretical profile is convoluted with the silicon Compton profile, which depends on the crystal orientation. The secondary electron bremsstrahlung is calculated as in Ref. [27] by applying the McKinley-Fesbach equation for elastic scattering and the treatment of Koch and Motz [28] on electron bremsstrahlung to atomic silicon. Using these calculations to adjust our experimental background is questionable for three reasons. (i) In the calculation, all secondary electrons are assumed to stop inside the crystal. In fact the range of a ''knockon'' electron with highest energy $E_{\max}=2\gamma^2\beta^2 m_e c^2=136$ keV is about 300 μm in silicon [29], which is much larger than our crystal thickness. (ii) In the calculations, the secondary electron bremsstrahlung emission is assumed to be isotropic. This is doubtful, particularly for hard photons which are emitted by energetic binary electrons, i.e., electrons scattered in the forward direction. (iii) The bremsstrahlung yield depends strongly on ion channeling effects (see Sec. III). However, as one observes that the calculations reproduce quite well the shape of the experimental background, we have decided to set primary and secondary electron bremsstrahlung amplitudes as free parameters in the fits of the spectra and to keep the calculated shape. For random spectra, typical multiplying factors used to adjust the calculations to the experimental background are in the range 0.8 to 1.5.

V. COMPARISON TO EXPERIMENTS

A. Fitting the x-ray spectra

In Fig. 12 we compare experimental and simulated x-ray spectra in the case of random and $\langle 110\rangle$ aligned geometries. For the simulations, the contributions of primary and secondary electron bremsstrahlung and the contributions of core and valence electrons to the REC peaks are indicated separately. The respective weights of all these contributions were adjusted in order to obtain the best fit: here, the simulations are only used to predict shapes. The random spectrum calculated this way is seen not to fit perfectly the experimental spectrum on the high energy side of the *K*-REC peak, corresponding to the capture of electrons with high initial momentum. This discrepancy is not related to the uncertainty in the calculated contribution of secondary bremsstrahlung, since this contribution is quite small in this region. Most probably, the use of the impulse approximation in Eqs. (4) and (5) is no longer valid when the binding energy of the electron to be captured becomes non-negligible as compared to its kinetic energy viewed from the projectile frame, and thus the wings of the REC peaks are not perfectly estimated. Except for this small discrepancy, the agreement between simulations and experiments in both spectra of Fig. 12 is remarkable.

B. Fitting the REC yield dips

As mentioned in Sec. III, we estimated, for each beam incidence angle ψ_0, the mean fraction of ions that capture mechanically one or more electrons inside the target. For Kr^{35+} ions we assigned a *K*-REC probability divided by 2;

of course, for lower charge states, there is no K-REC. In Fig. 13 we show the comparison of experimental and calculated K-REC dips, corresponding to the capture of valence electrons [Fig. 13(a)] and of core electrons [Fig. 13(b)]. All the dips are normalized with respect to the random REC yield, measured or calculated for $\psi_0 \gg \psi_c$. The experimental dips were obtained from the best fits of the spectra as shown in Fig. 12, i.e., by adjusting each contribution to the REC peak. Here the error bars are due to the uncertainties in the fit (subtraction of bremsstrahlung, partition between core and valence contributions when both are large), and to the uncertainty in the evaluation of the corrective term for the fraction of ions with one or more electrons inside the crystal. The calculated dips were obtained from the simulations, as described in Sec. IV D. Simulations were performed assuming an isotropic Gaussian beam angular divergence with various widths. The best agreement, for the dips corresponding to both valence and core electrons, is obtained for a value of 0.1 mrad HWHM projected along one direction, in good agreement with the value given by the accelerator staff.

Concerning the behavior of the valence electron contribution, the experiments and the calculations are in good agreement and show unambiguously the existence of a narrow dip. The uncertainty in the fit is here negligible since both bremsstrahlung background and core electron contributions to K-REC are very small close to the $\langle 110 \rangle$ orientation. The agreement is also very good for the core electron contribution. The value of the calculated minimum yield ($\chi_{core}=0.055$, with a 10% uncertainty due to the statistics of the simulations) reproduces correctly the measured ratio between axial and random orientation: $\chi_{core}=0.060 \pm 0.017$. Although strongly attenuated in alignment conditions, the core electron contribution to the total K-REC yield is found to be 15%, which is not negligible.

The shoulder effect observed on the experimental dip around $\psi_0=0.06°$, i.e., for entrance angles slightly greater than ψ_c, cannot be predicted by our simulations. The latter are based on rather simple approximations to describe channeling effects (see Sec. IV A). In particular, we assume that (i) particle trajectories are determined by a continuum axial potential, (ii) the ion flux distributions correspond to statistical equilibrium, and (iii) all entrance directions with given ψ_0 are equivalent, i.e., that planar channeling effects can be neglected. These three hypotheses, which are valid for $\psi_0 \leqslant \psi_c$, do not allow us to reproduce experimental shoulder effects that depend markedly on the scanning direction. One important result of Fig. 13(b) is that χ_{core} is significantly higher than the value $\chi_{\min}=0.025$, measured for L_α emission, for instance. This is due to the fact that the density associated with $2s$ and $2p$ Si electrons is significant even at distances of $\simeq 0.3$ Å from the nuclei (see Fig. 7), which are much larger than the rms amplitude of thermal vibrations. As a consequence, core electrons contribute to $\simeq 13\%$ of the total K-REC yield when the beam enters along the $\langle 110 \rangle$ direction.

C. Determination of the K-REC cross section

The K-REC cross section can be extracted from the absolute yield values measured for random orientation [Figs. 13(a) and 13(b)]. They are found to be nearly identical and close to the prediction of the nonrelativistic dipole approximation ($\sigma_{K\text{-REC}}=39\times10^{-24}$ cm^2): the cross sections per target electron obtained from the valence and from the core electrons contribution are, respectively, $\sigma_{K\text{-REC}}=(38.5 \pm 1.2 \pm 5.8)\times10^{-24}$ cm^2 and $\sigma_{K\text{-REC}}=(42.9 \pm 2.4 \pm 6.4) \times10^{-24}$ cm^2. The first uncertainty corresponds to the error bars in Fig. 13, and is thus related to the fitting procedure. The second one is our experimental absolute uncertainty (15%).

It is of interest to compare the $\sigma_{K\text{-REC}}$ values that we obtain to the compilation of experimental cross sections presented in Ref. [30], where cross sections are compared to the prediction of the nonrelativistic dipole approximation for a large variation range of the adiabaticity parameter $\eta=1/\zeta^2=(E_{ion}/Z^2E_{Bohr})(m_e/M_{ion})$ where $E_{Bohr}=13.6$ eV. Most of the results correspond to experiments performed with gas targets, and very often the measured values are systematically $\approx 30\%$ lower than the theoretical predictions. However, for η values in the 1–3 range, which corresponds to our experimental situation ($\eta=1.86$), the compiled data are in good agreement with the predictions. Also, in this η range, no difference is observed between cross sections measured for gas and solid targets. In a paper devoted to the study of REC by channeling, the authors of Ref. [3] have assumed, in order to interpret their results, that the REC yield for ions traveling into solids could be strongly enhanced by the so-called ''wake effect'' which modifies the electron density and momentum distribution around the ion. In fact, their conclusions on REC cross sections rely on an estimate of the mean electron density that is quite questionable. (They consider that the whole ion flux in $\langle 110 \rangle$ alignment conditions is strictly restricted within the central region of the channels. This is erroneous, since it is clear that even with a perfect beam, the particle flux extends to the whole transverse space, although in a nonuniform way, cf. our Sec. IV A.) It is, nevertheless, worthwhile to discuss the influence of the wake effect on REC, which, according to Pitarke *et al.* [31], should in principle affect the REC yield and also the shape and energy position of the REC lines. These authors show that the amplitude of the response of the target electrons to the ion passage scales as $\zeta=\eta^{-1/2}$, which should affect REC yields significantly for ζ values above unity. In our case, $\zeta=0.73$ and the wake effects on the yield should be quite small.

Concerning the position of the REC peak, the wake effect shift predicted by Pitarke *et al.* [31] should be around 20 eV, i.e., a value too small to be evaluated owing to our experimental precision. The REC yield is proportional, in a first approximation, to the electron density ρ^* around the ions, which should depend on the wake effect. The dependence of the K-REC peak width on ρ^* is weaker: in the simple case of a Fermi gas, this dependence scales as $(\rho^*)^{1/3}$. As indicated above, in the η range corresponding to our experiment, neither the results obtained on gas targets nor those corresponding to solid targets (i.e., our measurements, but also experiments performed with 295-MeV/u uranium ions on beryllium and carbon [30]) show any significant departure from the predicted cross sections. As, moreover, we find a good agreement between calculated and measured line shapes (see Fig. 12), we conclude that for $\zeta<1$ (i.e., $\eta>1$), wake effects have a negligible influence on REC.

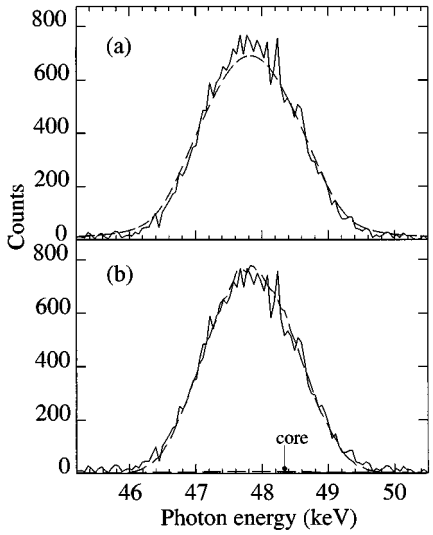

FIG. 14. Comparison of the K-REC line shape in the coincidence spectrum of Fig. 4 (solid line) to (a) the REC line associated with the valence electron Compton profile measured in Ref. [23] (dashed line) and (b) the REC line obtained from a Monte Carlo simulation with a nonuniform Fermi gas description of valence electrons (dashed line). The calculated small contribution of the core electrons is also represented.

D. K-REC of valence electrons

The coincidence spectrum shown in Fig. 4 is associated with the x-ray emission induced by the 45% ions having suffered the smallest energy losses (see Sec. III). Assuming to a first order a biunivocal relationship between the energy loss and the transverse energy of an ion, i.e., neglecting energy loss fluctuations, one can consider that these ions are the best channeled ones, with a well defined upper limit in transverse energy $(E_T/Q)_{\max}$. The K-REC peak observed (which we will call S_{expt}) corresponds thus essentially to the capture of target valence electrons. In Fig. 14(a) we compare S_{expt} to the K-REC peak (S_{calc}) calculated using the experimental Compton profile of Si valence electrons determined in Ref. [23] and taking for the K-REC cross section the value $\sigma_{K\text{-REC}}=38.5\times10^{-24}$ cm^2 that we have experimentally determined. In Fig. 14(a), the integral of S_{calc} was adjusted to that of S_{expt}, using a normalizing factor $\kappa=0.56$. S_{calc} corresponds to the valence contribution to K-REC for the whole incident beam at random incidence. As S_{expt} arises from an aligned incident beam and corresponds to a selection of part of this beam, it is natural to expect differences both in the integral (this explains why κ had to be introduced) and in the shape of S_{expt} and S_{calc}. In fact, one can observe in Fig. 14(a) that S_{expt} and S_{calc} have quite comparable shapes. However, the FWHM of S_{expt} is slightly narrower, 1.64 ± 0.05 keV against 1.8 keV for S_{calc}. As this width is related to the electron density of the captured electrons, this result demonstrates that the ions selected in the coincidence experiment sample valence electron densities hardly smaller than those sampled by a uniform ion flux.

We have used our Monte Carlo simulations in order to determine the characteristics of the channeled ions selected in the coincidence experiment. As shown in Sec. IV C, the simulations provide in particular the location $(\vec{r}_{i\perp},z_i)$ at which an ion with transverse energy E_{iT}, leaving the crystal with a charge state $35+$, has suffered a K-REC event. One can then determine to what fraction of the incident beam correspond the 45% best channeled ions with $35+$ outgoing charge state which were selected, and which electron densities they sampled. From our simulations (where we determine a cutoff in transverse energy in order to adjust the S_{calc} integral to S_{expt}), we find that the selected ions originate from 65% of the incident beam, with a cutoff $(E_T/Q)_{\max}=16$ eV. As the $V(\vec{r}_\perp)/Q$ value is around 19 eV in regions where the valence electron density is maximum, i.e., close to the cutoff value, we conclude that many of the selected ions may sample regions of high ρ_{val}. The simulations provide mean values of explored electron densities $\langle\overline{\rho_{val}}\rangle_i=(1/n)\Sigma_{i=1}^{i=n}\overline{\rho_{val}}(\vec{r}_{i\perp})=0.157$ Å^{-3} and $\langle\rho_{val}\rangle_i=(1/n)\Sigma_{i=1}^{i=n}\rho_{val}(\vec{r}_{i\perp},z_i)=0.223$ Å^{-3}. These mean values are slightly smaller than those sampled by a uniform flux, which are, respectively, equal to 0.2 Å^{-3} (four valence electrons per Si atom) and 0.255 Å^{-3}. This is consistent with the fact that S_{expt} is slightly narrower than S_{calc} in Fig. 14(a). It is also consistent with the fact that the normalizing factor $\kappa=0.56$ applied to S_{calc} is slightly smaller than the value 0.65 which corresponds to the fraction of the incident beam which was selected. Another conclusion of the simulation is that 97.5% of the selected ions have captured a valence electron and only 2.5% have captured a core electron.

In Fig. 14(b), we compare S_{expt} to the K-REC peak S_{sim} obtained from the simulation (see Sec. IV C). Let us recall that this calculation relies on a rather crude description of the valence electron momentum distribution. However, S_{sim} reproduces surprisingly well the shape of S_{expt}. In particular, the full width at half maximum of S_{sim} (1.61 keV) is found to be in good agreement with the experimental value (1.64 keV). There is still a small discrepancy in the wings corresponding to high longitudinal electron momenta, which are underestimated in S_{sim}. This discrepancy sets the limits of the free electron model that we have used.

VI. SUMMARY AND CONCLUSION

We have measured K-REC by channeled and unchanneled bare krypton ions in a thin silicon crystal. We have analyzed in detail the contribution of each electronic subshell of the target atoms. A complete decomposition of the K-REC peak has been obtained with the help of simulations which calculate the momentum distribution of captured valence, $2s$, and $2p$ electrons of silicon (the latter L-shell electrons contribute significantly—by 15%—to the REC peak in channeling conditions). The comparison between experiments and simulations provides information on the dependence of the electron momentum distributions on the position $\vec{r}_\perp$ in the transverse plane perpendicular to the $\langle110\rangle$ strings. This dependence is strong for both valence and $2p$ electrons. The K-REC cross section is found very close to the value obtained from the nonrelativistic dipole approximation calculation. We thus conclude that, for the value of the adiabaticity parameter η corresponding to our experiment, wake effects have a small influence on REC.

Beam angular divergence and multiple scattering of ions inside the quite thick crystal did not enable us to perform a specific study of hyperchanneled ions, i.e., ions which explore only regions in the transverse space very far from the atomic rows where valence electron Compton profiles are expected to be very narrow. However, we have measured a *K*-REC peak corresponding to the capture of valence electrons by the best channeled ions selected through their energy loss. This peak is well reproduced by simulations in which the valence electrons are described in the frame of a nonuniform Fermi gas model.

ACKNOWLEDGMENTS

We would like to thank J. Moulin and the CIRIL staff for their technical help, Y. Bernard for his help in x-ray topography measurements performed to check the crystal quality, and the GANIL accelerator crew for delivering us an ion beam of high quality. We thank also J. E. Miraglia, R. Gayet, and A. Salin for providing us the results of their calculations. The supports of NATO under research grant CRG890597 and of the French CNRS under GDR 86 are gratefully acknowledged.

[1] B.R. Appleton, R.H. Ritchie, J.A. Biggersaff, T.S. Noggle, S. Datz, C.D. Moak, H. Verbeek, and V.N. Neelavathi, Phys. Rev. B **19**, 4347 (1979).

[2] S. Andriamonje, M. Chevallier, C. Cohen, J. Dural, M.J. Gaillard, R. Genre, M. Hage-Ali, R. Kirsch, A. l'Hoir, B. Mazuy, J. Mory, J. Moulin, J.C. Poizat, Y. Quéré, J. Remillieux, D. Schmaus, and M. Toulemonde, Phys. Rev. Lett. **59**, 2271 (1987).

[3] L.C. Tribedi, V. Nanal, M.B. Kurup, K.G. Prasad, and P.N. Tandon, Phys. Rev. A **51**, 1312 (1995).

[4] S. Datz, C.R. Vane, P.F. Dittner, J.P. Giese, J. Gomez del Campo, N.L. Jones, H.F. Krause, P.D. Miller, M. Schulz, H. Schöne, and T.M. Rosseel, Phys. Rev. Lett. **63**, 742 (1989).

[5] A. Belkacem, E.P. Kanter, K.E. Rehm, E.M. Bernstein, M.W. Clark, S.M. Ferguson, J.A. Tanis, K.H. Berkner, and D. Schneider, Phys. Rev. Lett. **64**, 380 (1990).

[6] S. Andriamonje, M. Chevallier, C. Cohen, N. Cue, D. Dauvergne, J. Dural, R. Genre, Y. Girard, R. Kirsch, A. L'Hoir, J.C. Poizat, Y. Quéré, J. Remillieux, D. Schmaus, and M. Toulemonde, Phys. Lett. A **164**, 184 (1992).

[7] J.U. Andersen, J. Chevallier, G.C. Ball, W.G. Davies, J.S. Forster, J.S. Geiger, J.A. Davies, and H. Geissel, Phys. Rev. Lett. **70**, 750 (1993).

[8] N. Claytor, B. Feinberg, H. Gould, C.E. Bemis, J. Gomez del Campo, C.A Ludemann, and C.R. Vane, Phys. Rev. Lett. **61**, 2081 (1988).

[9] A. L'Hoir, S. Andriamonje, R. Anne, N.V. De Castro Faria, M. Chevallier, C. Cohen, J. Dural, M.J. Gaillard, R. Genre, M. Hage-Ali, R. Kirsch, B. Farizon-Mazuy, J. Mory, J. Moulin, J.C. Poizat, Y. Quéré, J. Remillieux, D. Schmaus, and M. Toulemonde, Nucl. Instrum. Methods Phys. Res. Sect. B **48**, 45 (1990).

[10] S. Andriamonje, R. Anne, N.V. De Castro Faria, M. Chevallier, C. Cohen, J. Dural, M.J. Gaillard, R. Genre, M. Hage-Ali, R. Kirsch, A. L'Hoir, B. Farizon-Mazuy, J. Mory, J. Moulin, J.C. Poizat, Y. Quéré, J. Remillieux, D. Schmaus, and M. Toulemonde, Phys. Rev. Lett. **63**, 1930 (1989).

[11] P.F. Dittner, C.R. Vane, H.F. Krause, J. Gomez del Campo, N.L. Jones, P. Zeijlmans van Emmichoven, U. Bechtold, and S. Datz, Phys. Rev. A **45**, 2935 (1992).

[12] J.E. Miraglia, R. Gayet, and A. Salin, Europhys. Lett. **6** , 397 (1988) and private communication for calculations on xenon.

[13] J.P. Rozet, C. Stephan, and D. Vernhet, Nucl. Instrum. Methods Phys. Res. Sect. B **107**, 67 (1996).

[14] S. Andriamonje *et al.*, Nucl. Instrum. Methods Phys. Res. Sect. B **107**, 1 (1996).

[15] A. Doyle and I. Turner, Acta Crystallogr. Sect. A **24**, 390 (1968).

[16] J. Lindhard, Mat. Fys. Medd. Dan. Vidensk. Selsk. **34**, No. 14 (1965).

[17] J.H. Barrett, Phys. Rev. B **3**, 1527 (1971).

[18] E. Bonderup, H. Esbensen, J.U. Andersen, and H.E. Schiott, Radiat. Eff. **12**, 261 (1972).

[19] H.E. Schiott, E. Bonderup, J.U. Andersen, and H. Esbensen, in *Atomic Collisions in Solids*, edited by S. Datz, B.R. Appleton, and C.D. Moak (Plenum Press, New York, 1975), Vol. 2, p. 843.

[20] C.F. Bunge, J.A. Barrientos, and A.V. Bunge, At. Data Nucl. Data Tables **53**, 113 (1983).

[21] J.R. Chelikovsky and M.L. Cohen, Phys. Rev. B **14**, 556 (1976).

[22] F. Biggs, L.B. Mandelsohn, and J.B. Mann, At. Data Nucl. Data Tables **16**, 201 (1975).

[23] N. Sakai, N. Shiotani, F. Itoh, O. Mao, M. Ito, H. Kawata, Y. Amemya, and M. Ando, J. Phys. Soc. Jpn. **58**, 3270 (1989).

[24] M. Stobbe, Ann. Phys. **7**, (Leipzig) 661 (1930).

[25] E. Spindler, H.D. Betz, and F. Bell, Phys. Rev. Lett. **42**, 832 (1979).

[26] K. Bernhardi, E. Haug, and K. Wiesemann, At. Data Nucl. Data Tables **28**, 461 (1986).

[27] R. Anholt, C. Stoller, J.D. Molitoris, D.W. Spooner, E. Morenzoni, S. Andriamonje, W.E. Meyerhof, H. Bowman, J.S. Xu, Z.Z. Xu, J.O. Rasmussen, and D.H.H. Hoffmann, Phys. Rev. A **33**, 2270 (1986).

[28] H.W. Koch and J.W. Motz, Rev. Mod. Phys. **31**, 920 (1959).

[29] L. Pages, E. Bertel, H. Joffre, and L. Sklavenitis, At. Data **4**, 1 (1972).

[30] Th. Stöhlker, C. Kozhuharov, P.H. Mokler, A. Warczak, F. Bosch, H. Geissel, R. Moshammer, C. Scheidenberger, J. Eichler, A. Ichihara, T. Shirai, Z. Stachura, and P. Rymuza, Phys. Rev. A **51**, 2098 (1995).

[31] J.M. Pitarke, R.H. Ritchie, and P.M. Echenique, Phys. Rev. B **43**, 62 (1991).

1-3-3 L'Ionisation par Impact d'Electrons (EII)

Ce processus est le mode dominant d'ionisation d'un ion canalisé lorsque, vu de son référentiel, l'énergie cinétique des électrons qui le bombardent est supérieure à l'énergie de liaison de ses électrons.
Notre collaboration a effectué trois expériences au cours desquelles l'ionisation par impact d'électrons a été étudiée [L'Hoir 90] [Dauvergne 99] [L'Hoir 06]. Dans les trois cas nous avons utilisé des projectiles loin de l'équilibre de charge, avec un excédent d'électrons (typiquement avec une couche M partiellement remplie), ce qui rend ce mode d'ionisation très probable, bien que très dominé par l'ionisation par impact sur les noyaux cible (les sections efficaces par atome sont typiquement dans le rapport Z_{cible} loin du seuil d'ionisation). Cette situation permettait en effet d'identifier aisément la contribution de l'EII et celle de la NII en fonction de l'état de charge du projectile en sortie du cristal (et éventuellement de sa perte d'énergie): les ions bien canalisés subissent quelques événements EII, et les ions mal canalisés subissent un grand nombre d'événements NII.
L'article "Charge states and energy loss of 300 MeV/u U^{73+} ions channeled in a silicon crystal" [Dauvergne 99], reproduit ci-dessous, rapporte les résultats de la première expérience de canalisation que nous avons effectuée au GSI en 1993. Contrairement aux autres publications de ce mémoire, je n'ai pas été l'auteur principal de cet article. Néanmoins j'ai contribué à la préparation, la menée et l'analyse de cette expérience, notamment lors de mon séjour au GSI cette année là. Les simulations ont été réalisées au GPS, et j'ai contribué à la collecte des sections efficaces nécessaires.

Ces expériences en conditions d'incidence hors équilibre sont donc surtout sensibles aux sections efficaces EII des couches n=3, et dans une moindre mesure n=2 du projectile. Cette restriction est imposée par la détermination de l'énergie transverse, et donc de la densité électronique rencontrée. On ne peut pas déterminer la section efficace EII pour des ions dont l'énergie transverse autorise l'ionisation par les noyaux lorsqu'ils s'approchent des rangées ou des plans cristallins (cf. la figure 11 de l'article [Dauvergne 99]).
La mesure en canalisation de l'ionisation K par impact d'électrons est certes possible. Il faut cependant mesurer avec précision l'énergie transverse au moyen de la perte d'énergie, afin de s'assurer que la NII ne contribue pas à l'ionisation. Ceci n'a jamais été fait. La seule expérience, au BEVALAC, ayant étudié l'ionisation K en canalisation a largement surestimé les résultats pour l'EII-K pour cette raison [Claytor 88].
Nos résultats d'ionisation par impact d'électron font apparaître des différences notables avec les calculs dans l'approximation des collisions binaires (ou BEA : Binary Encounter Approximation). Dans le cas des ions U^{73+} de 300 MeV/u, les valeurs nécessaires pour obtenir un bon ajustement des données sont d'un facteur 2 environ au-delà de ces valeurs théoriques (voir tableau 1 de l'article). De même, un facteur similaire doit être utilisé pour décrire l'ionisation d'ions Pb^{56+} de 29 MeV/u [L'Hoir 06]. On sait que, pour l'ionisation en couche K, des calculs relativistes dans le formalisme CDW permettent de reproduire cette différence d'un facteur 2 avec les calculs BEA dans le cas de l'uranium. Ces calculs CDW reproduisent bien les mesures obtenues avec des pièges EBIT. Cependant il n'est pas évident qu'il faille extrapoler ce facteur pour les couches plus externes.
D'autres effets peuvent intervenir dans une cible cristalline, comme les processus à plusieurs étapes (excitation/ionisation), dont on tient pourtant compte dans les simulations Monte-Carlo, et peut-être aussi les effets cohérents : bien que le champ électrique d'un noyau cible soit trop faible à grand paramètre d'impact pour ioniser le projectile, la somme cohérente des champs des noyaux alignés peut jouer un rôle, avec des interférences aussi bien constructives

que destructives [Salin 98]. Une étude systématique de l'ionisation d'un ion hors équilibre en canalisation planaire, en faisant varier l'angle d'incidence dans le plan sur quelques degrés, pourrait permettre d'étudier de tels effets de cohérence.

Charge states and energy loss of 300-MeV/u U^{73+} ions channeled in a silicon crystal

D. Dauvergne,[1] C. Scheidenberger,[2] A. L'Hoir,[3] J. U. Andersen,[4] S. Andriamonje,[5] C. Böckstiegel,[6] M. Chevallier,[1] C. Cohen,[3] N. Cue,[7] S. Czajkowski,[2] J. S. Forster,[8] H. Geissel,[2] H. Irnich,[2] T. Kandler,[2] R. Kirsch,[1] A. Magel,[9] P. H. Mokler,[2] G. Münzenberg,[2] F. Nickel,[2] Yu. L. Pivovarov,[10] J-C. Poizat,[1] M. F. Politis,[3] J. Remillieux,[1] D. Schmaus,[3] Th. Stöhlker,[2] T. Suzuki,[2] and M. Toulemonde[11]

[1] *Institut de Physique Nucléaire de Lyon and IN2P3, Université Claude Bernard Lyon-I, 43, Boulevard du 11 Novembre 1918, 69622 Villeurbanne Cedex, France*

[2] *Gesellschaft für Schwerionenforschung mbH Darmstadt, Planckstrasse 1, D-64291 Darmstadt, Germany*

[3] *Groupe de Physique des Solides, CNRS UMR 7588, Université Paris 7 et Paris 6, 75251 Paris Cedex 05, France*

[4] *Institute of Physics and Astronomy, University of Aarhus, DK 8000 Aarhus C, Denmark*

[5] *Centre d'Etudes Nucléaires de Bordeaux-Gradignan and IN2P3, le Haut-Vigneau, 33175 Gradignan Cedex, France*

[6] *Institut für Kernphysik, Technische Hochschule Darmstadt, Schlossgartenstrasse 9, D-64289 Darmstadt, Germany*

[7] *Department of Physics, The Hong Kong University of Science and Technology, Kowloon, Hong Kong*

[8] *Engineering Physics Department, McMaster University, Hamilton, Ontario, Canada L8S 4M1*

[9] *Universität Giessen, Heinrich-Buff-Ring 16, D-35392 Giessen, Germany*

[10] *Nuclear Physic Institut, P.O. Box 25, 634050 Tomsk, Russia*

[11] *Centre Interdisciplinaire de Recherche avec les Ions Lourds, UMR 11 CNRS-CEA, rue Claude Bloch, 14040 Caen Cedex, France*

(Received 11 June 1998; revised manuscript received 21 October 1998)

We have studied the emerging charge states q_{out} and energy loss of 300-MeV/u U^{73+} incident ions transmitted along a $\langle 110 \rangle$ axis of a 120-μm-thick Si crystal. The emerging charge state distribution $F_C(q_{out})$ for well-channeled ions is governed mainly by electron impact ionization (EII). The corresponding EII cross sections were obtained by fitting the experimental $F_C(q_{out})$ with Monte Carlo simulations. For M shell ionization, they were found to be twice larger than those given by the binary encounter dipole approximation. The measured energy loss spectra were also compared to Monte Carlo simulations. The mean values and widths of these spectra increase with q_{out}, reflecting the increase of the stopping power S with increasing transverse energy $E_\perp$. The measured stopping for channeled ions with frozen charge state $73+$ and for nonchanneled ions with charge state close to $90+$ is in good agreement with theoretical estimates. Owing to the very high ion velocity, there is a significant contribution (25%) to the stopping from Si-L shell excitation even for the best channeled ions. The width and the asymmetrical shape (skewness μ) of the energy-loss spectra depend strongly on q_{out} ($\mu>0$ for very well-channeled ions, $\mu<0$ for poorly channeled ions). For well-channeled ions, energy-loss spectra were reproduced by Monte Carlo simulations with the $S(E_\perp)$ curve extracted from fitting the mean energy losses. [S1050-2947(99)01604-2]

PACS number(s): 61.85.+p, 34.80.Dp

I. INTRODUCTION

Channeling of swift ions allows detailed investigations of energy loss and other atomic-collision processes such as ionization, excitation, and capture for such ions, under restricted impact parameters. In particular, by a selection of particles with low transverse energy $E_\perp$, one may suppress all atomic processes involving the target nuclei, such as mechanical electron capture (MEC) and nuclear impact ionization (NII), and to some extent one may isolate the contribution of valence electrons from that of core electrons for processes such as ionization, excitation, capture, and energy loss. Particles with well-defined $E_\perp$ may be selected in various ways. One can take advantage of the fact that, for ions of given velocity v and charge state q, the energy-loss spectrum $g(\Delta E)$ of the channeled beam is broad, reflecting the dependence of the stopping power $S(E_\perp)$ on transverse energy $E_\perp$ [1]. The $E_\perp$ selection is here performed through a selection in energy loss. This procedure may be used in experiments with incoming bare or nearly bare ions at high energy: in this case, the dominant charge exchange process is target electron capture [radiative electron capture (REC) [2], dielectronic recombination [3]), but the corresponding cross sections are small enough to ensure that the charge state of an ion in the crystal is nearly constant and depends little on its transverse energy. Another method was applied in planar channeling experiments [4], where the $E_\perp$ discrimination was obtained through a selection of particles with well-defined oscillation wavelengths. A third method was used in [5], where the $E_\perp$ discrimination was performed through a selection of the emergent charge state q_{out}. This method is particularly attractive when the initial charge state q_{in} of the ion is much lower than the equilibrium charge state, leading to a broad emergent charge state distribution $F_C(q_{out})$. The charge exchange processes are here dominated by the ionization of the projectile by the target electrons [electron impact ionization (EII)] with an efficiency that increases with the mean encountered electron density $\overline{\rho_e}(E_\perp)$ and hence with $E_\perp$. In particular, if $F_C(q_{out}=q_{in}) \ll 1$, selection of the frozen charge state $q_{out}=q_{in}$ can be used to select particles with very low $E_\perp$.

Our previous experiments at GANIL [5] are here extended to higher energies and heavier ions by using a

300-MeV/u uranium beam transmitted through a silicon crystal. The value of the Bohr parameter κ:

$$\kappa = \frac{2Z_1 v_o}{v} = 2\frac{Z_1}{137\beta} \tag{1}$$

corresponding to 300 MeV/u bare uranium ions is $\kappa \simeq 2$, i.e., greater than unity; a classical approach to calculation of energy transfers to target electrons is thus permitted [6].

The principal aims of the experiment presented in this paper are (i) to deduce EII cross sections from $F_C(q_{out})$ measurements for very high Z ions, for which simple perturbation treatments are questionable even at high velocities, (ii) to obtain experimental energy loss spectra as a function of q_{out} for comparison with semiclassical calculation of energy loss in channeling.

Our results on EII will be compared to various theoretical predictions and to other measurements, in particular to those of Claytor *et al.* [7], who also performed channeling measurements with uranium ions at similar energies, but using nearly stripped incident ions. More generally, an extended review of charge exchange processes for heavy ions in channeling was recently given by Krause and Datz [8]. In this review, the EII results obtained by channeling and by other methods such as electron beam ion trap (EBIT) are compared to theory.

In Sec. II we describe the experimental setup that allows charge state and energy analysis of the transmitted ions. In Sec. III we present our experimental data that include charge state distributions $F(q_{out})$ and energy loss spectra for given q_{out}, $g(\Delta E|q_{out})$. In Sec. IV we describe a simulation code that enables us to calculate both $F(q_{out})$ and $g(\Delta E|q_{out})$. The comparison of simulated and measured profiles is presented in Sec. V and the results are compared to theoretical calculations.

II. EXPERIMENT

We have used relativistic uranium ion beams [$Z_1=92$, $M_1=238$, $E_o=300$ MeV/u, i.e., $\beta=v/c=0.654$ and $\gamma=(1-\beta^2)^{-1/2}=1.32$] with $q_{in}=73$. The thickness $t=120$ μm of the silicon ($Z_2=14$) single crystal target along the $\langle 110\rangle$ axis was large enough to ensure a broad emergent charge state distribution $F_C(q_{out})$ (i.e., a good $E_\perp$ selection) and measurable energy loss distributions for each emergent charge state.

The experiment was performed at the heavy ion synchrotron SIS at GSI (Gesellschaft für Schwerionenforschung, Darmstadt), which provided a 300 MeV/u U^{73+} beam. The projectiles were injected into a high-resolution magnetic spectrometer (fragment separator FRS [9]), which consists of four ion optical stages each having one dipole magnet, five quadrupole magnets, and four hexapole magnets. The first two stages were used to prepare a beam of small angular divergence (see Fig. 1), which is a most important parameter in the experiment. The spot size on the silicon crystal was of the order of 10×15 mm^2. This large spot size was a necessary consequence of the optimization of the beam angular divergence. It had, however, minor influence on the experimental results as the rather thick silicon single crystal was large (20-mm diameter) and x-ray topography measurements

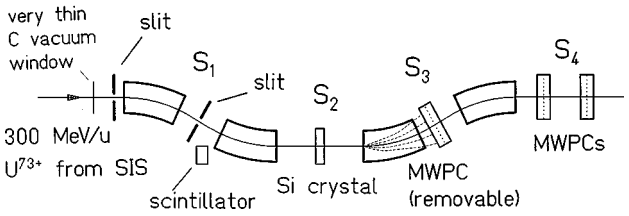

FIG. 1. Schematic layout of the experimental setup for channeling studies at the fragment separator FRS.

indicated negligible misalignment or mosaic spread. The beam intensity from SIS was typically $\approx 10^6$ ions per second. After charge and emittance selection by slits, it was $\approx 10^2$ ions per second on the crystal. The beam dose was calibrated and monitored using a scintillator outside the vacuum system, which measured secondary radiation due to the fraction of U ions hitting the slits.

The Si crystal target was mounted on a remotely controlled, high-resolution, three-axis goniometer designed for ultrahigh vacuum, placed at S_2, which could be moved with an accuracy of 0.01mrad. In the focal planes after the third and fourth stages of the FRS, the charge state distribution was measured using multiwire chambers [multiwire proportional counter (MWPC)] in S_3 and S_4. The wire chambers were used to determine the integral, position, and shape of the peak of a specific exit charge q_{out} state, giving information on the emergent charge state distribution, energy loss, and energy loss straggling. The correspondence between the position w (in mm) on the MWPC and the longitudinal momentum p of the particles, which depends on the measured rigidity Br (B, magnetic field; r, bending radius), is given by the dispersion D (in mm) via $\Delta p/p=\Delta w/D$ for our ion optical setting. In the FRS, one has $D_3=1380$ mm (for S_3) and $D_4=9530$ mm (for S_4). The charge state distributions were measured at S_3 and energy loss spectra at S_4. The variations Δp of momentum and variations ΔE of energy are related by $\Delta E/E=(1+1/\gamma)\Delta p/p=1.756\Delta p/p$, which gives $\Delta E_4=0.0553$ MeV/u and $\Delta E_3=0.38$ MeV/u for $\Delta w=1$ mm, respectively, in S_4 and S_3.

The alignment of the crystal for $\langle 110\rangle$ channeling was achieved either by maximizing the frozen charge state 73+ yield or by minimizing the 90+ emerging charge state yield (these yields were measured using a scintillator placed after the MWPC in S_4, in relation to the monitor scintillator near S_1). In reality, the observation of the frozen charge state yield gives here a much more precise alignment than given by the observation of the 90+ charge state yield (see Sec. III).

III. EXPERIMENTAL RESULTS

In Fig. 2 we present the measured yields of the emergent charge states $q_{out}=73$ (frozen) and $q_{out}=90$ as a function of the tilt angle φ_o between the beam direction and the $\langle 110\rangle$ axis. The angular distribution of the 73+ ions is very narrow, with a half width at half maximum of $\Psi_{1/2}^{73+}=0.11$ mrad. The observed angular scan for 90+ emergent ions is dominated by particles with high transverse energy, which were mostly ionized by close encounters with target nuclei (NII). The half width $\Psi_{1/2}=0.285$ mrad of the 90+

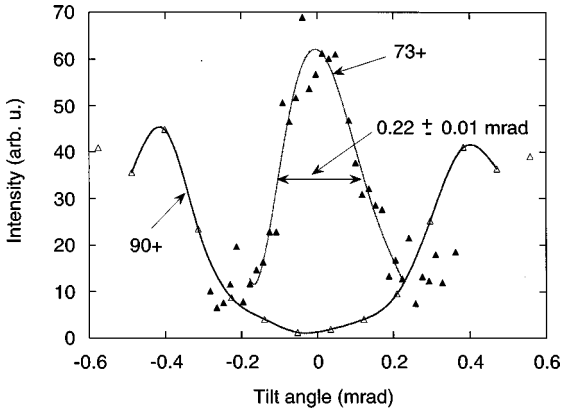

FIG. 2. Variations of the intensities of emergent charge states $q_{out}=q_{in}=73$ (closed triangles) and $q_{out}=90$ (open triangles) as a function of the angle φ_o between the beam and the $\langle 110\rangle$ axis of the Si crystal (lines through the points are drawn to guide the eye).

scan is thus, of course, larger than that of the 73+ scan. $\Psi_{1/2}$ is clearly related to the transverse energy $E_{\perp c}$ required to approach atomic strings at a distance of the order of ρ_{th}, the 2D rms of the thermal displacements of atoms perpendicular to the strings: $E\Psi_{1/2}^2 \simeq E_{\perp c} \simeq U_s(\rho)$, U_s being the string potential. The value of the Lindhard relativistic critical angle [10] $\psi_1=\sqrt{4Z_1Z_2e^2/pvd}$ is 0.39 mrad. Thus, we find a value $\Psi_{1/2}=0.73\psi_1$, somewhat smaller than extrapolated from numerical simulations [11] for a trial charge in silicon at room temperature, which gives $\Psi_{1/2}=0.85\psi_1$. An upper limit of the critical transverse energy $E_{\perp c}^{73+}$ to emerge in the frozen charge state $q_{out}=73$ is related to $E_{\perp c}$ by $E_{\perp c}^{73+}=(\Psi_{1/2}^{73+}/\Psi_{1/2})^2 E_{\perp c} \simeq 0.15E_{\perp c}$. In fact, $\Psi_{1/2}^{73+}$ is mainly determined by the beam angular divergence, as will be demonstrated in Secs. IV and V, and thus $E_{\perp c}^{73+}$ is certainly significantly smaller than this upper limit. The particles emerging with $q_{out}=73$ are very well-channeled ions, but $E_\perp$ selection through q_{out} is less accurate than that in Ref. [5]: the $q_{out}=73$ ions, which represent 3.8% of the emergent beam, are not all hyperchanneled (see Secs. IV and V). The minimum yield of the 90+ scan is $\simeq 5\%$. This is somewhat higher than the $\simeq 2\%$ yield obtained in Monte Carlo calculations by Barrett [11] or measured with MeV light ions on the same crystal and axis [12] for close encounter events. This may be explained, at least partially, by the fact that NII is not the only process for $q_{out}=90$ production; the binding energy of the L electrons of uranium is $B_L \simeq 20$ keV (it depends on the charge state) and the maximum energy transfer in a close encounter EII process is $\simeq Em_e/M_U=164$ keV. Hence, EII alone may produce 90+ uranium ions. Another important contribution to the 5% minimum yield comes from tails in the incoming beam angular distribution and to dechanneling (see Sec. IV).

Typical spectra measured with MWPCs at S_3 and S_4 are shown in Fig. 3. In Fig. 3(a) we show the charge state distribution $F_C(q_{out})$ at S_3 $(73 \leqslant q_{out} \leqslant 77)$ with the $q_{out}=73$ peak at the center. Figures 3(b) and 3(c) show the spectra for $q_{out}=73$ measured at S_4, respectively, with and without the silicon crystal. In Fig. 3(d), we show a spectrum for rather poorly channeled ions ($q_{out}=83$); the peak is broader than for $q_{out}=73$ reflecting larger energy loss fluctuations.

The measured emergent charge state distributions are given in Fig. 4, for $\langle 110\rangle$ aligned and random orientations. The distributions were obtained by measuring sequentially the intensity of three neighboring peaks for which the transmission from the Si crystal at S_2 to the MWPC at S_3 was equal to 1. In the random case, the narrow distribution $F_R(q_{out})$, centered around $q_{out}=90$, does not correspond to equilibrium: the target is not thick enough, considering the very small capture cross sections (MEC, REC) for the relativistic uranium ions studied. A tail towards low charge states, representing about 3% of the total beam is observed and we attribute this to planar channeling effects.

The aligned distribution $F_C(q_{out})$ is broad, as expected, reflecting the influence of $E_\perp$ on q_{out}. The upper region

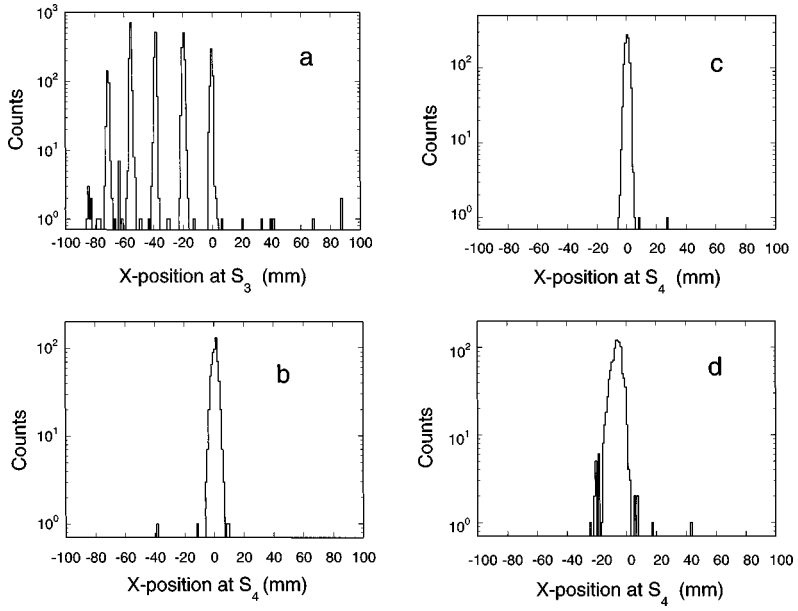

FIG. 3. Spectra measured with MWPCs at S_3 and S_4. (a) Charge state distribution at S_3 for $73 \leqslant q_{out} \leqslant 77$. (b) $q_{out}=q_{in}=73$ peak at S_4 with the crystal. (c) $q_{out}=q_{in}=73$ peak at S_4 for the direct beam. (d) $q_{out}=83$ peak at S_4.

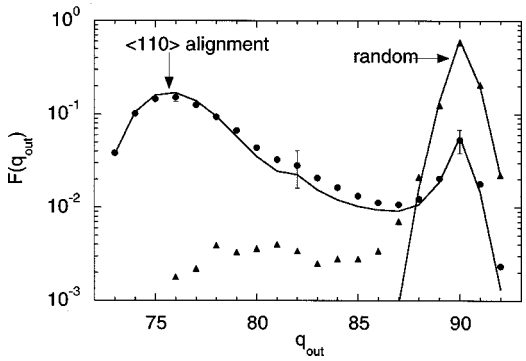

FIG. 4. Charge state distributions obtained for U^{73+} incident ions at 300-MeV/u after transmission through a 120-μm-thick Si crystal, for alignment along the $\langle 110 \rangle$ direction [$F_C(q_{out})$, closed circles] and for random orientation [$F_R(q_{out})$, closed triangles]. The solid lines correspond to Monte Carlo calculations (see Sec. V).

($q_{out} \gtrsim 87$) of $F_C(q_{out})$ corresponds to very poorly channeled, nonchanneled, or dechanneled ions. This region contains about 10% of the distribution. Dechanneling alone cannot explain this rather high value, which is mainly attributed to the angular spread of the incoming beam (see Sec. IV).

In Fig. 5 the mean energy losses $\overline{\Delta E}(q_{out})$, measured with the MWPCs, for $\langle 110 \rangle$ alignment, are plotted as a function of emergent charge state q_{out} together with random values measured for $q_{out}=89$ to 92. The increase of $\overline{\Delta E}$ with q_{out} arises (i) from the increase with q_{out} of the mean charge state $q_{av}(q_{out})$ of the particles inside the target. Here, $q_{av}(q_{out})$ is defined in such a way that the mean energy losses $\Delta E(q_{out})$ scales approximately as $q_{av}^2(q_{out})$ [see Sec. V B, Eq. (7)] (ii) from the increase of $E_\perp$ with q_{out} and the increase of stopping power S with $E_\perp$. Hence, the ratio $\overline{\Delta E}(q_{out})/q_{av}^2(q_{out})$ (also represented in Fig. 5), gives the influence of the transverse energy on mean energy loss. As in Ref. [5] for Xe ions, the mean energy loss in the random case is lower than the $\overline{\Delta E}(q_{out})$ value obtained under channeling conditions for very high transverse energies (here q_{out}

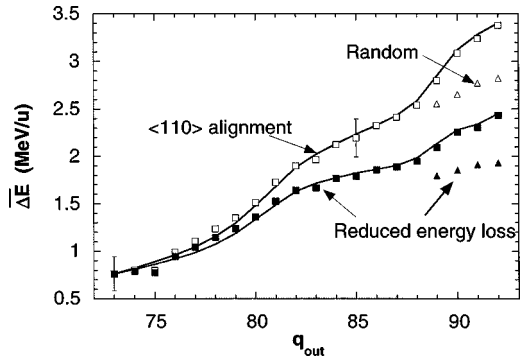

FIG. 5. Mean energy loss $\overline{\Delta E}(q_{out})$ measured with the wire chamber at S_3 as a function of emerging charge state q_{out} for U^{73+} incident ions transmitted in $\langle 110 \rangle$ alignment conditions (open squares). The mean energy loss for random orientation and for $89 \leqslant q_{out} \leqslant 91$ are also shown (open triangles). The closed squares and triangles correspond to a reduced mean energy loss $\overline{\Delta E}(q_{out}) q_{in}^2/q_{av}^2(q_{out})$ using the calculated mean charge state q_{av} in the target (see Sec. V). The solid lines are the results of the Monte Carlo calculations.

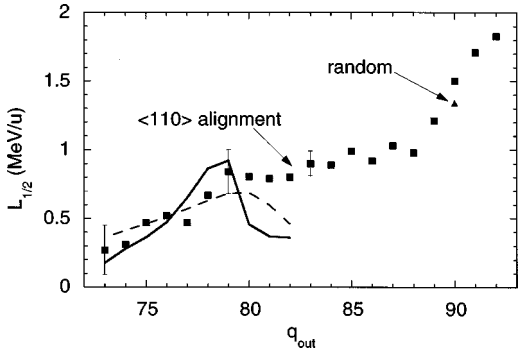

FIG. 6. FWHM of the energy-loss spectra $g(\Delta E|q_{out})$ as measured by the wire chamber at S_4, as a function of emergent charge state q_{out} for $\langle 110 \rangle$ alignment (closed squares), and for random orientation ($q_{out}=90$, closed triangle). All of the data have been corrected for the resolution. The lines correspond to the Monte Carlo calculations: calculated FWHM (solid line), 2.355Ω (dotted line), where Ω^2 is the calculated variance.

$\geqslant 89$). This is a ''shoulder effect'': due to blocking by planes, particles with high transverse energy spend a larger part of their path close to the target nuclei than particles with random trajectories. The angular divergence of the beam being very small, even the measurement for the random incidence is not comparable to a measurement performed on an amorphous silicon target since channeling phenomena cannot be completely suppressed. This is obvious when one considers the shape of the energy loss spectra $g(\Delta E|q_{out})$. The full width at half maximum (FWHM) $L_{1/2}(q_{out})$ of the $g(\Delta E|q_{out})$ spectra is shown in Fig. 6. These FWHM values have been corrected for the distribution without the crystal (see Fig. 3), using a simple quadratic procedure. One observes an increase of the energy straggling with q_{out} for similar reasons as for $\overline{\Delta E}$. For the random measurement, the fluctuations are much larger than calculated by Monte Carlo simulations, whereas the mean value compares reasonably well with theory or compilation of experimental results (see Sec. V). In Fig. 7, we present the asymmetry figure $\mu^{1/3} = (\mu_3/\sigma^3)^{1/3}$ (μ is the skewness, μ_3 is the centered third order moment, and σ the standard deviation) of the energy loss spectra as measured with the MWPCs at S_4. Due to the

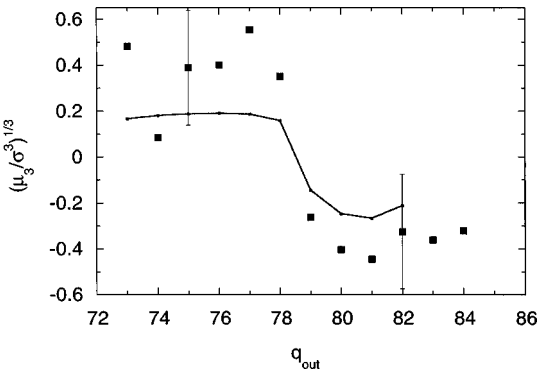

FIG. 7. Asymmetrical figure $\mu^{1/3} = \mu_3^{1/3}/\sigma$ of the energy loss spectra $g(\Delta E|q_{out})$ as a function of emergent charge state q_{out} in $\langle 110 \rangle$ alignment. The points (closed squares) correspond to measurements made at the wire chamber in S_4. The Monte Carlo calculated $\mu^{1/3}$ is represented by the solid line.

very large uncertainties in the experimental results, only the qualitative behavior of $\mu^{1/3}$ should be considered. One observes clearly a sudden change in the sign of μ between $q_{out}=78$ ($\mu>0$, tail toward high energy losses) and $q_{out}=79$ ($\mu<0$, tail towards low energy losses). For $q_{out}<78$ one may consider $g(\Delta E|q_{out})$ as made up of a peak corresponding to well-channeled ions plus a tail corresponding to particles with higher $E_\perp$ whereas for $q_{out}>79$, $g(\Delta E|q_{out})$ consists of a peak corresponding to poorly channeled ions plus a tail corresponding to rather well-channeled ions, which have a finite probability to go out with $q_{out}>79$. This behavior was a useful guide in our simulations.

IV. MONTE CARLO SIMULATIONS

Simulations based on the calculation of ion flux distribution inside the crystal were used to calculate the emergent charge state distributions $F_C(q_{out})$ and energy loss spectra for a given exit charge state $g(\Delta E|q_{out})$. Less complex Monte Carlo simulations were used to simulate $F_R(q_{out})$ and $g(\Delta E|q_{out})$ corresponding to the random orientation. Similar simulations were already used and are described in Refs. [5] and [2]. We will only describe the most important features of the model.

For calculation time reasons, the simulations (for channeling or random cases) are not full Monte Carlo simulations, i.e., successive atomic collisions are not explicitly calculated. One consequence is that the behavior of ions with very high $E_\perp$ is not very well described because shoulder effects are not reproduced.

A. Calculation of the particle flux: Variations of the transverse energy with depth

An ion penetrating the crystal with energy E_o is given an entrance position $\vec{r}_{0\perp}$ (uniformly distributed in the transverse plane), and an entrance angle $\psi=\psi_o+\delta\psi$, which is distributed according to the beam angular distribution $h_b(\delta\psi)$ around the mean incident direction at angle ψ_0 to a $\langle 110\rangle$ axis. The precise knowledge of $h_b(\delta\psi)$ is crucial. Overall agreement between calculations and experimental results is found when $h_b(\delta\psi)$ is assumed to be the sum of a Gaussian with a 1D rms deviation of 0.075 mrad (i.e., $0.075\times\sqrt{2}=0.105$ mrad for the 2D distribution) and a much wider Gaussian distribution (1D rms 0.20 mrad), which contains 20% of the incident ions. Such a decomposition was necessary in order to reproduce the narrow angular scan $q_{out}=73$ of Fig. 2 and the emergent beam charge state distribution $F_C(q_{out})$ of Fig. 4, for $q_{out}\gtrsim 80$.

Particles are assumed to move in the continuum transverse potential U calculated in Ref. [5] for the $\langle 110\rangle$ axis of Si, corrected near the strings for thermal vibrations of the crystal atoms by using the single string potential of Ref. [13]. Statistical equilibrium is assumed for the transverse motion, and hence, a particle of given E_T has a uniform probability to be at any point in the accessible area of the transverse plane $A_\perp(E_\perp)$ [10]. This is true only sufficiently far from the crystal entrance since the incoming ions keep a ''phase memory'' at the beginning of their path [11] over a characteristic path length Λ. In our case, the crystal thickness ($t=120$ μm) is much greater than $\Lambda\approx 6$ μm and one may consider that statistical equilibrium prevails throughout the crystal (the Λ value was estimated from the Monte Carlo calculations of Barrett [11] and from the scaling $\lambda/2\approx d_n/\psi_c$ [14] for the oscillation length λ of close encounter yield due to neighboring strings at distance d_n). However, channeling with respect to planes introduces a more stable division of the transverse phase space of axially channeled particles into planar channeled and blocked trajectories, respectively [15]. This division is responsible for shoulder effects like the increase of the stopping power above the random value and the increase of energy loss fluctuations, which was not taken into account in the simulation.

Multiple scattering, which tends to increase the transverse energy, is taken into account. The changes in $E_\perp$ result from multiple scattering on target electrons and on screened target nuclei. A good estimate of the contribution of target electrons to multiple scattering can be obtained following Bonderup *et al.* [16], from the mean energy loss of these particles in the crystal. According to [16], the 2D variance $\delta\varphi_e^2$ of the angular distribution for a given path δx is

$$\overline{\delta\varphi_e^2}=\frac{m_e}{M_1}\frac{\overline{\delta E}_{close}}{E}, \tag{2}$$

where m_e is the electron mass and $\overline{\delta E}_{close}$ is the mean energy loss corresponding to close collisions with target electrons; roughly, $\overline{\delta E}_{close}=\frac{1}{2}\overline{\delta E}$. If δx is small enough to ensure a quasiconstant value of the transverse position $\vec{r}_\perp$ and of the angle $\vec{\varphi}$ of the trajectory with respect to the axis, the corresponding increase $\delta E_\perp$ in transverse energy is given by $E(\vec{\varphi}+\delta\vec{\varphi}_e)^2-E\varphi^2$, where $\delta\vec{\varphi}_e$ is a random deflection angle with variance given by Eq. (2). In what follows, the transverse energy will be systematically normalized to the unit charge and we then write:

$$q_{in}\delta E_\perp=E(\vec{\varphi}+\delta\vec{\varphi}_e)^2-E\varphi^2=2E\vec{\varphi}\cdot\delta\vec{\varphi}_e+E\,\delta\varphi_e^2. \tag{3}$$

This contribution to $\delta E_\perp$ by electron multiple scattering is taken into account in the Monte Carlo simulations.

Over the target thickness t, using the typical value $\overline{\Delta E}=1$ MeV/u for channeled ions (see Fig. 5), the contribution of the quadratic term in Eq. (3) is $E\overline{\Delta\varphi_e^2}/q_{in}=5$ eV. This can be compared to the critical transverse energy $E_{\perp c}=E\psi_1^2/q_{in}=150$ eV. The mean value of the nonquadratic term in Eq. 3 is null. Thus, this term contributes only to the transverse energy spread.

For the contribution to dechanneling of screened target nuclei we used the treatment proposed in Ref. [10] and developed in Ref. [17]. As for multiple scattering in a random medium, dechanneling by target nuclei for a given crystal and axial direction scales approximately as Z_1/E [10]. If, for example, one considers the experimental backscattering results of Ref. [12] for light ions along a $\langle 110\rangle$ axis of silicon, the reduced path length Z_1x/E for reaching a close encounter yield equal to 10% of the random yield is 2.7 μm MeV^{-1}, which gives $x\simeq 2$ mm in our case: dechanneling by target nuclei is thus small in our 0.12-mm-thick target.

When the transverse energy of a given ion exceeds a value $E_{\perp max}>E_{\perp c}$ we assume that the ion is no longer channeled (the code is in any case not able to describe particles

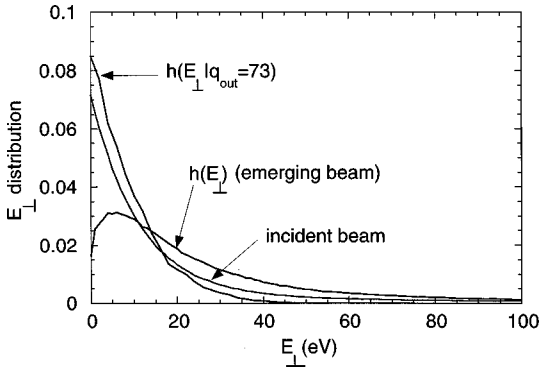

FIG. 8. Transverse energy distributions for the incident beam (characterized by its angular distribution, described by two Gaussians, see text), for the emerging beam and for emerging ions with $q_{out}=73$.

with very high $E_\perp$ correctly). If this occurs at depth x with a charge state q, it is necessary to calculate the charge state distribution of such an ion after traversing a random silicon target of thickness $t-x$ and with initial charge q: $F_R(q_{out}|q,t-x)$. This was done once, using the code ETACHA [18] for $73 \leqslant q \leqslant 92$ and various thicknesses x. Above a threshold value of 140 eV we found that the value of the parameter $E_\perp$ had no influence on the results. The curves presented in Sec. V were calculated with $E_{\perp max}=160$ eV; consequently, 3% of the beam was considered as random at $x=0$.

We show in Fig. 8 the transverse energy of the incoming beam, of the emerging beam, and of the 3.8% fraction of the emerging beam, which corresponds to $q_{out}=73$. This figure illustrates the influence of dechanneling on the overall beam. It also shows that this influence is very small for well-channeled particles emerging with $q_{out}=73$.

B. Charge exchange

Ionization and capture processes induced by target electrons (EII, REC) and by target nuclei (NII, MEC) are included in the simulations as well as excitation by electrons and nuclei, radiative and Auger decay. Ionization and excitation are assumed to be close encounter events with a probability proportional to the local electron or nucleus density. For a particle with a given $E_\perp$, the probability for target electron-induced processes is proportional to the mean electron density $\overline{\rho_e}(E_\perp)$ in $A(E_\perp)$. For nuclei, a cylindrical geometry around the strings was used (see [5]). The spatial extension of the ion electronic wave functions has nearly no effect on processes involving target electrons as the target electron density varies little at the scale of K,L,M orbital extension of uranium. For processes involving target nuclei (see [5]), a characteristic length is given by the 2D thermal vibrational amplitude $\rho=0.11$ Å at room temperature.

1. EII cross sections

The emergent charge state distribution $F_C(q_{out})$ is governed mainly by the EII processes; this means that rather significant uncertainties in NII, excitation and capture cross sections used in the simulations has a relatively minor influence on the determination of EII cross sections from the experiment. Conversely, it also means that the experiment is not appropriate to determine cross sections of other processes than EII. Although reliable values of NII, MEC, etc… cross sections are necessary in the simulations; some of these parameters may be varied over a reasonable range in order to improve the overall agreement with experimental results [in particular $F_R(q_{out})$] or to determine the precision that we may claim on the determined EII cross sections. For the EII cross sections themselves, we used theoretically calculated cross sections as a starting point and modified them until an optimum fit to the experiment was obtained.

For simplicity reasons, all cross sections were averaged over subshells in a given shell n. This is a fair approximation, as the main information that we reach is the EII cross section for M shell (see Sec. V A 1). In Sec. V A, the fitting values σ_{nfit}^{EII}, corresponding to EII in n shell will be compared to available theoretical predictions and to other experimental results. We now discuss the cross sections (other than EII) used in the Monte Carlo calculations.

2. NII cross sections

The NII cross sections were calculated in the plane wave Born approximation (PWBA) as described in Ref. [18], using screened hydrogenic wave functions for the initial and final states of atomic electrons. The calculated NII cross sections σ_n^{NII} per ion electron in shell n and per target nucleus are presented in Table I. They are two to three orders of magnitude higher than the corresponding σ_n^{EII} values. In particular, for the outer shells ($n>2$), the ratio $\sigma_n^{NII}/\sigma_n^{EII}$ is close to the square of the Si nuclear charge. Thus NII completely dominates for random ions, which shows that channeling is absolutely necessary to obtain information on σ_n^{EII}.

3. REC and MEC cross sections

REC cross sections for fully stripped ions were calculated according to the Bethe-Salpeter formula [19] and are given in Table I.

For MEC, we used two sets of cross sections. One set was calculated in the continuum distorted wave (CDW) approximation [20] using the code of Gayet [21]. The other set was calculated [22] in the simpler relativistic eikonal approximation [23,24]. The influence of the population of shells and subshells was taken into account by using the procedure suggested in [18], according to which the capture cross section to a given subshell is assumed to be simply proportional to the number of available vacancies.

4. Excitation cross sections

Cross sections σ_ν^{Exc} for excitation by target nuclei were calculated by Salin [25] for $n \leqslant 3$ using the PWBA approximation. Excitation cross sections for $n>4$ shells were extrapolated using a $1/n^3$ scaling. The σ_ν^{Exc} values are in the range 10^{-25} to 10^{-22} cm^2. The excitation cross sections by target electrons σ_e^{Exc} were calculated from the excitation cross section by target nuclei assuming a Z_2^2 scaling law.

5. Recombination processes

For an ion in a solid, intrashell mixing takes place and the mean life τ of an excited state is mainly governed by the

TABLE I. Theoretical cross sections averaged over subshells σ_{th} (in barns) (for EII cross sections, the index *Y* refers to Younger [33], *S* to Scofield [43], *F* to Fontes *et al.* [36], and *Kim* to calculations performed by [35] using the BED model of Kim and Rudd [34]). The cross sections σ_{fit} leading to the best overall agreement with the experimental results are expressed as a function of the σ_{th}.

Shell n	σ_{th}^{MEC}	σ_{th}^{REC}	σ_{th}^{NII}	σ_{th}^{EII}
1	17.8	71	600	0.6^{Kim}, 0.6^{Y}, 1.24^{F}
	$2s$:15.3			
2		14.8	5.9×10^{3}	18^{Kim}, 19^{Y}, 36^{S}
	$2p$:45.8			
	$3s$:5.5			
3	$3p$:16.6	4.3	1.6×10^{4}	76^{Kim}, 48^{Y}
	$3d$:27.7			
4	30	1.8	3.2×10^{4}	170^{Kim}
5	19	0.9	5.4×10^{4}	320^{Kim}
1–5	$\sigma_{fit}^{MEC}=0.5\sigma_{th}^{MEC}$	$\sigma_{fit}^{REC}=\sigma_{th}^{REC}$	$\sigma_{fit}^{NII}=1.3\times\sigma_{th}^{NII}$	$\sigma_{fit}^{EII}=(1.9\pm0.4)\times\sigma_{Kim}^{EII}$

fastest transitions, i.e., electric-dipole transitions [26]. We used the tables of Omidvar [27] that give the transition probabilities and branching ratios for electric-dipole transitions between levels of hydrogenlike atoms, using the $1/Z_1^4$ scaling (typical τ values are between 10^{-17} and 10^{-14} s). In the Monte Carlo code, Auger decay was taken into account for transitions from *M* to *L* shell only. The fluorescence yield (i.e., the probability of radiative decay) is $r_F=0.42$ [28] for a filled *M* shell (and at least a vacancy in *L* shell). For a given number m of *M* electrons ($1\leqslant m\leqslant 18$), $r_F(m)$ was calculated by assuming that the probability for Auger decay is proportional to $m(m-1)$ and the probability for radiative decay is proportional to m.

In our experiments, the dominant charge exchange process is ionization: capture and recombination processes have a relatively minor influence on the charge state distributions.

C. Energy loss

For the simulation of energy loss spectra, if one assumes statistical equilibrium, the only needed function is $S(E_\perp)$ that is an averaged value over the accessible transverse space $A(E_\perp)$ of the stopping power $S(\vec{r}_\perp)$ for an ion at position $\vec{r}_\perp$ in the transverse plane. We impose the asymptotic behavior at large $E_\perp$ to be

$$S(E_\perp)=S_R\left[1-\alpha\exp\left(-\frac{E_\perp d}{Z_2e^2}\right)\right], \tag{4}$$

where d is the interatomic distance along the $\langle 110\rangle$ axis and α an adjustable parameter; S_R is the stopping power for very large $E_\perp$, i.e., for random orientation. Expression (4) may be derived using the hypothesis of statistical equilibrium and the string potential $U_s(R)\simeq(Z_1Z_2e^2/Ed)\ln(1+3a^2/R^2)$ (where a is a screening radius) derived by Lindhard [10]. We assumed a q^2 dependence of $S(E_\perp)$ with the charge state ($73\leqslant q\leqslant 92$). This is reasonable, owing to the ion velocity and to the restricted spatial extension of the orbitals of uranium ions (see Sec. V B 2). Hence, one can write, for instance, $S(E_\perp,q)=S(E_\perp,q_{in})\times q_{in}^2/q^2$. In the following, we essentially use $S(E_\perp,q_{in})$, where $q_{in}=73$.

For channeled particles, the energy loss spectra are mainly determined by the shapes of the $E_\perp$ distribution $g(E_\perp)$ and of $S(E_\perp)$. At given $E_\perp$, one must consider fluctuations in energy loss, which arise from fluctuations in charge state q and from fluctuations in energy transfer in individual electronic collisions. The fluctuations in q are taken into account in the simulations through a q^2 dependence of the stopping power. In order to calculate the variance $\delta\Omega_T^2$ associated with the statistical variation in the energy transfer in successive collisions with electrons, we used recent theoretical [29] and experimental [30] results. At relativistic velocities, $\delta\Omega_T^2$ for a path length δx may be expressed as

$$\delta\Omega_T^2=4\pi q^2e^4\overline{\rho_e}\delta x\gamma^2X=\delta\Omega_B^2\gamma^2X, \tag{5}$$

where $\overline{\rho_e}$ is the mean electron density experienced, $\delta\Omega_B^2$ represents the nonrelativistic free-electron Bohr result [6], and X accounts for departure from the Rutherford scattering law. In our case, from [29] and [30] one finds $X\simeq 1.7$. An upper limit for Ω_T, which should correspond to the random case, is $\Omega_T=0.031$ MeV/u using $q=92$ and $\overline{\rho_e}=14$ electrons per atom.

All of these contributions to energy loss fluctuations are taken into account in the Monte Carlo calculation to construct the $g(\Delta E|q_{out})$ curves.

D. Simulations for random orientation

In order to calculate the charge state distributions $F_R(q_{out})$ and the energy loss spectra $g(\Delta E|q_{out})$ for random orientation, we used a special random code. In this program the ion history is described as a succession of binary collisions on homogeneous, randomly distributed atoms or valence electrons. There is, of course, no $E_\perp$ dependence in the random code. As in the channeling code, the individual interactions leading to energy loss are not described. However, charge-changing events are simulated and hence the main contribution to energy loss fluctuations is fully included.

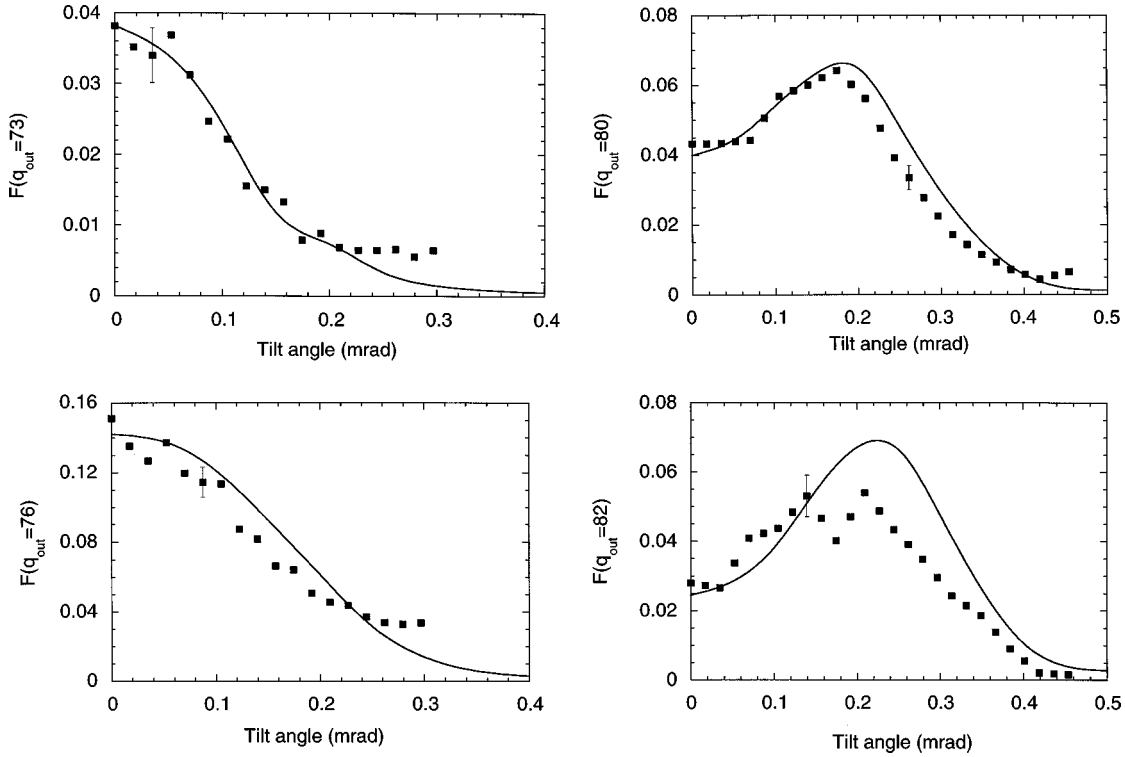

FIG. 9. Experimental angular scans (closed squares) of the fraction of emergent charge states $q_{out}=73,\ 76,\ 80,$ and 82 as a function of the angle between the beam and the $\langle 110\rangle$ axis of the Si crystal. The solid lines correspond to Monte Carlo calculations.

E. Fitting the experimental results

The experimental emergent charge state distributions $F_C(q_{out})$ and $F_R(q_{out})$, respectively, for $\langle 110\rangle$ channeling and for a random orientation, together with the energy loss spectra $g(\Delta E|q_{out})$, were fitted at the same time to ensure self-consistency. In order to limit the number of free parameters, we assumed in a first step that the ratios between theoretically calculated cross sections given in Table I corresponding to the different shells (for example, $\sigma_1^{EII}/\sigma_2^{EII}$) were reliable. In addition, excitation cross sections, REC cross sections (which play a minor role here), and decay probabilities were held fixed at their theoretical values. The adjustable parameters were then the scaling factor for the EII cross sections, the widths and proportion of the two Gaussians describing the incident beam angular divergence (see Sec. IV A) and the curve $S(E_\perp)$.

The Monte Carlo calculations were performed considering only 5 shells ($n\leqslant 5$): capture to higher excited states is nearly always followed immediately by ionization and these two events cancel.

V. RESULTS

A. Charge state distributions and EII cross sections

1. Charge states

Our best overall agreement leads to the solid lines in Fig. 4. The fitting of the random curve $F_R(q_{out})$ is sensitive mainly to NII and, to a lesser extent, to MEC. The fitting of the experimental $F_R(q_{out})$ does not lead to a unique set of cross sections. However, it appears that the calculated NII cross sections are not large enough to reproduce the large ($\simeq 55\%$) U^{90+} fraction and/or that calculated MEC cross sections are too large. The theoretically calculated MEC cross sections reported in Table I are those of [22] (eikonal approximation) for $n\leqslant 3$ and CDW cross sections [21] for $n>3$. These cross sections have a rather weak influence on the fitting of $F_C(q_{out})$ obtained for $\langle 110\rangle$ alignment. The solid curve in Fig. 4 was obtained with the fitting cross sections given in Table I.

The fit of $F_C(q_{out})$ is satisfactory. In particular, the region of $F_C(q_{out})$ with a quasirandom shape, which represents $\sim 10\%$ of the emergent ions, is well reproduced. The region $73\leqslant q_{out}\leqslant 80$ that corresponds to $\sim 75\%$ of the beam and for which $F_C(q_{out})$ is mainly due to EII in the uranium M shell is very well reproduced. The quality of the fit is highly sensitive to values of σ_3^{EII} introduced in the simulations. *The solid curve of Fig. 4 have been obtained with* $\sigma_{3fit}^{EII}=145b$ *per M shell electron.*

Experimental angular scans for four q_{out} values (73, 76, 80, 82) are shown in Fig. 9, together with the Monte Carlo calculated curves. It should be noted that, although we do not use a true channeling Monte Carlo code (statistical equilibrium is assumed), the calculated curves reproduce reasonably well the experimental data, considering that our main effort was devoted to the best channeled ions, i.e., $q_{out}=73$.

In order to gain more insight into the behavior of the channeled ions, we show in Figs. 10 and 11 various parameters given by the simulations, as a function of q_{out}: the mean transverse energy $\overline{E_\perp}(q_{out})$ (per unit charge), the mean sampled electron density $\rho_e(q_{out})$, the mean charge state in the target $q_{av}(q_{out})$, and the mean number of EII and NII events per ion, $N_{EII}(q_{out})$ and $N_{NII}(q_{out})$. The definition of q_{av} is based on the assumed q^2 scaling of the energy losses. If L_i represents the total path length travelled by an ion with

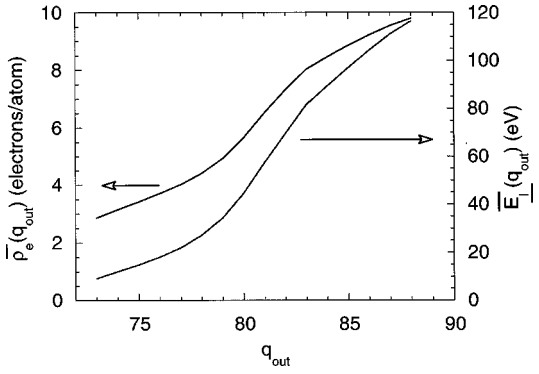

FIG. 10. Calculated mean transverse energy $\overline{E_\perp}(q_{out})$ (in eV, for unit charge) and mean sampled electronic density $\rho_e(q_{out})$ (in number of electrons per silicon atom) as a function of the exit charge state q_{out}. Calculations were carried out with the fitting parameters leading to the solid lines in Figs. 4 and 5.

transverse energy $E_\perp$ in charge state q_i, the mean energy loss in the target is

$$\overline{\Delta E}(E_\perp)=\overline{\sum_i q_i^2 S(E_\perp)L_i}=q_{av}^2 S(E_\perp)\times t. \tag{6}$$

We therefore define $q_{av}(q_{out})$ as

$$q_{av}^2(q_{out})=\left(\overline{\frac{1}{t}\sum_i L_i q_i^2}\right)_{q_{out}}. \tag{7}$$

$\overline{\Delta E}(q_{out})/q_{av}^2(q_{out})$ is the relevant parameter to relate the energy loss to $E_\perp$.

The $\overline{E_\perp}(q_{out})$ curve (Fig. 10) gives $\overline{E_\perp}(q_{out}=73)\simeq 9$ eV, whereas the map of the potential $U(\vec{r}_\perp)$ of Ref. [5] shows that ions are hyperchanneled for $U(\vec{r}_\perp)<2.2$ eV. The analysis of the distribution $h(E_\perp|q_{out}=73)$ shown in Fig. 8 demonstrates that this is the case only for 30% of the ions

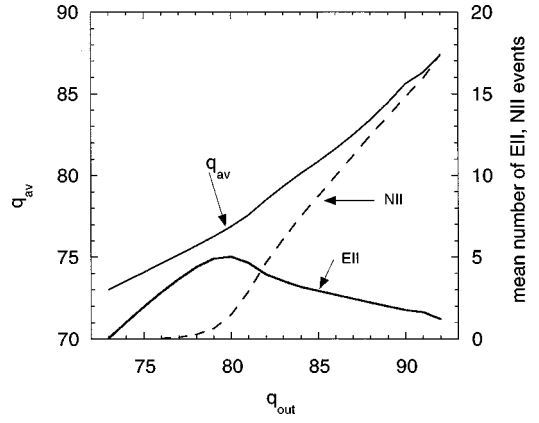

FIG. 11. Calculated mean charge state in the silicon crystal $q_{av}(q_{out})$ [as defined by Eq. (7)], mean number $N_{EII}(q_{out})$ of EII events per ion, and mean number $N_{NII}(q_{out})$ of NII events per ion, as a function of the exit charge state q_{out}. Calculations were carried out with the fitting parameters leading to the solid lines in Figs. 4 and 5.

emerging with $q_{out}=73$. The mean electron density $\overline{\rho_e}(q_{out}=73)$ sampled by $q_{out}=73$ ions is 2.8 electrons per atom (see Fig. 10).

EII events (see Fig. 11) dominate over NII events for $q_{out}\lesssim 81$, which confirms that our experiment allows a precise determination of the σ_3^{EII}(M shell) cross sections. However, due to the increasing role of NII, the sensitivity decreases rapidly for $q_{out}\gtrsim 82$. EII cross sections σ_2^{EII} for L shell electrons are not tested with precision and EII for K shell electrons (σ_1^{EII}) is not tested at all. The uncertainties in the NII cross sections are not the only source limiting the precision of the determination of σ_1^{EII} and σ_2^{EII} for high q_{out} (i.e., high $E_\perp$): $N_{NII}(q_{out})$ is very sensitive to the particle flux near the strings, which is not determined precisely enough in our simulations.

We now discuss our precision on the σ_3^{EII} cross sections determination and compare our results to other experimental results and theoretical predictions of the literature.

2. Precision on σ_3^{EII}

The precision on σ_3^{EII} relies on (i) the experimental uncertainties on $F_C(q_{out})$, (ii) the sensitivity of the fit to the σ_3^{EII} values, (iii) the various hypotheses introduced in the simulations to describe the particle flux, mainly the assumption on the beam angular divergence and the hypothesis of statistical equilibrium, and (iv) the precision on the knowledge of the electron density in the channel. When all parameters are fixed except the σ_3^{EII} value, the latter one can be varied by $\pm 10\%$ in order to remain within the error bars of $F_C(q_{out})$. The beam angular divergence is determined with precision when fitting the angular dependence of the various emergent charge states, particularly of the frozen charge state ($q_{out}=q_{in}=73$). Within the hypothesis of statistical equilibrium, the particle flux in the channels is mostly determined by the uniform distribution of the entrance impact parameter (the beam angular divergence and dechanneling effects introduce some modifications, which are taken into account in the simulations). We have seen above that the mean-free-path for the establishment of statistical equilibrium ($\sim 6\mu$m) is ~ 20 times smaller than t. The uncertainty on σ_3^{EII} introduced both by the small uncertainty on the incident beam angular divergence and by the hypothesis of statistical equilibrium is thus certainly small at the scale of 10%.

As for the mean electron density $\overline{\rho_e}(\vec{r}_\perp)$ in the transverse plane, we have compared predictions obtained by pseudopotential calculations [31] and values extracted by Scheringer [32] in order to fit the experimental x-ray form factors for silicon. The agreement between the two density maps is very good for $\vec{r}_\perp$ such that $U(\vec{r}_\perp)>10$ eV. However, discrepancies exist near the channel center, which never exceed 30%. When considering the available transverse space for frozen $73+$ ions, the overall discrepancy between the sampled electron density $\overline{\rho_e}(E_\perp;q_{out}=73)$ obtained from [31] and [32] does not exceed 15%. This is thus also the typical precision on σ_3^{EII} specifically related to the uncertainties on $\overline{\rho_e}(\vec{r}_\perp)$. In Sec. V B 2, we show that the agreement between the extrapolated stopping power at the channel center and theoretical estimates is better than 10%. This agreement is a good check of the theoretical predictions on energy loss, but it also

indicates that the $\overline{\rho_e}(\vec{r}_\perp)$ values that we introduced in our simulations are reliable, which comfort our confidence on the σ_3^{EII} determination. Finally, considering all sources of uncertainties, we conclude that the overall precision on the values of σ_3^{EII} that we determine is $\sim 25\%$.

3. Comparison with EII calculations

Very few theoretical calculations of σ_3^{EII} are available in our experimental situation. The kinetic energy E_e of the target electrons in the ion rest frame ($E_e = 164$ eV) is large compared to the mean M-shell binding energy of uranium ($B_M \simeq 10.3$ keV), a situation favorable for a perturbation treatment. However, the presence of many electrons and the very high nucleus charge introduce difficulties, which may lead to rather approximate results. A value can be extrapolated from Younger [33] (nonrelativistic distorted-wave Born exchange approximation, sodiumlike ions), giving $\sigma_{3Y}^{EII} = 45$ b per M-shell electron. This estimate is ~ 3 times smaller than the value σ_{3fit}^{EII} extracted from our measurements. We have also compared our results to the prediction for σ_{nKim}^{EII} of Kim and Rudd [34], which combines the binary encounter approximation with the dipole interaction of the Bethe theory [binary encounter dipole approximation (BED)]. Calculations based on this model were performed [35] using a relativistic Hartree-Fock Slater description of the uranium ion. The result is $\sigma_{3_{BED}}^{EII} = 76$ b per M-shell electron, i.e., ~ 1.9 times smaller than σ_{3fit}^{EII}. This is a fair agreement considering the degree of approximation of the BED model for very heavy ions with many electrons. Relativistic distorted-wave EII calculations have recently been published by Fontes *et al.* [36] for the ionization of K-shell H-like and He-like uranium ions, for an electron energy ($E_e = 198$ keV) close to ours. These calculations show that when the generalized Breit interaction is taken into account [distorted wave Breit approximation (DWB)], the cross section $\sigma_{1_{FBreit}}^{EII}$ calculated is ~ 1.5 times higher than predicted when only taking into account the Coulomb interaction beween bound and free electrons. $\sigma_{1_{FBreit}}^{EII}$ is found $\sim$ twice higher than the value σ_{1Y}^{EII} obtained from Younger [37]. Assuming that the ratio $\sigma_Y^{EII}/\sigma_{FBreit}^{EII}$ is also $\simeq 0.5$ for L or M shells, we would expect $\sigma_{3_{FBreit}}^{EII}$ to be ~ 1.5 times smaller than our measured value. Given the uncertainty of 25% in our measurement, this may appear as a reasonable agreement, even though the extrapolation may not be fully valid.

4. Comparison with other EII measurements

We have not found experimental information on σ_3^{EII} measurements for very heavy ions. The data available concern σ_1^{EII} and σ_{2s}^{EII}. For these cross sections, results were obtained for highly stripped uranium ions, with E_e rather close to ours. In electron beam ion trap (EBIT) experiments, Marrs *et al.* [38] find σ_{1s}^{EII} and σ_{2s}^{EII} in very good agreement with the values of $\sigma_{1sFBreit}^{EII}$ and $\sigma_{2sFBreit}^{EII}$ calculated by Fontes *et al* [36]. The EII cross sections for K and L-shell ionization of uranium ions with $E_e = 222$ keV have been measured by Claytor *et al.* [7] in a pioneer channeling experiment in silicon, using 405 MeV/u uranium ions with charge state $88 \leqslant q_{in} \leqslant 92$. The authors of Ref. [7] take benefit in the fact that channeled ions have charge exchange only through EII and REC. Assuming the REC cross section to be known, the analysis of $F_R(q_{out})$ and $F_C(q_{out})$ provides the fraction of channeled ions, the mean electron density $\overline{\rho_e}$ sampled by channeled ions and ultimately σ_1^{EII} and σ_{2s}^{EII}. The result for K-shell ionization is rather surprising: the authors find a value $\sigma_1^{EII} \sim 3$ times larger than predicted by Fontes *et al.* and ~ 6 times higher than predicted by Younger [37]. However, the agreement becomes fair for L-shell ionization, for which the experimental value is ~ 1.5 greater than predicted by Younger [33,37]. The surprisingly high values found for σ_1^{EII} in Ref. [7] may be due to the fact that for 90^+ and 91^+ incident ions, there is a strong overlap between $F_C(q_{out})$ and $F_R(q_{out})$ and thus that NII events may interfere when estimating σ_1^{EII}. The main difference between the experiment [7] and ours is related to the fact that in our case the incident ion charge is much farther from the equilibrium charge state reached in a random Si medium. We are thus able to discriminate between the available accessible areas experienced by ions emerging with different q_{out}. Consequently, in our case the mean electron density sensed is a function of q_{out} [for example, $\overline{\rho_e}(q_{out}=74) = 3.1$ electron per atom and $\overline{\rho_e}(q_{out}=80) = 5.6$ electron per atom, see Fig. 10]. Moreover, the σ_{3fit}^{EII} value we obtain must be consistent not only with the measured broad distribution $F_C(q_{out})$ but also with the energy loss spectra for each q_{out}. On the contrary, in Ref. [7] a single mean electron density is considered, corresponding to an average over all channeled ions, whatever q_{out} is. As the beam angular divergence was not small at the scale of $\Psi_{1/2}$ and as moreover some crystal bending effects were observed, the mean electron density was rather high, $\overline{\rho_e} = 6.2$ electrons per atom.

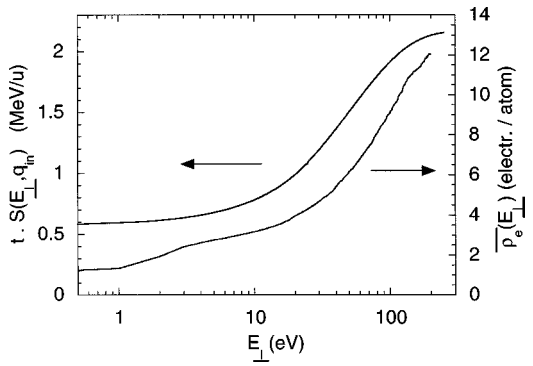

FIG. 12. Calculated curve for the mean energy loss $S(E_\perp, q_{in})t$ as a function of $E_\perp$ (in eV, for a unit charge), for an ion of charge state q_{in} in $\langle 110 \rangle$ alignment. The mean electron density $\overline{\rho_e}(E_\perp)$ sampled by ions of given transverse energy $E_\perp$ is also shown.

B. Energy loss

1. Fitting the experimental results

If one keeps constant all the adjustable parameters used to fit the experimental results for charge states, the energy loss results can be fitted using various $S(E_\perp)$ trial curves. A good overall agreement between experiment and calculation is obtained with the the mean energy loss curve $tS(E_\perp, q_{in})$ of Fig. 12. In this figure we show also the mean electronic

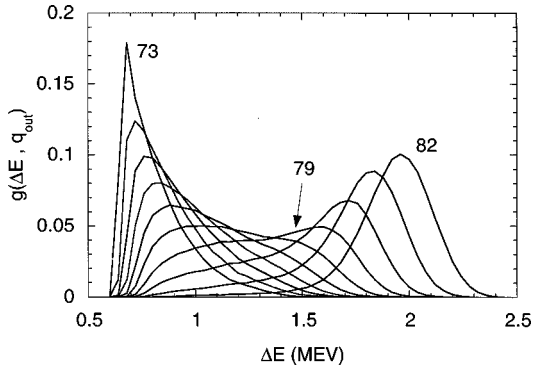

FIG. 13. Energy-loss spectra $g(\Delta E|q_{out})$ obtained by Monte Carlo simulations for $73 \leqslant q_{out} \leqslant 82$.

density $\overline{\rho_e}(E_\perp)$ sampled by ions of transverse energy $E_\perp$. Energy loss spectra $g(\Delta E|q_{out})$ were calculated using the $tS(E_\perp, q_{in})$ curve of Fig. 12 and the $E_\perp$ distribution experienced in the crystal by ions emerging with q_{out}. These calculated spectra are shown in Fig. 13 for $73 \leqslant q_{out} \leqslant 82$, i.e., in a transverse energy domain ($E_\perp \lesssim 70$ eV) for which the calculation is expected to give reliable results. These curves are, in most cases, asymmetrical and change rapidly in mean value and width from one charge state to the next. A broad $g(\Delta E|q_{out})$ curve corresponds to a broad transverse energy distribution $h(E_\perp|q_{out})$ and to a large slope of the $S(E_\perp)$ curve in the $E_\perp$ region covered by this distribution.

The mean values $\overline{\Delta E}(q_{out})$ of the calculated $g(\Delta E|q_{out})$ curves (the mean energy losses) are compared to the measurements in Fig. 5 (solid line). The calculated FWHM $L_{1/2}$ values of the $h(E_\perp|q_{out})$ curves are compared to the measured values in Fig. 6. The agreement is satisfactory for $q_{out} < 79$. On the contrary, for high q_{out}, the calculated values of $L_{1/2}$ (not shown) are much smaller than the measured ones. This is also the case for the calculated values of $L_{1/2}$ associated with random energy loss. One obtains $(L_{1/2}^{rand})_{calc} = 0.129$ MeV/u, a value nearly independent of q_{out} and slightly dominated by the charge state fluctuations. This Monte Carlo FWHM is calculated with a reasonable precision but is however ~ 10 times smaller than the experimental value $(L_{1/2}^{rand})_{exp} = 1.3$ MeV/u. Such a result is rather intriguing even if the concept of random orientation in a single crystal is rather questionable.

The asymmetry figure $\mu^{1/3} = (\mu_3)^{1/3}/\sigma$ is presented in Fig. 7. We did not measure reliable absolute values of μ. Nevertheless, the simulations reproduce the qualitative behavior of μ, i.e., a sudden change in the sign of μ between $q_{out} = 78$ and $q_{out} = 79$, with slower variations on either side. The $78 \leqslant q_{out} \leqslant 79$ region corresponds to the broadest calculated $g(\Delta E|q_{out})$; $L_{1/2}$ is of the order of 70% of the mean energy loss [broad $h(E_\perp|q_{out})$ and large slope for $S(E_\perp)$].

The most reliable information that we obtain on stopping is the mean energy loss, particularly for ions with very small $E_\perp$. The measured value $\overline{\Delta E}(q_{out} = 73) \simeq 0.76$ MeV/u together with the slope of the fitting curve $S(E_\perp)$ determined from low q_{out} mean losses ($tdS/dE_\perp \simeq 20$ keV/u per eV) give the extrapolated value $tS(E_\perp = 0) \simeq 0.57$ MeV/u. At low $E_\perp$ (see Fig. 12), the variation of $S(E_\perp)$ with $E_\perp$ is slower than the variation of the mean sampled electronic density, but however the $S(E_\perp)$ variation is faster than for 27 MeV/u Xe ions (see Ref. [5]). Interpreting this difference is not easy: it depends on the relative contributions of small and large impact parameters to energy loss due to valence and core target electrons. The results of energy loss for well-channeled uranium ions are analyzed in some detail in Sec. V B 2.

2. Theoretical survey. Comparison to experimental results

In this section, our aim is to estimate the theoretical energy loss $\overline{\Delta E}(E_\perp = 0)$ at the center of the channel and to compare it to the experimental extrapolated value.

The case of 300-MeV/u U^{73+} ions is rather complex for the following reasons: (i) the velocity is relativistic ($\beta = 0.654$). (ii) The Bohr parameter κ is larger than 1 ($\kappa = 2$ for bare uranium), which is not usually the case for high velocities. (iii) The ion velocity is much larger than orbital velocities of the target electrons, which would usually imply a perturbation treatment.

(a) Mean energy loss to valence electrons. Let us first consider the mean energy loss $\overline{\Delta E}_{val}^{max}$ for a uniform flux of point charge particles (i.e., a random beam). For relativistic ions with $\kappa > 1$, $\overline{\Delta E}_{val}^{max}$ may be expressed as

$$\overline{\Delta E}_{val}^{max} = t \frac{4\pi q^2 e^4}{m_e v^2} \overline{\rho}_{val} [L_B^{val} + \ln(\gamma^2) - \beta^2 + \Delta_{LS}(\gamma)], \tag{8}$$

where $\overline{\rho}_{val}$ is the mean valence electron density (4 electrons per silicon atom). L_B^{val} is a logarithmic term which may be expressed as

$$L_B^{val} \simeq \ln\left(\frac{p_{\max}}{p_{\min}}\right) = \ln\left(\frac{1.123 v/\omega}{b/2}\right) = \ln\left(\frac{1.123}{\kappa} \frac{2 m_e v^2}{\hbar \omega}\right). \tag{9}$$

In Eq. (9), p_{max} and p_{min} are effective integration limits over the impact parameter p. The higher limit, $p_{\max} = 1.123 v/\omega$ is an adiabatic cutoff [6]. A simple estimate of ω is given by the plasma frequency $\omega_p = (4\pi \overline{\rho}_{val} e^2/m_e)^{1/2}$ which gives $\hbar\omega_p = 16.6$ eV. For 300 MeV/u U ions, one finds $p_{\max} = 8.73$ nm, i.e., a very large value on the atomic scale. The effective lower limit $p_{min} = b/2$ is given by the collision diameter:

$$b = \frac{2qe^2}{m_e v^2}. \tag{10}$$

The second and third term in the bracket of Eq. (8) represent the usual relativistic correction of the first-order quantum perturbation theory.

$\Delta L_{LS}(\gamma)$ is a correction term representing the deviation to the perturbation theory, which has been recently calculated by Lindhard and Sørensen [29] (see Fig. 1 of this reference). The predicted value $\Delta L_{LS}(\gamma)$ has been confirmed experimentally by Datz *et al.* [39] for ultrarelativistic Pb ions. In our case, ΔL_{LS} represents $+3\%$ of the overall bracket term in Eq. (8). Then, with $q = 73$, Eq. (8) gives $\overline{\Delta E}_{val}^{max} = 155.5$ MeV $= A \times 0.654$ MeV/u. This value, calculated

with $\overline{\rho}_{val}=4$ electrons/atom, is an upper limit for the energy loss to the target valence electrons of channeled U^{73+} (it corresponds to the random case).

(b) Mean energy loss at $E_\perp=0$: contribution of valence and core electrons. A precise determination of the mean energy loss $\overline{\Delta E}_{val}$ for a channeled beam may be reached by an impact parameter approach (which is possible for $\kappa>1$) and by integration in the channel using local electronic densities $\overline{\rho_e}(\vec{r}_\perp)$ (here, averaging on ρ_e is performed along the $\langle 110\rangle$ direction only). For symmetry reasons (cylindrical geometry may be used), this type of calculation is tractable for ion trajectories just in the middle of the channel. This approach, leading to a calculated value based on the variations of ρ_{val} with the distance from the channel center, was already used in [5] and is presented in detail in Ref. [3]. Using Eq. (23) of [3], one finds

$$\overline{\Delta E}_{val}(q_{out}=73,E_\perp=0)=0.415 \text{ MeV/u}. \tag{11}$$

This value is 37% smaller than $\overline{\Delta E}_{val}^{max}$ and is to be compared with the overall mean energy loss 0.57 MeV/u extrapolated with the help of simulations from the experimental result.

This comparison indicates that, as pointed out in [3], and in contrast to the case of MeV light ions, the contribution of Si core electrons to the energy loss of very well-channeled swift heavy ions is not negligible. Whereas the adiabatic cutoff for *K*-shell Si electrons is small ($p_{ad}^K=0.40$ Å, using $\hbar\omega_K=3.2$ keV) as compared to the distance p_{str} between the channel center and the neighboring strings (of the order of 2 Å), this is not the case for *L* electrons: $p_{ad}^L=4.16$ Å , using $\hbar\omega_L=0.31$ keV. The adiabaticity parameter for ions at the channel center in their interaction with *L* target electrons is $\xi=p_{str}/p_{ad}^L\simeq 0.5$. Using Eqs. (19) and (20) of Ref. [3], one finds, using a similar notation, $R(\xi)=0.9$, $\overline{\Delta E^L}_{free}=0.17$ MeV/u, i.e., a mean energy loss to *L* electrons $\overline{\Delta E^L}=R(\xi)\overline{\Delta E^L}_{free}=0.15$ MeV/u, which represents 36% of the mean energy loss to valence electrons. The theoretical mean energy loss for U^{73+} ions channeled with zero transverse energy is then

$$\overline{\Delta E}(q_{out}=73,E_\perp=0)=\overline{\Delta E^L}+\overline{\Delta E}_{val}=0.565 \text{ MeV/u}. \tag{12}$$

This theoretical result is in excellent agreement with the experimental extrapolated result, 0.57 MeV/u at $E_\perp=0$. Such a good agreement is somewhat surprising when considering both the experimental uncertainties and the theoretical approximations. In particular, the above calculations assume the ion to be a point charge (perfect screening), which is not such a good approximation in the case of U^{73+} ions. The spatial extension of *M*-shell orbitals of uranium is of the order of $r_M=0.07$ Å . Using simple electrostatics and the shell electron density, one can estimate the effective charge q_{eff} seen by a target electron in an electron-U^{73+} interaction with an impact parameter *p*: qualitatively, $q_{eff}(p>r_M)=73$ and $q_{eff}(p<r_M)>73$. The influence of the variations of q_{eff} on mean energy loss was crudely calculated classically, by integration over impact parameters ($p_{min}<p<p_{max}$), which leads to an increase of 5% of the loss, i.e., $\overline{\Delta E}(q_{out}=73,E_\perp=0)=0.595$ MeV/u. Even with this correction, the agreement with the experimental result is still fair (4% discrepancy, of the order of the precision of the measurements). Hence, the semiclassical approach presented above is appropriate to describe energy loss processes for hyperchanneled 300-MeV/u U^{73+} ions.

Finally, it is interesting to note that one may associate with Eq. (11) an effective valence density $\rho_{eff}^{val}=4\overline{\Delta E}_{val}/\overline{\Delta E}_{val}^{\max}=2.54$ electron per atom. This value is much larger than the mean electronic density at the center of the channel (one electron per atom), which shows that the contribution of distant collisions is very important. When considering the $\rho_e^{val}(\vec{r}_\perp)$ and $U(\vec{r}_\perp)$ maps [5], one may anticipate that for $E_\perp\gtrsim 10$ eV the loss to valence electrons is independent of $E_\perp$ (and equal to $\overline{\Delta E}_{val}^{\max}$) and thus that the slope of $S(E_\perp)$ Fig. (12), which is determined with precision in this experiment, is entirely due to the contribution of core electrons.

3. Random energy loss

For random orientation, one may calculate the mean energy loss using a similar semiclassical approach (Eq. 8). The electron density is now $\overline{\rho}_e=Z_{Si}=14$ electrons per atom and the frequency ω in Eq. (9) is now an averaged value ($\hbar\omega=174$ eV) with weighting factors given by the dipole oscillator strengths of Ref. [40]. We obtain $\overline{\Delta E}_{R_{th}}(q=90)=2.605$ MeV/u. For comparison, the tabulation of Ziegler [41] gives $\overline{\Delta E}_R=2.87$ MeV/u. The experimentally determined values $\overline{\Delta E}_{R_{\exp}}(q_{out}=89)=2.5$ MeV/u and $\overline{\Delta E}_{R_{\exp}}(q_{out}=90)=2.65$ MeV/u are not to be compared directly to the above prediction, obtained for $q=90$. For the incident $q_{in}=73$ beam and the thickness $t=120$ μm, the mean charge state q_{av} throughout the target [see Eq. (7)] is somewhat smaller than q_{out}. Using the Monte Carlo random code, we calculated q_{av} as a function of q_{out} and obtained $q_{av}(q_{out}=89)=87.05$ and $q_{av}(q_{out}=90)=87.85$. Using these values, the theoretical mean energy losses are now $\overline{\Delta E}_{R_{th}}(q_{out}=89)=2.43$ MeV/u and $\overline{\Delta E}_{R_{th}}(q_{out}=90)=2.48$ MeV/u, which are smaller, but close to the experimental results. However, even in the measurements performed in the ''random'' orientation, channeling effects clearly appear as demonstrated by the very large width of the energy loss spectra. These effects may seriously affect the experimental mean energy loss value. It is hence hardly possible to confirm the general trend observed in Ref. [42] for relativistic very heavy ions, with $\kappa<1$, i.e., a stopping value $\sim$ 10% higher than given by the Born approximation.

Assuming a q^2 law, the random energy loss for $q=73$ would be $2.65\times(73/87.85)^2=1.83$ MeV/u. The mean energy loss $\overline{\Delta E}_c(73)$ for channeled $q=73$ ions, normalized to the random energy loss is then $\overline{\Delta E}_c(73)/\overline{\Delta E}_R(73)=0.76/1.83=0.41$. This ratio may appear rather high if directly compared to the mean encountered electronic density $\overline{\rho}_e(q=73)=2.8$ electron per atom normalized to the overall electronic density, i.e., $2.8/Z_2=0.2$. It illustrates again the large contribution of distant collisions.

VI. SUMMARY AND CONCLUSIONS

We have performed a channeling experiment with 300-MeV/u U^{73+} ions on a silicon single crystal. The angu-

lar divergence of the beam in the fragment separator FRS at GSI (Darmstadt), which was checked in our Monte Carlo simulations, was small as compared to the channeling critical angle.

The incoming charge state ($q_{in}=73$) of the beam was chosen to be much lower than the equilibrium charge state in silicon in order to discriminate among particles of various transverse energies by selecting emergent charge states. In particular, the ions transmitted in a frozen charge state ($q_{out}=q_{in}$) have travelled through the crystal with small transverse energies (1/15 of the critical transverse energy). The measurement of the energy loss of these ions was used to study the contribution of the various electron shells of silicon. The experimental results are consistent with the semiclassical model of Bohr, which predicts a large contribution (25%) of energy loss to silicon *L*-shell electrons, for ions with zero transverse energy. The main features of the variations of the width and asymmetry of the energy loss spectra are well reproduced by Monte Carlo simulations for well-channeled ions. In particular, the energy loss spectra for ions with $q=78$ and 79 are very broad (FWHM values of the order of 70% of the mean energy loss) and have opposite asymmetries.

The good agreement between measured and predicted energy losses for well-channeled ions provides a strong indication that the mean electron densities $\overline{\rho_e}(E_\perp)$ used in the Monte Carlo code are reliable with a precision better than 10%. These densities enter directly in the extraction of the EII cross sections from the experimental results. We have thus been able to obtain reliable quantitative information on the dominant charge exchange process for well-channeled ions. The simulations show that our experiment tests mainly and precisely the *M*-shell ionization of the uranium ions. Fitting the measured experimental emergent charge state distribution gives σ_3^{EII} cross sections that are twice larger than the values calculated using the binary encounter dipole model. Recent calculations of σ_1^{EII} using the relativistic distorted wave approximation with Breit corrections provide very good agreement with precise experimental EII cross section measured by EBIT for uranium, using electrons with energy E_e close to ours. It would be interesting to compare our results with an extension of such calculations to the *M*-shell of heavy ions with many electrons.

ACKNOWLEDGMENTS

The authors are very grateful to P. Indelicato, C. de Billy, A. Salin, C. Stefan, R. Gayet, and J.P. Rozet for their calculations of ionization, excitation, and capture cross sections, and for fruitful discussions. We thank the GSI facility operating staff, and K.H. Behr, A. Brünle, and K. Burkhard for technical assistance. This work was partially supported by the IN_2P_3-GSI collaboration agreement and the CNRS under GDR 86. We also acknowledge NATO support through Collaboration Grant No. CRG 901025.

[1] B.R. Appleton, C. Erginsoy, and W.M. Gibson, Phys. Rev. **161**, 330 (1967).
[2] S. Andriamonje, M. Chevallier, C. Cohen, N. Cue, D. Dauvergne, J. Dural, F. Fujimoto, R. Kirsch, A. L'Hoir, J.-C. Poizat, Y. Quéré, J. Remillieux, C. Röhl, H. Rothard, J.P. Rozet, D. Schmaus, M. Toulemonde, and D. Vernhet, Phys. Rev. A **54**, 1404 (1996) .
[3] J.U. Andersen, J. Chevallier, G.C. Ball, W.G. Davies, J.S. Forster, J.S. Geiger, J.A. Davies, H. Geissel, and E.P. Kanter, Phys. Rev. A **54**, 624 (1996).
[4] B.R. Appleton, R.H. Ritchie, J.A. Biggersaff, T.S. Noggle, S. Datz, C.D. Moak, H. Verbeek, and V.N. Neelavathi, Phys. Rev. B **19**, 4347 (1979).
[5] A. L'Hoir, S. Andriamonje, R. Anne, N.V. De Castro Faria, M. Chevallier, C. Cohen, J. Dural, M.J. Gaillard, R. Genre, M. Hage-Ali, R. Kirsch, B. Farizon-Mazuy, J. Mory, J. Moulin, J.C. Poizat, Y. Quéré, J. Remillieux, D. Schmaus, and M. Toulemonde, Nucl. Instrum. Methods Phys. Res. B **48**, 45 (1990).
[6] N. Bohr, K. Dan. Vidensk. Selsk. Mat. Fys. Medd. **27**, No. 15 (1948).
[7] N. Claytor, B. Feinberg, H. Gould, C.E. Bemis, J. Gomez del Campo, C.A. Ludemann, and C.R. Vane, Phys. Rev. Lett. **61**, 2081 (1988).
[8] H.F. Krause and S. Datz, in *Advances in Atomic, Molecular, and Optical Physics*, edited by B. Bederson and H. Walther (Academic, New York, 1996), Vol. 37, p. 139.
[9] H. Geissel *et al.*, Nucl. Instrum. Methods Phys. Res. B **70**, 279 (1992).
[10] J. Lindhard, Mat. Fys. Medd. K. Dan. Vidensk. Selsk. **34**, No. 14 (1965).
[11] J.H. Barrett, Phys. Rev. B **3**, 1527 (1971).
[12] D. Schmaus, F. Abel, M. Bruneaux, C. Cohen, A. L'Hoir, G. Della Mea, A.V. Drigo, S. Lo Russo, and G.G. Bentini, Phys. Rev. B **19**, 5581 (1979).
[13] A. Doyle and I. Turner, Acta Crystallogr., Sect. A: Cryst. Phys., Diffr., Theor. Gen. Crystallogr. **24**, 390 (1968).
[14] *Channeling, Theory, Observation, and Applications*, edited by D.V. Morgan (Wiley, New York, 1973), p. 100.
[15] J.U. Andersen, B. Bech Nielsen, A. Uguzzoni, E. Fuschini, E.F. Kennedy, and V.A. Ryabov, Nucl. Instrum. Methods Phys. Res. B **90**, 166 (1994).
[16] E. Bonderup, H. Esbensen, J.U. Andersen, and H.E. Schiott, Radiat. Eff. **12**, 261 (1972).
[17] H.E. Schiott, E. Bonderup, J.U. Andersen, and H. Esbensen, in *Atomic Collisions in Solids*, edited by S. Datz, B.R. Appleton, and C.D. Moak (Plenum Press, New York, 1975), Vol. 2, p. 843.
[18] J.P. Rozet, C. Stephan, and D. Vernhet, Nucl. Instrum. Methods Phys. Res. B **107**, 67 (1996).
[19] H.A. Bethe and E.E. Salpeter, *Quantum Mechanics of One and Two-Electron Atoms* (Academic Press, New York, 1957).
[20] Dz. Belkic, R. Gayet, and A. Salin, Comput. Phys. Commun. **32**, 385 (1984).
[21] R. Gayet (private communication).
[22] J.P. Rozet (private communication).
[23] J. Eichler, Phys. Rev. A **31**, 3505 (1985).

[24] W.E. Meyerhof, R. Anholt, J. Eichler, H. Gould, Ch. Munger, J. Alonso, P. Thieberger, and H.E. Wegner, Phys. Rev. A **32**, 3291 (1985).
[25] A. Salin (private communication).
[26] S. Andriamonje, M. Chevallier, C. Cohen, N. Cue, D. Dauvergne, J. Dural, F. Fujimoto, R. Kirsch, A. L'Hoir, J.C. Poizat, Y. Quéré, J. Remillieux, C. Röhl, H. Rothard, J.P. Rozet, D. Schmaus, M. Toulemonde, and D. Vernhet, Nucl. Instrum. Methods Phys. Res. B **107**, 3291 (1996).
[27] K. Omidvar, At. Data Nucl. Data Tables **28**, 1 (1983).
[28] M.O. Krause, J. Phys. Chem. Ref. Data **8**, 307 (1979).
[29] J. Lindhard and A.H. Sørensen, Phys. Rev. A **53**, 2443 (1996).
[30] C. Scheidenberger, H. Geissel, H.H. Mikkelsen, F. Nickel, S. Czajkowski, H. Folger, H. Irnich, G. Münzenberg, W. Schwab, T. Stöhlker, T. Suzuki, and B. Voss, Phys. Rev. Lett. **77**, 3987 (1996).
[31] J.R. Chelikowsky and M.L. Cohen, Phys. Rev. B **14**, 556 (1976).
[32] C. Scheringer, Acta Crystallogr., Sect. A: Found. Crystallogr. **36**, 205 (1980).
[33] S.M. Younger, Phys. Rev. A **24**, 1272 (1981).
[34] Y.-K. Kim and M.E. Rudd, Phys. Rev. A **50**, 3954 (1994).
[35] P. Indelicato (private communication).
[36] C.J. Fontes, D.H. Sampson, and H.L. Zhang, Phys. Rev. A **51**, R12 (1995).
[37] S.M. Younger, Phys. Rev. A **22**, 111 (1980); **22**, 1425 (1980).
[38] R.E. Marrs, S.R. Elliot, and D.A. Knapp, Phys. Rev. Lett. **26**, 4082 (1994).
[39] S. Datz, H.F. Krause, C.R. Vane, H. Knudsen, P. Grafström, and R.H. Schuch, Phys. Rev. Lett. **77**, 2925 (1996).
[40] J.L. Dehmer, M. Inokuti, and R.P. Saxon, Phys. Rev. A **12**, 102 (1975).
[41] J.F. Ziegler, *Handbook of Stopping Cross-Sections for Energetic Ions in All Elements* (Pergamon Press, New York, 1980).
[42] C. Scheidenberger, H. Geissel, H.H. Mikkelsen, F. Nickel, T. Brohm, H. Folger, H. Irnich, A. Magel, M.F. Mohar, G. Münzenberg, M. Pfützner, E. Roeckl, I. Schall, D. Schardt, K.-H. Schmidt, W. Schwab, M. Steiner, T. Stöhlker, K. Sümmerer, D.J. Viera, B. Voss, and M. Weber, Phys. Rev. Lett. **73**, 50 (1994).
[43] J.H. Scofield, Phys. Rev. A **18**, 963 (1978).

1-4 Dépendance en paramètre d'impact de la Capture Mécanique

Captures mécanique et radiative sont deux processus qui entrent en compétition dans les collisions ion-matière. La figure ci-dessous, extraite de la référence [Stoehlker 98], montre qu'aux énergies non-relativistes, la capture mécanique est le processus dominant pour des ions uranium nus en collision avec des atomes d'azote. Aux énergies ultra-relativistes, c'est un troisième processus, la capture par création de paire, qui est dominant [Belkacem 97]. Pour des ions non-complètement épluchés, la capture résonante RTE contribue à certaines énergies, avec une amplitude comparable à celle de la capture radiative.
Le GSI permet, après accélération, épluchage, stockage et ralentissement dans l'anneau ESR, d'extraire des ions hydrogénoïdes de basse énergie, tels que le paramètre d'adiabaticité η, égal au rapport des vitesses du projectile à celle d'un électron sur sa couche n, soit très inférieur à l'unité pour n=1,2. On peut donc étudier la capture électronique dans des conditions très loin de l'équilibre de charge. Les sections efficaces de MEC sont alors colossales (supérieures au Mbarn), et, pour pouvoir étudier ce processus en condition de collision unique, des cibles ultra-minces sont nécessaires.

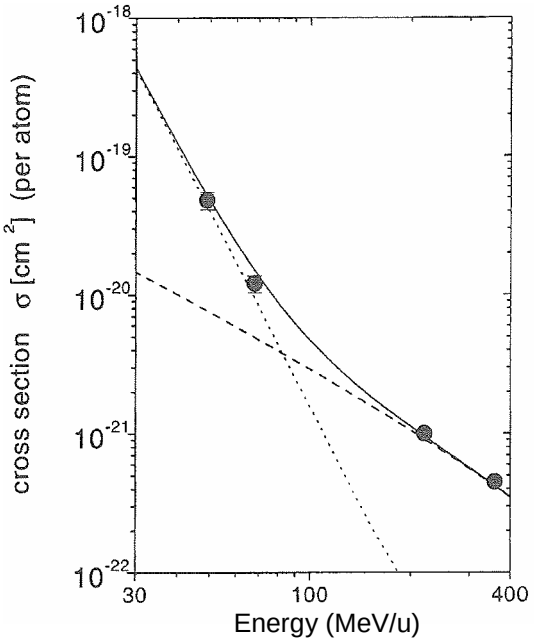

***Figure 4** : sections efficaces de capture électronique par des ions U^{92+} lors de collisions avec des atomes N en fonction de l'énergie des ions uranium. La ligne en pointillés représente la MEC, et la ligne en tirets la REC. D'après [Stöhlker 98].*

Des études menées avec des cibles de carbone minces et un faisceau de plomb de 50 MeV/u environ, auxquelles nous avons participé au GSI, ont montré l'influence que peuvent avoir les impuretés déposées en surface : des taux de capture multiple ont été mesurés [Bräuning 01], incompatibles avec une distribution d'événements de capture indépendants. Cependant, des mesures ultérieures ont permis de montrer que l'état de surface des cibles utilisées était largement responsable de ces taux de capture multiple anormaux (présence d'impuretés). Nous reviendrons toutefois sur ce point plus loin.
La canalisation d'ions dans un cristal permet d'avoir une approche originale de l'étude de la MEC dans ce régime. En effet, la distribution en énergie transverse d'un faisceau canalisé, et

donc la distribution en paramètre d'impact aux atomes cibles, peuvent être contrôlés et identifiés, ce qui permet d'étaler, même avec des cristaux très épais de plusieurs microns, le régime de capture mécanique depuis des conditions de collision unique (pour les ions bien canalisés qui voyagent loin des atomes) jusqu'au régime où l'équilibre de charge peut être atteint.
Ce fut en grande partie l'objet de nos études en cave A au GSI lors des dix dernières années. Une première expérience réalisée en 1995 avec des ions Au^{79+} de 53 MeV/u a permis de caractériser le faisceau extrait de l'ESR ([Prinz 97], [Andriamonje 97]), et de motiver nos demandes pour obtenir des faisceaux davantage ralentis.
Les articles suivants ont été rédigés à partir des résultats de la seconde expérience réalisée en 2001, avec des ions U^{91+} de 20 MeV/u. Le premier article, "Impact parameter dependent electron capture by decelerated U91+ ions at 20 MeV/u using crystal channeling conditions" [Dauvergne 03], correspond à une présentation de ces résultats encore préliminaires lors de la conférence HCI 2002.
L'analyse minutieuse de cette expérience et les simulations associées ont été menées par Etienne Testa dans notre groupe, depuis son stage de DEA jusqu'à sa thèse à l'automne 2005. Grâce aux corrélations entre l'état de charge des ions transmis, les multiplicités d'électrons collectés à la surface du cristal, et les taux de raies X caractéristiques des différents types de capture (mécanique ou radiative), nous avons pu obtenir une information très détaillée sur les probabilités de capture en fonction du paramètre d'impact.

Available online at www.sciencedirect.com
SCIENCE DIRECT®
ELSEVIER
Nuclear Instruments and Methods in Physics Research B 205 (2003) 773–778
NIM B
Beam Interactions with Materials & Atoms
www.elsevier.com/locate/nimb

Impact parameter dependent electron capture by decelerated U^{91+} ions at 20 MeV/u using crystal channeling conditions

D. Dauvergne [a,*], A. Bräuning-Demian [b], F. Bosch [b], H. Bräuning [c], M. Chevallier [a], C. Cohen [d], A. Gumberidze [b], A. L'Hoir [d], R. Kirsch [a], C. Kozhuharov [b], D. Liesen [b], P.H. Mokler [b], J.C. Poizat [a], C. Ray [a], Th. Stöhlker [b], M. Tarisien [b], E. Testa [a], S. Toleikis [b], M. Toulemonde [e]

[a] *IPNL,CNRS/IN2P2, Université Lyon I, 4 rue E. Fermi, 69622 Villeurbanne cedex, France*
[b] *GSI, Planckstrasse 1, D-64291 Darmstadt, Germany*
[c] *Institut für Kernphysik, University of Giessen, Leihgesterner Weg 217, 35392 Giessen, Germany*
[d] *GPS, Universités Paris VI–Paris VII, 2 place Jussieu, 75251 Paris cedex 05, France*
[e] *CIRIL, CEA/CNRS rue Claude Bloch, BP5133, 14040 Caen cedex, France*

Abstract

We present results of an experiment using decelerated U^{91+} ions, extracted from the GSI-ESR storage ring, and transmitted through a thin silicon crystal in channeling conditions. Charge state at emergence, secondary electron multiplicity and X-rays are measured simultaneously. These conditions allow to study the competition between mechanical electron capture (MEC) and radiative electron capture (REC) as a function of impact parameter. We observe that REC is the dominant charge exchange process for the best channeled ions, i.e. those travelling always far from the silicon target core electrons. For ions with high transverse energy, MEC into highly excited states is counterbalanced by enhanced ionization arising from a succession of close collisions along atomic rows.

PACS: 61.85.+p; 34.70.+e
Keywords: Highly charged ions; Channeling; Charge exchange; Radiative electron capture; Mechanical electron capture

Fast heavy ions travelling inside matter undergo charge exchange during collisions with target atoms. The cross-sections for projectile ionization and electron capture depend on the projectile velocity and charge, and on the target properties. Starting from any particular charge state at incidence, charge state equilibrium in matter is reached when, for a given projectile – target system, electron loss and capture probabilities are equal in the average. At equilibrium, the occupancy of a given electronic shell n of an ion depends on the adiabaticity parameter $\eta_n = (m_e E_{ion}/M_{ion} E_n)^{1/2}$, where m_e and M_{ion} are the

* Corresponding author. Tel.: +33-4-7244-6257; fax: +33-4-7243-1243.
E-mail address: d.dauvergne@ipnl.in2p3.fr (D. Dauvergne).

0168-583X/03/$ - see front matter
doi:10.1016/S0168-583X(03)00541-X

electron and ion masses, respectively, E_{ion} the ion kinetic energy and E_n the electron binding energy in the n-shell. For non-relativistic projectiles η_n is simply the ratio of the ion velocity to that of the electron in the bound orbital. Very roughly, if $\eta_n \gg 1$ or $\eta_n \ll 1$, the n-shell is respectively empty or filled. If $\eta_n \approx 1$, it may be partly populated (depending on the nature of the target).

Fully stripped (or H-like) ions can now be produced with $\eta_K \ll 1$, but at still relatively high velocities ($v \gg v_0$, where v_0 is the Bohr velocity), using the acceleration–stripping–storage–deceleration technique developed at the GSI-ESR storage ring [1]. Such ions are far from their charge equilibrium in matter, and electron capture probabilities are much larger than ionization ones. In this velocity regime, several processes contribute to electron capture [2]. The mechanical electron capture (MEC) is a three-body process, in which energy and momentum are conserved by means of the target atom recoil. At high velocities, MEC cross-sections depend strongly on the projectile – target system: $\sigma_{MEC} \propto Z_p^5 Z_t^5 v_{ion}^{-11}$. For lower velocities, this dependence becomes weaker because cross-sections saturate. Radiative electron capture (REC) is the time – reversed process of photoionisation. The emitted photon carries out the energy excess resulting from the electron capture, and allows the momentum conservation. The radiative capture of an initially bound electron results in a shift and a broadening of the photon energy distribution as compared to the capture of a free electron at rest. Actually the shape of REC photon peaks reveals the initial longitudinal momentum distribution of the captured target electron (Compton profile). Also, at some given energies, the capture process called resonant transfer and excitation takes place [3], and, at highly relativistic energies, electron capture can occur by means of electron – positron pair production, the electron being created directly into a bound state [4]. This last process is predicted to be the dominant one at ultra-relativistic energies.

For the present experimental case with U^{91+} ions at 20 MeV/u ($\eta_K \approx 0.085$, $\eta_L \approx 0.35$, $\eta_M \approx 0.8$), and a silicon target ($Z_t = 14$), electron capture can occur through MEC and REC, and MEC is by far the dominant process during collisions with silicon atoms. This is illustrated in Fig. 1, where partial cross-sections for the MEC and REC processes are represented as a function of the final n-shell. MEC cross-sections correspond to CDW calculations [5] and the REC ones are calculated within the dipole approximation [6]. REC cross-sections being more than two orders of magnitude smaller than MEC ones, REC has no influence on the total capture probability during ion–atom collisions for such a system.

However, MEC probabilities are peaked at relatively small impact parameters because, first, the target atom recoil is needed for energy and momentum conservation during the charge exchange process, and, second, the overlap between initial and final wave functions of the transferred electron is required both in spatial and momentum spaces. In the present case, MEC cross-sections are maximum for $n_f = 5$–6 (i.e. η_{nf} values close to 1). For $n_f = 6$ orbitals of uranium, a scaling, based on the Bohr hydrogenic model, provides a mean radius of about 0.15 Å. In this situation, CDW calculations [5] show that MEC results mainly from the capture of target K-electrons (85%) and L-electrons (15%, the mean radius of an L-orbital in silicon being about 0.15 Å). In the case of an isolated silicon target atom, the capture from the M-shell of silicon is only about 0.5% of the total MEC cross-section. On the other side, to the first order, all target electrons contribute with the same weight

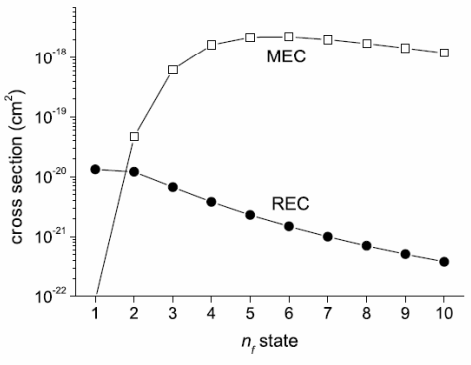

Fig. 1. Calculated values of MEC [5] and REC [6] partial cross-sections for 20 MeV/u U^{91+} ions incident on a silicon atom, as a function of the final n_f-state (see text for details).

to the REC, and radiative capture occurs preferentially into low n, l values of the final state. Thus, for increasing impact parameters, above 0.2–0.3 Å, REC probabilities may become of the same order as, and even larger than MEC ones.

Crystal channeling allows such a redistribution of impact parameters. Channeled positive ions are repelled by the continuum potential of atomic strings and planes. At the entrance of the crystal, they are given a transverse energy that depends on their position and angle relative to the crystallographic axis or plane, and they remain confined inside an accessible transverse space that defines the range of impact parameters: smaller impact parameters are allowed for larger transverse energies ($E_\perp$). Well channeled ions experience mainly quasi-free electrons of the valence or conduction gas, compared to unchanneled ions that interact with all the target electrons. The reduction of the sampled electron density is reflected by the reduction of energy loss and electron emission from the target surfaces, and also by the reduction of charge exchange probabilities: both MEC, REC and ionization are reduced, but in different ways. Thus, using incident ions far from their equilibrium charge, one can study in details the competition between the various charge exchange processes as a function of impact parameter. The range of impact parameters in such experiments extends from about 0.1 Å (i.e. the extension of the target atom spatial distribution due to their thermal vibrations) to more than 1 Å: the maximum impact parameter is conditioned by the geometry of crystal channels. Channeling experiments have been performed in the past for studying ionization [7,8] and also REC (observation of impact parameter dependent Compton profiles) [9].

As already mentioned, 20 MeV/u U^{91+} ions were extracted from the ESR storage ring at GSI, after cooling, deceleration, and slow extraction by radiative recombination of bare ions in the electron cooler, extending the method described in [10] to lower energies. This slow extraction mode is used in order to preserve the reduced beam emittance achieved by cooling inside the ring. During extraction, the beam intensity on the target varied from 4×10^4 down to 5×10^3 ions/s. A 9.6 μm thick (1 1 1) Si crystal was used as a target. The sample was tilted at 35.2° to the beam in order to align it along the ⟨1 1 0⟩ axis. The target was biased at −10 kV, so that two grounded silicon detectors could attract and collect slow electrons emitted from the entrance and exit surfaces. The amplitude of the signal delivered by a detector was then proportional to the electron multiplicity. This technique was developed in [11]. Two germanium detectors were used to detect X-rays at 90° relative to the beam direction, one of them being collimated at ±1° angular aperture in order to reduce the Doppler broadening. The second detector had a larger solid angle to improve statistics. Transmitted ions were charge and energy analyzed by a magnetic spectrometer, and collected by a 2D position sensitive detector at the focal plane. Fig. 2 shows how ion charge and energy distributions could be obtained in the horizontal plane for the ⟨1 1 0⟩ axial orientation of the crystal. Ion charges were not completely separated by the spectrometer (see Fig. 2(b)). The reasons are (i) a not very good experimental resolution. This is due both to the spectrometer optics and to the beam spot size on

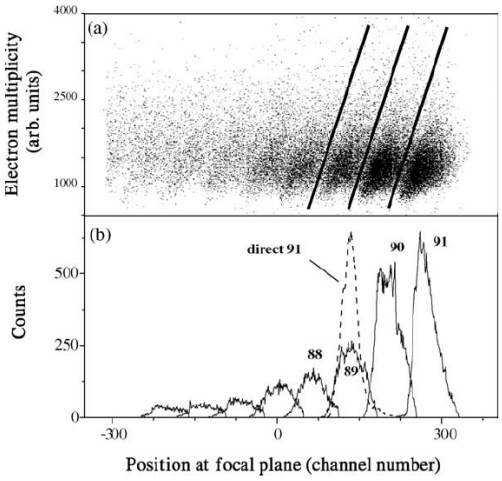

Fig. 2. Distribution of transmitted ions after magnetic analysis, for ⟨1 1 0⟩ axial orientation. (a) scatter plot of forward electron emission multiplicities as a function of position in the focal plane. The lines indicate the separation of charge states. (b) Charge by charge projection of the above distribution. The projection of the direct beam is shown (dashed line).

target (3 mm horizontally), which is not small compared to the spacing between two transmitted charges (about 1 cm at the focal plane). The image of the direct beam is superimposed in Fig. 2(b), and it is about the same width as for a transmitted charge. (ii) The contribution of energy straggling to the broadening of a given charge peak.

In order to improve the identification of charge states, we used the property that electron emission yield is also connected to the electron density sampled by channeled ions. Fig. 2(a) shows how this correlation is used to separate charge states on a 2D distribution of forward electron multiplicities as a function of position (i.e. momentum). Note that for the very best channeled ions (select for instance electron multiplicities lower than the value 1000 on the graph), the charges are very well separated. For these very well channeled ions, the energy straggling, due to statistical fluctuations in the energy transferred during close collisions with target electrons, is very small, because such close collisions are rare events.

Charge state distributions obtained for random and axial orientations are shown in Fig. 3. For a random orientation, charge equilibrium is reached, with a mean charge of about 74. We estimate that this equilibrium is reached inside the target after only 1 μm, due to the very large cross-sections for charge exchange. On the other hand, the axial channeling charge state distribution ranges from 91 (28% of frozen ions) to charges also observed in

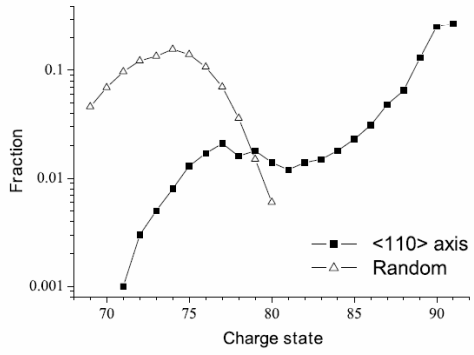

Fig. 3. Charge state distributions of transmitted ions for random and axial crystal orientations.

random conditions. The distribution for the highest charge states (88–91) shows that the average number of electron captures is less than 1 for well channeled ions. Ions with a high transverse energy capture many electrons, and they exhibit a maximum around 78 in the charge distribution, which is quite different from the most probable value, 74, at equilibrium. This may appear surprising as ions with high $E_{\perp}$ have access to small enough impact parameters to undergo as many MEC events as in random conditions. The reason is that MEC occurs mainly at small impact parameter, into highly excited states of uranium ions, and thus captured electrons have a very high probability to be further ionized. Since the trajectory of such ions is nearly parallel to the crystal axis during the capture, a series of a few tens of sequential collisions at about the same impact parameter will occur within a period of time of 6×10^{-18} s (atoms are separated by 3.8 Å along the $\langle 1\,1\,0 \rangle$ axis of silicon). This time is much smaller than the lifetime of any excited state in uranium. As a comparison the distance between two atoms along the $\langle 1\,1\,0 \rangle$ axis of silicon is 40 times smaller than the mean free path for collisions at impact parameters smaller than 0.2 Å in random orientation conditions. This effect reduces considerably the decay probability of excited states, and thus the probability of stabilizing the captured electrons in the inner shells of the projectile.

More details on the charge exchange can be obtained from X-ray spectra. Fig. 4 shows some characteristic spectra recorded with the high resolution detector. The spectrum of Fig. 4(a) was obtained for a random crystal orientation. It is in fact independent of the emerging charge state. The three other spectra (Fig. 4(b)–(d)) were obtained for various charges at emergence for $\langle 1\,1\,0 \rangle$ axial alignment: Fig. 4(b) corresponds to $Q_{\text{out}} = 76$–80, a charge range also reached in random conditions. Such ions have the highest transverse energy. Fig. 4(c) corresponds to $Q_{\text{out}} = 83$–89, i.e. to charges associated to channeled ions with intermediate transverse energy values. Fig. 4(d) corresponds to well channeled ions that have captured only one electron ($Q_{\text{out}} = 90$). The spectra show mainly transitions into the K- and L-shells of the uranium ions. In all cases the K-shell has been filled once,

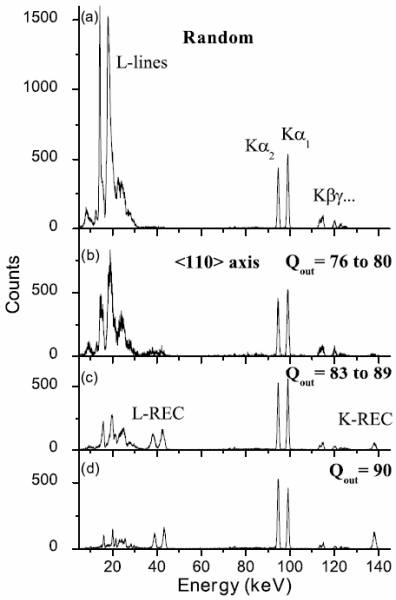

Fig. 4. X-ray spectra recorded at 90° in the laboratory frame: (a) random orientation; (b)–(d) axial orientation, in coincidence with transmitted ions of various charge states. All spectra have been normalized to the same number of transmitted ions in the considered charge state range. They are not corrected for the energy dependence of detection efficiency.

either by K emission, or by K-REC (K-Auger decay is negligible for the high-Z uranium ions). This property has been used for the normalization of the four spectra to the same number of ions transmitted in each considered charge state range. A striking feature is that K-REC and L-REC are almost absent in random conditions: MEC probabilities are so high that the $n = 1$ and 2 levels of the projectile ions are filled within a very short path length, thus preventing REC from occurring into these shells (although REC probabilities are maximum since all target electrons can contribute). Higher n_f-REC contribute in random conditions, even if their probabilities are smaller than K- and L-REC ones. Unfortunately, the M- and N-REC photon energies are around 24 and 18 keV, respectively. They are masked by the L-lines in all the spectra, and thus no information can be extracted on higher n_f-REC. Note that the overlap between M-REC and L-lines indicate that some LMN-RTE may occur. However, the RTE cross-sections are expected to be small compared to MEC ones. In random conditions, all K-lines correspond to the radiative decay after the first MEC event. L-lines are partly due to radiative decay after MEC, but also to the decay after L-shell ionization or excitation, that has a higher probability when the L-shell is filled. The respective contributions of capture and excitation/ionization can be distinguished by observing the two first lines (16 and 20 keV). These two lines are transitions from $n = 3$ to $n = 2$, $j = 3/2$ and $n = 2$, $j = 1/2$, respectively. They are broadened by the presence of various electronic configurations (from $Q = 90$ to $Q = 82$), which changes the energy of the transition during the filling of the L-shell. Once the L-shell is filled, only ionization or excitation events can cause such transitions. In Fig. 4(a), these events correspond to narrow peaks sitting on top of broader ones (or rather at slightly lower energies), the latter resulting from capture. These narrow components do not show up in alignment conditions (Fig. 4(b)), which demonstrates again that equilibrium charge state cannot be reached by projectiles of high transverse energy. The amplitudes of the broad peaks in Fig. 4(a) and (b) are found to be similar. Indeed, in both cases, the selected charges correspond to a full L-shell, which implies that the number of L transitions after MEC events be the same.

In channeling conditions (Fig. 4(b)–(d)), K- and L-REC become more and more important as the transverse energy of the ions decreases, because MEC probabilities decrease with decreasing transverse energy. As we will see below, for $Q_{out} = 90$, REC is the dominant capture process. The relative amplitudes of $K_{\alpha 1}$ to $K_{\alpha 2}$ lines are inverted in Fig. 4(d) compared to the others. This is due to the major contribution of the decay after L-REC, that favors the $j = 1/2$ final state [6]. Actually one can evaluate the residual contribution of MEC for channeled ions: $K_{\beta,\gamma,...}$ result from capture into higher n-states, and thus are more likely due to de-excitation after MEC than after REC (REC occurs preferentially in low n-states). Thus one can compare MEC and REC probabilities by comparing the amplitudes of K-REC and

$K_{\beta,\gamma,\ldots}$ lines. For $Q_{out} = 90$, we find that REC corresponds to 70% of the capture events, MEC representing the residual 30%. By making further selection of ions associated with small energy losses and low electron multiplicities, in order to select the very best channeled 90+ ions, we find that the fraction of MEC events can only be reduced to 20%. We attribute this last contribution of MEC to the capture in the thin amorphous layers at the crystal surfaces. Indeed, using the CDW cross-sections for MEC, a capture rate of 20% corresponds to a total amorphous silicon layer of about 30 Å, which is reasonable.

Another important point is that nearly all K-REC events correspond to the capture of valence electrons of silicon. This can be deduced from the narrowness of the K-REC peak, as the core electrons of silicon have a much broader Compton profile than valence electrons. This statement is confirmed by studies of REC and MEC yields as a function of the tilt angle between the $\langle 1\,1\,0\rangle$ axis and the beam: giving an incidence angle Ψ relative to the axis increases $E_\perp$ by $E\Psi^2$, E being the total ion kinetic energy. Then one can vary the minimum impact parameter for all incident channeled ions. It is observed that ions with $Q_{out} = 91$ disappear at a tilt angle of about 0.04°. Such an angle is much smaller than the Lindhard critical angle for channeling ($\Psi_c = 0.1°$). For an ion penetrating at the center of the $\langle 1\,1\,0\rangle$ channel, the angle of 0.04° corresponds to a transverse energy that allows a minimum impact parameter of 0.4 Å, which is very close to the maximum radial extension of the core electrons in silicon. Moreover, we observe that K- and L-REC yields also decrease significantly with increasing tilt angle (although the mean sampled electron density increases with $E_\perp$). This shows that, at impact parameters as large as 0.4 Å, REC in deeply bound states is already overwhelmed by MEC in outer-shells, followed by decay into the K- and L-shells. Then, we can conclude that ions penetrating inside the core electron orbitals of silicon do capture many electrons by MEC, and that REC is the dominant process only at quite larger impact parameters.

To summarize, these preliminary results show that MEC and REC compete with similar probabilities at impact parameters slightly greater than the core electron orbital extension. Further analysis with the help of Monte Carlo simulations will provide more detailed results on this competition. We have shown that the close collisions along atomic rows prevent electrons captured into highly excited states from decaying down to deeply bound states. Thus, in our thick crystal, charge state equilibrium cannot be reached for ions with very high transverse energies in axial alignment. The high fraction of frozen 91+ ions transmitted through a rather thick target encourages us to extend these studies towards lower energies or thicker crystals. In such a situation, the survival probability of frozen highly charged ions will depend more and more on their transverse energy.

Acknowledgements

The efficient collaboration of the ESR staff is greatly acknowledged. This program was supported by the GSI-IN2P3 collaboration agreement.

References

[1] B. Franzke et al., GSI scientific report 1995, GSI 96-1, p.159.
[2] B.H. Bransden, M.R.C. McDowell, Charge Exchange and the Theory of Ion–Atom Collisions, Clarendon press, Oxford, 1992.
[3] J.A. Tanis, Nucl. Instr. and Meth. A 262 (1987) 52.
[4] A. Belkacem, H. Gould, B. Feinberg, R. Bossingham, W.E. Meyerhof, Phys. Rev. A 56 (1997) 2806.
[5] D. Belkic, R. Gayet, A. Salin, Comput. Phys. Commun. 32 (1984) 385;
J-P. Rozet, private communication.
[6] M. Stobbe, Ann. Phys. 7 (1930) 661.
[7] A. L'Hoir, S. Andriamonje, R. Anne, N.V. De Castro Faria, M. Chevallier, C. Cohen, J. Dural, M.J. Gaillard, R. Genre, M. Hage-Ali, et al., Nucl. Instr. and Meth. B 48 (1990) 45.
[8] D. Dauvergne, C. Scheidenberger, A. L'Hoir, J.U. Andersen, S. Andriamonje, C. Böckstiegel, M. Chevallier, C. Cohen, N. Cue, S. Czajkowski, et al., Phys. Rev. A 59 (1999) 2813.
[9] S. Andriamonje, M. Chevallier, C. Cohen, N. Cue, D. Dauvergne, J. Dural, F. Fujimoto, R. Kirsch, A. L'Hoir, J.C. Poizat, et al., Phys. Rev. A 54 (1996) 1404.
[10] H.T. Prinz, D. Dauvergne, S. Andriamonje, K. Beckert, M. Chevallier, C. Cohen, J. Dural, H. Eickhoff, B. Franzke, H. Geissel, et al., Hyperfine Interact. 108 (1997) 325.
[11] Y. Yamazaki, K. Kuroki, Nucl. Instr. and Meth. A 262 (1987) 118.

Des simulations ont été entreprises pour extraire des données quantitatives de cette expérience. Elles constituent une large part de la thèse d'Etienne TESTA dans notre groupe. Nous avons choisi de ne pas faire de simulations complètement Monte Carlo, dans lesquelles nous aurions suivi l'histoire des événements d'échange de charge par les ions au cours de leur trajectoire dans le cristal. Ces simulations sont trop coûteuses en temps de calcul, et il n'aurait pas été possible de reproduire l'ensemble de nos données. Nous avons donc choisi d'étudier, dans le cas de la MEC, le taux de "capture effective" en fonction de la distance minimale d'approche aux rangées ou aux plans suivant l'orientation du cristal. Par capture effective, nous entendons une capture électronique conduisant à la réduction d'une unité de l'état de charge de l'ion en sortie du cristal, c'est-à-dire que l'électron capturé (le plus souvent en couche externe ($n > 4$)) n'est pas ré-ionisé. C'est ce choix qui permet la meilleure confrontation entre les simulations et les données expérimentales dans le domaine de sensibilité de cette expérience pour l'étude de la MEC en fonction du paramètre d'impact (entre 0,2 et 0,5 Å), et avec le minimum de paramètres ajustables dans les simulations : la divergence angulaire du faisceau, l'effet du réchauffement transverse des ions canalisés dans ce cristal relativement épais (11µm), l'influence des couches amorphes en surface du cristal, et bien entendu un éventuel facteur d'ajustement des probabilités de capture MEC et REC en fonction du paramètre d'impact.

Ce domaine de sensibilité de 0,2 à 0,5 Å en paramètre d'impact dépend en grande partie du choix de l'épaisseur de cible : la limite inférieure correspond au seuil en dessous duquel les ions capturent plus d'une dizaine d'électrons, et donc pour lesquels on n'a plus d'information par l'émission X, limitée au remplissage des couches n=1 et n=2 du projectile (raies K et L) avec les détecteurs germanium utilisés. Une cible beaucoup plus mince (~ 1µm) aurait réduit considérablement le nombre d'électrons capturés, et aurait déplacé cette fenêtre vers les plus petits paramètres d'impact. Cependant la perte d'énergie n'aurait pas été mesurable (voir section 1-6 plus loin), et l'influence relative de la capture dans les couches amorphes en surface aurait été plus importante.

L'article *"Impact parameter charge exchange studies with channeled heavy ions"* [Dauvergne 06] a fait l'objet d'une conférence invitée à la conférence ICPEAC 2005, Rosario, Argentine. Il doit paraître prochainement dans les actes de cette conférence.

Il présente le plus brièvement possible les résultats de ces simulations, sachant qu'un article est en cours de préparation sur l'ensemble du travail de thèse d'Etienne Testa.

IMPACT PARAMETER DEPENDENT CHARGE EXCHANGE STUDIES WITH CHANNELED HEAVY IONS

D. DAUVERGNE, M. CHEVALLIER, J.-C. POIZAT, C. RAY, E. TESTA

Institut de Physique Nucléaire de Lyon, CNRS- IN2P3 and Université Claude Bernard Lyon 1, F-69622 Villeurbanne, France

A. BRÄUNING-DEMIAN, F. BOSCH, S. HAGMANN, C. KOZUHAROV, D. LIESEN, P. MOKLER, TH. STÖHLKER, M. TARISIEN[†], P. VERMA

Gesellschaft für Schwerionen Forschung (GSI), D-64291 Darmstadt, Germany

C. COHEN, A. L'HOIR, J.-P. ROZET, D. VERNHET

Institut des Nano-Sciences de Paris, CNRS-UMR75-88, Universités Paris VI et Paris VII, 75251 Paris cedex 05, France

H. BRÄUNING

Institut für Atom- und Molekülphysik, Justus Liebig Universität, D-35392 Giessen, Germany

M. TOULEMONDE

Centre Interdisciplinaire de Recherche Ions-Lasers, UMR 11 CEA-CNRS, 14040 Caen cedex, France

We use decelerated (below 20 MeV/u) H-like heavy ions extracted from the GSI-ESR storage ring to study electron capture processes such as Radiative Electron Capture (REC) and Mechanical Electron Capture (MEC) in channeling conditions. With the help of simulations, we show that MEC occurs at relatively large impact parameters into highly excited states. REC studies provide information about the electron gas polarization.

Introduction

Bare heavy ions can be decelerated down to a few MeV/u at the Experimental Storage Ring facility (GSI, Germany). Such ions are very far from their charge equilibrium in matter, since their velocity is much smaller than the velocity of their inner-shell bound electrons. The extraction of such beams allows one to study their collision with solid targets. Their interaction with matter should provide a very strong perturbation, along with a very high cross section for electron capture.

We present here some results concerning the impact parameter dependence of the electron capture processes competing inside a crystalline target under alignment conditions.

Indeed, channeling of charged particles in a crystal leads to a redistribution of the ion flux inside the target. Channeled ions have a restricted accessible transverse space, which is determined by their transverse energy [1]. In the continuum potential approximation, the collisions of particles along atomic strings or planes are described as deflections by a continuum potential, which is averaged along the crystallographic direction. With the help of simulations, detailed information can be extracted on the impact parameter dependence of interaction processes such as charge exchange and energy loss, provided that the transverse energy of channeled ions can be determined. This is what has been done in this work, which presents part of the results obtained recently with decelerated heavy ions at 20 MeV/u and below.

[†] Present address: CENBG, CNRS-IN2P3 and Université Bordeaux 1, Le Haut Vigneau, 33175 Gradignan cedex, France.

Experiment

A detailed description of the production of decelerated H-like heavy ions has been given in ref. [2].
Briefly, some 10^7 highly-charged ions, accelerated up to a few hundreds of MeV/u by the heavy-ion synchrotron SIS-18, are fast extracted. They are further totally stripped in a thick stripper foil placed between the SIS and the storage ring ESR, and then injected at once inside the ESR. After cooling and deceleration, they are extracted continuously from the ring by means of radiative recombination inside the electron cooler, which changes the magnetic rigidity relative to stored bare ions. Due to different orbits, the H-like ions can be deflected into the extraction channel by a septum magnet. The electron current in the cooler is tuned in order to adjust the extracted ion beam intensity. Thus, within a full cycle of about 6 minutes, a continuous beam is extracted during 4 minutes, exponentially decreasing with time from a few 10^4 ions/s down to 5.10^3 ions/s typically. The beam is transported towards the experimental cave and focused with the most possible parallel optics on the crystal target. Behind the target, transmitted ions are analyzed in charge and momentum by a magnetic spectrometer. As targets, we have used silicon crystals of various thicknesses and orientations. Before setting a crystal under vacuum, its surfaces were cleaned by means of a fluorhydric acid solution.
In all experiments, X-rays are detected at 90° from the beam direction. The target is biased, in such a way that emitted electrons from the surfaces are collected by grounded silicon detectors located in front of the two surfaces of the thin crystal.
At the focal point of the spectrometer, a position sensitive detector (microchannel plate counter with delay-line readout) allows to detect the selected ions and to perform an event by event acquisition containing coincidences between X-rays, electron multiplicities and transmitted ions of identified magnetic rigidity.

Results and simulations

We will concentrate mainly on the experiment performed with 20 MeV/u U^{91+} ions channeled in an 11.7 micrometer thick crystal. Some of the results have been presented in ref. [3]. Here we add more refined analysis obtained by means of simulations, which need to be described first.

Principles of the simulations

These simulations are aimed to estimate the mean number of electron captures by aligned projectiles as a function of their transverse energy, assuming statistical flux equilibrium for channeled ions. The simple idea behind the statistical flux equilibrium is that channeled ions of given transverse energy explore uniformly all their accessible transverse space. Thus the transverse energy of a channeled ion defines its impact parameter distribution along the path inside the crystal. The charge state at emergence is then calculated by injecting in Monte Carlo simulations an impact parameter dependent capture probability. Such simulations have the advantage to avoid full trajectory calculations, which spares computation time (trajectory calculations are made once for each transverse energy in order to implement the impact parameter distributions). The drawback is that multiple charge exchange effects, arising when an ion approaches close to a string or a plane, cannot be taken into account. This is why we have limited these simulations to ions with a relatively low transverse energy, i.e. for which each single charge exchange event can be considered independently. For high transverse energy ions, suffering close collisions along atomic strings, full Monte Carlo calculations are needed to follow the evolution of the electronic configuration. Such a work, devoted to the study of a “super-density effect” associated to the very high rate of atomic collisions near strings, has been described separately [4].
The transverse energy distribution of the incoming beam depends on the crystal orientation and on the beam angular distribution. The latter is a parameter in the simulations, which has to be adjusted according to our observations. We take into account the dechanneling effects that tend to increase the transverse energy of channeled ions inside this relatively thick crystal. The number of electron captures is estimated as following:
REC probabilities are proportional to the sampled local electron density, and depend on the occupation of inner shells (REC cross sections decrease as the mean quantum number n of the final state increases). MEC probabilities are adjusted as a function of impact parameter to get the best possible agreement with the various measurements. A small probability of MEC into the thin amorphous surface layers is also considered, which does not depend on the ion transverse energy.

Results

Figure 1 shows the charge state distributions obtained for random, (110) planar and <110> axial orientations, after crossing a 11.7 µm thick crystal. In such a thick crystal, the charge equilibrium is reached only for a random target orientation. In channeling conditions, the charge state distributions are much broader and extend from frozen 91+ ions to very low charge states.

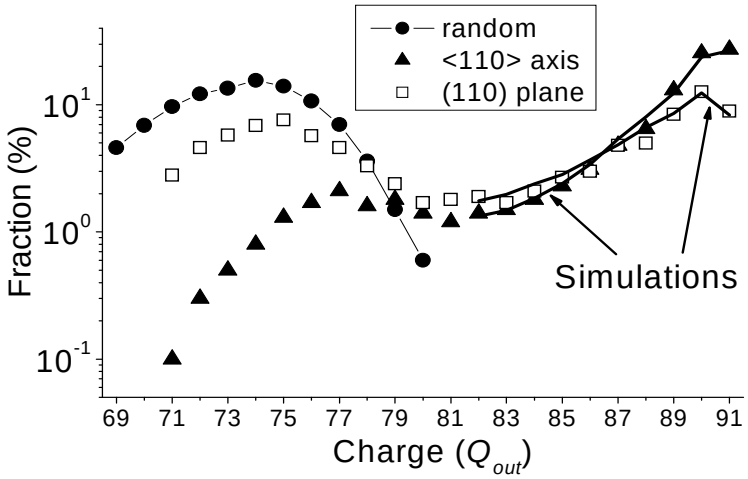

Figure 1. Charge state distributions obtained for 20 MeV/u incident U^{91+} ions on a 11.7 µm thick Si crystal for various orientations. The thick solid lines are simulations (see text).

These distributions reflect the transverse energy distributions of channeled ions, frozen ions being the best channeled ones. The results of the simulations are superimposed. They agree fairly well, both in the shape and in the absolute amplitude of the distributions (although ions with a high transverse energy are not considered in the simulations, we evaluated this fraction of ions that reach charge states below 82+).

Tilting the crystal by an angle $\delta\psi$ relative to the incident beam increases the transverse energy $E_\perp$ of each incident particle by the amount $\delta E_\perp = E(\delta\psi)^2$, where E is the total ion kinetic energy. Thus the charge state distribution strongly depends on the crystal orientation. This is shown in figure 2, where we present the evolution of charge fractions 91 and 87 as a function of the tilt angle relative to the <110> axis. The frozen ion fraction disappears almost completely at a tilt angle which is less than half the channeling critical angle. The fraction of the lower charge state 87, increases for increasing small angles and rapidly decreases at angles only slightly larger than for frozen ions. This shows that many electron capture events occur for ions with relatively small transverse energy, since an incidence angle of 0.04° corresponds to a minimum distance of approach to atomic strings of about 0.4 Å for ions entering the crystal at the center of the channel. Again the simulations are able to reproduce the data.

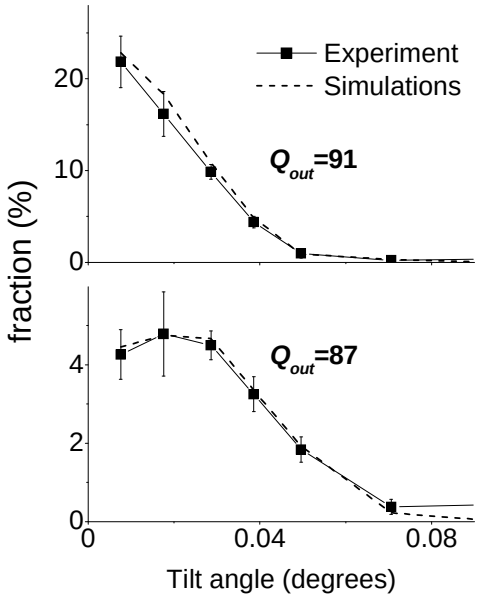

Figure 2. Evolution, with the angle relative to the <110> axis, of charge state fractions 91 and 87 for 20 MeV/u incident U^{91+} on a 11.7 µm thick Si crystal. The dashed lines are simulations.

Information on the nature of electron capture is deduced from the X-ray observation. This is illustrated in figure 3, where two X-ray spectra are shown: one for axial crystal orientation (in coincidence with 90+ transmitted

ions), and the other one for a random orientation. Both spectra show mainly transitions into n=1 and n=2 levels of the uranium projectiles. They correspond either to inner-shell transitions (K and L-lines) or to REC into K- and L-shells. As MEC occurs into excited states, the filling of the K and L-shells following MEC causes the emission of K and L lines. In the random spectrum, a large fraction of the L-lines is also due to the creation of L vacancies once the charge equilibrium is reached in this thick target, or at least once the L-shell is filled. Note that K- and L-REC lines are almost absent from the random orientation spectrum. The reason is that those inner shells are very rapidly filled inside the target by MEC, which prevents REC from occurring. On the contrary, ions emerging as 90+ under axial alignment are well channeled ions, for which MEC is strongly reduced inside the crystal.

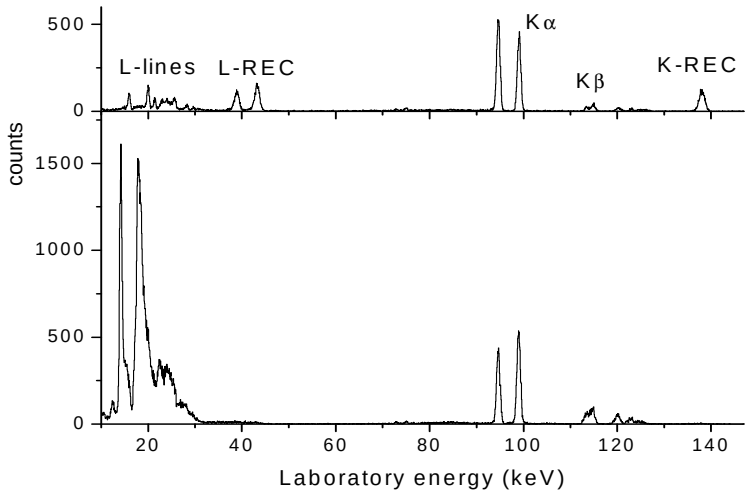

Figure 3. X-ray spectra recorded at 90° for 20 MeV/u incident U^{91+} on a 11.7 µm thick Si crystal. Upper spectrum: axial orientation, in coincidence with U^{90+} transmitted ions. Lower spectrum: random incidence. The spectra are normalized to the same number of transmitted ions.

For those ions, REC is the dominant capture process, and the corresponding peaks are easily observed. Here, even K_α lines are mainly due to the decay of electrons captured by REC into low j-values of the L-shell (note that the ratio $K_{\alpha1}/K_{\alpha2}$ is inverted on the two spectra in fig. 3). Thus, REC and MEC capture rates can be evaluated for any transverse energy of channeled ions, that are selected either by their charge state at emergence, or by their electron multiplicities from the crystal surface. This is shown in figure 4, where average MEC and REC rates are represented as a function of the minimum distance of approach to the atomic strings along the path inside the crystal (axial orientation). This curve is obtained as a direct output of the simulations. One can see the very fast increase of MEC events when ions are able to approach the strings at distances smaller than 0.4 Å to atomic strings. REC contributes significantly at large distances. However, no increase of the REC yield is found close to the target atoms, although the mean electron density sampled by ions with increasing transverse energy increases. This is again due to the rapid filling of inner shells by MEC and electron cascades close to the entrance of the crystal (ions with parallel incidence with the crystal axis penetrate the crystal at the minimum distance of approach to strings, and so the MEC rate is maximum there).

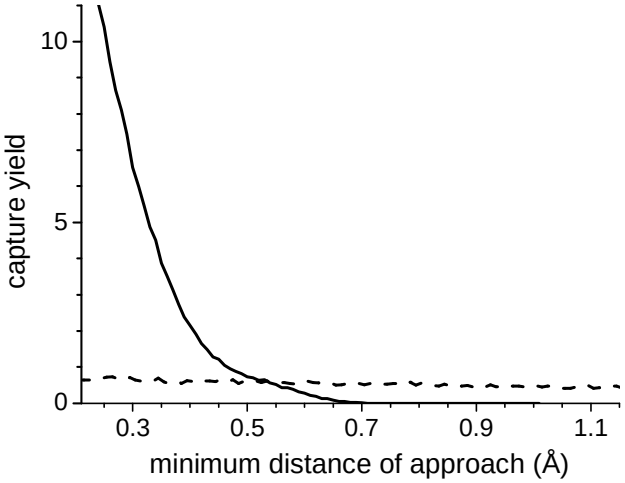

Figure 4. Estimates, deduced from simulations, of the total capture yields for 20 MeV/u incident U^{91+} inside the 11.7 µm thick Si crystal, as a function of the minimum distance of approach to the <110> atomic strings for channeled ions. Solid line: MEC yield, dashed line: REC.

Discussions

Mechanical Electron Capture

The knowledge of the complete impact parameter distribution for channeled ion trajectories inside the crystal is needed to extract the atomic impact parameter probabilities of MEC. In particular, one has to take into account the thermal vibrations of the target atoms, and dechanneling effects. This makes the dependence with atomic impact parameter of MEC significantly narrower than shown in Fig.4. Our experiments are mainly relevant in the impact parameter region 0.2 – 0.4 Å, where a maximum of constraints on the fitting procedure can be extracted from the experimental observations. Actually, we show in Fig.4 an effective capture probability, i.e. the probability to capture an electron and not to lose it by ionization afterwards. At distances of approach smaller than 0.2 Å, a much thinner crystal would be needed to limit the number of electron captures so that information can still be extracted from X-rays (no more L-lines consecutive to capture are emitted beyond 9 captured electrons). At distances of approach larger than 0.4 Å, the origin of the uncertainties is the determination of the absolute REC probabilities, of the MEC capture yield in the thin surface amorphous layers and the knowledge of the beam angular divergence.

The impact parameter dependent MEC probabilities have been deduced from the capture yield presented in Fig.4, and the impact parameter distributions calculated by means of trajectory simulations. They have been compared with CDW-EIS calculations performed by P. Abufager et al. [5]. These calculations were limited up to n=5 due to the very large complexity of such analytical calculations for higher projectile n-shell values. These calculations show that for n<6 MEC occur mostly at impact parameters smaller than 0.25 Å, i.e. in a region where our experiments do not provide very accurate information. In fact, MEC capture into these “inner” shells is not the dominant process.. Actually, integrated CDW calculations show that the cross section is maximum for final states equal to 5 and 6, and only slowly decreases for higher n-shells. Additional CTMC calculations of MEC probabilities as a function of impact parameter are now in progress.

Radiative Electron Capture

The analysis of the K- and L-REC peaks (energy values, shape and amplitude) provide detailed information on the ion-electron interaction by such highly charge ions in a dense electronic medium. We have reported in ref. [6] that a shift of about -100 eV of the REC lines is observed compared to the calculated values corresponding to the capture of a free electron isolated in vacuum. This shift is attributed to the dynamic electron gas polarization by the high projectile charge, slowly moving inside the medium. This energy shift is found in agreement with values calculated by the linear response theory [7].

Another consequence of the dynamic response of the electron gas is the local increase of the local electron density at the ion site, which may increase the REC yield compared to a non perturbed electron gas. Indeed, we do observe an increase of about 40% [6]. This increase of the local electron density is much smaller than predicted by the linear response theory. Actually, this is not surprising, because the first order perturbation calculations are certainly not valid for such a system. Non perturbative calculations are obviously needed to provide an accurate description of the electron gas polarization by such high charges moving in matter at these velocities.

Conclusion

We have shown that charge exchange by decelerated highly charged ions can be studied in details as a function of impact parameter using crystal channeling. For 20 MeV/u U^{91+} ions, non radiative capture (MEC) into highly excited states is the dominant capture process at small impact parameters. Complete calculations of the impact parameter dependence of MEC are still in progress, the analytical CDW-EIS being limited to relatively low-lying states. REC is the dominant capture mechanism at large distances from the target atoms, and provides interesting information on the dynamic electron gas polarization. In a more general review on these experiments, to be published, we will also discuss particular aspects of energy loss, the very high charge of channeled ions being responsible for very high energy loss rates.

Acknowledgments

We gratefully thank P. Abufager and R. Rivarola who provided us with calculations of electron capture.
This work was supported by the French – German GSI-IN2P3 collaboration agreement 97-35.

References

1. D. S. Gemmell, Rev. Mod. Phys. 46 (1974) 129.
2. H. T. Prinz *et al.*, *Hyperfine Interactions* **Cf22**, 1729 (1995).
3. D. Dauvergne *et al*., Nucl. Instr. And Meth. Phys. Res. **B205,** 773 (2003).
4. A. L'Hoir *et al*., to be published in Nucl. Instr. and Meth. Phys. Res. B.
5. P. Abufager and R. Rivarola, private communication
6. E. Testa *et al*., to be published in Nucl. Instr. and Meth. Phys. Res. B
7. P. M. Echenique, R. H. Ritchie, and W. Brandt, Phys. Rev. **B20**, 2567 (1979).

Pour compléter les informations contenues dans cet article, la figure ci-dessous montre la comparaison entre les probabilités de capture MEC en fonction du paramètre d'impact, pour des ions U^{91+} de 20 MeV/u et un atome de silicium, calculées et ajustées dans les simulations.

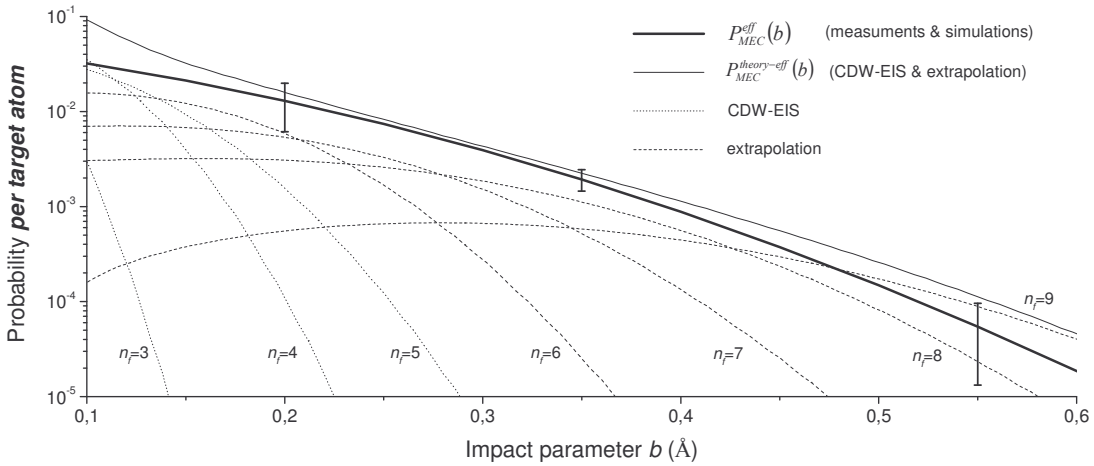

Figure 5 *: Probabilités de capture MEC par des ions U^{91+} de 20 MeV/u en collision avec des atomes de silicium, en fonction du paramètre d'impact. Les lignes en pointillés correspondent à des calculs CDW-EIS pour les états finals jusqu'à n = 5, et extrapolés au-delà. La ligne continue, avec les barres d'erreur, correspond au résultat des simulations permettant l'accord avec les données de l'expérience. Courbe extraite de la thèse d'Etienne Testa [Testa 05].*

Les calculs CDW-EIS ont été faits par Paula Abufager et Roberto Rivarola, de l'université de Rosario (Argentine), avec lequel nous avons collaboré durant cette période. Ces calculs sont compliqués, et n'ont pas pu être développés au-delà de la couche $n = 5$ du projectile, en raison du trop grand nombre de configurations électroniques à prendre en compte pour les états finals (en ce qui concerne les états initiaux, ce sont principalement les électrons 1s du silicium qui sont capturés). Or la probabilité de MEC est maximum pour $n > 4$ (cf. la figure 1 de l'article [Dauvergne 03]), et, de plus, notre expérience était sensible à la contribution à grand paramètre d'impact (b > 0,2 Å), qui correspond à $n > 3$ (je rappelle que je sous-entends par « sensible » le fait que l'on peut étudier la capture en fonction de l'énergie transverse, et donc que le nombre d'électrons capturé doit rester suffisamment faible pour ne pas atteindre l'état de charge à l'équilibre ; c'est la cas ici pour les ions avec une couche L partiellement remplie, ce qui permet de plus d'extraire une information des raies X_L). Il a donc fallu extrapoler ces probabilités de MEC au-delà de $n = 5$ [Testa 05], en tenant compte de la forme des orbitales considérées [Indelicato 03] et de la section efficace partielle de capture sur chaque couche n, qui est disponible par ces calculs CDW-EIS. La figure, extraite de la thèse d'Etienne Testa, montre le bon accord obtenu dans le domaine 0,2 – 0,5 Å. Aux faibles paramètres d'impact, l'ionisation après capture sur des niveaux n élevés est importante, ce qui limite la précision des ajustements. A grand paramètre d'impact (b > 0,5 Å), la précision est limitée par l'incertitude sur la probabilité de REC, qui est le processus dominant, ainsi que par la connaissance de la divergence angulaire du faisceau, qui conditionne la distribution du flux des ions canalisés.

En conclusion, cette expérience souligne le manque de calculs théoriques adaptés à la description de la capture MEC aux faibles valeurs de η. Des calculs de type CTMC seraient certainement mieux adaptés à cette description. Ces calculs ont été entrepris en collaboration avec Michael Beuve.
Cette expérience a également démontré que la probabilité de MEC à grand paramètre d'impact est importante. Deux expériences ont été depuis réalisées au GSI par notre collaboration, l'une avec des ions Pb^{81+} à 13 MeV/u en 2003, et la dernière avec des ions U^{91+} à 12 MeV/u en mai 2005. La mise en évidence, dans cette dernière, d'ions gelés à la sortie d'un cristal de 18µm, montre qu'on n'a pas atteint encore le régime dans lequel tous les ions capturent des électrons par MEC, quelle que soit leur énergie transverse. Ce sera forcément le cas en dessous d'une certaine énergie, où les électrons seront capturés dans des états de Rydberg très loin du noyau projectile.

A ce stade je ferai une courte parenthèse sur la capture multiple (capture de plusieurs électrons au cours d'une collision avec un seul atome). Nous avons discuté, au début de cette section, de la nécessité d'utiliser des cibles très minces pour se placer en condition de capture unique avec des ions très chargés ralentis. Or, la sélection des ions les mieux canalisés à la traversée d'un cristal permet de se placer dans ces conditions très particulières vis-à-vis de la capture dans les couches amorphes de surface d'un cristal manipulé sans précautions particulières: une couche amorphe de SiO_2 d'une cinquantaine d'Angström correspond typiquement à une cible ultra-mince de 1 µg/cm^2. Un ion très bien canalisé « voit » donc deux cibles minces amorphes (de l'ordre de 10^{16} atomes/cm^2 chacune), entourant une cible « épaisse » d'électrons de quelques 10^{20} électrons/cm^2. Cette dernière est inactive pour la capture MEC, qui ne peut donc se produire qu'aux surfaces.
La figure 6 ci-dessous, extraite de la thèse d'Etienne Testa, montre comment on peut obtenir la distribution de charge associée à ces ions les mieux canalisés, à l'aide de la multiplicité d'électrons émis en surface.

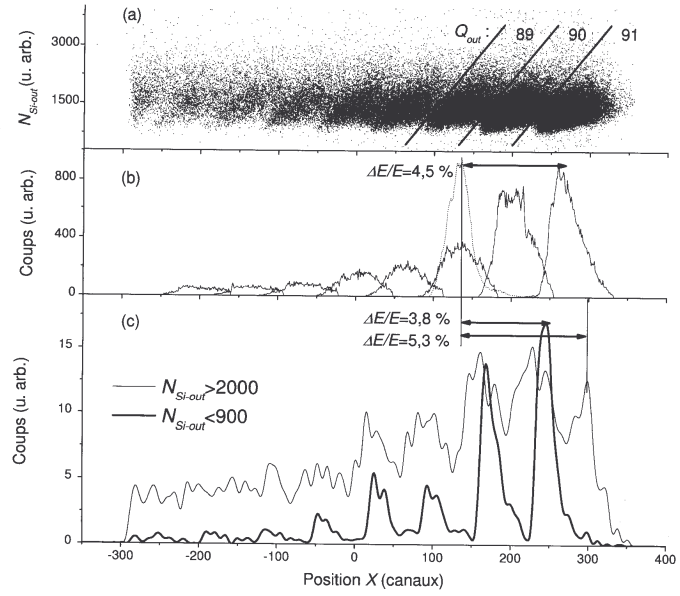

Figure 6 : *Distributions d'ions U^{91+} incidents de 20 MeV/u transmis à travers un cristal de silicium de 11µm aligné selon l'axe <110>, détectés après analyse magnétique.(a) Distribution des multiplicités électroniques en fonction de la position pour les ions de charges les plus élevées ; (b) projection unidimensionnelle de cette distribution, en utilisant les séparatrices d'états de charge indiquées en (a). Le profil du faisceau direct est indiqué. c) Projections correspondant aux fortes et aux faibles multiplicités électroniques.*

Nous discuterons de la corrélation entre émission électronique et perte d'énergie dans la section 1-6. Cette corrélation se manifeste dans la distribution bi-paramétrique de la position au plan focal en fonction de la multiplicité d'électrons en face avant (sortie) du cristal. On utilise cette corrélation pour séparer les états de charge. La projection de cette distribution avec la séparation des pics d'états de charge est montrée sur la partie b de la figure 6. En c sont projetées deux distributions, l'une avec les plus faibles multiplicités électroniques (les mieux canalisés) et l'autre avec les plus fortes multiplicités.
Si on considère la distribution de charge associée aux ions les mieux canalisés, on se rend compte que la fraction des ions ayant subi un nombre N de captures ne suit pas du tout une loi en $P_{capt}^{N}/N!$, où P_{capt} serait une probabilité unique de simple capture à la traversée de la cible. L'étude conjointe des spectres X a permis d'identifier les processus responsables de ces captures. Bien que la capture radiative soit responsable de la majorité des événements de capture pour $N = 1$, elle ne contribue pratiquement plus au-delà, en tous cas plus pour $N = 3$, car ce processus fait effectivement intervenir des événements de capture indépendants les uns des autres. C'est donc bien la capture mécanique en couche amorphe qui est responsable des captures multiples. La probabilité d'un événement MEC simple en couche amorphe est de 0,22. La probabilité de deux événements consécutifs devrait donc être dans ces conditions de 0,024, et pour 3 événements, de 0,0018. Or les fractions d'ions 89+ et 88+ sont toutes deux proches de 10%, et celle des ions 88+ d'environ 5%. Seule la capture de plusieurs électrons d'un même atome peut permettre d'expliquer cette distribution. Les calculs CDW-EIS de Roberto Rivarola déterminent les probabilités de « capture simple », c'est-à-dire que dans la voie de sortie, l'atome cible a perdu un électron et le reste du cortège électronique reste non perturbé. Ils ne peuvent donc pas tenir compte de la multi-capture.

Nous reviendrons sur d'autres aspects des résultats des ces expériences avec des ions ralentis dans les sections 1-5 et 1-6 de ce chapitre.

1-5 Aspects spécifiques de l'interaction ion lourd-cristal

Dans cette section, nous évoquerons quelques aspects très particuliers associés à l'évolution des états de charge et des configurations électroniques des ions lourds en condition de canalisation dans un cristal. Certains de ces aspects sont liés à l'interaction des ions avec un gaz dense d'électrons, et font intervenir des collisions dites « distantes » car les transferts d'énergie mis en jeu sont faibles (mélanges intra-couche), ou bien mettent en jeu la réponse collective du gaz d'électron (effet de sillage, ou « wake »). D'autres aspects sont plus directement liés aux collisions rapprochées des ions le long des rangées (effet de « superdensité » et excitation cohérente résonante).

1-5-1 Collisions distantes : Mélange intra-couche et effet de sillage

Les sections efficaces de mélange intra-couche (*nl-nl'*) par transitions dipolaires électriques lors de collisions avec les noyaux écrantés ou les électrons sont très grandes, et ce mélange détermine en grande partie les populations des sous-niveaux d'un ion dans une cible solide.
L'évolution des populations des niveaux excités lors du passage d'ions rapides dans des cibles solides très minces a fait l'objet d'études poussées au GANIL par le groupe de physiciens atomistes du GPS ([Lamour 06], [Rozet 99]). Ces études ont permis de montrer l'influence du mélange purement collisionnel, et de la contribution de l'effet Stark au mélange de sous-niveaux, en raison du champ électrique dû à la polarisation dynamique du gaz d'électrons, responsable de la force de ralentissement de l'ion par le solide.

L'intérêt de la canalisation dans des cristaux est qu'elle permet une population directe et sélective de certains états métastables. Par exemple la capture radiative en couche L d'un ion nu peuplera de préférence le sous niveau 2s, qui est métastable, dans le sens où la désexcitation dipolaire électrique vers le niveau n=1 est interdite. De même, avec un ion lithiumoïde, l'ionisation K par impact d'électron laissera l'ion dans une configuration 1s2s également métastable. De plus, l'évolution de ces états dans la cible pourra être observée sur des temps très longs (10^{-14} typiquement), car les ions ont une faible probabilité d'être perturbés par une collision violente sur les atomes cible, ou par un autre processus d'échange de charge.
Nous avons donc réalisé une étude, en sous-produit de l'expérience sur la capture radiative avec des ions krypton de 60 MeV/u au GANIL [Andriamonje 96], dans laquelle nous avons observé plus spécifiquement les photons K retardés du projectile, c'est-à-dire émis après que les ions soient ressortis de la cible. Le temps de transit dans la cible était de 10^{-13}s environ.
Les résultats de ces observations ont été reportés dans l'article ci-dessous : *"Influence of intrashell excitation (n=2) on the population of metastable states of H- and He-like krypton ions in channeling conditions"* [Andriamonje 96B], publié dans les actes de la conférence SHIM 95. Nous avons démontré que, lorsque l'ion traverse un gaz dense d'électrons, la durée de vie des niveaux métastables est diminuée de plusieurs ordres de grandeur par rapport à la valeur dans le vide. Une section efficace pour le mélange 2s-2p dans le krypton a été obtenue.
On peut regretter que cet article ait eu peu d'impact, car il constitue une mesure propre et directe de ce mélange intra-couche. Un plus grand intérêt de la part de la communauté des physiciens des collisions atomiques aurait permis de pousser ces études en fonction de l'énergie transverse. En effet, on peut supposer que la probabilité d'excitation et de désexcitation intra-couche dépend peu du paramètre d'impact aux atomes. Par contre, la modification des niveaux d'énergie, due à l'effet Stark causé par le champ électrique (longitudinal et transverse), dépend de l'énergie transverse.
D'autre part, des études menée par une collaboration GSI-Argonne cherche à étudier avec précision la distribution en énergie du spectre à deux photons 2E1 de la désexcitation d'un niveau 2s en couche K. La comparaison de ces distributions pour plusieurs noyaux doit dépendre du couplage hyperfin. La canalisation serait un moyen efficace pour peupler ce niveau 2s par REC-L, tout en réduisant considérablement le bruit de fond associé à tous les autres processus.
Pour donner quelques ordres de grandeur, un cristal aligné de quelque 10 µm d'épaisseur permet de peupler par REC-L environ 10% du faisceau incident dans l'état 2s, et ceci avec un faisceau de 10^7 ions/s. Un détecteur X peut détecter les photons de REC-L avec une efficacité de 1 à 10%. On peut donc « étiqueter » des événements de population du niveau 2s avec un taux de 10^4 à 10^5 par seconde, ce qui permettrait de faire une spectroscopie fine de la désexcitation X, prompte ou retardée, de ce niveau à l'aide de détecteurs X conventionnels.
Récemment, V. Balashov a proposé d'étudier l'excitation intra-couche par Excitation Résonante Cohérente [Balashov 06]. Ce dernier facteur, qui est associé à la périodicité du champ coulombien excitateur, doit être pris en compte, et donc mesuré. Nous y reviendrons plus loin.

Nuclear Instruments and Methods in Physics Research B 107 (1996) 1-5

ELSEVIER

NIM B
Beam Interactions with Materials & Atoms

Influence of intrashell excitation ($n = 2$) on the population of mestastable states of H- and He-like krypton ions in channeling conditions [1]

S. Andriamonje [a], M. Chevallier [b], C. Cohen [c], N. Cue [d], D. Dauvergne [b,*], J. Dural [e], F. Fujimoto [f], R. Kirsch [b], A. L'Hoir [c], J.-C. Poizat [b], Y. Quéré [f], J. Remillieux [b], C. Röhl [a], H. Rothard [e], J.P. Rozet [c], D. Schmaus [c], M. Toulemonde [e], D. Vernhet [c]

[a] *Centre d'Etudes Nucléaires de Bordeaux- Gradignan and IN2P3, le Haut-Vigneau, 33175 Gradignan Cedex, France*
[b] *Institut de Physique Nucléaire de Lyon and IN2P3, Université Claude Bernard Lyon-I, 43, Bd du Novembre 1918, 69622 Villeurbanne Cedex, France*
[c] *Groupe de Physique des Solides, CNRS URA 017, Université Paris VII et Paris VI, 75251 Paris Cedex 05, France*
[d] *Department of Physics, The Hong Kong University of Science and Technology, Kowloon, Hong Kong*
[e] *CIRIL, UMR 11 CNRS-CEA, rue Claude Bloch, 14040 Caen Cedex, France*
[f] *Laboratoire des Solides Irradiés, Ecole polytechnique, 91128 Palaiseau Cedex, France*

Abstract

We have observed delayed K_α photons emitted by 60 A MeV H-like and He-like krypton ions leaving a 37 μm silicon crystal, both for random and ⟨110⟩ axial alignment of the target. We could extract intrashell ($2s \rightarrow 2p$) excitation probabilities, which are compared with values deduced from PWBA calculations.

1. Introduction

Swift heavy ions travelling inside a disordered material reach very rapidly a statistical equilibrium in both distributions of charge and excitation states [1,2]. On the contrary, heavy ions channeled in a thin crystal interact mainly with outer-shell target electrons. Thus channeling allows observation of processes such as radiative electron capture (REC) [3] and electron impact ionization (EII) [4,5]. In particular these processes can lead to the population of metastable states. In this paper we are interested in the influence of collisional intrashell ($\Delta n = 0$) excitation on the lifetimes of metastable states of H-like and He-like krypton ions channeled in a Si crystal. Low lying ($n = 1$ and $n = 2$) level structures of H-like [6] and He-like [7] krypton ions are presented in Fig. 1. Among them, the $2s_{1/2}$ (H-like), 1s2s $^1S_0$ and $^3S_1$, 1s2p $^3P_0$ and $^3P_2$ levels cannot decay to the ground state via a single electric dipolar transition E1 [8]. Intrashell excitations, with small momentum transfers, involve large impact parameters, and thus may occur even in channeling conditions. So they may influence considerably the population of metastable states by shortening their lifetime inside the crystal. 2s–2p excitation probabilities were studied theoretically by McGuire et al. [9] in the semiclassical Coulomb approximation for proton–neutral atom collisions, and by Nicolai et al. [10] within the PWBA approximation. To our knowledge there are only a few experimental results on this matter up to now. However a recent experiment pointed out that PWBA calculations underestimate the measured cross section in the case of 13.6 MeV/u argon ions in collisions with gas targets [11].

2. Experiment

During an experiment devoted to REC measurements in channeling conditions [12], that was performed on the LISE beam line at GANIL with 60A MeV krypton ions, we have observed the delayed M1 K_α lines. As shown in Fig. 1, the decay lengths associated with the lifetimes are of the order of a few millimeters for projectiles of this velocity. Incident krypton ions, of charge 36+, 35+ and 33+, respectively, were channeled along the ⟨110⟩ axis of a 37 μm silicon crystal. The beam emittance was 0.1π mm mrad in the two transverse directions. Ions emerging

* Corresponding author, e-mail: dauvergne@lyolav. in2p3.fr.
[1] This work was partly supported by CNRS through GDR86.

0168-583X/96/$15.00
SSDI 0168-583X(95)00837-3

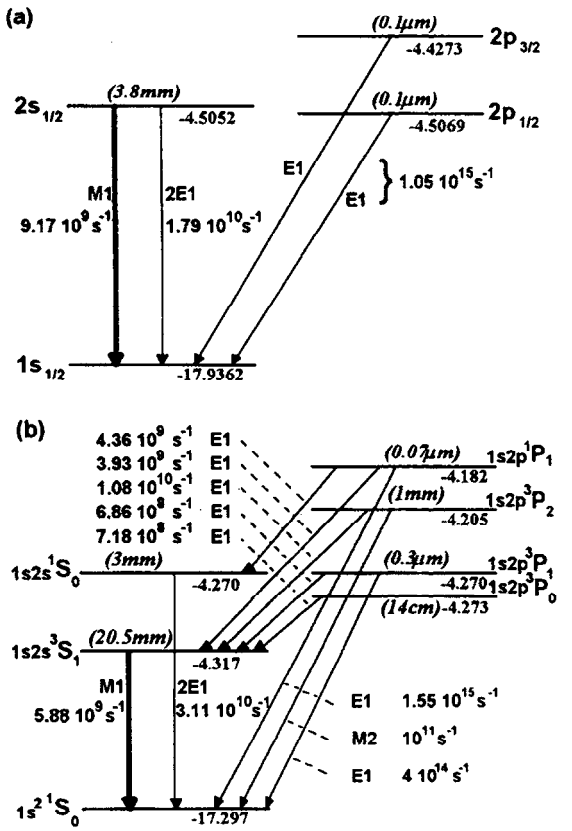

Fig. 1. Low energy level diagrams and radiative transition rates for H-like (a) and He-like (b) Kr ions. Energies are in keV. The distances in parentheses represent the mean free path in the laboratory frame for an ion travelling at a velocity $v = 0.343c$. $2s \rightarrow 1s$ and $2^3S_1 \rightarrow 1^1S_0$ M1 transitions, that are of interest in this work, are indicated by a thicker line.

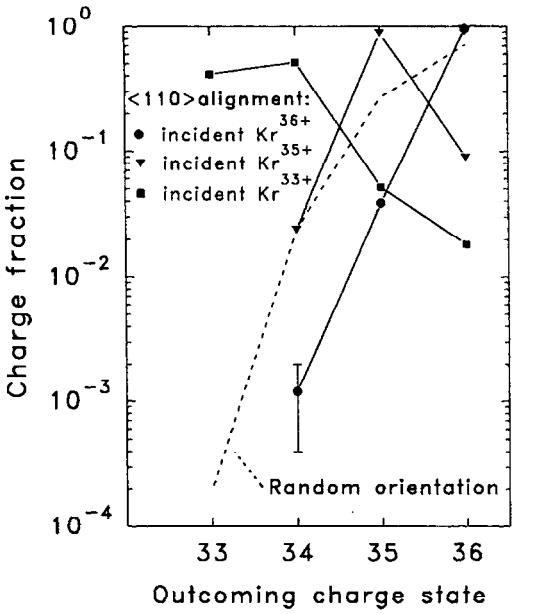

Fig. 2. Charge state distributions obtained with 60 A MeV krypton ions of various incident charge states, emerging from a 37 μm Si crystal, for alignment with the ⟨110⟩ axis, and for random incidence.

from the crystal were charge- and energy-analysed by means of a magnetic spectrometer. A Si(Li) diode was set at 90° and at a distance of 17 cm from the beam. A 3 mm thick lead shield was inserted between the crystal and the detector, in such a way that photons emitted inside the crystal could not be detected. The absolute dose was monitored by a beam chopper. A more detailed description will be given in a forthcoming paper on our REC measurements [12].

Charge state distributions, measured with a multiwire proportional gas chamber, are presented in Fig. 2 for respective incident charges 33+ , 35+ and 36+ , for both axial and random crystal orientations. In the latter case, the distributions for the three incident charges are found identical, indicating charge equilibrium. This result is well reproduced by a depth dependent calculation of projectile charge states, using the code ETACHA [1,2], that gives the evolution of each *nl* state for random orientation. For Kr^{36+} incident ions in ⟨110⟩ alignment, the single collision regime for electron capture (by REC) is found to be valid since only 4% of the incident ions could capture one electron, and less than 0.2% of them captured two electrons successively. For Kr^{35+} incident ions, the probability

Table 1
Measured probabilities and corresponding mean free paths for various charge-exchange processes for 60 A MeV Kr ions channeled in a 37 μm Si crystal aligned along the ⟨110⟩ axis. Capture probabilities are given for a bare ion. Ionization probabilities are given per electron on the corresponding shell

	K-REC	L-REC (2s-REC)	K-EII	L-EII
Probability 37 μm Si⟨110⟩	0.03 ± 0.005	0.006 ± 0.001 (0.005 ± 0.001)	0.09 ± 0.015	0.4 ± 0.06
Mean free path λ [μm]	1210 ± 200	6100 ± 1000 (7300 ± 1400)	392 ± 62	72 ± 11

of losing the K-electron by target electron impact ionization is 9%. For Kr^{33+} incident ions, the probability of at least one EII reaches $\simeq 60\%$, and the capture probability (by L-, M- $\cdots$ REC) is too small to be measured. As only unchanneled ions can lose three electrons (see Table 1), the unchanneled fraction of the beam can be deduce from the 36+ fraction, and is estimated to be 2%. All these numbers are confirmed by the analysis of X-rays emitted by the projectile at the crystal site, and detected at 90° and 125° by two Ge detectors [12]. Extracted probabilities for single charge exchange events by a channeled ion are given in Table 1, together with the corresponding mean free paths. From this we will deduce the production rates of the metastable states of Kr^{35+} and Kr^{34+}, as discussed below.

3. Results and discussion

In Fig. 3 we present three delayed X-ray spectra obtained with the Si(Li) detector for random incidence (Fig. 3a), for alignment conditions of Kr^{33+} (Fig. 3b) and Kr^{36+} (Fig. 3c) incident ions respectively. The three spectra are normalized to the same number of incident ions. In random conditions (Fig. 3a), as charge equilibrium is reached, different incident charges lead to the same spectrum. The He-like $2^3S_1 \rightarrow 1^1S_0$ M1 transition is clearly observable, with a low energy tail due to the Doppler shift accompanying the exponential attenuation within the 2 cm decay length after the crystal. Unfortunately, the $2s \rightarrow 1s$ H-like M1 transition (12.5 keV) cannot be distinguished from the Pb L_β fluorescence line at 12.6 keV (that is expected to be of the same order of magnitude as the Pb L_α line which is clearly seen at 10.5 keV). These lines are part of the fluorescence X-ray spectrum due to the material in the target chamber: Ni, Fe, Cu and Pb of the shield. Fig. 3 shows that this fluorescence is reduced by a factor of 2 in alignment conditions (a continuous background, due to surrounding radioactivity, is also present and depends mainly on acquisition duration). All we can say is that the H-like contribution appears smaller than the He-like one. However as the lead shield could have masked a zone extending at most up to 2 mm after the crystal, the corresponding counting loss could reach about 40% for the H-like case and 10% for the He-like case (cf. the "radiative" path lengths of Fig. 1). In this latter case, from our estimated detection solid angle of $\Omega/4\pi = (5.3 \pm 0.5) \times 10^{-5}$, we deduced a 2^3S_1 population of $(6.8 \pm 1.6) \times 10^{-4}$, and the value predicted by the code ETACHA, that takes *nl–nl'* intrashell excitations into account within the PWBA approximation, is 5.8×10^{-4}, then in rather good agreement. However, the test of PWBA is not very severe, since a variation by a factor 2 of the given cross section in the code ETACHA leads to a variation of only 16% of the 2^3S_1 population (this means that other processes such as capture, ionization and intershell excitation dominate the evolution of the population of this state).

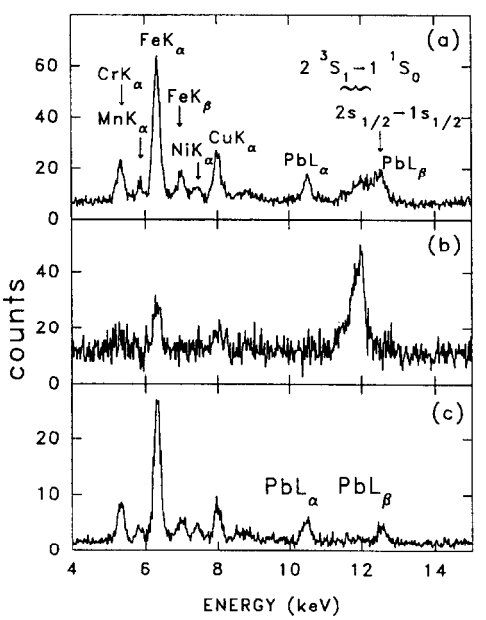

Fig. 3. Spectra of delayed photons detected at 90° from the beam axis. The crystal target area was hidden to this detector. (a) Random crystal orientation, (b) ⟨110⟩ alignment conditions with Kr^{33+} incident ions, (c) ⟨110⟩ alignment conditions with Kr^{36+} incident ions. The three spectra are normalized to the same number of incident ions.

In the spectrum of Fig. 3b, obtained with incident Kr^{33+} ions, the $2^3S_1 \rightarrow 1^1S_0$ line is clearly observed. The shape of the line has been reproduced by a simulation taking into account the detection geometry, the detector resolution and a decay length of 2 cm (lifetime of 2×10^{-10} s). The area of this peak can then lead to an estimate of the fraction of ions emerging in the metastable state 2^3S_1, which is found to be $(2.3 \pm 0.5) \times 10^{-3}$ of the total transmitted beam. The uncertainty is due to statistics, background subtraction and solid angle determination. We compare now this number with the production yield of the metastable 2^3S_1 state, that can be calculated if intrashell collisional mixing is disregarded: the most probable way of getting this 2^3S_1 state is the removal of one of the two K-electrons by target electron impact ionization, the two other electrons remaining unperturbed (note that the same process could lead to the 2^1S_0 state, the relative probability being proportional to the $(2J + 1)$ term). If we neglect less probable multistep processes, the probability for getting a metastable 1s2s 2^3S_1 state from an incident $1s^22s$ Kr^{33+} ion in a target of thickness t may then be written

$$P(^3S_1) = \frac{3}{4}\frac{1}{\lambda_{K-EII}}\int_0^t e^{\frac{-2x}{\lambda_{K-EII}}} \cdot e^{-\frac{(t-x)}{\lambda_{K-EII}}} \cdot e^{-\frac{t}{\lambda_{2s-loss}}}\, dx, \quad (1)$$

in which the first exponential factor (when divided by λ_{K-EII}) corresponds to the probability for a K-electron to be lost between x and $x + dx$, and the two other exponential factors correspond to the probability for the other K-electron and the 2s electron, respectively, to stay in their initial state (cf. Table 1). The factor 3/4 corresponds to the probability of forming a triplet state (see above). Note that the radiative decay of the 2^3S_1 state is negligible inside the target itself, which means that $\lambda_{2s-loss}$ is here taken equal to λ_{L-EII}. The calculated value of $P(^3S_1)$ is 0.075 ± 0.02. The comparison of this number with the measured value $(2.3 \pm 0.5) \times 10^{-3}$ clearly shows that the $^3S_1$ state is in fact rapidly depopulated inside the crystal. The process that may depopulate this state is the collisional nl–nl' intrashell excitation. Eq. (1) is no longer valid, since one has to consider 2s → 2p transitions, as well as 2p → 2s transitions that populate the 2^3S_1 state (note that the 2p → 2s transition does not occur in the H-like case, since all 2p states decay promptly to the 1s ground state). Each transition occurs between states that have the same spin, and is weighted by the ratio of the final to the initial degeneracy factor $g_F/g_I = (2J_F + 1)/(2J_I + 1)$. We performed a simulation to extract the value λ_{2s-2p} of the mean free path for 2s–2p collisional excitation, in which we determine the evolution of the populations of the four $^3S_1$, $^3P_0$, $^3P_1$ and $^3P_2$ triplet states inside the crystal target after K-ionization, as a function of λ_{2s-2p}. Further K- and L-ionization probabilities were taken into account. For low values of λ_{2s-2p} ($\lambda_{2s-2p} \ll t$), we assumed that all 1s2l states are statistically populated $(2J + 1)$, at the time of the projectile K-electron removal. Another assumption was that λ_{2s-2p} does not depend on the transition energy (it is confirmed in this case by the PWBA calculations). Then the main contribution to the triplet state depopulation is $^3S_1 \rightarrow {}^3P_1$, since the lifetime for radiative $2^3P_1 \rightarrow 1^1S_0$ deexcitation is much smaller than that for collisional mixing, as far as $\lambda_{2s-2p} \geq 1$ μm (cf. Fig. 1).

The result leads to $\lambda_{2s-2p} = 1.0$ μm (with $0.7 \leq \lambda_{2s-2p} \leq 1.7$ μm). This value validates our hypothesis that $\lambda_{2s-2p} \ll t$. We can then deduce a cross section per target Si atom: $\sigma_{2s-2p} = 2.4 \times 10^{-19}$ cm^2 ($1.7 \times 10^{-19} \leq \sigma_{2s-2p} \leq 4.0 \times 10^{-19}$ cm^2). Within these uncertainties, this value is only slightly smaller than the theoretical one obtained within the PWBA approximation (4.1×10^{-19} cm^2). However, since we cannot verify whether PWBA describes correctly 2s–2p excitation for random conditions (see above), we cannot conclude on a reduction of intrashell excitation in channeling (if, as in Ref. [11], the PWBA cross section is too small by a factor 2 , then the 2s–2p excitation probability would be reduced by a factor 2 to 5 by channeling).

Let us consider now the last spectrum (Fig. 3c), obtained with Kr^{36+} incident ions in channeling conditions. Here the He-like $2^3S_1 \rightarrow 1^1S_0$ line does not emerge from the background, since the Kr^{34+} emergent fraction is quite small (cf. Fig. 2). As in random conditions, we cannot observe the H-like 2s → 1s line, since the Pb L_α and Pb L_β lines are present. In this case however, we have also recorded X-ray spectra (Fig. 4) where photons were detected in coincidence with well channeled transmitted Kr^{35+} ions (Fig. 4a) and Kr^{34+} ions (Fig. 4b) by selecting half of the ions with low energy loss. The spectrum (Fig. 4a) is similar to fortuitous coincidence spectra and thus shows that the 2s → 1s transition is not observed within our statistics. We find that the absence of this transition is compatible with the value of λ_{2s-2p} obtained above, taking into account that detection might be delayed until 2 mm after the crystal. On the contrary we do observe the $2^3S_1 \rightarrow 1^1S_0$ transition in the spectrum (Fig. 4b), and the corresponding $P(2^3S_1)$ value is $(11.1 \pm 3) \times 10^{-6}$. As the metastable He-like state is formed mainly by a sequence of two REC events, the second one being a capture into the L shell, we can again deduce the cross section for 2s–2p mixing, by means of a simulation of the same kind as above: $\sigma_{2s-2p} = 3.8 \times 10^{-19}$ cm^2 ($1.4 \times 10^{-19} \leq \sigma_{2s-2p} \leq 9.4 \times 10^{-19}$ cm^2), which agrees with the value deduced above from our Kr^{33+} experiment.

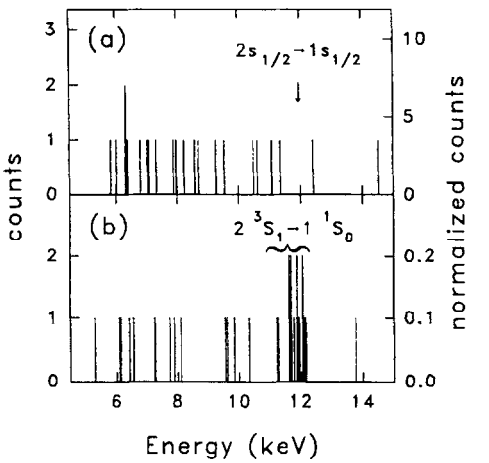

Fig. 4. Delayed photon spectra (for incident Kr^{36+} ions) in coincidence with well channeled transmitted ions of charge state 35+ (a) and 34+ (b). The left scale corresponds to the normalization to the same number of incident ions as in spectrum of Fig. 3c.

4. Conclusion

We have studied the populations of metastable states 2^3S_1 and $2s_{1/2}$ of Kr^{34+} and Kr^{35+} ions respectively, coming out from a 37 μm Si crystal in channeling conditions. Both populations are strongly reduced inside the crystal. In both cases this reduction is due to 2s–2p collisional intrashell excitation. We could determine the corresponding cross section, and, within an accuracy of

50%, we found it only slightly smaller than a PWBA calculation for a neutral target atom.

References

[1] J.-P. Rozet et al., J. Phys. B22 (1989) 33.
[2] J.-P. Rozet, C. Stephan and D. Vernhet, these proceedings (SHIM 95), p. 67.
[3] S. Andriamonje et al., Phys. Rev. Lett. 59 (1987) 2271.
[4] N. Claytor et al., Phys. Rev. Lett. 61 (1988) 2081.
[5] A. l'Hoir et al., Nucl. Instr. and Meth. B 48 (1990) 45.
[6] J.-P. Desclaux, private communication.
[7] J. Hata and I.P. Grant, J. Phys. B14 (1981) 2111.
[8] R. Marrus, Adv. At. Mol. Phys. 14 (1978) 181.
[9] J.H. McGuire, D.J. Land, J.G. Brennan and G. Basbas, Phys. Rev. A 19 (1979) 2180.
[10] P. Nicolai et al., J. Phys. B 23 (1990) 3609.
[11] L. Adoui et al., Nucl. Instr. and Meth. B 98 (1995) 312.
[12] S. Andriamonje et al., to be published.

Un autre aspect remarquable de l'interaction ion-solide qui peut être mis en évidence par la canalisation d'ions très lourds est la polarisation du gaz d'électron, induite par la forte perturbation que cause un ion très chargé et peu rapide au gaz dense des électrons d'un solide. Cette perturbation est un effet collectif, qui conduit à des fluctuations de la densité électronique au voisinage de l'ion. Si la propagation de ces fluctuations est moins rapide que l'ion, il se développe des fronts d'interférences à la manière des vagues dans le sillage d'un bateau (d'où le nom d'effet de sillage).

Une description de l'effet de sillage en terme de perturbations au 1er ordre [Echenique 79] montre que la variation relative de la densité électronique locale (sur le site même de l'ion) est égale à $\Delta\rho / \rho = \pi Z_p v_0 / v$, où Z_p et v sont la charge et la vitesse du projectile, et v_0 la vitesse de Bohr. Cette même théorie de la réponse linéaire du milieu prévoit un déplacement du niveau d'énergie du continuum, et donc de l'énergie de liaison des électrons, de $\lim_{r\to 0}\left(\Phi - Z_p e^2 / r\right) = -\pi Z_p \hbar\omega_p / 2\left(v / v_0\right)$, où $\Phi(r)$ est le potentiel de sillage, et ω_p la pulsation de plasmon associé au gaz d'électrons.

La densité électronique locale et le potentiel dépendent donc du projectile *via* le paramètre $\zeta = Z_p v_0 / v = \eta^{-1/2}$, η étant le paramètre d'adiabaticité.

Une étude de l'amplitude de l'effet de sillage sur le site de l'ion peut être faite au moyen d'un processus permettant de caractériser ce gaz d'électrons localement : c'est le cas de la capture REC en couche interne d'un ion lourd. En effet, la capture radiative est un processus local, au sens où un électron est capturé à un paramètre d'impact de l'ordre de l'extension de la fonction d'onde dans l'état final. L'énergie des photons REC, somme de l'énergie cinétique de l'électron à capturer dans le référentiel du projectile et de l'énergie de liaison de cet électron dans l'état final, traduit le décalage en énergie induit par le sillage. La probabilité de REC est directement proportionnelle à la densité électronique locale.

Une étude en canalisation a été réalisée par Tribedi et al. [Tribedi 95] avec des ions légers, et pour des valeurs de ζ proches de 1. Leurs résultats semblent montrer une évolution du décalage en énergie des photons REC-K en fonction de ζ.

En ce qui concerne la densité électronique locale, une différence systématique entre sections efficaces de REC mesurées en cibles solides et cibles gazeuses a été observée par Stöhlker et al. [Stöhlker 98], et peut être interprétée par l'effet de sillage en cible dense.

Les ions très lourds et très chargés, ralentis et extraits de l'anneau ESR du GSI, permettent d'obtenir les perturbations les plus fortes pour des ions rapides.

L'article ci-dessous *"Electron gas polarization effect induced by heavy H-like ions of moderate velocities channeled in a silicon crystal"* par E. Testa et al. [Testa 06], correspond aux mesures réalisées lors des expériences de 2001 et 2003, avec des ions U^{91+} de 20 MeV/u et Pb^{81+} de 13 MeV/u. Elles ont permis d'atteindre des valeurs de $\zeta = 3{,}3$ et 3,6 respectivement. L'analyse spectroscopique minutieuse a été réalisée par Etienne Testa, et est rapportée dans sa thèse.

Les conditions de ces expériences sont telles que la capture REC ne peut se produire que sur les électrons de valence, car la MEC bloque très rapidement la REC-K et L dans la cible pour les ions mal canalisés, ce qui permet de ne pas avoir à prendre en compte un éventuel décalage en énergie des photons REC dû aux électrons de cœur de la cible (ce décalage intervient à la fois par leur énergie de liaison, et par la dispersion en énergie des photons REC, couplée avec une forte variation de la section efficace avec l'énergie). Ce décalage n'a certainement pas été pris en compte par Tribedi et al.

Available online at www.sciencedirect.com
SCIENCE DIRECT
Nuclear Instruments and Methods in Physics Research B 245 (2006) 47–51
NIM B
Beam Interactions with Materials & Atoms
www.elsevier.com/locate/nimb

Electron gas polarization effect induced by heavy H-like ions of moderate velocities channeled in a silicon crystal

E. Testa [a], D. Dauvergne [a,*], A. Bräuning-Demian [b], F. Bosch [b], H. Bräuning [c], M. Chevallier [a], C. Cohen [d], A. Gumberidze [b], S. Hagmann [b], A. L'Hoir [d], R. Kirsch [a], C. Kozhuharov [b], D. Liesen [b], P.H. Mokler [b], J.-C. Poizat [a], C. Ray [a], J.-P. Rozet [d], Th. Stöhlker [b], S. Toleikis [b], M. Toulemonde [e], P. Verma [b]

[a] *Institut de Physique Nucléaire de Lyon, CNRS-IN2P3, Université Claude Bernard Lyon 1, F-69622 Villeurbanne, France*
[b] *Gesellschaft für Schwerionen Forschung (GSI), D-64291 Darmstadt, Germany*
[c] *Institut für Kernphysik, Justus Liebig Universität, D-35392 Giessen, Germany*
[d] *Institut des Nano-Sciences de Paris, CNRS-UMR75-88, Universités Paris VI et Paris VII, 75251 Paris cedex 05, France*
[e] *Centre Interdisciplinaire de Recherche Ions-Lasers, UMR 11, CEA-CNRS, 14040 Caen cedex, France*

Available online 28 December 2005

Abstract

We report on the observation of a strong perturbation of the electron gas induced by 20 MeV/u U^{91+} ions and 13 MeV/u Pb^{81+} ions channeled in silicon crystals. This collective response (wake effect) induces a shift of the continuum energy level by more than 100 eV, which is observed by means of radiative electron capture into the K- and L-shells of the projectiles. We also observe an increase of the REC probability by 20–50% relative to the probability in a non-perturbed electron gas. The energy shift is in agreement with calculations using the linear response theory, whereas the local electron density enhancement is much smaller than predicted by the same model. This shows that, for the small values of the adiabaticity parameter achieved in our experiments, the density fluctuations are not strongly localized in the vicinity of the heavy ions.

PACS: 61.85.+p; 34.70.+e

Keywords: Channeling; Highly charged ions; Radiative electron capture (REC); Wake effect

1. Introduction

Highly charged ions of moderate velocities induce a strong perturbation of the electron gas in a solid. This perturbation consists in a dynamic screening of the projectile charge by the electrons of the medium. If the particle propagates much faster than the Fermi velocity of the electrons, a trailing polarization cone takes place, which is due to the collective excitation of the electron gas (wake effect). The wake potential manifests itself through the electric field, acting as the stopping force on the projectile, and is also responsible for a Stark splitting of bound states of an ion, which influences the transport of excited states in solids. For a review on the wake effect, see e.g. [1–3] and references therein. In the vicinity of the projectile, the polarization of the electron gas produces a shift, relative to vacuum, of the continuum energy levels in the projectile frame. This reduces the absolute binding energies of electrons in an ion. Echenique et al. [2] estimated this shift, using the linear response theory, to be $\lim_{r\to 0}(\Phi - Z_p e^2/r) = -\frac{\pi Z_p \hbar\omega_p}{2v/v_0}$, where Φ is the potential, Z_p and v are the ion charge and velocity, respectively, $\hbar\omega_p$ the plasmon excitation energy of the target electrons,

* Corresponding author. Tel.: +33 4 72 44 62 57; fax: +33 4 72 43 14 52.
E-mail address: d.dauvergne@ipnl.in2p3.fr (D. Dauvergne).

0168-583X/$ - see front matter © 2005 Elsevier B.V. All rights reserved.
doi:10.1016/j.nimb.2005.11.073

and v_0 the Bohr velocity. For a free electron gas of density ρ_e, $\omega_p = (4\pi\rho_e e^2/m_e)^{1/2}$, where m_e is the electron mass. Also related to the wake are the fluctuations of the electron density around the projectile. Still within the first order perturbation, the authors of [2] also predicted that the relative enhancement of the local electron density ρ_e should be $\Delta\rho_e/\rho_e = \pi Z_p v_0/v$.

Practically, transitions between bound states of an ionic projectile may be affected only by Stark splitting of these states, whereas transitions between continuum states and bound states are modified in energy. Among them, radiative electron capture (REC) of target electrons provides a local probe for the electron gas polarization in a solid. First, since REC consists in the emission of a photon, the energy of which is the sum of the kinetic energy of the target electron in the ion frame, and the binding energy in the final bound state, it gives access to the energy shift (decrease of the emitted photon energy) [3,4]. Second, REC into deeply bound states of a heavy ion is a very localized process (at the scale of the final bound orbital size). So the measurement of absolute REC probabilities is a test for a possible enhancement of the local electron density at the projectile site.

The problem arising is that strong enough perturbations to be measurable are obtained for high Z_p/v values, for which REC is hardly observable in solids, because it requires inner-shell vacancies.

Ion channeling leads to a non homogeneous flux inside a crystal, preventing ions from undergoing close impact parameter collisions with target atoms. Thus channeled ions sample mainly the quasi-free valence electron gas, and close interaction with core electrons is substantially attenuated. This allows REC to be the dominant electron capture process, even at low energy. Another interesting feature related to the impact parameter distribution is that detailed information can be obtained by analyzing the shape of REC lines, which depends on the longitudinal momentum distribution of the target electrons in their initial state (Compton profile). In particular this enables to identify the contributions of core electrons, and valence or conduction electrons [6]. Finally, the knowledge of the ion flux in the crystal, combined with the precise measurements of the REC line intensities, allows one to evaluate the electron density at the ion site.

2. Experiment

We used 20 MeV/u U^{91+} and 13 MeV/u Pb^{81+} ions extracted from the GSI–ESR storage ring, for which $Z_p v_0/v$ values are 3.26 and 3.57, respectively. The process for cooling, deceleration and slow extraction of H-like ions by radiative recombination inside the electron cooler has been described in [7]. During the extraction cycle, a continuous beam of some 10^4 ions/s is sent onto the target with an angular divergence suitable for channeling experiments. The beam impact on the target is less than 3 mm in width, and 7 mm in height. A 9.6 μm thick (1 1 1) Si crystal (tilted at 35° for alignment along the ⟨1 1 0⟩ axis) was used as a target during the experiment with U^{91+} ions. For the Pb^{81+} ion experiment, a thin (0.8 μm) (1 0 0) silicon crystal was tilted at 45° to allow the same axial orientation. Transmitted ions were charge- and energy-analyzed by a magnetic spectrometer, and detected at the focal point by a 2D- position sensitive particle detector.

X-rays emitted at the target were detected by a 1 cm thick germanium detector at 90° from the beam direction. The detector was set at 135 mm from the beam impact in both experiments. The Doppler broadening of X-rays by the detector angular aperture was limited by vertical collimating slits of lead (6 mm) in the U^{91+} experiment, and of tantalum (8 mm) for the Pb^{81+} experiment.

The acquisition was done event by event, allowing for instance the selection of coincidences between X-rays and a given charge state at emergence.

3. Results

Part of the experimental details and results has been reported already in [8] for the U^{91+} experiment. In particular the charge state distribution for ⟨1 1 0⟩ axial orientation of the 11 μm thick target showed a fraction of ~25% of frozen ions, and about the same for ions emerging as 90+. For the latter most of the capture was due to REC. An illustration is given in Fig. 1, which shows X-rays recorded for both axial and random incidences during this experiment. The axial spectrum is recorded in coincidence with ions emerging from the crystal with the charge 90+, i.e. ions having captured only one electron. In the axial spectrum, the K-REC and L-REC peaks are observed with a very good statistics, whereas they are reduced by nearly

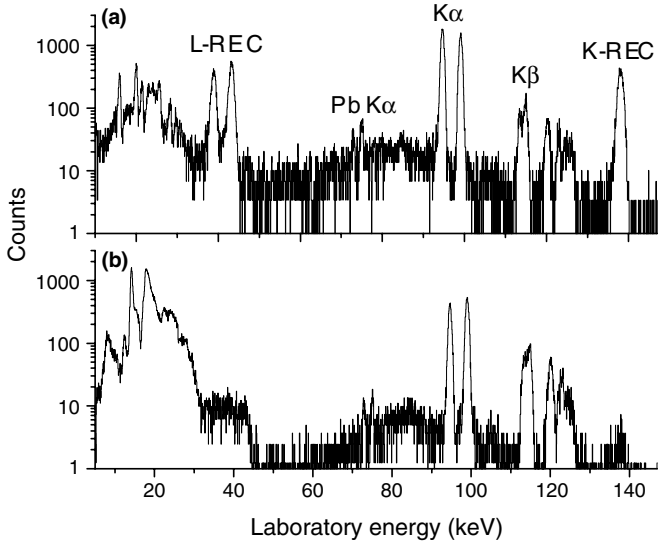

Fig. 1. X-ray spectra detected at 90° from the beam direction for U^{91+} ions incident on a 11 μm thick silicon crystal. (a) ⟨1 1 0⟩ axial orientation, in coincidence with ions transmitted in the 90+ charge state. (b) Random orientation. Both spectra are normalized to the same number of selected transmitted ions.

two orders of magnitude for a random orientation. The non-radiative capture (or mechanical electron capture, MEC) is the dominant capture process in random geometry. In this case, charge state equilibrium is reached and K- and L-shell vacancies are rapidly filled below the surface. The signature of MEC is still present in the axial spectrum, with the presence of K and L lines, that come from a large part from decays after MEC into excited states ($n > 2$). For well channeled ions, like ions emerging as 90+, most of the MEC events occur in the thin amorphous layers at the crystal surfaces. For a more detailed discussion on the X-ray spectra, see [8].

The situation is similar for 13 MeV/u Pb^{81+} ions channeled in a 1.1 μm crystal. In this case the frozen ion fraction was 60%, and the 80+ fraction was 20%. The target being much thinner, the statistics on REC are lower than in the former experiment. A spectrum recorded for the axial orientation, in coincidence with He-like transmitted ions, is shown in Fig. 2. The proportion of K lines is higher, due to the larger relative contribution of amorphous layers to the MEC single capture events.

Both spectra in Figs. 1 and 2 are not corrected for detection efficiency.

The measurements of absolute energy shifts for REC peaks require precise energy calibration. This was made in various ways in the whole energy range described here. First radioactive γ-ray sources were used, without the beam on target. We also used the Pb and Ta Kα fluorescence lines (for instance the Pb Kα lines can be observed on the spectra of Fig. 1). Additional information for the linear calibration offset is obtained by setting the differences between K- and L-REC peak energies equal to the Kα energies. The precise knowledge of the K and L peak energies in the laboratory frame allows the correction of the Doppler shift of the photon energy emitted by fast projectiles: the derivative of the Doppler shift is maximum at 90°, and so a small deviation of the mean laboratory angle has to be taken into account. The energy loss inside the target was taken into account to determine the mean energy of REC photons emitted during the path of the ions in the crystal. For Pb^{81+} in the 1.1 μm thick target the energy loss was almost negligible.

As done in [6], we have performed simulations based on the statistical flux equilibrium for channeled ions in the crystal, according to the experimental conditions (beam angular divergence, energy loss, Doppler shift and broadening, detector resolution). These simulations provide the full calculation of the REC line shape, conditioned by the local electron density sampled by channeled ions. The Compton profile is calculated using the local density approximation of a free valence electron gas. For core electrons, an impact parameter dependent Fourier transform of spatial wave functions is performed. Fig. 3 shows the results of such a simulation for the K-REC line shape of U^{91+} ions in the laboratory frame. This simulation was made assuming that all incident ions in channeling conditions could undergo REC in the crystal. Among them, ions with a high transverse energy can approach the target atoms sufficiently close, so that they can capture core electrons of silicon. The corresponding Compton profile is much broader than the Compton profile of valence electrons. As silicon atoms have 10 core electrons and 4 valence electrons, one can see that the calculated rate for the capture of core electrons is strongly reduced by channeling. In order to reproduce our experimental observations (angular scans), we used a beam angular divergence made of two components: a narrow one (85% of the beam), of rms $\sigma_x = \sigma_y = 0.2$ mrad, and a broad one (15%), rms $\sigma_x = \sigma_y = 3.5$ mrad (i.e. larger than the channeling critical angle). According to this, the mean sampled electron densities are calculated to be 0.16 $e^- Å^{-3}$ for valence electrons, and 0.053 $e^- Å^{-3}$ for core electrons. The experimental peak is superimposed on the calculations. One can see that the calculated core electron contribution is obviously overestimated, and that valence electrons represent almost all the contribution to the K-REC peak. Actually, as we already stated in [8], ions with high enough transverse energy to

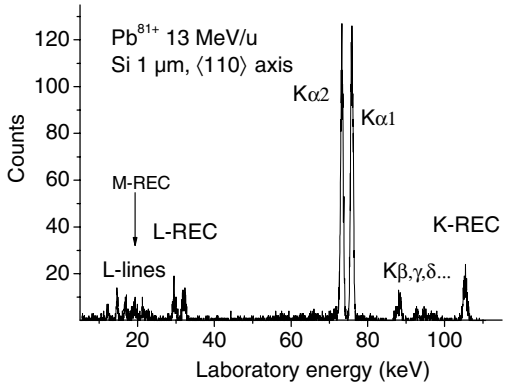

Fig. 2. X-ray spectrum detected at 90° for Pb^{81+} incident ions at 13 MeV/u on a 1.1 μm thick silicon crystal, aligned along the ⟨1 1 0⟩ direction.

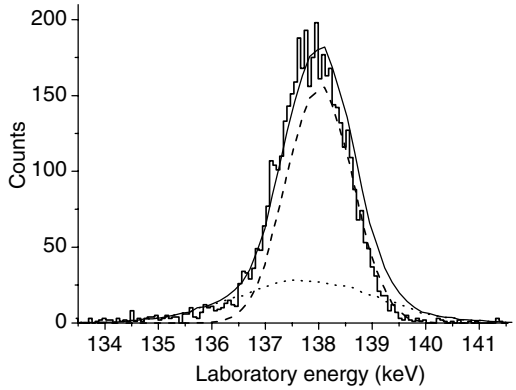

Fig. 3. K-REC line shape at 90° in the laboratory frame for 20 MeV/u U^{91+} ions channeled in the ⟨1 1 0⟩ axis of a 11 μm silicon crystal. Histogram: experiment. Solid line: simulation. The contributions from the capture of core silicon electrons (dotted line) and valence electrons (dashed line) are shown. The height of the calculated peak has been normalized to the experimental one.

approach the target atoms as close as 0.5 Å undergo many MEC capture events, which rapidly fill their inner-shell and prevent REC to occur. So only ions with a restricted transverse energy are able to make REC in the target. The simulations show that their mean sampled electron density is 0.17 $e^- Å^{-3}$. This is an important point since, as calculated for instance in [4], the strong dependence of REC cross section on the relative velocity of target electron would make REC peaks strongly asymmetric, which induces a negative average energy shift of the REC peak because of the Compton profile. This has to be taken into account to correctly estimate the wake shift. In the present case where mainly valence electrons are captured, the shift due to the Compton profile is minimum. The comparison between calculated and measured peaks in Fig. 3 exhibits a shift by about −100 eV for the experimental one, that we attribute to the wake effect.

The shift for the L-REC lines, which has to be the same as for K-REC, is also measured, and is found in agreement within the calibration uncertainties. Thus we present in Table 1 the measured values in both experiments, which are averaged for K- and L-REC. These shifts were measured by selecting REC photons in coincidence with He-like emergent ions, i.e. ions with a small transverse energy. The advantages are: (i) contributions of core electrons to REC are even smaller than in Fig. 3, (ii) their energy loss is minimum and (iii) no additional shift on the L-REC energy comes from the various lower charge states. The error bars come from the determination of the peak positions in the spectra, the X-ray energy calibration, the evaluation of the energy loss in the case of the uranium experiment, and the theoretical knowledge of the binding energies for the He-like ions (taken from [9]). Calculations for the energy shift were made using the commonly admitted formula indicated in the introduction, and using an electron gas density equal to the average valence electron density of silicon (i.e. $\hbar\omega_p = 16.6$ eV). This value assumes that the whole valence electron gas contributes collectively to the energy shift, i.e. that the polarization is a long range effect. It also supposes that core electrons of silicon do not contribute significantly to the collective response, which may somehow underestimate this response. The agreement between experimental and theoretical values is quite good.

As for the absolute REC cross-sections, they can be evaluated, although the absolute detector efficiency was not measured by another mean than by geometrical calculations. When looking at Figs. 1 and 2, one can get an absolute normalization of the X-ray yields, since all the ions having captured at least one electron in the crystal have emitted one, and only one, photon corresponding to the filling of the K-shell. These photons are $K_{\alpha\beta\ldots}$ and K-REC (in this case the fluorescence yield is 100% for the initial K-vacancy). For a given charge state used to select X-rays, the yields of K- and L-REC photons in the spectra (corrected from the intrinsic detector efficiency), multiplied by the charge fraction, provide the K- and L-REC probabilities. Simulations, to be described in a forthcoming paper, allow us to estimate the mean unperturbed electron density $\langle\rho_e\rangle$ sampled by channeled ions, as a function of their emerging charge state. Accounting for the angular distribution of REC photons in the laboratory frame [10], one can then give the absolute value of the K- and L-REC probabilities. We use the Stobbe formulae [11] of REC cross sections σ_{REC}, which are commonly used to estimate the absolute REC cross-sections as a function of the adiabaticity parameter $\eta = (v/Z_p v_0)^2$ (assuming non-relativistic velocities for both the projectile and the electron in a bound orbital, η is the ratio of the kinetic energy of a target electron viewed by the projectile to the binding energy in the final state) [10]. The K- and L-REC probabilities are found to lie between 20% and 60% above the values given by $P_{REC} = 1 - \exp(-\sigma_{REC} \times \langle\rho_e\rangle \times \ell)$, where ℓ is the crystal thickness. Moreover, the non-relativistic dipole approximation calculations of Stobbe formulae tend to be systematically above the experimental values by at least 25%, as reviewed in [10]. Note that exact relativistic calculations have been performed by Eichler and Ichihara in the case of 20 MeV/u U^{91+} ions [12]. Their K-REC cross section is 20% lower than Stobbe's one, and higher n-REC cross-sections are in agreement within 10%. This justifies the use of Stobbe's values as a fairly good reference on one hand, and, on the other hand, makes our electron density enhancement even higher. Actually, some solid state measurements at high Z_p/v values tend to lead to higher values of the REC cross-sections. For instance, our former measurements of K-REC with 60 MeV/u Kr^{36+} ions ($Z_p v_0/v = 1.1$) under channeling conditions agree perfectly with the Stobbe formula (with an absolute uncertainty of ±10%) [6]. Tribedi et al. [5] used the linear response scaling [2] of the local electron density to explain the excess of REC cross-sections in channeling relative to gas targets. We prefer to consider an increase of electron density instead of an increase of cross-sections, which are defined for a single ion–electron (or ion–atom) collision. In the present case, this density enhancement would be by a factor 10, which is certainly not observed. However, our values are significantly above the calculations using a non-perturbed electron gas. We can already claim that the local density enhancement by the wake effect is not as localized as predicted by the linear response theory (which could be expected since we are not at all in a regime where $Z_p v_0/v \ll 1$). On the other hand, the induced potential at the projectile site results from an integration of the polarization over a very large scale (a typical scaling of the perturbation is given by $v/\omega_p \sim 10$ Å), which makes the

Table 1
Measured and calculated energy shifts of the continuum due to the electron gas polarization effect

	$Z_P v_0/v$	ΔE REC (eV)	$-\frac{\pi Z_p \hbar\omega_p}{2v/v_0}$ (eV)
U^{91+} 20 MeV/u	3.26	−92 ± 41	−85
Pb^{81+} 13 MeV/u	3.57	−122 ± 47	−93

The calculated values are given for a plasmon energy of 16.6 eV.

perturbation approximation more realistic for the REC energy shift than for the REC probability. However, in order to get a better understanding of the whole dynamic polarization effect on REC energies and probabilities, the comparison with REC during collisions in gas is highly desirable, as well as a non perturbative theoretical description of the effect.

4. Summary and conclusion

We have measured K- and L-REC with highly charged, decelerated heavy ions in channeling conditions, which allows to keep inner-shell vacancies, and to perform ion–electron interaction inside a solid target. We report on a very strong value of the energy shift due to the polarization of the dense electron gas sampled in the solid ($\sim$100 eV), in good agreement with theoretical expectations based on first order perturbation. Our data show an enhancement of the total REC probabilities with respect both to theoretical calculations (by 20–60% relative to the non-relativistic dipole approximation cross sections) and to measurements performed at $Z_p v_0/v \sim 1$ (by more than 50% compared to gas target experiments). This is likely due to the polarization effect around an ion, this effect being much smaller than predicted by the linear response theory.

Acknowledgements

We would like to thank J.M. Pitarke and M. Seliger for helpful discussions, and J. Eichler and A. Ichihara for providing us with REC cross-sections. The support by GSI-IN2P3 collaboration agreement #97-35 is acknowledged.

References

[1] J. Burgdörfer, Nucl. Instr. and Meth. B 67 (1992) 1.
[2] P.M. Echenique, R.H. Ritchie, W. Brandt, Phys. Rev. B 20 (1979) 2567.
[3] T. Minami, C.O. Reinhold, M. Seliger, J. Burgdörfer, C. Fourment, B. Gervais, E. Lamour, J.-P. Rozet, D. Vernhet, Nucl. Instr. and Meth. B 193 (2002) 79.
[4] J.M. Pitarke, R.H. Ritchie, P.M. Echenique, Phys. Rev. B 43 (1991) 62.
[5] L.C. Tribedi, V. Nanal, M.B. Kurup, K.C. Prasad, P.M. Tandon, Phys. Rev. A 51 (1995) 1312.
[6] S. Andriamonje, M. Chevallier, C. Cohen, N. Cue, D. Dauvergne, J. Dural, F. Fujimoto, R. Kirsch, A. L'Hoir, J.-C. Poizat, et al., Phys. Rev. A 54 (1996) 1404.
[7] H.T. Prinz, D. Dauvergne, S. Andriamonje, K. Beckert, M. Chevallier, C. Cohen, J. Dural, H. Eickhoff, B. Franzke, H. Geissel, et al., Hyperfine Interact. 108 (1997) 325;
S. Andriamonje, K. Beckert, M. Chevallier, C. Cohen, D. Dauvergne, J. Dural, H. Eickhoff, B. Franzke, H. Geissel, R. Kirsch, et al., J. Phys. B 30 (1997) 5099.
[8] D. Dauvergne, A. Bräuning-Demian, F. Bosch, H. Bräuning, M. Chevallier, C. Cohen, A. Gumberidze, R. Kirsch, C. Kozhuharov, A. L'Hoir, et al., Nucl. Instr. and Meth. B 205 (2003) 773.
[9] G.W. Drake, Can. J. Phys. 66 (1988) 586.
[10] Th. Stöhlker, C. Kozhuharov, P.H. Mokler, A. Warczak, F. Bosch, H. Geissel, R. Moshammer, C. Scheidenberger, J. Eichler, A. Ichihara, et al., Phys. Rev. A 51 (1995) 2098.
[11] H.A. Bethe, E.E. Salpeter, Quantum Mechanics of One- and Two-Electron Atoms, Springer Verlag, Berlin, 1957.
[12] J. Eichler, A. Ichihara, private communication.

Les figures ci-dessous permettent de compléter cet article, en comparant nos mesures du décalage en énergie du continuum, mesuré à partir des photons REC-K et L, avec celles de Tribedi et al. (Figure 7). Les valeurs de ce décalage sont en bon accord avec les calculs selon la théorie de la réponse linéaire (perturbations au premier ordre), bien que cette théorie ne soit pas valable pour une perturbation aussi forte.

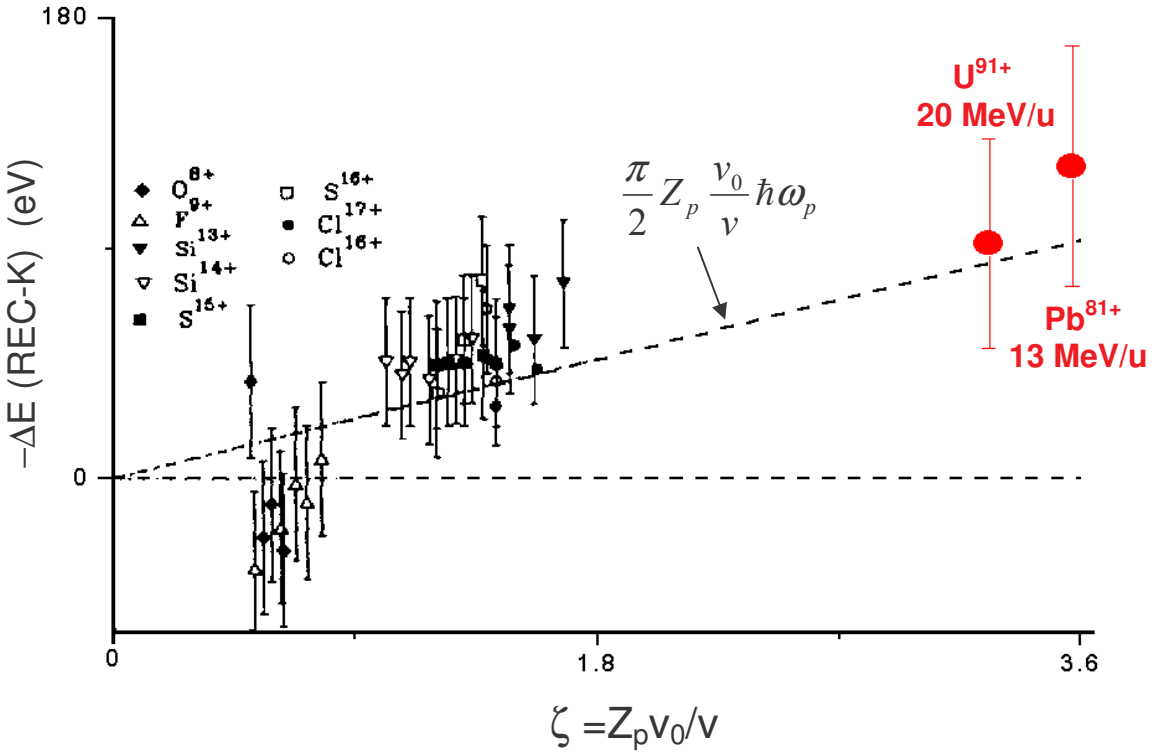

Figure 7 : *déplacement en énergie des raies REC-K et L dû au potentiel de sillage d'un ion en conditions de canalisation dans un cristal de silicium. Les données pour ζ <1,8 sont extraites de [Tribedi 95]. La courbe en pointillés correspond à un calcul perturbatif [Echenique 79] pour un gaz d'électrons libres de densité 0,2 $e^-/Å^3$ ($\hbar\omega_p = 16{,}6\ eV$). Les points en rouge correspondent à nos données avec des ions lourds ralentis au GSI ([Testa 06]).*

La figure 8 présente les valeurs de sections efficaces de REC-K par lacune K du projectile et par électron cible en fonction du paramètre d'adiabaticité. Ces valeurs ont été synthétisées par Thomas Stöhlker [Stöhlker 95]. Nous les comparons aux valeurs mesurées en conditions de canalisation par notre collaboration ([Andriamonje 87], [Andriamonje 96], [Testa 06]). Notons que pour le point avec les ions Kr^{36+} de 60 MeV/u, nous disposons d'une normalisation absolue hors canalisation, d'où la très faible barre d'erreur. La différence entre cibles solides et gazeuses n'est pas évidente sur les seules données du GSI. Cependant, on constate bien une augmentation systématique de nos valeurs mesurées par rapport aux valeurs calculées dans l'approximation dipolaire pour les faibles valeurs de η, ce qui n'est pas observé en cibles gazeuses. On peut associer l'augmentation de la section efficace en cible solide à une augmentation de la densité électronique locale (la section efficace par électron étant ce qu'elle est, indépendamment de la nature de la cible).

Cette augmentation de densité électronique aux faibles valeurs de η est très inférieure aux valeurs prédites par la théorie perturbative au 1er ordre : selon cette théorie, l'augmentation de

densité dans un gaz d'électrons libre devrait être d'un facteur 10 pour les plus faibles valeurs de η obtenues ici. Pour les projectiles U^{91+} de 20 MeV/u, nous obtenons un facteur d'augmentation relative $\Delta\rho / \rho = 1{,}5 \pm 0{,}3$.
Une mesure de section efficace à basse vitesse et en cible gazeuse dans l'anneau de stockage ESR permettrait de confirmer cet effet.

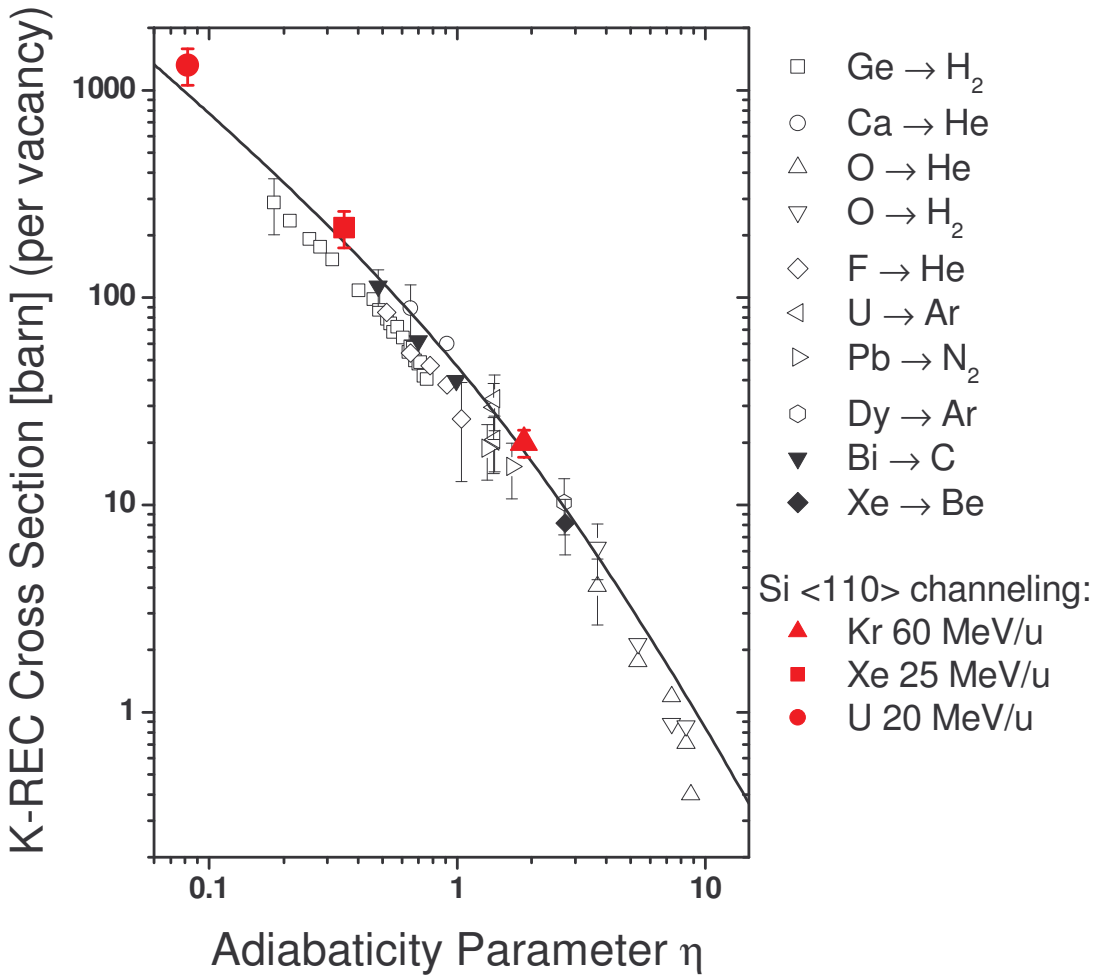

Figure 8 : Section efficaces de REC-K par lacune K et par électron cible, en fonction du paramètre d'adiabaticité. Les symboles en noir et blanc correspondent aux valeurs mesurées au GSI par Th. Stöhlker et al. [Stöhlker 95]. Symboles pleins : mesures en cibles solides. Symboles vides : cibles gazeuses. Les points en rouge correspondent aux mesures faites en conditions de canalisation axiale dans des cristaux de silicium par notre collaboration : ions Kr (canalisation et hors canalisation) : ref [Andriamonje 96], ions Xe : ref. [Andriamonje 87], ions U : ref. [Testa 06]. La courbe est un calcul théorique dans l'approximation dipolaire non-relativiste [Bethe 57].

La conclusion de ces deux observations semble être que la fluctuation de la densité associée à la forte perturbation d'un ion très chargé est peu locale (à l'échelles des orbitales K et L d'ions Pb ou U). L'intégration à grande distance, dont résulte le potentiel de sillage sur le site de l'ion, correspond bien à la valeur calculée par les théories au 1er ordre.
Des calculs non perturbatifs permettraient une estimation plus exacte de la densité électronique locale. De l'avis des théoriciens spécialistes, il s'agit de calculs laborieux…

1-5-2 Collisions proches : effet de superdensité

Cet aspect très particulier de l'interaction ion-cristal a été étudié récemment à la fois dans nos expériences au GANIL et au GSI. Les résultats de ces études ont été présentés par notre collègue l'éminent Professeur L'Hoir lors de la conférence SHIM 2005 [L'Hoir 06]. Je reprendrai quelques éléments de cette publication, également détaillés dans la thèse d'Etienne Testa [Testa 05] et dans la référence [Dauvergne 03] présentée section 1-4.
Un ion dont l'énergie transverse est proche de l'énergie transverse critique a une trajectoire dans le cristal telle que, lorsque son énergie transverse est entièrement potentielle, sa distance à une rangée ou un plan d'atomes est de l'ordre de l'amplitude des vibrations thermiques des atomes du cristal. Dans cette portion de sa trajectoire, cet ion subit donc un grand nombre de collisions à très petit paramètre d'impact sur les atomes d'une rangée. Typiquement, pour des ions U^{91+} de 20 MeV/u, ce nombre est d'environ 50, si la trajectoire n'est pas brusquement défléchie par une collision élastique à très grand angle.
Pour un faisceau incident parallèle à la direction d'un axe ou d'un plan cristallin, cette situation particulière correspond au pic de surface pour les collisions proches, ainsi nommé par le pic apparaissant sur les spectres RBS : sur le premier plan d'atome, la probabilité par ion incident de faire des collisions à petit paramètre d'impact est la même que pour une cible amorphe ; cette probabilité chute ensuite à cause de l'effet d'ombre correspondant à la déflection des trajectoires. Cependant, pour la petite fraction du faisceau qui pénètre dans le cristal dans l'espace transverse défini par l'extension des vibrations thermiques, la probabilité de collision proche sur les noyaux reste très supérieure à la probabilité moyenne hors canalisation, tant que ces ions ne sont pas repoussés à l'extérieur de cet espace transverse.
Dans le cas de la canalisation axiale, les ions qui rasent les rangées d'atomes subissent donc des collisions proches très rapprochées dans le temps : le temps séparant deux collisions consécutives le long d'une rangée <110> est compris entre 5.10^{-18} et 6.10^{-18}s pour des ions d'énergie cinétique de 20 à 30 MeV/u. Ce temps est inférieur à toutes les durées de vie des états excités atomiques d'un ion lourd (seule la durée de vie d'une lacune K de l'uranium est du même ordre de grandeur). Il en résulte une forte modification du régime des échanges de charge lorsque les ions rasent les rangées, en raison de la contribution importante des processus multi-collisionnels (excitation-ionisation, capture sur des états excités - ionisation). Lorsque ces ions s'écartent de la rangée, il n'y a plus (ou peu) de collisions sur les noyaux et sur les électrons, ce qui stoppe la capture et l'ionisation. Seule la désexcitation (radiative ou Auger) de l'ion non perturbé se produit, pendant un temps très long (10^{-15} s au moins) avant que l'ion se rapproche à nouveau d'une rangée (contrairement à la canalisation planaire, la probabilité de s'approcher à nouveau très près d'une rangée d'atome est petite).
Nous appelons cet effet « superdensité », par analogie à l'effet de densité, responsable d'une augmentation de la probabilité d'ionisation en cible solide par rapport à une cible gazeuse comportant le même nombre d'atomes par unité de surface, en raison du taux de collisions plus élevé dans la cible solide dense [Betz 70]. Notons qu'il ne fait pas intervenir *a priori* l'excitation cohérente, due à la périodicité du réseau.
L'effet de superdensité se traduit également par une forte augmentation locale du dépôt d'énergie, en raison de la forte densité électronique rencontrée au voisinage d'une rangée d'atomes. Pour un ion très lourd comme le plomb ou l'uranium, ce dépôt peut excéder 100 keV/nm sur quelques dizaines de nanomètres. Dans une cible suffisamment mince, cette augmentation du dépôt d'énergie sur une faible fraction du parcours d'un ion peut ne pas être compensée par le fait que, sur la majorité de son parcours, l'ion voyage dans des régions de faible densité électronique : un ion d'énergie transverse critique peut déposer davantage d'énergie dans un cristal mince qu'un ion non canalisé. Nous reviendrons sur ce point plus

loin, et notamment sur les applications potentielles sur la création de défauts dans des matériaux radio-résistants.
Nous avons pu observer cet effet de superdensité sur le régime des échanges de charge à la fois lorsque l'ionisation domine, avec des ions Pb^{56+} de 29 MeV/u au GANIL, et lorsque la capture électronique domine, avec des ions U^{91+} ralentis à 20 MeV/u au GSI. Dans ces deux expériences, l'utilisation d'ions incidents très loin de l'équilibre de charge dans une cible solide permet d'identifier et de caractériser cette petite fraction du faisceau.
L'expérience GANIL, réalisée avec un cristal de silicium de 1,1 µm, montre qu'on peut utiliser un cristal très mince pour produire des ions très épluchés. La figure 9 ci-dessous illustre ce propos : pour un cristal non aligné, la distribution de charge est centrée vers l'état de charge 69. La cible étant trop mince et la charge à l'incidence très faible, l'équilibre de charge n'est pas atteint. Une distribution à l'équilibre calculée à partir d'une formule empirique [Leon 98] est représentée, et prédit un état de charge moyen de 71,5. La distribution de charge pour une incidence axiale <110> s'étend depuis les ions gelés dans leur état de charge 56+ (ions bien canalisés), jusqu'à Q=78 pour les ions d'énergie transverse critique. Cette distribution s'étend donc bien au-delà de la distribution de charge hors canalisation. Même si on considère la distribution de charge qui aurait été obtenue à l'équilibre avec une cible plus épaisse (formule empirique), le rapport des fractions extrêmes (78 et 77) montre bien que la distribution associée aux ions d'énergie transverse critique est décalée vers les ions très épluchés. On peut optimiser la fraction des ions d'ions de forte énergie transverse en désalignant le cristal d'un angle proche de l'angle critique de canalisation axiale (et de préférence proche d'une direction planaire majeure, afin d'optimiser le nombre d'ions qui iront lécher une rangée sous la surface). C'est le cas de la distribution dite *critical incidence* sur la figure 9. Pour cette incidence, l'état de charge Q=72 est majoritaire, et la distribution s'étend jusqu'à Q=80, (avec une fraction de 4.10^{-6}). On peut de plus « étiqueter » ces ions qui rasent les rangées en condition d'incidence critique en les conditionnant par une forte perte d'énergie dans la cible: sur la figure 9 est représentée la distribution (en fraction du faisceau total incident) conditionnée par une perte d'énergie supérieure à deux fois la perte d'énergie hors canalisation.

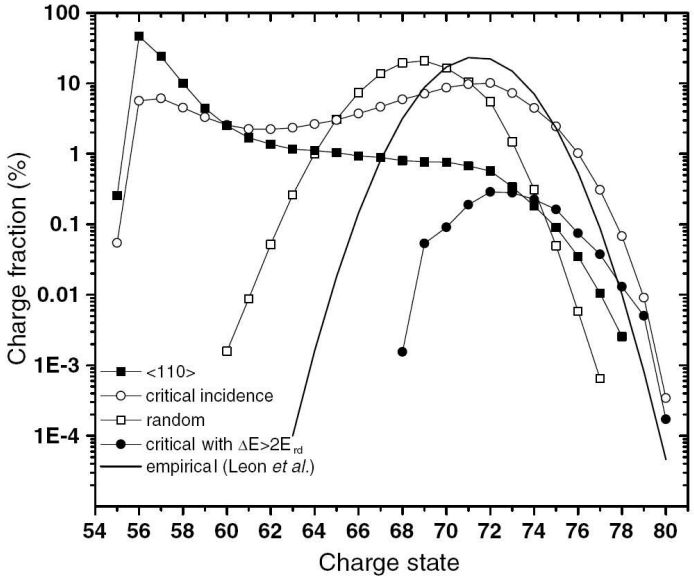

***Figure 9** : distributions de charges obtenues pour un faisceau d'ions Pb^{56+} incidents à 29 MeV/u sur un cristal de silicium de 1,1 µm d'épaisseur. D'après [L'Hoir 06].*

Des simulations Monte-Carlo calculant la configuration électronique de l'ion à chaque plan d'atomes traversé, ainsi que les densités électroniques locales rencontrées, ont permis de reproduire cet effet de superdensité, à la fois sur les distributions de charge et sur la perte d'énergie [L'Hoir 06].
Cette expérience a donc permis de mettre en évidence l'augmentation de la probabilité d'ionisation associée à l'effet de superdensité. Ceci n'avait pas été vu auparavant, car c'est un effet observable en cible mince uniquement : si la cible est trop épaisse, les ions d'énergie transverse critique sont décanalisés, et leur distribution de charge correspond à leur trajectoire proche de la sortie du cristal, c'est-à-dire sans l'influence des collisions rasantes le long des rangées cristallines.
L'expérience menée au GSI avec des ions U^{91+} de 20 MeV/u a permis de montrer que l'effet de superdensité non seulement augmente l'ionisation, mais également inhibe fortement la capture électronique lorsqu'elle se produit dans des états excités du projectile.

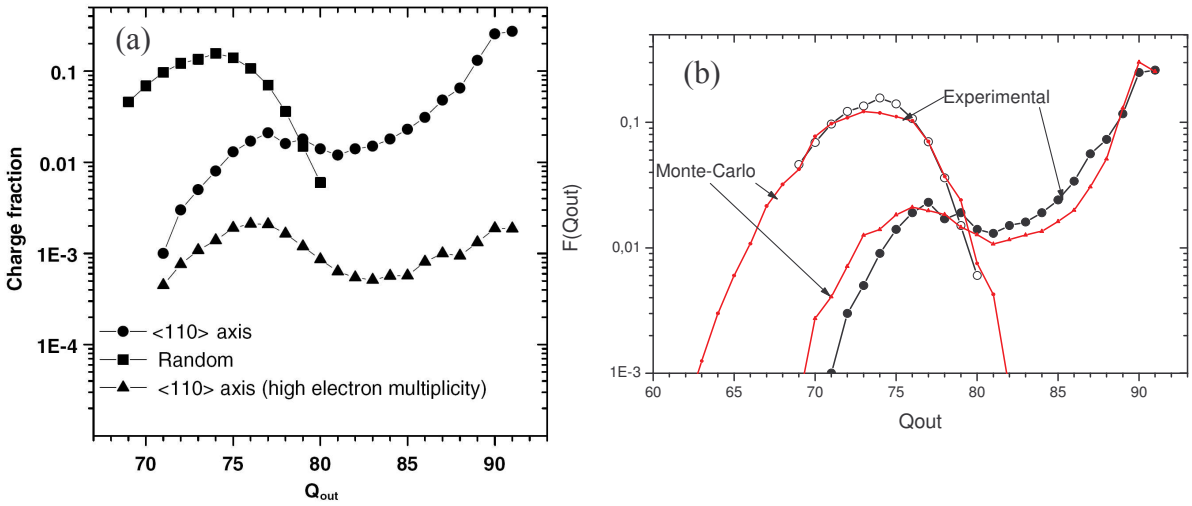

Figure 10 *: Distributions de charges obtenues pour un faisceau incident d'ions U^{91+} de 20 Mev/u et une cible cristalline de silicium de 11.7 µm d'épaisseur. Orientations quelconque (random) et axiale <110>. La distribution correspondant aux 2% des ions de plus forte multiplicité électronique est indiquée sur la figure (a). Sur la figure (b), les simulations reproduisant ces distributions sont présentées (d'après [L'Hoir 06]).*

La figure 10 montre les distributions de charge obtenues dans cette expérience. La distribution hors canalisation correspond ici à l'équilibre de charge. Celui-ci est atteint très rapidement dans la cible, après quelques µm de parcours. Les ions de forte énergie transverse en condition de canalisation axiale sont ceux qui capturent le plus d'électrons. On constate que la queue de distribution des ions les plus rhabillés dans l'axe est très décalée par rapport à la distribution hors canalisation. Si on sélectionne les ions pour lesquels la multiplicité électronique émise en surface est la plus forte (voir section I-6-1) on obtient une distribution centrée sur l'état de charge 76-77, décalé d'au moins deux unités par rapport à la charge moyenne d'équilibre hors canalisation. Les simulations menées par Alain L'Hoir reproduisent bien ce décalage (figure 10-b). Elles montrent que les ions capturés par MEC, au voisinage des rangées, dans des états excités $n > 3$ majoritairement, ont une forte probabilité d'être ré-ionisés par impact sur les électrons et les noyaux suivants de ces rangées.
Les spectres X correspondant sont montrés figure 11, et fournissent une information complémentaire. Je rappelle que ces spectres X correspondent essentiellement au remplissage des couches K (raies K et REC-K) et L (Raies L et REC-L) du projectile. La comparaison entre les figures 11-a (orientation quelconque) et 11-b (orientation axiale, sélection des états

de charge 76-80 en sortie, qui recouvrent les états de charge hors canalisation) est caractéristique de l'effet de superdensité : pour une orientation quelconque, les couches K et L du projectile sont très rapidement remplies, par capture mécanique MEC sur les couches de *n* élevé (4 et plus), puis décroissance des électrons vers les couches K et L. Lorsque la couche L est remplie, la probabilité d'excitation-ionisation L est grande, et les lacunes L sont rapidement comblées par cascade d'un électron M. Ces cascades sont observables dans les raies très intenses et étroites à 16 et 20 keV.

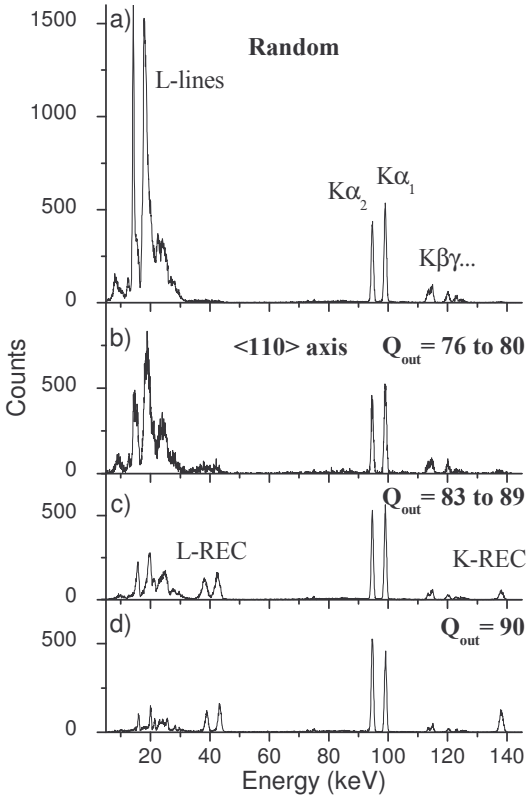

Figure 11 *: spectres X détectés à 90° de la direction du faisceau, pour des ions incidents U^{91+} de 20 MeV/u sur un cristal de silicium de 11,7 µm d'épaisseur. (a) orientation quelconque ; (b)-(d) orientation axiale <110>, avec sélection d'états de charge en sortie du cristal. Les 4 spectres sont normalisés au même nombre d'ions sélectionnés.*

Dans le cas de l'orientation axiale, les ions de forte énergie transverse qui atteignent les mêmes états de charge (76-80) que pour une orientation quelconque (figure 11-b) le font progressivement sur toute l'épaisseur du cristal : en effet, à la fois l'intensité et la forme des raies L sont très différentes de celles de la figure 11-a. Les raies sont très larges, et cette largeur est due à la superposition sur le spectre des transitions pour chaque état de charge 91 à 82. La composante étroite correspondant à une seule lacune L, très importante sur la figure 11-a, est absente.
La figure 12 permet de mieux voir cette différence, avec les spectres L superposés (le lecteur excusera cette coquetterie de ma part, qui me pousse à l'inonder de figures, au risque de le noyer sous les détails). Hors canalisation, on a bien l'ensemble des raies correspondant au remplissage séquentiel de la couche L, plus les raies étroites à basse énergie pour le remplissage de la couche L avec une seule lacune. L'absence de ces raies montre bien que, pour ces ions subissant l'effet de superdensité, toute l'épaisseur du cristal est nécessaire pour atteindre le remplissage de la couche L, car la plupart des électrons capturés sont ensuite perdus. Ceci est vérifié par les simulations.

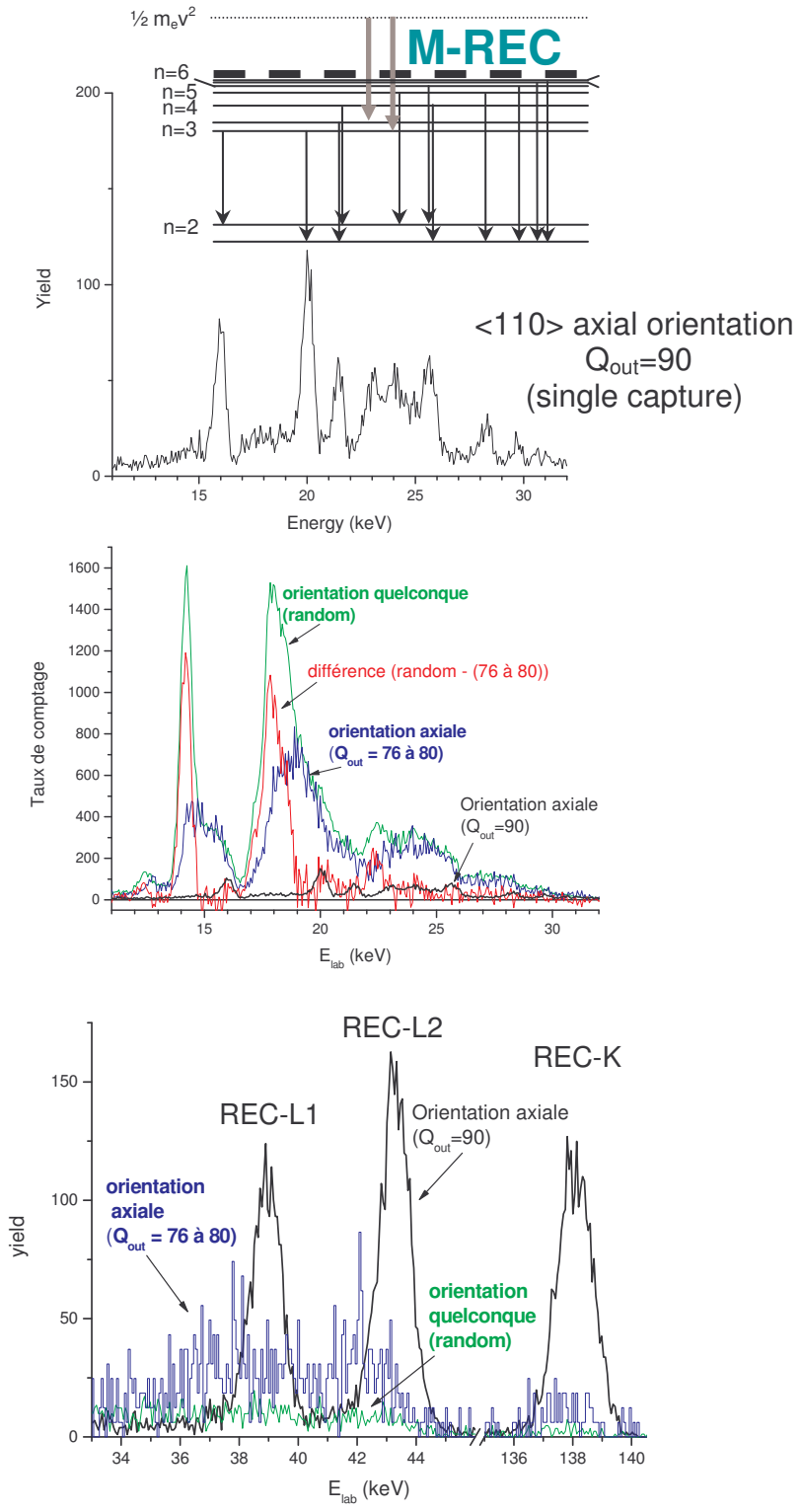

Figure 12 *: Spectres X détectés à 90° de la direction du faisceau, pour des ions U^{91+} de 20 MeV/u incidents sur un cristal de 11,7 µm de silicium. (a) Représentation, dans le référentiel du projectile, des transitions dans l'état héliumoïde (Qout=90) observées en canalisation axiale ; (b) Comparaisons des transitions L pour les orientations axiale (Qout= 76 à 80, et Qout=90) et quelconque (random), avec différence des spectres random et axial (Qout= 76 à 80) ; (c) comparaison des spectres de REC-L et REC-K pour les mêmes sélections qu'en (b).*

L'analyse des raies REC-K et L hors canalisation, très peu visibles sur la figure 11, mais davantage sur la figure 12, permet d'extraire des temps de survie des lacunes K et L pour un ion hydrogénoïde incident. En effet, on peut estimer la fraction d'événements de REC-K et L qui servent à remplir ces couches, qui est égale à la fraction du parcours durant laquelle ces événements de capture sont autorisés. On en déduit le temps de survie d'une lacune en couche K, $\tau_K=2.10^{-15}$ s, et en couche L, qui est deux à trois fois plus grand.
Dans le cas présent, on ne peut pas facilement comparer le temps de survie de la couche K et L hors canalisation et pour les ions subissant l'effet de superdensité. En effet, on voit bien en comparant les figures 11-a et 11-b, mais aussi sur la figure 12, que les taux de REC-K et L sont fortement augmentés pour les ions de forte énergie transverse ($Q < 80$) en alignement axial par rapport à une orientation quelconque (d'un facteur 2,1 et 2,4 respectivement). Cependant, le taux de REC est proportionnel à la densité électronique rencontrée. Or, en orientation axiale, celle-ci est maximum à l'entrée du cristal pour un ion de forte énergie transverse qui rase une rangée. Puis elle devient beaucoup plus faible lorsque l'ion s'éloigne des atomes entre les rangées. Les taux de REC-K et L ne fournissent donc pas une échelle de temps linéaire. Pour la couche K, on peut seulement dire que la lacune K survit au moins le temps d'une collision rasante le long de la rangée rencontrée à l'entrée du cristal, et moins que le temps nécessaire pour subir une seconde collision rasante, pendant lequel un électron capturé dans une couche de n élevé pourra décroître en couche interne.
En conclusion, à cette énergie, l'effet de superdensité se manifeste sur les taux de REC-K et L principalement par l'augmentation de la densité électronique rencontrée le long de la première rangée d'atomes.

Je reviendrais, à la fin de ce mémoire, sur l'intérêt possible de ce type de mesures pour la détermination de temps de fission nucléaire.

Il me semble également nécessaire de faire un bref commentaire sur les effets de l'excitation cohérente dans les cristaux, bien que nous n'ayons jamais participé à de telles études pour l'excitation atomique.
L'excitation cohérente résonnante (RCE) ou effet Okorokov, résulte de l'interaction d'une particule avec le champ électrique périodique du cristal. Une présentation de cet effet est faite dans la section 5 de l'article d'introduction [Cohen 04] de ce mémoire.
Notons, dans le cadre de ce chapitre, que les transitions électroniques mesurées par cette technique permettent elles aussi d'accéder à la perturbation causée par l'effet Stark sur le projectile : celui-ci est dû au champ électrique de sillage et/ou au champ statique moyen ressenti par un ion au voisinage d'un plan ou d'une rangée. Crawford et Ritchie ont calculé les contributions respectives de ces deux champs dans le cas d'ions légers [Crawford 79]. Pour des ions légers rapides, au-delà de 10 MeV/u, le champ de sillage a un effet négligeable devant le champ statique transverse sur les décalages en énergie des sous niveaux Stark. Les expériences menées par Datz et al. [Datz 95] et, plus récemment, par la collaboration japonaise [Azuma 99], ont permis d'étudier l'influence de l'énergie transverse sur les niveaux d'énergie n=2 mis en jeu dans les excitations cohérentes.
Très récemment, la collaboration japonaise a présenté des résultats concernant l'excitation résonnante cohérente d'ions hors canalisation. Contrairement aux ions canalisés, les résonances ne sont pas élargies par le potentiel statique du cristal (pas d'effet Stark dépendant de la position dans le plan transverse). La précision spectroscopique des transitions se trouve donc améliorée par rapport aux conditions de canalisation ; c'est le but recherché par cette collaboration : la mesure de précision de Lamb shift sur des ions hydrogénoïdes.
L'existence d'effets cohérents hors canalisation amène des questionnements importants sur les mesures de processus d'excitation d'ions dans des solides. En effet, la structure d'un

solide est toujours cristalline localement. Comme l'ont montré Salin et al. [Salin 98], la part cohérente de l'excitation par un réseau périodique peut être soit constructive (à la résonance) soit destructive hors résonance, ce qui affecte considérablement les sections efficaces, que l'on rapporte toujours à des collisions binaires décorrélées. De même les résultats des mesures de transport d'états excités dans des solides peuvent dépendre fortement de l'orientation des cibles. A ma connaissance, ceci n'est jamais pris en compte.
Enfin, il faut bien rappeler que l'excitation résonnante cohérente n'a encore jamais été observée sur des noyaux, malgré un fort intérêt de théoriciens [Pivovarov 98] et une première étude de faisabilité réalisée par notre collaboration en 1994 au GANIL sur des noyaux isomériques de $^{45}Ti^{m}$. Ce sujet de recherche, sans cesse repoussé par notre collaboration, en raison d'autres programmes en cours, pourrait voir le jour au GSI si notre programme de recherche auprès de FAIR est validé par nos instances dirigeantes. Il pourrait également être repris au GANIL si ces mêmes instances ne nous bloquent pas. Là encore, comme pour la capture NEEC, il s'agit de faire des mesures d'excitation coulombienne de noyaux, qui sont d'ordre fondamental.
Malheureusement, il ne s'agit pas de noyaux exotiques…

I-6 Aspects originaux du dépôt d'énergie dans un cristal aligné

Dans cette section, j'évoquerai les mesures de corrélation entre perte d'énergie et taux d'émission électronique pour des ions en conditions de canalisation. Je reviendrai brièvement sur les très forts dépôts d'énergie associés à l'effet de superdensité pour les ions d'énergie transverse critique. Enfin je décrirai l'intérêt que peut avoir la canalisation pour la décélération de faisceaux d'ions lourds fortement chargés.

I-6-1 Corrélation entre perte d'énergie et émission électronique secondaire.

Lors de l'expérience réalisée en 2000 au GANIL dans SPEG, avec des ions incidents Pb^{56+} de 29 MeV/u sur un cristal de silicium mince de 1,1 μm, nous avons étudié le taux d'émission électronique associé à chaque ion incident, sur les faces d'entrée et de sortie du cristal. Pour ce faire, nous avons polarisé la cible à un potentiel de -10 kV. Deux détecteurs silicium à la masse faisaient face au cristal et collectaient donc avec une très bonne efficacité les électrons lents émis, l'impulsion délivrée par le détecteur étant proportionnelle à la multiplicité d'électrons collectés. La très haute résolution en énergie de SPEG nous a permis d'étudier la corrélation étroite qui existe entre perte d'énergie et rendements d'électrons émis à chaque face de la cible, et ce en fonction de l'énergie transverse des ions canalisés. Rappelons que, en utilisant des ions incidents loin de l'équilibre de charge, l'état de charge en sortie du cristal dépend lui-même fortement de l'énergie transverse des ions.
L'analyse de ces données a été réalisée dans notre groupe par Cédric Ray, sous les conseils avisés de Jean-Claude Poizat.
La figure 13 ci-dessous est extraite de la référence [Barrué 04] et illustre cette corrélation.
Les distributions correspondant à l'état de charge 56+ sont celles d'ions bien canalisés, gelés dans leur état de charge d'origine. Ils représentent 55% du faisceau incident. Parmi eux, une sélection sévère des ions hypercanalisés (le « leading edge », correspondant à moins de 1% du faisceau incident) a été faite à partir du minimum de perte d'énergie. A l'opposé, les ions émergeant dans l'état de charge 72+ sont des ions de forte énergie transverse, qui rentrent dans le cristal en rasant les rangées d'atomes. Les distributions de multiplicités d'électrons et de perte d'énergie (normalisée) pour une orientation quelconque sont également représentées.

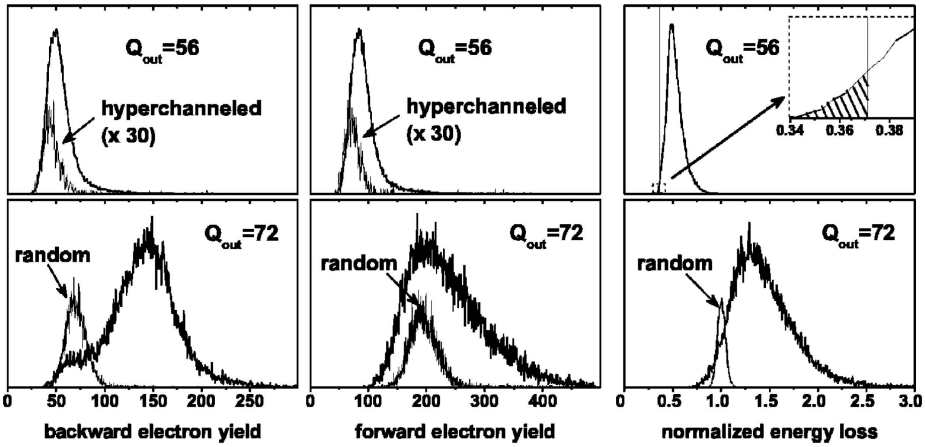

Figure 13 : Distributions, pour des ions Pb^{56+} incident à 29 MeV/u sur un cristal de silicium de 1,1 µm de silicium aligné selon l'axe <110>, de rendements d'électrons à l'entrée (gauche) et à la sortie (centre) du cristal, et distribution en énergie des ions émergents (gauche) pour deux états de charge en sortie : 56+ (haut) et 72+ (bas). Pour les ions 56+, une sélection des ions les mieux canalisés (indiquée dans l'encart en haut à droite) est comparée. Les distributions pour une orientation quelconque (random) sont également comparées à celle des ions 72+. La perte d'énergie est en unités de perte d'énergie hors canalisation, et est corrigé de la dépendance en Q^2.

Le taux d'émission électronique à l'entrée de la cible reflète la densité électronique rencontrée sur les premiers nanomètres, voire dizaines de nanomètres de parcours (la faible dispersion pour l'orientation dite quelconque, qui n'est décalée que de quelques degrés par rapport à l'axe, montre que cette distribution est moyennée sur tout l'espace transverse). Les ions les mieux canalisés ont un rendement environ deux fois plus faible que pour une orientation quelconque. A l'opposé, les ions qui pénètrent dans le cristal en rasant une rangée ont un rendement d'émission électronique deux à trois fois supérieur à la valeur « normale ». Ces facteurs de réduction ou d'augmentation sont inférieurs aux facteurs de réduction ou d'augmentation de la densité électronique locale rencontrée, ce qui montre que la partie distante de la perte d'énergie électronique joue un rôle important dans le rendement d'émission arrière. Le rendement d'émission électronique en sortie de cible montre une différence plus importante entre les ions très bien canalisés et l'orientation quelconque, égal au facteur de réduction de la perte d'énergie. Pour les ions de forte énergie transverse, la valeur la plus probable est égale à la valeur obtenue hors canalisation, mais la distribution est très asymétrique, et s'étend jusqu'à plus de 2 fois la valeur « normale ». Ceci montre que le rendement d'électrons avant reflète la perte d'énergie intégrée sur un grand parcours, sur lequel presque tout l'espace transverse accessible est exploré par ces ions mal canalisés. Une contribution des électrons deltas (électrons énergétiques émis davantage vers l'avant que vers l'arrière) est responsable du plus fort rendement avant qu'arrière.
En résumé, le rendement d'émission électronique à l'entrée de la cible renseigne sur le paramètre d'impact à l'entrée du cristal, tandis que le rendement avant est le reflet de la perte d'énergie.
Nous avons utilisé cette propriété de la corrélation entre rendement électronique et énergie transverse pour mieux identifier l'énergie transverse des ions transmis dans nos expériences au GSI, à l'aide d'un dispositif similaire à celui de l'expérience GANIL. Je montre à nouveau ci-dessous la figure déjà présentée dans la section I-4 pour discuter de l'influence de la capture électronique multiple en couche amorphe.

La figure 13-a montre, au plan focal image après analyse magnétique, la distribution horizontale des ions transmis en fonction de la multiplicité d'électrons émis en sortie de cible. La corrélation entre multiplicité électronique et perte d'énergie apparaît clairement, et a permis de séparer les différents états de charge à l'aide des séparatrices obliques indiquées sur cette figure. La projection des pics de charges ainsi résolus est montrée figure 13-b. La seule mesure par l'analyse de rigidité magnétique n'aurait pas permis de résoudre ces pics, en raison de l'importante dispersion en énergie des ions canalisés dans cette cible épaisse.

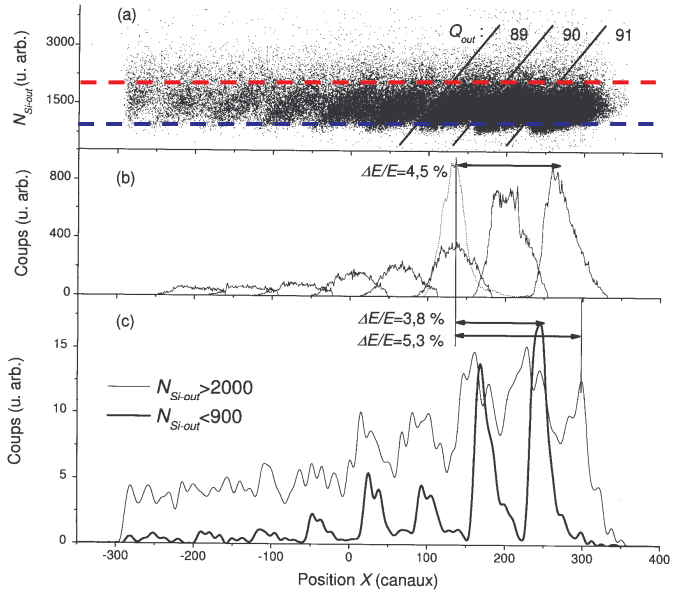

Figure 13 : *Distributions d'ions U^{91+} incidents de 20 MeV/u transmis à travers un cristal de silicium de 11µm aligné selon l'axe <110>, détectés après analyse magnétique.(a) Distribution des multiplicités électroniques en fonction de la position pour les ions de charges les plus élevées ; (b) projection unidimensionnelle de cette distribution, en utilisant les séparatrices d'états de charge indiquées en (a). Le profil du faisceau direct est indiqué. (c) Projections correspondant aux fortes et aux faibles multiplicités électroniques, selon les coupures indiquées en pointillées sur la figure (a).*

Nous (ou plutôt Etienne Testa lors de sa thèse) avons également utilisé le taux d'émission électronique pour effectuer des sélections en énergie transverse des ions canalisés. Les lignes horizontales indiquées figure 13-a représentent les seuils utilisés pour les deux sélections projetées figure 13-c : d'un côté les ions les mieux canalisés ($N_{SI\text{-}out}$ < 900 en unités arbitraires), de l'autre les plus mal canalisés ($N_{SI\text{-}out}$ > 2000).
Les deux distributions ainsi sélectionnées et projetées figure 13-c sont très différentes, à la fois en ce qui concerne la distribution de charge, et la position absolue au plan focal, c'est-à-dire la perte d'énergie. Ceci nous permet de faire la transition avec les sections suivantes sur les aspects originaux de la perte d'énergie des ions lourds en conditions de canalisation.

I-6-2 Perte d'énergie en canalisation critique

Ce sujet a déjà été présenté dans la section I-5-2. Je rappelle simplement que, lorsqu'un ion de forte énergie transverse subit une collision rasante avec une rangée d'atome, cet ion est dans une région de l'espace transverse dans laquelle la densité électronique locale est beaucoup plus élevée que la moyenne du cristal (plus d'un ordre de grandeur). Vickridge et al. [Vickridge 90] ont montré que, pour des protons de 992 keV subissant des réactions

nucléaires dans un cristal d'aluminium en alignement axial, le dépôt d'énergie local était augmenté d'un ordre de grandeur par rapport à la valeur normale hors canalisation. En extrapolant cette propriété pour des ions aussi lourds que le plomb ou l'uranium, le dépôt d'énergie pourra excéder 100 keV/nm, ce qui représente de l'ordre de 10 keV par atome rencontré à petit paramètre d'impact. Il en résultera une très forte ionisation de cet atome.
De telles valeurs de transfert d'énergie linéique sont très supérieures aux seuils connus de création de défauts dans des matériaux radio-résistants comme le germanium.
Notre programme en cours au GANIL cherche à étudier les effets de ce très fort dépôt d'énergie en surface d'un cristal sur l'endommagement, au moyen de l'émission ionique. L'information que l'on extraira de cette expérience permettra de savoir si un modèle d'explosion coulombienne d'une rangée d'atomes fortement ionisés est approprié à la description de l'endommagement de tels cristaux.

I-6-3 Ralentissement d'ions lourds très chargés.

Nous avons vu dans ce chapitre que des ions lourds hydrogénoïdes ralentis à des énergies inférieures à 20 MeV /u peuvent, en conditions de canalisation dans un cristal relativement épais, rester gelés dans leur état de charge initial qui est très loin de l'équilibre de charge dans la matière. Il en résulte que leur taux de perte d'énergie est très élevé, en raison de la dépendance en Q^2 de la perte d'énergie. Bien que les ions canalisés rencontrent une densité électronique réduite par rapport à la densité électronique moyenne d'un cristal, leur perte d'énergie peut excéder la perte d'énergie hors canalisation. Ceci est illustré figure 14, sur laquelle l'évolution du taux de perte d'énergie d'ions uranium dans le silicium est représentée en fonction de l'énergie des ions.

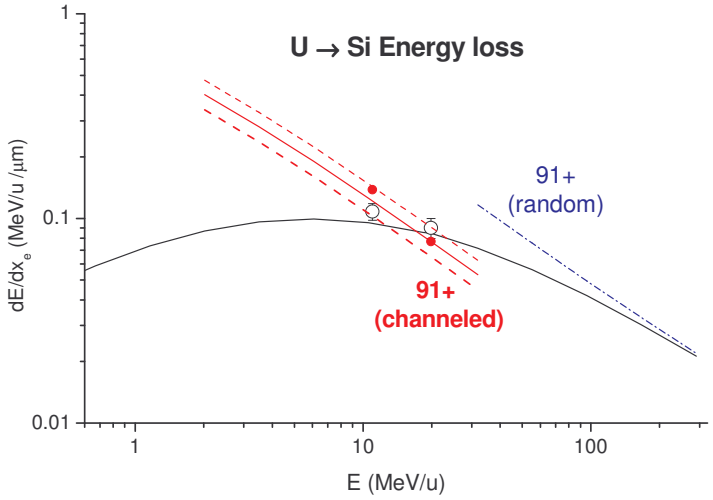

Figure 14 : *Taux de perte d'énergie d'ions uranium dans le silicium en fonction de l'énergie cinétique. La courbe continue noire correspond aux valeurs tabulées dans SRIM. Les points noirs sont les valeurs mesurées hors canalisation avec des ions incidents U^{91+} de 20 MeV/u (cible de 11,7 µm) et de 12 MeV/u (cible de 18 µm). La courbe point-tiret indexée 91+ random est une extrapolation de la perte d'énergie hors canalisation en supposant une charge constante 91+. Les points en rouge pleins sont les valeurs moyennes obtenues en canalisation : à 20 MeV/u, canalisation axiale <110> ; à 12 MeV/u, canalisation planaire (110). Les courbes en rouge (continue et pointillés) sont une extrapolation vers les basses énergies des valeurs mesurées pour q=91 à 20 MeV/u. Les courbes en pointillés délimitent l'enveloppe des valeurs mesurées (voir figure 13-c).*

Les valeurs tabulées dans SRIM pour une cible amorphe sont représentées, et présentent un maximum vers 5 MeV/u. Supposons que les ions ne capturent pas d'électrons lorsque leur vitesse est faible. Alors l'allure de cette courbe serait une courbe qui divergerait en 0, selon une loi en $1/v^2$ (courbe en points-tirets extrapolée pour des valeurs de l'énergie inférieures à 300 MeV/u). Cette situation n'est pas irréaliste en condition de canalisation car les ions canalisés ont une probabilité faible de capturer des électrons (par capture radiative) lorsqu'ils n'ont pas accès aux collisions à petits paramètres d'impact. Nous avons reporté les valeurs mesurées de perte d'énergie pour les ions U^{91+} gelés dans leur état de charge à 20 MeV/u en condition de canalisation axiale, ainsi que pour une orientation quelconque du cristal (avec une charge à l'équilibre Q=74). La valeur mesurée hors canalisation est légèrement supérieure à la valeur tabulée, peut-être en raison de la charge incidente supérieure à la charge d'équilibre (pour cette mesure hors canalisation, l'incertitude est grande en raison de l'impossibilité d'identifier les états de charge). La valeur moyenne du dépôt d'énergie en canalisation est réduite d'environ 10% seulement par rapport à la valeur hors canalisation, alors que le rapport des carrés de charge est de 1,5 ; les valeurs extrêmes (voir figure 13-c) s'étendent de part et d'autre de cette valeur moyenne. Cette dispersion de la perte d'énergie n'est pas due aux fluctuations sur les collisions proches, mais bien à la distribution en énergie transverse de ces ions, qui rencontrent des densités électroniques différentes. On peut donc extrapoler ces valeurs mesurées en canalisation vers les basses énergies. Pour une énergie inférieure à 15 MeV/u environ, la perte d'énergie d'ions hydrogénoïdes canalisés doit excéder la perte d'énergie d'ions non canalisés et à l'équilibre de charge. La dernière expérience réalisée au GSI en 2005 a permis l'observation d'ions U^{91+} gelés après transmission dans un cristal de silicium de 18 µm orienté selon le plan (110). Les valeurs de taux de perte d'énergie dans la cible sont reportées dans la figure 14, et on constate bien une perte d'énergie des ions canalisés supérieure à celle des ions non canalisés (144 keV/u/µm au lieu de 106 keV/u/µm).

Le fort taux de perte d'énergie d'ions hydrogénoïdes canalisés étant avéré, on peut se poser la question de l'intérêt d'utiliser un cristal comme ralentisseur d'ions lourds. Le ralentissement de ces ions en lui-même est utile. En effet, pour produire efficacement des ions nus ou hydrogénoïdes, il faut d'abord les accélérer à quelques centaines de MeV/u et les éplucher de leurs électrons. Des études de spectroscopie précise sur ces ions nécessitent de minimiser l'élargissement Doppler des raies X émises en vol, ce que facilitent les basses énergies. Enfin, toujours à des fins de spectroscopie, le dispositif HITRAP en cours d'installation au GSI cherche à piéger de tels ions après ralentissement. L'utilisation d'un cristal comme étage de ralentissement entre 10 et 5 MeV/u typiquement pourrait être concurrentiel par rapport à un LINAC.
Un certains nombre de questions se posent, plus ou moins fondamentales :

- La première est sur la nature même de la perte d'énergie électronique à basse énergie : supposons un ion, considéré comme une charge ponctuelle Z gelée et de vitesse v. Il transfert de l'énergie aux électrons cible par collisions binaires, selon l'expression classique en fonction du paramètre d'impact b : $T(b) = \frac{Z^2 e^4}{b^2 + \left(r_m^0/2\right)^2}$, où $r_m^0 = \frac{2Ze^2}{m_e v^2}$ est le diamètre de collision. Cette expression du transfert d'énergie est limitée aux grands paramètres d'impact à la fois par l'écrantage des électrons de la cible solide, mais également par la coupure adiabatique $b_{max}=v/\omega$, où ω est la pulsation d'un électron sur son orbitale. Typiquement, pour des électrons de cœur d'un atome cible, $\hbar\omega \approx 2E_B$, où E_B est l'énergie de liaison d'un électron sur une couche donnée [Andersen 96]. La valeur de b_{max} est indépendante de la charge du projectile. Or ce critère basé sur la comparaison du temps d'interaction avec la période de révolution de

l'électron dans l'état initial n'est pas valide dans le cas d'une forte perturbation. Par exemple, pour un ion U^{91+} de 20 MeV/u interagissant avec les électrons K du silicium ($\hbar\omega_K \approx 3600$ eV), on obtient b_{max}=0,05 Å. Or un tel électron lié avec une énergie de liaison de 1800 eV à l'atome cible sera plongé, pendant un temps long à l'échelle de $1/\omega_K$, dans le potentiel du projectile, qui sera très supérieur à son énergie de liaison pour des distances très supérieures à b_{max} (typiquement 2 Å). La description classique de la portée des collisions binaires n'est certainement pas valide. La description en termes de perturbations quantiques aux faibles ordres l'est encore moins. Une description rigoureuse du dépôt d'énergie dans ce régime des très fortes perturbations nécessite des développements théoriques, même si, d'après la figure 14, les valeurs mesurées de la perte d'énergie d'ions U^{91+} à 20 et 12 MeV/u ne semblent pas s'éloigner des valeurs extrapolées des tables. Ceci peut tenir au fait que pour les ions canalisés, la perte d'énergie par collisions distantes (excitations de plasmons) est très importante, et est elle aussi proportionnelle à Q^2.

- La seconde question est relative au rôle joué par le réchauffement transverse des ions canalisés. Pour que les ions restent gelés dans leur état de charge, il faut qu'ils restent éloignés à plus qu'une distance r_{max} des rangées ou des plans d'atomes. En dessous de r_{max}, la capture MEC devient possible et l'ion capturera inexorablement un grand nombre d'électrons. D'une façon générale, on estime le réchauffement transverse dû aux collisions proches sur les électrons par la formule suivante : $\Delta E_\perp = m_e / 2M_{ion}\ \Delta E$. Une autre expérience, réalisée en 2003, a permis de ralentir des ions incidents Pb^{81+} de 13 MeV/u dans un cristal aligné de 37 µm. L'énergie mesurée pour les ions canalisés émergeant était de 8,5 MeV/u (celle des ions non canalisés était de 9,5 MeV/u), c'est-à-dire que des ions canalisés peuvent perdre plus de 30 % de leur énergie cinétique, soit près de 1 GeV, sans être décanalisés. Dans cette expérience, nous n'avons pas pu identifier les états de charge. Nous savons que les ions ayant capturé un minimum d'électrons avaient effectué en moyenne 2,6 captures, dont 0,8 REC. Le nombre de 1,8 MEC peut être attribué à la capture d'électrons dans la couche amorphe de sortie du cristal. Une argumentation détaillée de ces chiffres, basée sur une analyse approfondie des spectres X et sur des simulations, figure dans le chapitre 5 de la thèse d'Etienne Testa. Selon l'expression ci-dessus, le réchauffement transverse par unité de charge pour les ions plomb devrait être de 15 eV. L'expérience réalisée en 2001 avec des ions U^{91+} de 20 MeV/u a montré que pour une telle énergie transverse, les ions capturent de nombreux électrons par MEC (cf. figure 2 de la référence [Dauvergne 06] et le commentaire associé), ce qui n'est pas le cas pour les ions Pb^{81+} ayant perdu 1 GeV dans le cristal. De même, lors de l'expérience réalisée en 2005, les ions U^{91+} de 12 MeV/u ayant perdu 620 MeV dans le cristal aligné selon le plan (110) auraient eu un réchauffement transverse de 8 eV, ce qui les ferait tous rentrer dans l'espace pour lequel la capture MEC devient importante (même en divisant cette valeur par deux, car seule la diffusion dans la direction perpendiculaire aux plans intervient, la distance minimale d'approche aux plans après réchauffement transverse serait de 0,5 Å). Or nous avons pu observer des ions gelés, ou n'ayant capturé des électrons que par REC. La valeur du réchauffement transverse donnée plus haut est probablement surestimée dans le cas des ions bien canalisés, pour lesquels le taux de diffusion angulaire sur les électrons est faible.
- Une autre question qui se pose est celle de la survie des ions dans leur état de charge initial. Cette question est triple : il faut i) que les ions survivent à la capture radiative REC tout en voyageant dans une cible « épaisse » d'électrons, ii) que les ions survivent à la capture MEC dans le cristal, cette capture pouvant se produire à des paramètres d'impact de plus en plus grands au fur et à mesure que la vitesse de l'ion

décroît, et iii) que les ions franchissent les couches désordonnées de surface sans subir de MEC.

Pour répondre au premier point, la figure 15 ci-dessous est un calcul, en fonction de l'épaisseur de cristal traversé (de densité électronique moyenne 0,2 $e^-/Å^3$), de l'énergie résiduelle et de la probabilité de ne pas capturer d'électrons par REC, pour des ions U^{91+} à deux énergies incidentes : 20 MeV/u et 12 MeV/u. L'augmentation de la section efficace de REC lorsque l'énergie diminue est prise en compte. Cette figure montre que de tels ions peuvent perdre environ le tiers de leur énergie, et survivre à la capture radiative avec une probabilité de l'ordre du pour cent.

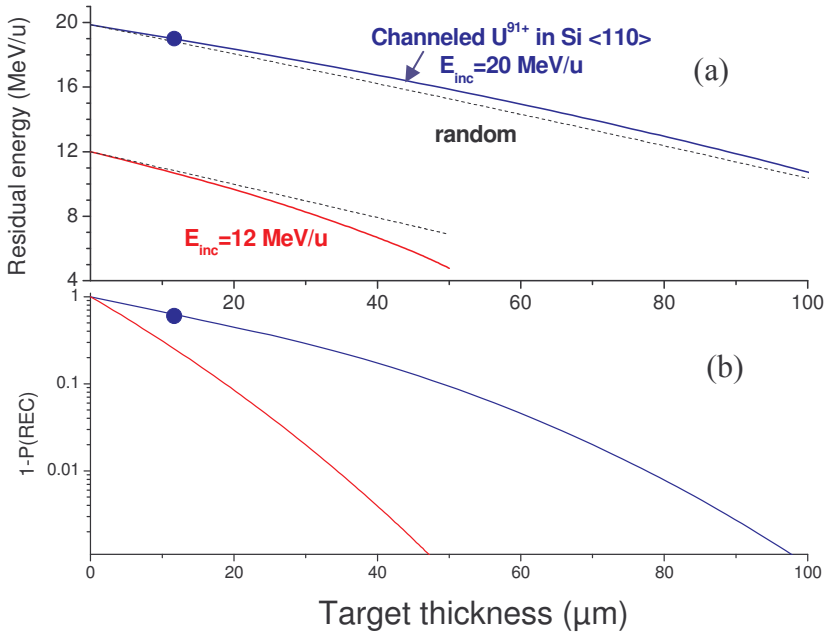

Figure 15 : Energie résiduelle (a) et probabilité de survivre à la capture radiative REC (b) pour des ions U^{91+} incidents de 20 MeV/u et de 12 MeV/u, canalisés dans l'axe <110> d'un cristal de silicium, en fonction de l'épaisseur de cristal traversé. En (a), les lignes en pointillés sont pour une orientation quelconque du cristal (« random »). Les points correspondent aux valeurs mesurées pour un faisceau de 20 MeV/u.

Le second point (l'augmentation de la capture MEC lorsque l'énergie diminue) est plus compliqué à estimer. En effet, la capture MEC ne dépend pas directement de la densité électronique rencontrée, et il faut connaître l'évolution de sa probabilité en fonction du paramètre d'impact aux atomes cible. Les mesures faites en 2003 et en 2005 montrent que des ions Pb^{81+} et U^{91+} peuvent ne pas capturer d'électrons en étant canalisés dans l'axe <110> (respectivement le plan (110)) à des énergies aussi faibles que 8,5 MeV/u et 9,4 MeV/u. La dernière mesure surtout est importante, car l'espace interplanaire est de 1,92 Å dans le silicium (110). L'existence d'ions « gelés » dans leur état de charge montre qu'ils peuvent ne pas capturer d'électrons à des paramètres d'impact de 0,8 Å. Certes, il y aura une limite aux basses énergies dans le transport d'ions hydrogénoïdes dans un cristal aligné. L'extrapolation de la courbe de perte d'énergie jusqu'à 2 MeV/u sur la figure 14 n'est certainement pas réaliste. Néanmoins, nous n'avons pas atteint cette limite inférieure pour l'uranium dans le silicium.

Le dernier point (la capture en couche amorphe en surface) mérite également d'être discuté au vu de nos résultats. Sans prendre de précautions particulières, avec des cristaux conservés

sous atmosphère ambiante, il se forme en surface des cristaux de silicium une couche d'oxyde de quelques nanomètres. Dans la section I-4 nous avons discuté des probabilités de capture électronique par des ions U^{91+} de 20 MeV/u dans de telles couches (en particulier pour la capture multiple), qui est de l'ordre de 10 à 15 %. Si on suppose que la section efficace de MEC varie comme $E^{-5,5}$, cette probabilité devrait être de 100% à 10 MeV/u. L'expérience menée avec des ions Pb^{81+} de 13 MeV/u en 2003 a montré, pour un cristal mince de 1 µm, que la probabilité de capture en couche amorphe est là aussi de 20% environ. Avec un cristal épais, la couche amorphe est traversée avec une énergie de 8,5 MeV/u, et, bien que nos données ne puissent pas nous permettre de l'affirmer avec certitude, il est possible que les ions capturent 1 à 2 électrons en couche amorphe de sortie. Lors de l'expérience menée en 2005 avec des ions U^{91+} de 12 MeV/u incidents (et ressortant de la cible de 18 µm de silicium avec une énergie inférieure à 10 MeV/u) nous avons nettoyé ce cristal à l'aide d'une solution d'acide fluorhydrique, puis tenté de passiver la surface avec un jet gazeux d'hydrogène, avant de mettre le cristal sous vide. Nous n'avons pas procédé par la suite à une caractérisation de cette surface nettoyée. Nous avons pu observer une petite fraction de 0,3% d'ions « gelés » dans leur état de charge hydrogénoïdes en canalisation planaire. Cette fraction peut se distinguer sur la figure 17, sur laquelle sont représentées les distributions des ions au plan

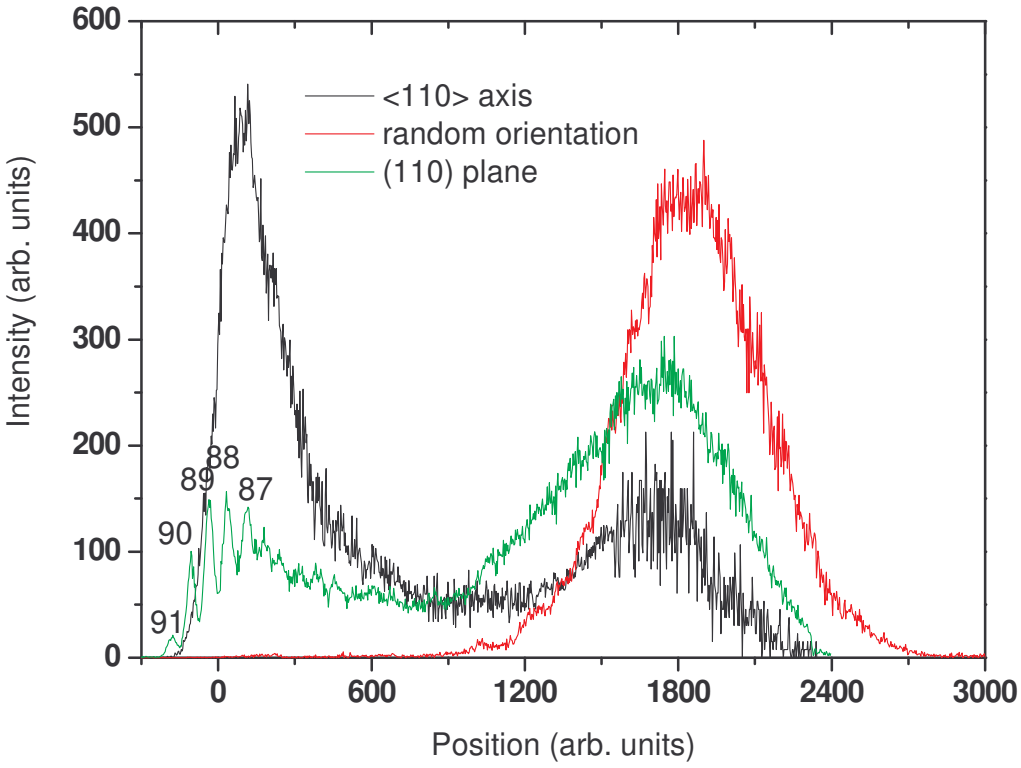

focal image, pour les orientations axiale, planaire et quelconque du cristal.
Figure 17 : Distributions des ions transmis au plan focal image après analyse magnétique, pour des ions U^{91+} incidents à 13 MeV/u sur un cristal de silicium de 18 µm d'épaisseur, pour trois orientations du cristal.

Malheureusement, la situation est plus complexe en canalisation axiale, soit pour des raisons d'optique du faisceau extrait, soit à cause d'une mauvaise planéité du cristal. Ces données sont en cours d'analyse dans le groupe. En tous cas, cette dernière expérience prouve que le problème de la capture MEC en couche amorphe peut être minimisé en nettoyant ces surfaces.

2 Mesures de temps de fission à l'aide d'un cristal

Ce chapitre, beaucoup plus concis que le précédent, traite de deux types de mesures de temps de fission au moyen d'un cristal cible.
La première partie est dédiée aux mesures par blocage cristallin. En collaboration avec des physiciens nucléaires du GANIL et de l'IPN d'Orsay, nous avons entrepris depuis une dizaine d'années des expériences au GANIL. Tout d'abord nous avons mesuré des temps de fission de noyaux uranium et plomb en fonction de leur énergie d'excitation (celle-ci étant mesurée par les multiplicités de neutrons dans le détecteur 4π ORION). Plus récemment, nous nous sommes engagés dans des mesures cherchant à mettre en évidence la restauration d'une barrière de fission dans les noyaux super-lourds vers l'îlot de stabilité Z~120 (avec la collaboration additionnelle du CEA-Saclay).
La seconde partie est plus spéculative, car il s'agit d'une étude sur l'intérêt d'utiliser un cristal aligné pour observer des temps de fission par spectroscopie X en utilisant des noyaux incidents hydrogénoïdes ralentis.

2-1 Mesures de temps de fission par blocage cristallin

De nouveau, je renvoie le lecteur à la lecture de la référence [Cohen 04] (section 3.2) reproduite au début du chapitre 1 de ce mémoire. Le principe du blocage cristallin y est très bien présenté, ce qui m'évitera de le paraphraser ici, et donc d'alourdir ce manuscrit.
Le blocage cristallin ne permet pas de mesurer précisément la distribution des temps de fission. Il permet surtout de mettre en évidence l'existence ou non d'une fraction des événements de fission à des temps longs (typiquement supérieurs à 10^{-18}s). Cette information est toutefois très importante pour plusieurs raisons :
- lors de la fission de noyaux dont la barrière de fission est relativement élevée (comme le plomb ou l'uranium), la fission est en compétition avec l'évaporation de particules légères et de photons gamma. Le fait qu'un noyau puisse fissionner à des temps supérieurs à 10^{-18}s ou plus après une collision, éventuellement après plusieurs émissions qui tendent à le refroidir, montre que la matière nucléaire possède une viscosité qui conditionne le temps moyen mis par le noyau pour atteindre le point de scission. En effet, la fission est un processus dynamique au cours duquel le noyau se déforme pour atteindre d'abord le point selle (où la fission devient irréversible) puis le point de scission. Pendant cette déformation, le noyau évapore des particules légères, ce qui modifie la barrière de fission, et donc la probabilité d'atteindre ce point selle. La viscosité de la matière nucléaire freine la déformation du noyau, ce qui favorise l'évaporation. L'existence d'une queue aux temps longs dans la distribution des temps de fission montre que des noyaux peuvent évaporer plusieurs particules légères et gammas, puis atteindre lentement le point de scission à faible énergie d'excitation résiduelle, pour laquelle l'évaporation n'est plus probable. La mesure de ces temps longs permet donc de contraindre fortement les paramètres de viscosité nucléaire.
- Pour des noyaux très lourds, et donc instables, la mise en évidence de temps de fission longs à faible énergie d'excitation implique que la barrière de fission n'est pas très petite pour ces noyaux composés. C'est donc un moyen d'identifier les nombres dits magiques de charge ou de masse pour lesquels les effets de couches restaurent la barrière de fission.

L'article ci-dessous *"Nuclear fission time measurements as a function of excitation energy : A crystal blocking experiment"* [Barrué 02] correspond aux actes de la conférence ICACS 2001, au cours de laquelle j'ai présenté les résultats de nos expériences de mesures de temps de

fission de noyaux d'uranium et de plomb en fonction de l'énergie d'excitation. Ces expériences avaient été réalisées au GANIL avec des faisceaux d'ions ^{238}U de 24 MeV/u et de ^{208}Pb de 29 MeV/u, incidents sur des cristaux de silicium.
Les résultats de l'expérience avec l'uranium ont été publiés par notre collaboration [Morjean 98], [Goldenbaum 00], et font apparaître une très nette évolution de la fraction d'événements de temps de fission longs avec l'énergie d'excitation du quasi-projectile.
Une partie de l'analyse de la seconde expérience, ainsi que les simulations associées à l'effet de blocage, ont été réalisées dans notre groupe dans le cadre de la thèse de Frédéric Barrué [Barrué 02B].

ELSEVIER

Nuclear Instruments and Methods in Physics Research B 193 (2002) 852–859

NIM B
Beam Interactions with Materials & Atoms

www.elsevier.com/locate/nimb

Nuclear fission time measurements as a function of excitation energy: A crystal blocking experiment

F. Barrué [a], S. Basnary [b], A. Chbihi [b], M. Chevallier [a], C. Cohen [c], D. Dauvergne [a,*], H. Ellmer [c], J. Frankland [b], D. Jacquet [d], R. Kirsch [a], P. Lautesse [a], A. L'Hoir [c], M. Morjean [b], J.-C. Poizat [a], C. Ray [a], M. Toulemonde [e]

[a] *IPNL, CNRS/IN2P3, Université Lyon I, 3 rue Enrico Fermi, 69622 Villeurbanne Cedex, France*
[b] *GANIL, DSM/CEA, IN2P3/CNRS, BP 55027, 14076 Caen Cedex, France*
[c] *GPS, Universités Paris VI and Paris VII, 2 Place Jussieu, 75251 Paris Cedex 05, France*
[d] *IPNO, CNRS/IN2P3, Université Paris XI, BP 1, 91406 Orsay Cedex, France*
[e] *CIRIL, CNRS/CEA, rue Claude Bloch, 14040 Caen Cedex, France*

Abstract

Fission times of lead and uranium nuclei have been measured at GANIL by the crystal blocking method. The inverse kinematics was used. Fragment atomic numbers and total excitation energies were determined. For data analysis, full Monte-Carlo trajectory calculations were used to simulate the blocking patterns. The effect of post-scission emissions, included in our simulations, is discussed. At high excitation energies, the scissions occur dominantly at times shorter than 10^{-19} s, whereas at low excitation energies ($E^* < 250$–300 MeV), scissions occurring at much longer times with sizeable probabilities are observed both for uranium and for lead nuclei, leading to average scission times much longer than those inferred from pre-scission emission.

PACS: 24.75.+i; 61.85.+p
Keywords: Fission; Blocking

1. Introduction

Measuring fission times of an excited nucleus provides information on nuclear dissipation [1]. During its deformation toward the saddle point (at which the fission process becomes irreversible), an excited nucleus cools down through particle evaporation (mainly neutron emission). During the cooling, the neutron binding energies as well as the fission barriers are modified at each evaporation step and, depending on the nuclei considered, the fission probability at very low residual excitation energies, after neutron evaporation, can either remain still sizeable or become negligible. Long lifetime components, associated with fission at low residual excitation energy, can thus show up for highly fissile nuclei. Therefore, the resulting statistical average fission times will strongly depend on the fission probability at low residual excitation energy. Moreover, damping of nucleon motion

* Corresponding author.
E-mail address: d.dauvergne@ipnl.in2p3.fr (D. Dauvergne).

0168-583X/02/$ - see front matter
PII: S0168-583X(02)00915-1

due to nuclear viscosity may slow down the whole evolution until the scission point is reached [2]. Thus the magnitude of the viscosity influences considerably the time needed by an excited nucleus to reach the scission point. The excited nucleus is thus a complex dynamical system. Its evolution depends on the interplay between cooling down and deformation, the velocity of which is limited by viscosity.

This shows the importance of measuring fission times for getting information on nuclear dissipation, and, in particular, long fission times ($>10^{-18}$ s) that cannot be predicted by the standard statistical theory [3] ignoring the effects of nuclear viscosity.

Various methods can be used to measure fission times. Pre-scission emission multiplicities (of particles as neutrons or giant dipole resonance (GDR) γ-rays) can be related to fission times [4]. However, such relations suffer from two drawbacks: first, the evaluation of the fission time depends on the theoretical model used to describe the evaporation, and, second, pre-scission neutron and GDR γ-ray emission probabilities become very small at low residual excitation energies, which makes this method very little sensitive to the long times that are associated to low residual excitation energies. The crystal blocking technique, as used in this work, is certainly more straightforward because it measures in a model-independent way the recoil distance covered by the excited nucleus during the whole fission process (starting from the initial collision and ending at the scission point).

2. Fission time measurements by crystal blocking

This application of the blocking technique was proposed very soon after channeling effects were observed to affect the propagation of charged particles in aligned crystals [5–7]. During the collision of a projectile with a crystal atom, a nucleus is given an excitation energy E^* and a recoil momentum $M\vec{v}$. Then the fission occurs at a recoil position $\vec{r}_f - \vec{v}t_f$, where t_f is the scission time. At this stage the continuum potential approximation is useful to understand the blocking effect. In this approximation [8], the target atomic potential is averaged along the crystallographic direction of interest (axis or plane). In the following we will focus on axial effects. The transverse motion of a particle is separated from its longitudinal one. Individual collisions with the target atoms are ignored, as well as multiple scattering on electrons. At the fission location $\vec{r}_f$ a fission fragment is given a transverse energy

$$E_\perp = q_f U(\vec{r}_{f\perp}) + E_f \Psi_f^2,$$

where q_f, E_f, Ψ_f are respectively the fragment charge, kinetic energy and emission angle relative to the atomic string in the laboratory frame. $U(\vec{r}_\perp)$ is the continuum potential of the string, at a position $\vec{r}_\perp$ in the transverse plane defined as the projection of the recoil vector $\vec{r}$ in this plane. $E_\perp$ is the sum of a potential term and a kinetic term. If one neglects energy loss and charge exchange, and uses the hypotheses mentioned above, $E_\perp$ is conserved throughout the fragment path in the crystal. Within this approximation, the condition for the fragment to emerge from the crystal at an angle θ smaller than the critical channeling angle $\Psi_c = \sqrt{q_f U_{max}/E_f}$ with respect to the axial direction is

$$E_\perp \leqslant q_f U_{max},$$

where U_{max} is the maximum value of the transverse potential. U_{max} is reached at distances from the strings closer than u_2, that characterizes the thermal vibrations of the lattice atoms. For very short t_f values, $U(\vec{r}_{f\perp}) \approx U_{max}$ and most of the fragments are deflected at angles greater than Ψ_c. The blocking effect is weaker if the fission fragment has a smaller transverse energy, i.e. if it is emitted at a larger distance from the string.

One can then define the time sensitivity range of the blocking method for fission time measurements. Consider the probability $dN/d\Omega(\theta \leqslant \Psi_c)$ for a fragment to emerge from the crystal at an angle smaller than Ψ_c with respect to the axial direction. In the time sensitivity range $dN/d\Omega(\theta \leqslant \Psi_c)$ increases with the mean fission time τ_f, i.e. the corresponding $\langle U(r_\perp)\rangle$ is a decreasing function of $\langle r_\perp(\tau_f)\rangle$.

For short times corresponding to transverse recoils $r_{f\perp} = v_\perp t_f$ smaller than u_2, the blocking effect is maximum. Such times, smaller than

$t_{\min} = u_2/v_\perp$, are out of the time sensitivity range and lead to the same result as infinitely short times.

On the other hand, the upper time limit $t_{\max}$ corresponds to transverse recoil distances typically larger than the lattice constant d_{lattice}. Fissions occurring at times longer than $t_{\max}$ will take place at positions where the transverse potential ranges randomly between 0 and $U_{\max}$. This leads to a uniform angular distribution $\mathrm{d}N/\mathrm{d}\Omega(\theta)$ at the crystal exit, because blocking effects are compensated by channeling effects (although Andersen et al. pointed out that, given a recoil direction, there are fission time distributions that might give rise to a flux peaking at $\theta = 0$ [9]).

For scission time distributions ranging from $t_f < t_{\min}$ to $t_f > t_{\max}$, blocking experiments can provide the relative fractions of short and long time components. However, when the scission time distribution is broad (of the order of the sensitivity range of the blocking technique or beyond), it becomes very difficult, due to the finite statistics available in any experiment, to extract univocally from the data the actual time distribution. The evaluation of mean fission times will depend essentially on the assumed longest scission times. This is illustrated in Fig. 1, where blocking dips around the $\langle 1\,1\,0\rangle$ axis of silicon are simulated for various time distributions in the case of the symmetrical fission of ^{208}Pb (for 29 MeV/u incident Pb ions, corresponding to one of the experimental situations described below). In this case, where the inverse kinematics is used, the time sensitivity window is found to range roughly between 3×10^{-19} and 10^{-16} s for exponential fission time distributions. Single exponential time distributions for the fission of an excited nucleus are certainly not realistic due to the complexity of this process, as mentioned in the introduction. We used another purely arbitrary type of time distribution to simulate another blocking dip shown in Fig. 1. We used a two-component distribution with one at very short times (mean value $\tau_f = 10^{-19}$ s $< t_{\min}$, the shape of this distribution being of no importance), and a second one being uniformly distributed between 0 and 6×10^{-16} s (providing a uniform distribution of $r_{f\perp}$ values). The relative weights of these two components are 97% and 3%, respectively, corresponding to an average time

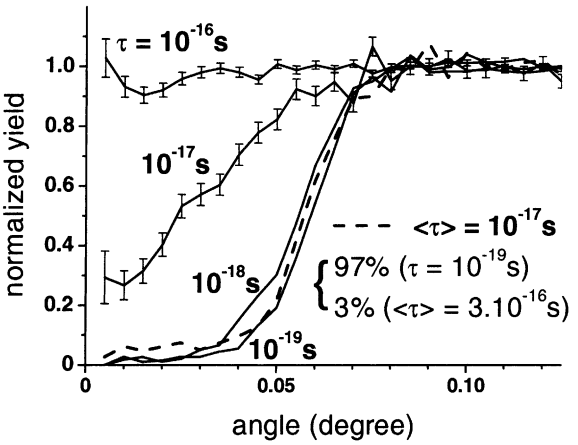

Fig. 1. Simulation of blocking dips for $Z = 41$ fission fragments of incident lead nuclei. The crystal axis is the $\langle 1\,1\,0\rangle$ axis of silicon, oriented at 5° from the incident 29 MeV/u ^{208}Pb beam. Various fission time distributions are used. All dips represented by solid lines correspond to simple exponential distributions. The dashed-line dip is obtained using a two-component time distribution (see text).

$\tau_f = 10^{-17}$ s. This time distribution may not be realistic either, although the longer time limit is of the order of the values obtained by Forster et al., in blocking experiments for the fission of lead-like nuclei with a sensitivity window shifted towards longer times [10] (due to the direct kinematics used in their case). The simulation performed with this two-component distribution shows that small fractions of long fission times may be evidenced experimentally by the blocking technique. This last simulated dip is nearly equal to the weighted sum of the dips obtained for $\tau_f < t_{\min}$ and for the uniform distribution corresponding to $\tau_f > t_{\max}$, respectively. The main difference with the distribution associated to $\tau_f < t_{\min}$ is the enhancement of the minimum of $\mathrm{d}N/\mathrm{d}\Omega(\theta)$ for $\theta \approx 0$. The difference between this dip and the one corresponding to a simple exponential distribution with same mean fission time $\tau_f = 10^{-17}$ s is striking.

So far we have described the principle of fission time measurements by blocking in terms of angular deflections caused by the continuum transverse potential at the place where scission occurs inside the crystal. Actually, a few points have to be discussed in order to go beyond this simple picture.

First of all, the continuum potential model cannot lead to a correct description of fragment trajectories close to the atomic strings. Individual atomic collisions have to be calculated in the simulations to account for elastic scattering by target nuclei.

Also, fission fragment blocking patterns may be influenced by the effects of electronic multiple scattering, energy loss and charge exchange, that cause the non-conservation of transverse energy. As we will see below, partial information on such effects can be obtained experimentally through blocking studies of a "zero lifetime" process, like Rutherford scattering.

After scission, the fission fragments are left in excited states. They will dissipate their excitation energy by emitting γ-rays or light particles like neutrons or α-particles. For each post-scission emission, the maximum angular deflection $\delta\theta_{\max}$ of the fragment is given by the ratio of the evaporated particle momentum p_{post} in the center of mass frame to the fragment momentum p_{f} in the laboratory frame: $\delta\theta_{\max} \approx p_{\text{post}}/p_{\text{f}}$. This deflection angle has to be compared to the characteristic magnitude of angular deflections caused by the blocking, i.e. the channeling critical angle Ψ_{c}. The influence of this effect on the blocking dip is then connected to the ratio

$$\frac{\delta\theta_{\max}}{\Psi_{\text{c}}} \approx \frac{p_{\text{post}}}{\sqrt{4Z_2 M_{\text{f}} q_{\text{f}} e^2/d}},$$

where Z_2 and d are the crystal atomic number and inter-atomic distance along the string, respectively, M_{f} and q_{f} are the fragment mass and charge. Thus, the relative perturbation of blocking effects by a single post-scission emission is seen to be independent of the fragment energy.

This effect of delayed particle emission by an excited nucleus after inelastic collisions has been previously studied for the blocking of light ions [11–13]. For heavy fission fragments, the emission of low momentum particles like γ-rays can generally be neglected. On the contrary, post-scission neutron evaporation can lead to noticeable modifications of the blocking dips. Nevertheless, the main problem for evaluating post-scission emission effects is the lack of accurate knowledge of the time and energy distribution for post-scission neutrons, and in particular when the fragments reach very low residual excitation energies. However, significant effects can be predicted for fragments formed after fast fissions ($\tau_{\text{f}} \leqslant t_{\min}$); these effects are associated to long particle emission times. In such cases the fragments are emitted with a transverse energy $E_{\perp} \geqslant q_{\text{f}} U_{\max}$. At the place where evaporation occurs, the potential term may be small, the recoil associated to the particle evaporation can then significantly lower the kinetic term, allowing the transverse energy of some fragments to fall below the critical transverse energy for blocking: the fragments cool down in the transverse space.

3. Experiments

We have studied fission times of uranium and lead as a function of excitation energy. For the first nucleus, that has a low fission barrier, the fission probability is sizeable whatever the excitation energy is. The existence of long fission time components had been already observed at low excitation energies in blocking experiments [14,15] and experiments using the time scale for X-ray filling of K-shell vacancies [16] whereas pre-scission neutron multiplicities [17] or GDR γ-rays [18] provided only times shorter than 10^{-18} s.

For lead nuclei, the fission at very high excitation energy is expected to be fast, like for uranium nuclei. The fission barrier is higher in the case of lead. Short fission times are also expected at low excitation energies, because only first chance fissions are allowed, as explained in the introduction. Longer fission times could be expected at intermediate excitation energies, where fission could still occur after several neutron emissions. Previous blocking experiments [9,10,19] have reported very high yields $\mathrm{d}N/\mathrm{d}\Omega(\theta \approx 0)$ of fission fragments observed close to axial directions, for fusion–fission of compound nuclei with $A \leqslant 200$, and excitation energies of the order of 100 MeV. These high yields were attributed to fission time components extending to times longer than 10^{-16} s (according to the time sensitivity window of these experiments).

The experimental setup as well as the results of our uranium experiment have been described in [20,21]. Briefly, 24 MeV/u ^{238}U ions (respectively 29 MeV/u ^{208}Pb ions) were sent onto a 6 μm (respectively 15 μm) thick silicon crystal. Both fission fragments were detected in coincidence and Z-identified using E–ΔE telescopes. The telescopes devoted to blocking were X and Y position sensitive, and located 3 m (respectively 3.5 m) behind the crystal. The blocking patterns of fission fragments were observed with the $\langle 1\,1\,0\rangle$ axis of silicon directed to the position sensitive telescope located at 7° (respectively 5°) with respect to the incident beam direction. The use of small forward angles for fission blocking observation is imposed by the inverse kinematics, which reduces the advantage of large fissioning nuclei velocities. However, the recoil velocity – and in particular the transverse component – is nearly the same for all excited nuclei (almost independent on the excitation energy and not sensitive to perturbations caused by pre-scission evaporations). This makes our configuration sensitive to shorter times than other blocking experiments using low energy light projectiles on heavy targets. Moreover, the use of swift fragments and of thin-, low Z-crystals minimizes the effect of angular multiple scattering.

The total excitation energy, ranging from 0 to 600 MeV (respectively 0–800 MeV) was measured for each fission event by the 4π ORION neutron detector. In the experiment using the lead ion beam, the beam intensity was 10^9 particle/s, two orders of magnitude higher than during the experiment with uranium ions, a counting rate too high to allow direct determination of neutron multiplicities. Thus we used the "prompt" signal from this detector, arising mainly from the energy loss of neutrons in the scintillator, and therefore correlated to the excitation energy [22].

Possible damaging of the irradiated crystal was controlled by measuring the quality of blocking for elastic scattering at 1° from the primary beam. No significant damage was observed after impact of more than 10^{12} uranium ions on a spot of about 1 mm diameter. For the lead experiment, the beam impact was changed periodically to keep the fluence at values below 10^{13} ions/mm^2. Elastic blocking patterns were recorded before and after each impact irradiation. Off-line analysis allowed us to check that crystal damaging was negligible.

4. Simulations and results

Simulations using full Monte-Carlo trajectory calculations are necessary to reproduce and interpret blocking dips. Each individual elastic collision with target atoms were calculated within the Moliere approximation of Thomas–Fermi potentials. Experimental factors that could lead to a filling of blocking patterns were taken into account empirically: such factors are the position resolution of the detector, the beam spot size, the electronic multiple scattering in the target and, possibly, crystal defects. To account for these factors we considered the blocking dips of projectiles elastically scattered at 1° from the beam. Such a typical dip is presented in Fig. 2 for lead projectiles, together with the corresponding simulation. In order to reproduce the experimental dip, the simulated angular distribution corresponding to an "ideal" experiment has been convoluted with a Gaussian distribution with $\sigma = 0.009°$, which shows that the dominant factor in this spread out is the beam spot shape. The same experimental factor has been used for all further fission fragment blocking pattern

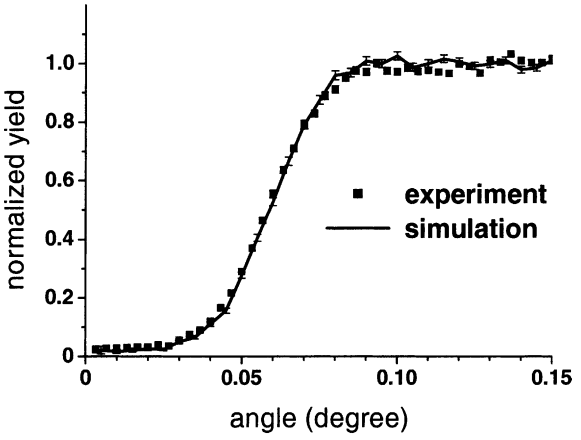

Fig. 2. Experimental blocking dip around the $\langle 1\,1\,0\rangle$ axis of silicon for elastic scattering at 1° from the incident Pb ion beam at 29 MeV/u. The line is the adjusted result of the simulations.

simulations. Hence we neglect possible (but minor) different influences due to different multiple scattering between fission fragments and elastically scattered incident ions.

Also charge exchange may modify the transverse energy of ions in the crystal. In particular, the charge state of an ion undergoing close collisions with the atomic string just after the violent nuclear collision may change during its path in the crystal. In our simulations we neglect charge exchange and use the mean charge state at equilibrium throughout the crystal. We consider that fragments are point-like charges.

The blocking dips obtained for the fission of uranium nuclei have been presented in Figs. 2 and 3 of Ref. [21] as a function of excitation energy (with the condition $Z_{f1} + Z_{f2} = 92 \pm 1$ for the detected fragments). The time distributions used to fit these dips are made up of two components: one corresponding to very short times ($\tau_f \approx 10^{-19}$ s $< t_{min}$) and a long time component (uniform distribution ranging from 0 to 6×10^{-17} s). Post-scission neutron emissions were included in the simulations according to the mean values for emission times and energies from a statistical code [23].

The relative weights X_{long} of the long time components decrease with excitation energy, with values $X_{long} \geqslant 40\%$, $X_{long} \approx 20\%$, 10%, 6% and 0%, corresponding to ranges of excitation energy with average values $\langle E^* \rangle \leqslant 20$, $\langle E^* \rangle \approx 60$, 120, 160 and 250 MeV, respectively. Such long fission time fractions are compatible with those measured in Refs. [14,15] at smaller excitation energies. Average fission times deduced in [21] from the long fission time fractions have been used by Gontchar et al. [24] to adjust phenomenologically the wall term of the wall-and-window formula for one-body dissipation in the CDSM2 model.

In the same way, we have selected excitation energies for the fission of lead ($Z_{f1} + Z_{f2} = 82$, with an uncertainty of one charge unit). Blocking dips corresponding to high ($E^* > 400$ MeV) and low ($E^* < 300$ MeV) excitation energies are presented in Fig. 3(a) and (b) respectively. They are associated to fragments emitted in the forward direction in the center of mass frame. In Fig. 3(a), the high excitation energy blocking dip is presented together with the results of simulations using a mean

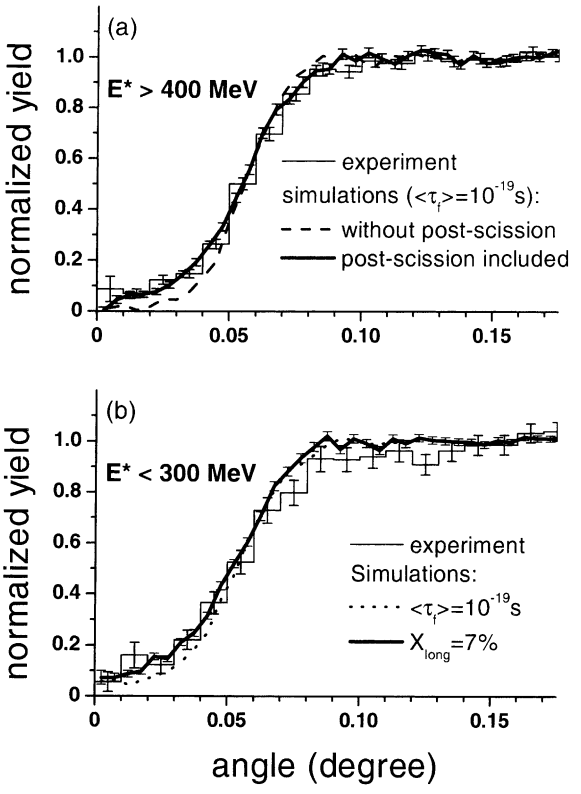

Fig. 3. Experimental blocking dips for the fission of lead-like nuclei ($Z_{f1} + Z_{f2} = 82$). The selected fragments were emitted in the forward direction in the center of mass. (a) $E^* > 400$ MeV. Dashed curve: simulation using $Z_1 = 41$, average fission time $\langle \tau_f \rangle \leqslant 10^{-19}$ s, without post-scission emission. Solid line: same simulation including post-scission emission. (b) $E^* < 300$ MeV. Dotted curve: simulation with average fission time $\langle \tau_f \rangle \leqslant 10^{-19}$ s, including post-scission emission. Solid line: Simulation using 93% of short fission times as above, and 7% of fission times ranging uniformly between 0 and 10^{-16} s.

fission time $\tau_f \leqslant 10^{-19}$ s (presented as a dashed curve). The bottom of the experimental dip is significantly higher than what is predicted by this simulation. This could suggest the existence of longer fission times. However, such a long fission time fraction should decrease when E^* increases, a behavior that is not observed in the data (subdivision in energy ranges between 300 and 800 MeV provides identical dips). Actually, this poor agreement has been obtained with a simulation in which the effects of post-scission emission have been neglected, although in the case of "fast"

fission, the fission fragments are left after scission with rather high excitation energies. We have therefore included this effect in our simulations, considering neutron evaporation by initial fragments with $Z_f = 41$, $A = 104$ and $E^* = 100$ MeV. The characteristics of the neutrons (energy and emission time) have been calculated with the statistical code SIMDEC [25]. As discussed in Section 2, only neutrons emitted at sufficiently long time after fission ($t > 10^{-18}$ s, i.e. at low residual excitation energies) have a significant influence on the blocking dips. This is indeed confirmed in our Monte-Carlo simulations. However, the neutron emission times are strongly dependent on the level density parameter value assumed in SIMDEC. In order to get the most reliable behavior at long emission time, we used the value inferred from neutron resonance studies [26] at low excitation energies for nuclear masses around $A = 100$. As shown in Fig. 3(a), a significantly better agreement with the data is reached. Considering the rough assumptions performed on the fission fragment mass, charge and energy, and the difficulty to adjust the statistical model parameters for post-scission emission, such an agreement can be considered as quite satisfactory, particularly in the minimum yield.

Similar simulations to the ones that fit satisfactorily the experimental dip in Fig. 3(a) ($E^* > 400$ MeV) are compared, in Fig. 3(b) (dotted line), to the experimental dip corresponding to low excitation energies ($E^* < 300$ MeV). A significant difference is observed. As the effect of post-scission neutron evaporation is already included in the simulations, the discrepancy, in this case, can only be attributed to a contribution of long fission times that did not show up at high excitation energies. We have therefore introduced a fraction X_{long} of fission events occurring at times ranging uniformly from 0 to 10^{-16} s. As shown by the full curve in Fig. 3(b), a better agreement is obtained, especially for the bottom of the dip, with $X_{long} = 7 \pm 3\%$.

New information will be extracted from the present experiment after further analysis. For instance, fission occurring at lower excitation energies (after emission of an α-particle) will be studied separately. Also planar blocking effects can be used to study very long fission times (above 10^{-16} s), because the crystal orientation was chosen in such a way that the time needed by the excited nuclei to recoil from the (1 0 1) plane ($t_{min} = 2 \times 10^{-17}$ s) was more than one order of magnitude longer than for the $\langle 1\,1\,0 \rangle$ axis. This will be used to improve the scission time distribution introduced in our simulations to extract the fraction X_{long}.

The existence of long fission times for $E^* < 300$ MeV observed in the present experiment seems to be in agreement with the conclusions of previous blocking experiment for the fission of lead nuclei with $A \leqslant 200$ [9,10,19] (according to Sierk systematics, the fission barriers (around 13 MeV) decrease by less than 1 MeV between $A = 207$ and 200; therefore the different lead isotopes considered in the various blocking experiments should only take into account weak discrepancies). Nevertheless, although these experiments were less sensitive to post-scission emissions (due to the use of high-Z crystals), the long fission time components that were deduced from these experiments were probably overestimated, because post-scission emission was neglected in their analysis. However, all the experiments performed up to now in order to reach pieces of information on the fission time scales involved in the fission process of lead nuclei have shown the existence of long fission times with sizeable weights, corresponding to average scission times longer than 10^{-19} s. Like in the case of uranium [21], a strong discrepancy seems to exist between these long average times and the much shorter times inferred from pre-scission emission [4].

5. Summary

We have measured fission times by the blocking technique in single crystals over a wide range of excitation energies for two very different nuclei. For highly fissile uranium nuclei, a large fraction of long fission times (above 10^{-17} s) is observed at low excitation energy, and vanishes progressively above 200 MeV. Such long times are in agreement with previous blocking measurements at low excitation energies, and they provide a new piece of information on nuclear dissipation. For the much less fissile lead nuclei, the evolution of the blocking

dips has been analyzed for excitation energies larger than 400 MeV and lower than 300 MeV. The blocking dip measured for the highest excitation energy is reproduced by simulations considering only short fission times ($\tau_f \leqslant 10^{-19}$ s), provided the huge effect of post-scission emission is taken into account. For the lowest excitation energies, a significant fraction of long fission times is observed, leading to an average fission time longer than 10^{-19} s. Like in the case of uranium, the fission times inferred by the blocking technique seem much longer than those inferred from pre-scission emission.

References

[1] D. Hilscher, H. Rossner, Ann. Phys. Fr. 17 (1992) 471.
[2] Yu.A. Lazarev et al., Phys. Rev. Lett. 70 (1993) 1220.
[3] N. Bohr, J.A. Wheeler, Phys. Rev. 36 (1939) 426.
[4] D.J. Hinde, Nucl. Phys. A 553 (1993) 255c.
[5] A.F. Tulinov, Dokl. Akad. Nauk. SSSR 162 (1965) 546 (Sov. Phys.-Doklady 10 (1965) 463).
[6] D.S. Gemmell, R.E. Holland, Phys. Rev. Lett. 14 (1965) 945.
[7] W.M. Gibson, Ann. Rev. Nucl. Sci. 25 (1975) 465.
[8] J. Lindhard, K. Dan. Vidensk. Selsk. Mat. Fys. Medd. 34 (1965) 14.
[9] J.U. Andersen et al., K. Dan. Vidensk. Selsk. Mat. Fys. Medd. 40 (1980) 7.
[10] J.S. Forster, I.V. Mitchell, J.U. Andersen, A.S. Jensen, E. Laegsgaard, W.M. Gibson, K. Reichelt, Nucl. Phys. A 464 (1987) 497.
[11] R.F.A. Hoernlé, R.W. Fearick, J.P.F. Sellschop, Phys. Rev. Lett. 68 (1992) 500.
[12] F. Malaguti, G. Giardina, P. Olivo, Nucl. Instr. and Meth. B 129 (1997) 341.
[13] S.A. Karamyan, Nucl. Instr. and Meth. B 51 (1990) 354.
[14] J.U. Andersen, K.O. Nielsen, J. Skak-Nielsen, R. Hellborg, K.G. Prasad, Nucl. Phys. A 241 (1975) 317.
[15] Yu.V. Melikov, Yu.D. Otstavnov, A.F. Tulinov, N.G. Chetchenin, Nucl. Phys. A 180 (1972) 241.
[16] J.D. Molitoris et al., Phys. Rev. Lett. 70 (1993) 537.
[17] D.J. Hinde, D. Hilscher, H. Rossner, Nucl. Phys. A 502 (1989) 497c.
[18] R. Butsch, D.J. Hofman, C.P. Montoya, P. Paul, M. Thoennessen, Phys. Rev. C 44 (1991) 1515.
[19] V.V. Kamanin, S.A. Karamyan, F. Normuratov, S.P. Tret'Yakova, Sov. J. Nucl. Phys. 16 (1973) 249 (Yad. Fyz. 16 (1972) 447).
[20] M. Morjean et al., Nucl. Phys. A 630 (1998) 200c.
[21] F. Goldenbaum et al., Phys. Rev. Lett. 82 (2000) 5012.
[22] M. Morjean et al., Nucl. Phys. A 591 (1995) 371.
[23] R.J. Charity et al., Nucl. Phys. A 483 (1988) 371.
[24] I. Gontchar, M. Morjean, S. Basnary, GANIL P0018, 2000.
[25] M. Ohta et al., in: Proceedings of Tours Symposium on Nuclear Physics II, World Scientific, 1994, p. 480.
[26] J.R. Huizenga, L.G. Moretto, Ann. Rev. Nucl. Sci. 22 (1972) 427.

Le noyau de plomb étant beaucoup moins fissile que celui d'uranium, la statistique sur les événements de fission à faible énergie d'excitation était très faible dans cette expérience. Néanmoins, une analyse minutieuse a été réalisée par Frédéric Barrué (ainsi que par Stéphane Basnary au GANIL [Basnary 02]), qui a permis de faire ressortir les faibles évolutions constatées des temps de fission en fonction du numéro atomique et de l'énergie d'excitation du noyau fissionnant.
Il me semble important de rappeler les résultats présentés ci-dessous, qui sont extraits de la thèse de Frédéric Barrué. En particulier, ils mettent en évidence, et ce pour la première fois, l'intérêt des effets de blocage planaire pour mieux identifier la contribution des neutrons retardés.
Le principe est simple : le blocage cristallin se caractérise par la présence du potentiel cristallin sur le site de l'émission d'un fragment chargé ; ce potentiel modifie la distribution angulaire des fragments en les éloignant des directions d'axe et de plans. D'une direction cristallographique à une autre, le potentiel répulsif n'est pas le même ; de plus le temps mis par le noyau composé pour reculer d'un plan ou d'une rangée dépend de l'orientation choisie de la cible par rapport au faisceau incident. On a donc accès à des informations différentes sur les temps de fission si on observe la fission par rapport à plusieurs directions cristallographiques simultanément. Cependant cette information est restreinte par la petite ouverture angulaire de l'émission des fragments, surtout en cinématique inverse. Une image de blocage permet ainsi de cumuler plusieurs plans, mais un seul axe.
De plus, l'effet des émissions de neutrons de post-scission sur un creux de blocage sera maximum si i) les neutrons sont émis loin des rangées ou des plans, c'est-à-dire longtemps après la fission (l'impulsion transverse peut alors réduire l'angle d'un fragment par rapport à la direction planaire ou axiale) et ii) le potentiel cristallin du plan ou de l'axe est faible (la perturbation angulaire pour « ramener » un fragment dans la direction cristallographique peut être obtenue avec des neutrons faiblement énergétiques).
C'est le principe du travail qui a été détaillé dans cette thèse. Je rappelle brièvement quelques uns des résultats obtenus dans l'expérience ^{208}Pb+Si à 29 MeV/u (cette analyse n'a malheureusement pas été faite pour l'expérience de fission de noyaux uranium).
L'identification de la charge du noyau fissionnant a été obtenue (au moyen de l'analyse en charge des deux fragments Z1 et Z2), et trois lots de noyaux ont été étudiés : Z1+Z2=83-84, Z1+Z2=82, Z1+Z2=80-81. Comme dans la référence [Barrué 02] présentée plus haut, deux lots d'énergie d'excitation ont été étudiés : E*<300 MeV et E*>400 MeV. D'avantage d'intervalles en énergie ont été pris en compte dans la thèse de Stéphane Basnary, mais seul le blocage axial y est considéré, et la statistique associée aux petites énergies d'excitation est faible.
Le cristal était positionné de telle façon que le plan (110) était à seulement 4° de la direction du faisceau incident. Il en résulte que le temps nécessaire pour qu'un noyau recule au-delà des vibrations thermiques dans ce plan était un ordre de grandeur plus élevé (quelques 10^{-17}s) que pour les autres orientations majeures prises en compte dans cette analyse. La figure 18 montre une image de distribution spatiale de fragments de fission obtenue sur le détecteur (à 5° du faisceau incident). Les ombres dessinées par l'axe <110> et les plans majeurs (100), (110) et (111) sont clairement visibles.

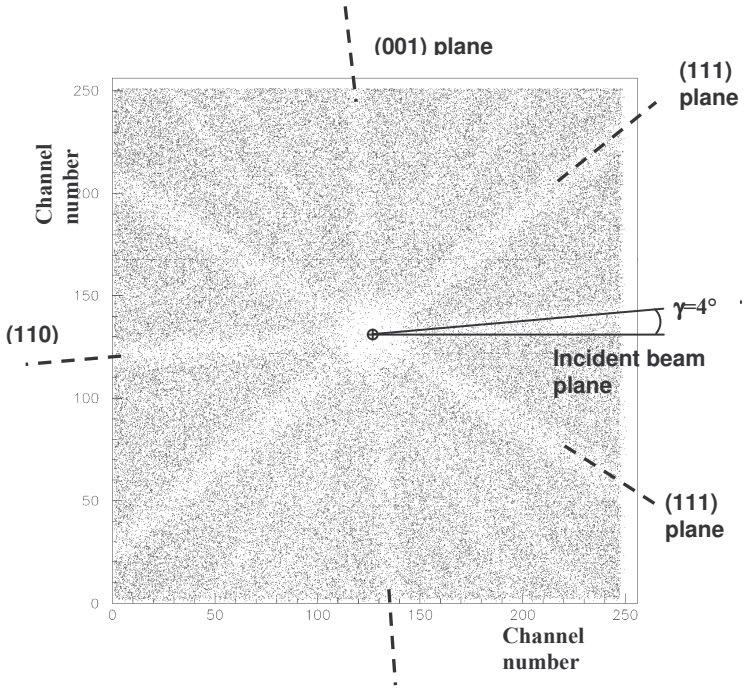

Figure 18 : *distribution de fragments de fission à 5° du faisceau incident de ^{208}Pb à 29 MeV/u sur un cristal de silicium. Le plan horizontal correspond au plan du faisceau.*

Les résultats des intégrations angulaires des fragments émis autour de l'axe sont représentés figure 19 ci-dessous :

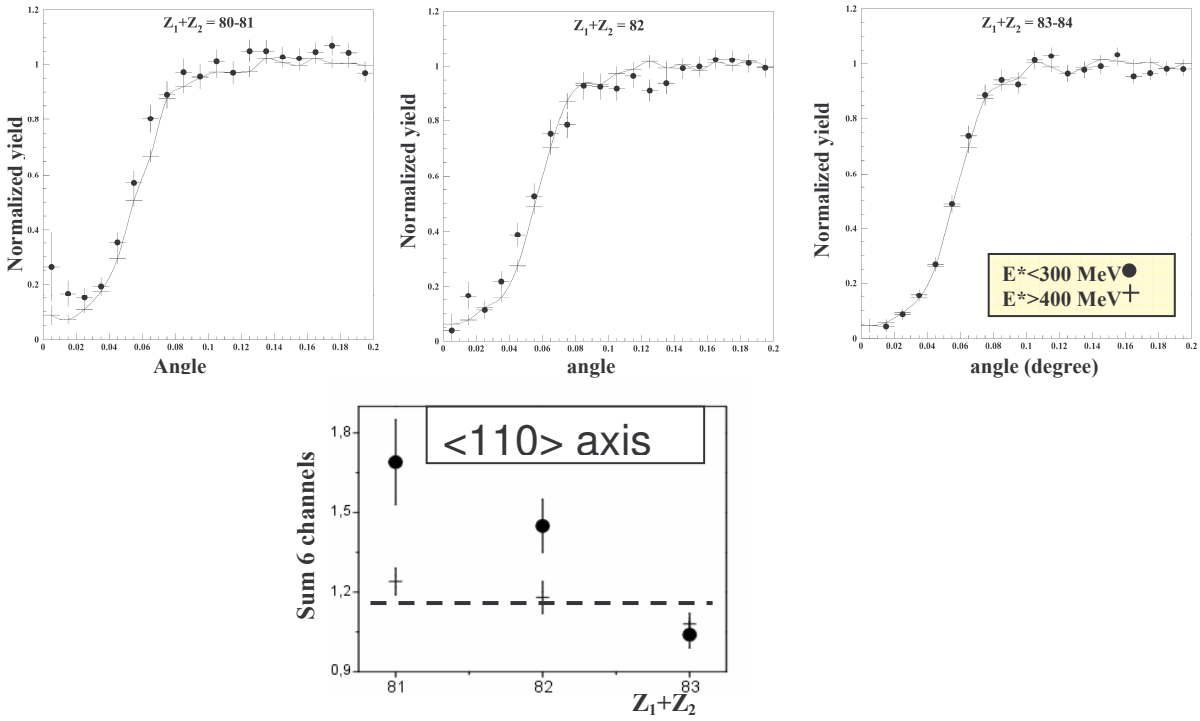

Figure 19 : *Creux de blocage axial <110> pour des fragments de fission (émis vers l'avant dans le centre de masse du noyau) pour trois charges du noyau qui fissionne et pour deux domaines d'énergie d'excitation. La figure du bas représente l'évolution pour la somme des 8 canaux du fond du creux (environ 0,06°).*

L'effet de blocage est nettement diminué (le creux se remplit) à faible énergie d'excitation pour les noyaux de Z inférieur à 82. Pour Z=82, cette différence existe mais elle est plus faible. Pour Z>82, il n'y a pas de variation avec l'énergie d'excitation. Par ailleurs, à forte énergie d'excitation, les creux de blocage sont identiques pour toutes les charges.
La figure 20 montre les creux de blocage planaire obtenus pour les plans (100) et (110), et les résultats intégrés sur la demi-largeur de ces creux (qui incluent le plan (111)). A faible énergie d'excitation, on retrouve bien un remplissage significatif des creux de blocage pour Z<82 pour les 3 orientations planaires, y compris pour le plan (110) pour lequel le seuil de sensibilité aux temps de fission longs est au-delà de 10^{-17}s. Pour Z= 82, l'effet observé dans l'axe n'apparaît plus.
Le résultat plus surprenant est que pour le plan (110), mais aussi pour le plan (100) dans une moindre mesure, on constate un remplissage important des creux de blocage à forte énergie d'excitation. Pour les charges supérieures ou égales à 82, ils sont même plus remplis qu'à faible énergie d'excitation. Pour le plan (111), on retrouve le comportement observé dans l'axe <110>.

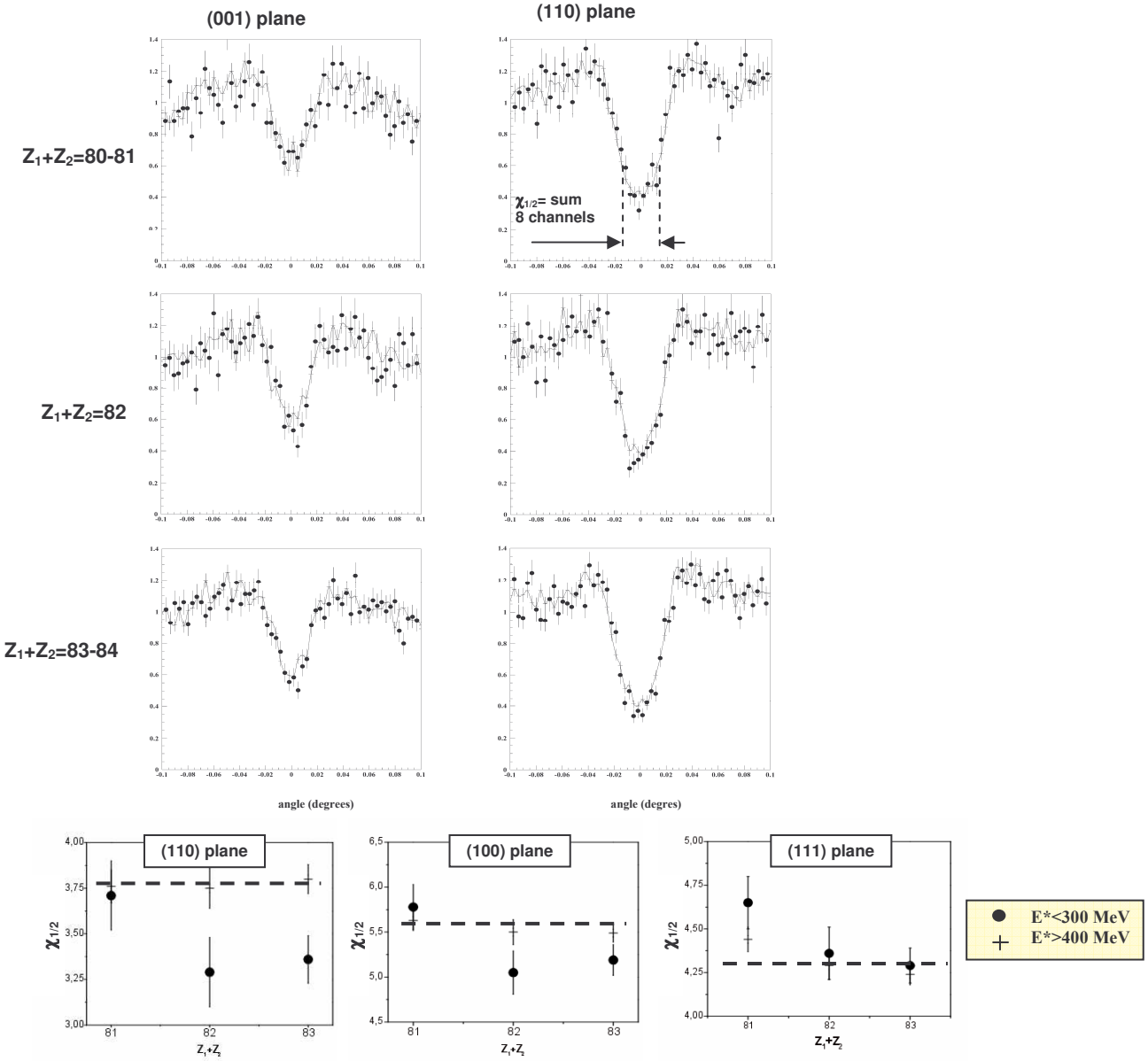

Figure 20 : *creux de blocages planaires dans les mêmes conditions que pour la figure 19. En bas, les creux ont été intégrés pour les trois plans étudiés.*

Ce phénomène a pu être expliqué et reproduit à l'aide des simulations, en incluant de façon détaillée l'effet des neutrons de post-scission. Ces simulations utilisent une distribution de temps de fission à deux composantes, l'une courte ($<3.10^{-19}$s) et l'autre uniformément distribuée de 0 jusqu'à 10^{-16}s. L'introduction de temps aussi longs est nécessaire pour reproduire le point Z=80-81 dans le plan (110).
L'émission des neutrons de post-scission par les fragments a été calculée par un code statistique (SIMDEC). Dans ce code, la distribution en énergie d'excitation résiduelle des fragments a été considérée dépendante de l'énergie d'excitation initiale ; cette hypothèse paraît justifiée car le temps de fission associé dépend lui-même de cette énergie d'excitation initiale. Les paramètres de densité de niveau ont été ajustés à une valeur raisonnable dans cette région de masse (voir figure IV-14 de la thèse de Frédéric Barrué), bien que supérieure à la valeur moyenne A/8 généralement utilisée. Cet ajustement a permis de reproduire l'effet associé à la multiplicité de neutrons émis à des temps longs après la fission ($> 10^{-17}$s), seuls ces neutrons ayant un effet sur les creux de blocage, pour les événements de fission à forte énergie d'excitation (E*>400 MeV). Je rappelle que pour ces événements à forte énergie d'excitation, les résultats montrent que les temps de fission sont tous courts, quelle que soit la charge du noyau. Seuls les neutrons de post-scission très retardés peuvent donc contribuer à un remplissage des creux de blocage.
A faible énergie d'excitation, la multiplicité des neutrons émis au delà de 10^{-17}s après la fission est plus faible (typiquement 0,3 au lieu de 1 neutron en moyenne pour les événements avec E*>400 MeV). La perturbation des creux de blocage est plus petite. La figure 21 illustre le bon accord entre les mesures et les résultats de ces simulations.

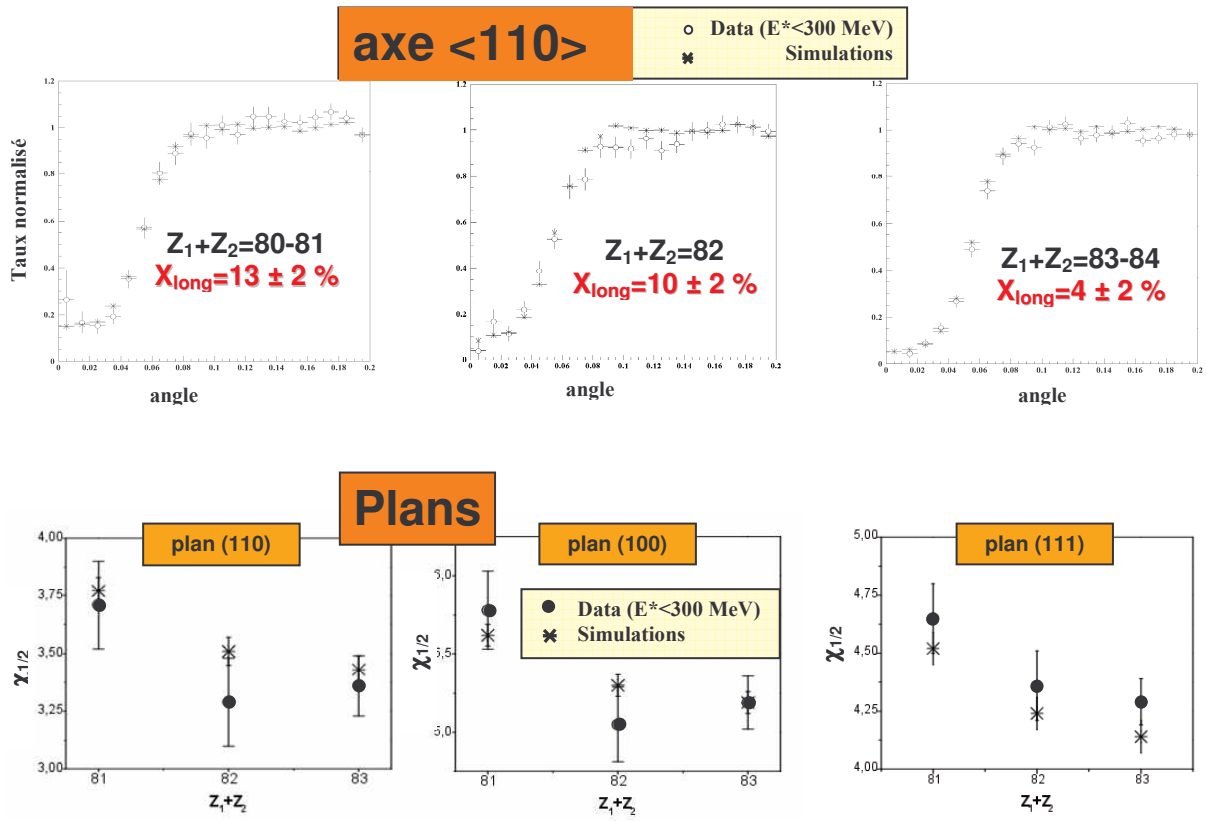

Figure 21 *: comparaison entre simulations et mesures pour les événements de fission à faible énergie d'excitation (E*<300 MeV). La fraction X_{long} indiquées dans les creux axiaux représente la fraction de la composante à temps longs (entre 0 et 10^{-16}s) utilisée pour chaque groupe de charge. Les résultats des simulations planaires ont été normalisés aux résultats à forte énergie d'excitation.*

Pour conclure cette section, j'ai tenu à repréciser que l'analyse fine des effets de blocage planaire et axial a permis de montrer que des informations enrichies sur la distribution des temps de fission peuvent être obtenues par rapport au seul blocage autour d'une direction d'axe. Cette analyse n'avait jamais été effectuée auparavant dans une expérience de mesures de temps de fission par blocage. En particulier, le choix judicieux d'un plan majeur presque rasant par rapport au faisceau incident permet de mettre en évidence des temps de fission très longs (supérieurs à 10^{-17}s dans le cas présent). Cette analyse montre de plus que l'effet des neutrons de post-scission doit être pris en compte de façon très détaillée pour reproduire les creux de blocage dans toutes les directions. En particulier, le taux d'émission des neutrons très retardés, responsable du remplissage des creux de blocage en l'absence de temps de fission longs, semble dépendre de l'énergie d'excitation initiale du noyau composé. Cette hypothèse est nécessaire pour obtenir un bon ajustement par les simulations.
Ce dernier point est important car nous ne pouvons plus affirmer que le blocage cristallin est une méthode de mesure « directe » des temps de fission, c'est-à-dire indépendante de tout modèle pour la fission. Cette remarque est dérangeante, car elle peut permettre aux détracteurs de ces expériences de critiquer l'existence de temps de fission beaucoup plus élevés obtenus dans certaines expériences de blocage cristallin, que les prédictions par les modèles, ainsi que par les mesures (très modèle-dépendantes) par émission de neutrons ou gammas de pré-scission, ou d'asymétrie de fission.
Il faut toutefois préciser que la prise en compte d'un effet de neutrons de post-scission, plus important à forte qu'à faible énergie d'excitation dans cette expérience, ne fait qu'augmenter la fraction d'événements de fissions à temps longs que l'on trouve à faible énergie d'excitation.

Après ce qui me semble être le point fort de notre apport sur ces expériences de blocage, il me faut également mentionner les dernières expériences, menées en 2003 et 2005, sur la recherche de temps de fission longs dans les noyaux super-lourds. Ces expériences cherchent à observer des réactions de fusion-fission, dans lesquelles la présence de temps de fission longs est une signature de la restauration de la barrière de fission au voisinage de l'îlot de stabilité prédit pour les super-lourds. Ces expériences ont été réalisées dans le détecteur de particules 4π-INDRA, afin d'identifier le 2^{e} fragment de fission (le 1er étant détecté en position et identifié en charge au moyen d'un télescope DE-E), mais aussi la présence éventuelle de particules chargées légères.
La figure 22 est extraite de la référence [Drouart 06] et permet une présentation des résultats de la première expérience, réalisée avec un faisceau d'ions ^{238}U de 6,6 MeV/u et un cristal cible de nickel. La partie gauche est une distribution bidimensionnelle DE-E dans le télescope de blocage cristallin. Des lignes permettent d'identifier les charges émises à un angle proche de 20° (lignes de Z indexées sur la figure). Des zones indexées 1 à 5 correspondent à certains types d'événements. En particulier la zone 2 très intense correspond aux reculs de noyaux de Ni lors de collisions quasi-élastiques. La zone 4 est dominée par la fission séquentielle de l'uranium, avec une distribution asymétrique. La zone 5 correspond à une région en Z correspondant soit à de la quasi-fission, soit à des événements de fusion-fission U+Ni, avec un noyau de charge proche de 120. L'identification du 2^{e} fragment et la vérification du très faible taux d'émission de particules légères avec INDRA ont permis la sélection d'événements binaires tels que Z1+Z2=120.
Les creux de blocage axial (axe <110>) pour les zones 2,4,5 sont présentés dans la partie droite de la figure 22. Brièvement, ces creux montrent que la diffusion quasi-élastique des ions Ni est bien un événement instantané à l'échelle des temps mesurables par le blocage cristallin ; on retrouve les temps longs pour la fission séquentielle de l'uranium (l'énergie disponible dans le centre de masse est beaucoup plus faible ici que dans l'expérience à

24 MeV/u de la référence [Goldenbaum 99]). Pour la zone de quasi-fission et fusion-fission, la valeur minimum au fond du creux est environ 10% plus élevée que pour les reculs quasi-élastiques de nickel (zone 2). Nous attribuons ce réhaussement à la contribution de réactions de formation de noyaux composés de Z=120, suivie de fission à des temps supérieurs à 10^{-18}s, qui est la limite inférieure de sensibilité aux temps longs dans cette expérience de blocage. Les neutrons de post-scission ne devraient pas jouer un rôle dans les réactions de quasi-fission (Maurice Morjean, communication privée), contrairement à nos précédentes expériences.

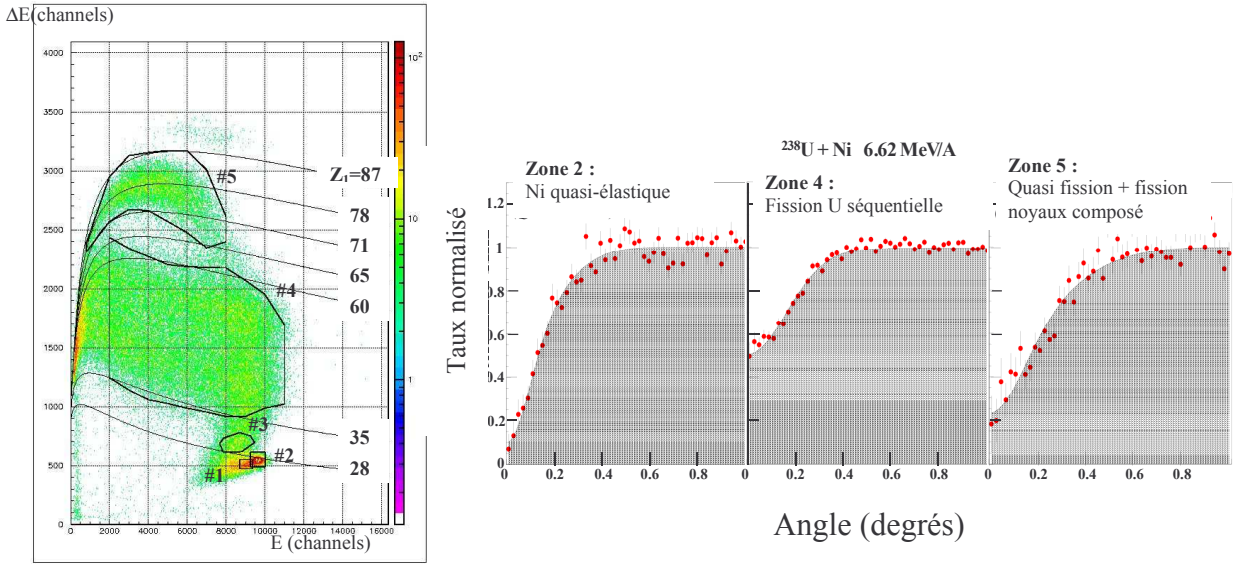

Figure 22 *: A gauche, distribution bidimensionnelle de particules chargées, détectées par le télescope de blocage cristallin situé à 20° de la direction du faisceau incident, pour des ions ^{238}U de 6,6 MeV/u incident sur un cristal de Ni. A droite, creux de blocage axial intégrés et normalisés pour les régions notées 2,4,5 de la partie gauche.*

Ce résultat implique donc une contribution importante de ces réactions de fusion-fission de l'élément Z=120 formé dans ces collisions.
Les simulations associées pour reproduire la forme de l'ensemble des creux de blocage obtenus dans cette expérience ont été entreprises à Paris par Alain L'Hoir. Ce dernier s'est heurté à la difficulté de reproduire la forme du creux obtenu pour les reculs quasi-élastique du nickel. En effet, ce creux a une forme anormale en entonnoir. La raison semble être un biais dans l'analyse, avec un brouillage de l'image dans la sommation de plusieurs acquisitions pour lesquelles l'impact du faisceau a été déplacé sur la cible. Le creux associé aux ions Ni, qui est plus étroit que celui des fragments de fission en raison de la charge, est donc plus sensible à ce brouillage. De plus les cristaux de nickel utilisés ont une mosaïcité importante, ce qui dégrade la sensibilité de l'expérience de blocage. Les simulations ne permettront donc pas de préciser beaucoup mieux la fraction d'événements de fission à temps longs de ces noyaux Z=120, en raison du trop grand nombre de paramètres ajustables.
La seconde expérience a été menée en 2005 avec le même dispositif expérimental, mais cette fois avec des ions ^{238}U et ^{208}Pb incidents à la même énergie de 6,6 MeV/u sur des cristaux de germanium. Le but était d'étudier ces événements de fusion-fission avec des noyaux composés de Z=114 et Z=124, en espérant trouver des résultats différents de ceux avec les noyaux Z=120. Ce serait la preuve que les temps de fission longs observés pour les noyaux Z=120 correspondent bien à l'îlot de stabilité des noyaux super-lourds. Les résultats sont en cours d'analyse au GANIL. En parallèle, une expérience sera proposée au LEA de Legnaro pour observer les temps de fission par spectrométrie X dans la collision U+Ni.

2-2 Mesures de temps de fission par spectroscopie X. Spéculons…

2-2-1 Méthode de mesure de temps de fission longs avec des ions hydrogénoïdes ralentis

Nous avons vu qu'un ion hydrogénoïde ralenti à 20 MeV/u (12 MeV/u) conserve sa lacune K pendant 2.10^{-15}s ($1{,}2.10^{-15}$s) lorsqu'il pénètre dans une cible solide de silicium non alignée. La précision sur ces mesures est de l'ordre de 30 à 40%. Les parcours l_K correspondant au temps de survie τ_K d'une lacune K sont de 1200 Å à 20 MeV/u et de 600 Å à 12 MeV/u.

τ_K est la somme de deux temps : le temps τ_{capt} nécessaire à la capture d'au moins un électron, et le temps τ_{casc} de la première décroissance en couche K (radiative ou Auger) d'un électron depuis les états électroniques très excités sur lesquels la capture MEC s'effectue. La capture mécanique est en effet le processus de loin le plus probable hors canalisation (par comparaison, le temps nécessaire pour faire un REC-K est de l'ordre de10^{-13}s à ces énergies).

τ_{capt} est inversement proportionnel au produit de la section efficace de MEC par le taux moyen de collisions, donc augmente avec l'énergie comme E^5 dans le régime des vitesses élevées.

τ_{casc} doit dépendre beaucoup moins violemment de l'énergie du projectile : lorsque E diminue, d'un côté les électrons sont capturés sur des niveaux *n* du projectile de plus en plus élevés, ce qui rallonge le temps moyen des cascades, mais, d'un autre côté, le nombre moyen d'électrons capturés par collision augmente, car σ_{MEC} augmente, ce qui a tendance à raccourcir le temps des cascades. Il est toutefois possible d'estimer τ_{casc} à l'aide de simulations numériques, car les probabilités de transitions radiatives et Auger sont calculables.

La faible variation de τ_K entre les deux énergies incidentes montre que ce temps est en grande partie dû à la durée des cascades électroniques, la capture d'électrons sur des états très excités étant, quant à elle, très rapide dans la matière amorphe.

Le transport de ces ions avec une lacune K présente un intérêt pour des mesures de temps de fission nucléaire : supposons qu'un tel noyau, très en dessus de sa charge à l'équilibre, subisse une collision avec un noyau de la cible. Le noyau composé ou quasi-projectile lourd aura nécessairement capturé des électrons lors de la collision du projectile avec le noyau cible (atome neutre). Dans le cas d'une collision dissymétrique entre un projectile lourd et une cible légère, cette capture préservera la lacune K car la probabilité de MEC en couche K d'un ion lourd est très faible aux vitesses en question ici (≤ 20 MeV/nucléon). Si ce noyau survit suffisamment longtemps à la fission, il y aura réarrangement du cortège électronique, en un temps qui est de l'ordre de 10^{-15}s au maximum. Ce temps limite peut être raccourci d'un ordre de grandeur si les électrons se trouvent sur des états *n* faiblement excités après la collision entre les deux noyaux, car la collision nucléaire correspond à un paramètre d'impact nul à l'échelle atomique (ce qui favorise la capture sur les *n* faibles). On peut se servir de la durée de vie d'une lacune K comme d'un chronomètre pour la survie d'un noyau excité. Dans le cas où la lacune K est créée par ionisation lors de la collision, cette méthode est assez ancienne et des articles de revue ont été publiés dans les références [Massa 1982], [Meyerhof 1985] ; plus récemment des mesures ont été réalisées pour la fission de noyaux lourds par Molitoris et al. [Molitoris 93] ou, plus récemment, par Wilschut et al. [Wilschut 2004]. La spectroscopie X autorise une très bonne identification du numéro atomique du noyau émetteur : pour Z~100 ou plus, le décalage en énergie des X_K ou X_L correspondant à une unité de charge est d'environ 2%, ce qui est facilement mesurable (avec toutefois un bémol en raison des multiples configurations électroniques conduisant à ces émissions X).

Par rapport aux expériences citées dans les références ci-dessus, l'avantage de la méthode proposée ici est de fournir la lacune K avec des ions hydrogénoïdes incidents : pour une cible

d'épaisseur inférieure à l_K, à peu près 100% des candidats à la fission émettront un rayonnement K après avoir subi leur collision nucléaire: soit celui du noyau composé, soit celui d'un des fragments de fission si celle-ci est rapide. L'inconvénient par rapport aux deux références [cite Molitoris et Wilschut] est que la durée de vie de la lacune K n'est pas aussi courte que dans le cas où une seule lacune est créée dans la collision alors que la couche L est partiellement (au moins) remplie. On a donc accès par cette méthode à des temps plus longs et moins bien définis : en effet, quelle est la configuration électronique juste après une collision nucléaire lorsque l'ion le plus lourd est en cours de rhabillage et possède une lacune K, et le plus léger est neutre initialement ?
Quoi qu'il en soit, l'observation éventuelle des rayonnements X_K d'un noyau composé lourd en coïncidence avec des fragments de fission serait une preuve de l'existence de temps de fission longs.
On peut aussi envisager de mesurer la capture radiative REC-K ou REC-L sur un noyau composé s'il survit plus que quelques 10^{-17} s. Cependant, les sections efficaces de capture radiative sont beaucoup plus faibles que celles de MEC, bien qu'elles mettent en jeu principalement les couches K et L. Par rapport aux rendements X_K, les rendements de REC du noyau composé seront au moins deux ordres de grandeur plus petits. Cependant, leur observation est intéressante du point de vue de la physique atomique. En particulier, l'observation de photons REC-K ou REC-L n'a jamais été faite sur des noyaux composés lourds ($Z > 92$).
Pour les mesures de fluorescence X_K, il est préférable d'utiliser des cibles minces, d'épaisseur de l'ordre de l_K. En effet, si le cristal est plus épais, les événements de fission consécutifs à une collision nucléaire au-delà de l_K seront en coïncidence avec des rayonnements X_K correspondant au rhabillage du projectile incident avant cette collision, ce qui créera un bruit de fond dénué d'information sur les temps de fission.
Si on veut se placer légèrement au dessus de la barrière coulombienne, pour étudier des temps de fission de noyaux composés faiblement excités, on peut supposer que τ_K ne diminue pas par rapport à la valeur déduite à 12 MeV/u, pour les raisons discutées plus haut. A 7 MeV/u, l_K est de 400 Å environ pour un noyau d'uranium dans une cible de silicium.
La figure 23 ci-dessous représente le résultat d'une simulation réalisée pour un faisceau de 20000 ions U^{91+} de 12 MeV/u dans une cible de silicium non alignée. La probabilité de capture mécanique en fonction du paramètre d'impact a été extrapolée à partir des calculs utilisés à 20 MeV/u, avec une dépendance en $E^{-5,5}$ de la section efficace totale de capture.
La figure 23-a représente la distribution des événements de capture en fonction de l'épaisseur traversée, avec une épaisseur totale de 2300 Å. Le nombre de captures par ion est de 37 en moyenne. Les oscillations observées correspondent au fait que, pour l'orientation choisie, la concentration d'atomes cibles varie en fonction de la profondeur à cause de la structure ordonnée de la cible. En d'autres termes, il est très difficile d'obtenir une direction de propagation pour laquelle les collisions avec les atomes sont de type aléatoire avec un cristal ordonné. Ceci n'a pas de conséquence pour la présente étude.
La figure 23-b représente la distribution des positions où la première capture électronique s'effectue. La valeur moyenne obtenue ici est de 118,5 Å. Une telle distance est parcourue en $2{,}5.10^{-16}$s à cette énergie, qui correspond à τ_{capt}.
La figure 23-c représente la distribution des événements de collisions à un paramètre d'impact inférieur à 1000 fm. Cette valeur est très petite devant l'amplitude des vibrations thermiques et le rayon d'écrantage atomique. Par un facteur d'échelle on obtiendra donc la probabilité d'avoir une réaction nucléaire. Par exemple, si on fait l'hypothèse d'une section efficace géométrique de 1 barn, cela correspond à un paramètre d'impact de 5,6 fm, et l'intégrale de la distribution est de $(5{,}6/1000)^2$ fois la valeur représentée dans la figure.

La figure 23-d représente la même probabilité qu'en 1-c, mais avec en plus la condition que le projectile ait encore sa lacune K dans la cible au moment de la collision à b < 1000 fm. Le temps τ_{casc} a été pris égal à 10^{-15}s d'après notre expérience. L'épaisseur "utile" maximum de cible est de 800 Å, en accord avec la valeur moyenne l_K de 600 Å estimée plus haut pour le parcours avec une lacune K. Encore une fois, cette valeur de 800 Å dépend fortement du choix de l'orientation du cristal.

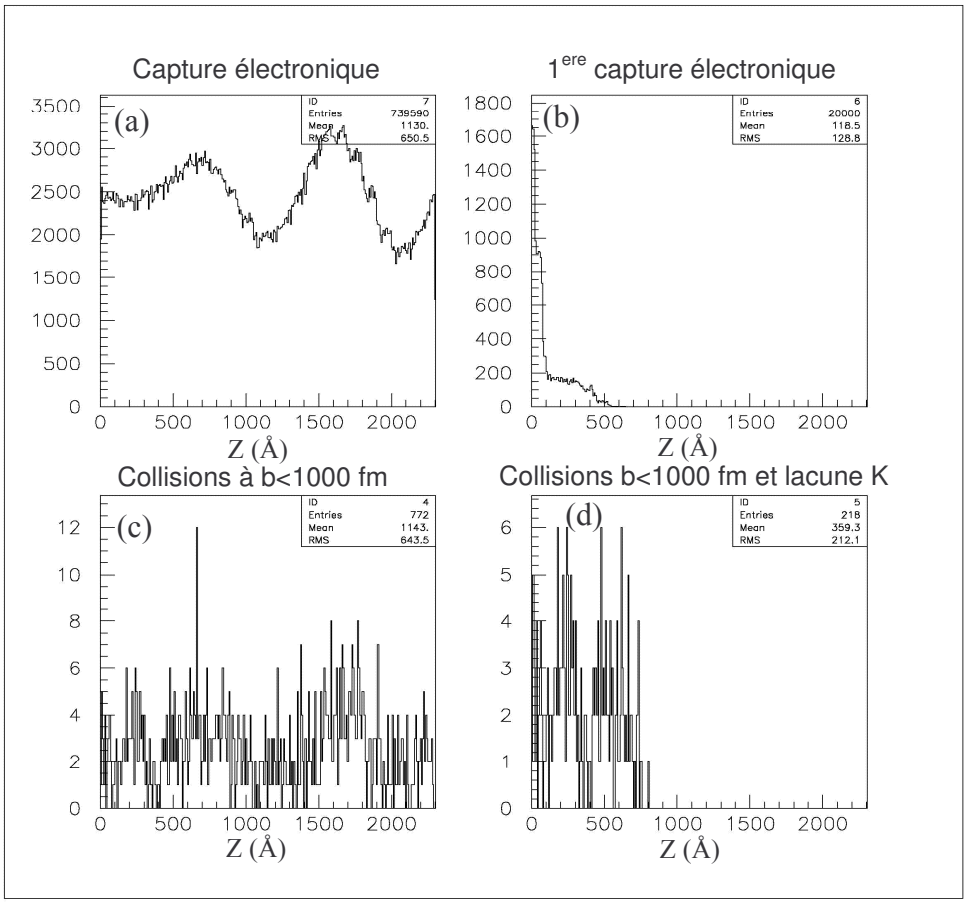

Figure 23 : Simulation, hors condition de canalisation, du taux de collisions en fonction de la profondeur pour des ions U^{91+} incidents à 12 MeV/u sur une cible de silicium. (a) Evénements de capture électronique. (b) Premier événement de capture. (c) Collisions à paramètre d'impact inférieur à 1000 fm. (d) Idem, avec survie de la lacune K du projectile pendant 10^{-15}s après la 1ère capture électronique. Le nombre de tirages est de 20000, le pas des histogrammes est de 2 fois la distance interatomique d_{110}, soit 7,68 Å .

La probabilité d'obtenir une réaction nucléaire à un paramètre d'impact inférieur à 5,6 fm pour un ion uranium avec une lacune K est de $3{,}4.10^{-7}$ par ion 91+ incident à 12 MeV/u, pour une cible d'épaisseur au moins égale à 800 Å. Une simulation similaire pour une énergie incidente de 7 MeV/u conduit à une probabilité de $2{,}3.10^{-7}$, dans une cible d'au moins 500 Å.

2-2-2 Intérêt de l'utilisation d'un cristal.

L'utilisation d'un cristal convenablement aligné peut permettre d'augmenter la probabilité de collisions nucléaires sur des parcours du même ordre. En effet, on peut optimiser la fraction d'ions de forte énergie transverse qui subissent des collisions rasantes sur les rangées

d'atomes au voisinage de la surface d'un cristal. On s'intéresse ici à l'effet de superdensité associé au pic de surface (ou de l'épaulement dans le cas d'un cristal légèrement désaligné).
Nous avons vu (section I-5-2) que, en canalisation axiale, les ions hydrogénoïdes de très forte énergie transverse font plus de REC-K et L que pour une orientation quelconque du cristal, car ils conservent leur lacune K sur une distance telle que la densité électronique intégrée est supérieure à $\langle\rho\rangle l_K$, où $\langle\rho\rangle$ est la densité électronique moyenne du silicium. Nous avons vu également que les ions de forte énergie transverse se rhabillent moins rapidement que pour une orientation quelconque du cristal, car le temps τ_{casc} est fortement rallongé en raison de la probabilité augmentée d'ionisation des couches *n* élevées près des rangées. L'expérience menée avec les ions U^{91+} de 20 MeV/u a permis de constater que les ions émergeant du cristal aligné selon l'axe <110> avec les mêmes états de charge que pour une orientation quelconque conservent leur lacune K pendant un temps supérieur ou égal à la durée d'une collision rasante à l'entrée du cristal.
On utilisera donc, pour des ions hydrogénoïdes incidents, le fait que la probabilité de collision nucléaire est augmentée, de même que la durée de vie de la lacune K.

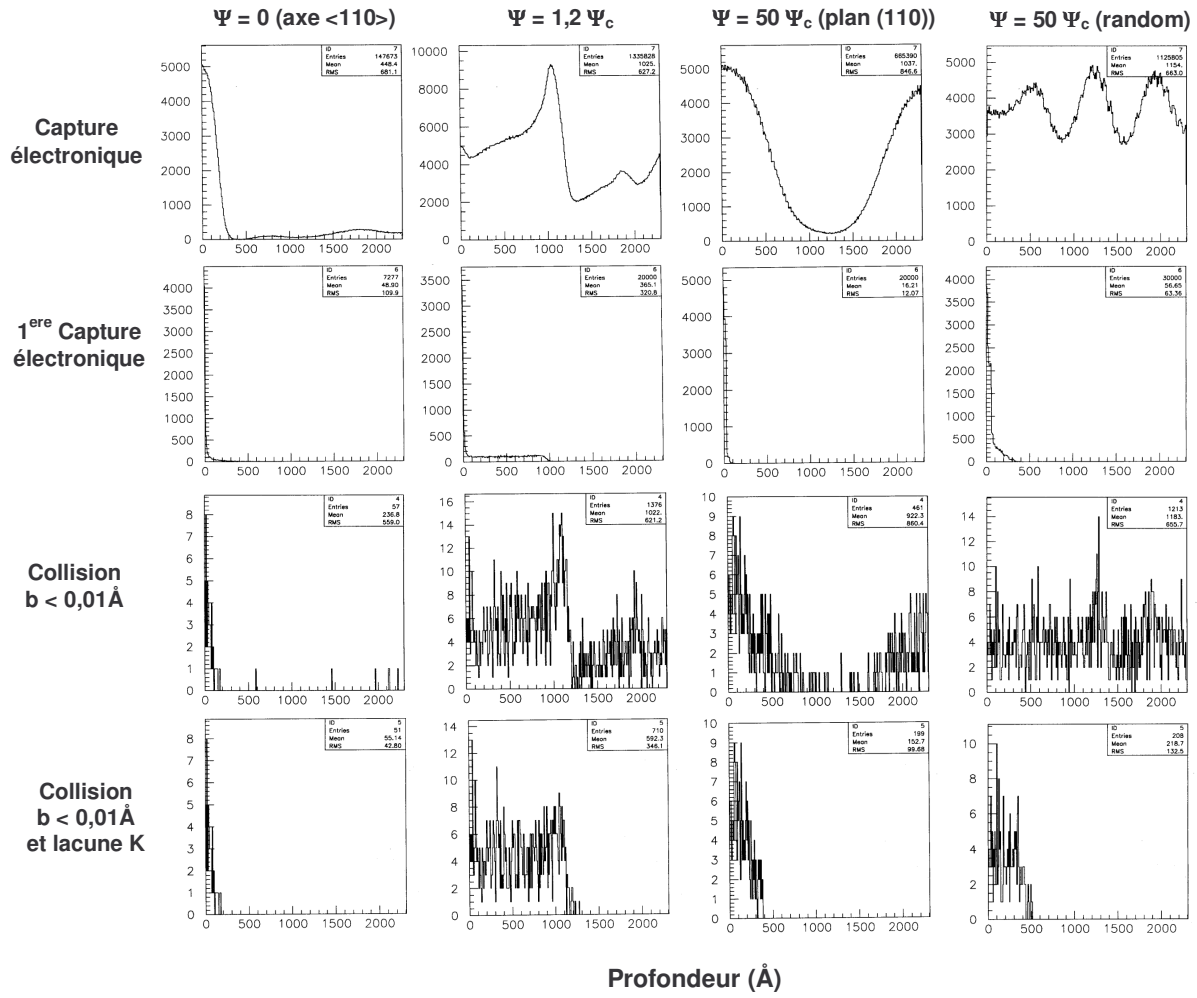

Figure 24 : Simulations analogues à celles de la figure 23, pour des ions U^{91+} incidents à 7 MeV/u . Les quatre colonnes représentent quatre orientations du cristal, par rapport à la direction de l'axe <110>. Ψ_c est l'angle critique de canalisation axiale de Lindhard. Le nombre de tirages est de 20000 pour les trois premières colonnes, et de 30000 pour l'orientation « random ». Les distributions correspondant à cette orientation doivent être multipliées par un facteur 1,5 pour être normalisées aux trois autres, pour lesquelles le tirage a été limité à une distance de ±0,3 Å des plans (110).

Les simulations présentées figure 24 ont été réalisées pour des projectiles U^{91+} de 7 MeV/u en incidence parallèle le long de l'axe <110> du silicium (1ère colonne), à un angle légèrement supérieur à l'angle critique de Lindhard par rapport à cet axe, mais parallèlement au plan (110) (2e colonne), en canalisation planaire (110) à grand angle par rapport à l'axe (3e colonne), et pour une orientation « quelconque », loin de toute direction cristallographique majeure (dernière colonne). Ces simulations sont semblables à celle décrite dans la figure 1, avec un temps $\tau_{casc} = 2.10^{-15}$ s.
Lorsque le faisceau est aligné avec l'axe cristallin, 1 à 2% des ions incidents vont subir à la surface une série de collisions proches, dont le paramètre d'impact est gouverné essentiellement par les vibrations thermiques des atomes cible. Ces collisions rasantes se produisent sur une profondeur d'environ 150 Å, ce qui correspond à une durée de 4.10^{-16} s. Au-delà, les ions sont repoussés par la rangée, et ils ne subissent pratiquement aucune collision proche sur les noyaux au cours des 1500 Å suivants, qui est la distance nécessaire pour rejoindre une autre rangée. Pendant ce temps, les électrons capturés à la surface remplissent la couche K. Le pic de surface pour les collisions nucléaires avec conservation de la lacune K correspond à une réduction d'un facteur 6 seulement par rapport au cas d'une incidence « quelconque ».
En canalisation planaire, le pic de surface des collisions proches est intégré sur une distance plus grande que dans l'axe, et le temps mis par les ions pour ressortir des vibrations thermiques est supérieur au temps τ_{casc}. Il en résulte que le rendement de collisions nucléaires avec lacune K est environ 60 % du rendement hors canalisation, alors que moins de 40 % des ions s'approchent suffisamment près des plans d'atomes pour subir de telles collisions.
Cependant, le cristal peut être orienté à une incidence dite critique par rapport à la direction axiale, telle qu'un maximum d'ions puisse se rapprocher d'une rangée à paramètre d'impact nul dès la première approche. Ceci est illustré par la 2e colonne de la figure 24, qui montre que l'utilisation d'un cristal légèrement désaligné augmente considérablement la probabilité de collision nucléaire durant le temps de survie d'une lacune K (augmentation d'un ordre de grandeur au moins de la probabilité totale de collision nucléaire par rapport à l'incidence axiale). Notons que les ions qui pénètrent dans le cristal loin des rangées ne captureront pas d'électrons avant de s'approcher de celles-ci, ce qui préserve leur lacune K : l'événement de 1ère capture électronique peut se produire jusqu'à 1000 Å de la surface. Notons toutefois qu'il ne s'agit pas vraiment de conditions de « canalisation critique », car les ions ont tous une énergie transverse supérieure à l'énergie critique : ils traversent la rangée avec un angle non nul, ce qui ne rallonge pas leur temps d'interaction avec celle-ci. Nous avons choisi de désaligner le cristal par rapport à l'axe tout en restant dans un plan. Ceci permet de contrôler la distance d'approche à la première rangée, mais n'optimise peut-être pas le rendement de collisions nucléaires avec lacune K. Pour cette orientation particulière, la probabilité d'obtenir une réaction nucléaire à un paramètre d'impact inférieur à 5,6 fm pour un ion uranium avec une lacune K est de 5.10^{-7} par ion 91+ incident à 7 MeV/u, pour une cible d'épaisseur au moins égale à 1300 Å. Cette valeur est deux fois plus élevée que pour une cible d'orientation quelconque.

Les résultats complets des simulations réalisées sont reportés figure 25, sur laquelle est représentée la probabilité de collision nucléaire ($b < 5,6$ fm) en fonction de l'angle d'incidence par rapport à l'axe <110> du silicium. Nous avons utilisé plusieurs valeurs de τ_{casc}, depuis la valeur surestimée de 2.10^{-15} s jusqu'à une valeur de 2.10^{-16} s, qui est très inférieure à la valeur mesurée à 12 MeV/u. Comme discuté plus haut, la valeur la plus réaliste de τ_{casc} se situe entre 5.10^{-16} et 10^{-15} s à cette énergie de 7 MeV/u. De plus nous avons tenté de rendre compte de l'effet de superdensité sur le rallongement de la durée de vie des lacunes profondes lorsque l'ion est au voisinage d'une rangée : nous avons arbitrairement rallongé le

temps des cascades par un facteur 2 lorsque l'ion subit des collisions à un paramètre d'impact inférieur à 0,25 Å à chacun des plans d'atomes distants de 3,8 Å les uns des autres. Lorsque cet effet conduit à des valeurs différentes des calculs ne le prenant pas en compte, nous avons

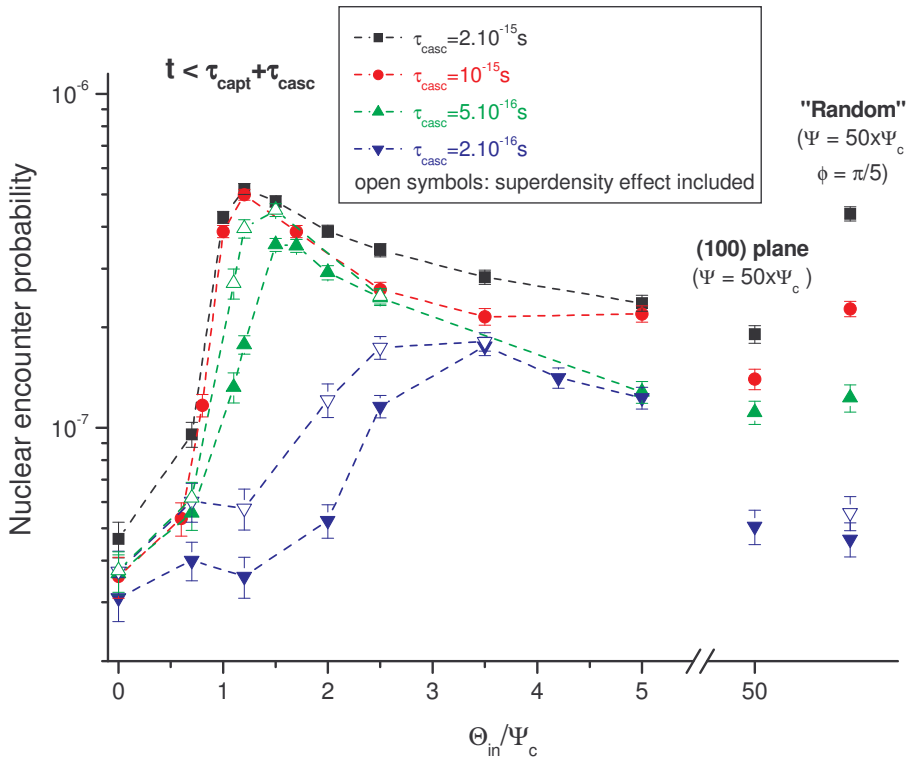

indiqué les valeurs sous forme de symboles ouverts.

Figure 25 : Dépendance angulaire du taux de collisions à b<5,6 fm dans lesquelles les ions ont conservé leur lacune K pour des projectiles incidents U^{91+} de 7 MeV/u dans un cristal de silicium. Position 0 : alignement axial <110>. Les angles en abscisse sont exprimés en unité de l'angle critique de Lindhard de canalisation axiale.

De cette figure on peut conclure que l'augmentation, par rapport à une orientation quelconque, du taux de collisions nucléaires avec lacune K conservée avec un cristal légèrement désaligné est d'autant plus grande que τ_{casc} est petit, et que l'effet de superdensité a pour conséquence de renforcer l'effet d'épaulement pour les temps τ_{casc} courts. Pour les valeurs vraisemblables de τ_{casc}, cette augmentation est d'au moins un facteur 2.
En remarque, on peut revenir sur l'intérêt d'observer la capture radiative REC-K ou REC-L sur un noyau composé s'il survit plus que quelques 10^{-17} s : l'effet de renforcement du taux de production observé pour la décroissance K_α sera encore plus fort pour le REC car la densité électronique rencontrée au voisinage de la rangée (après la collision nucléaire) reste très élevée pendant quelques 10^{-16} s.
La méthode de mesure de temps de fission par spectroscopie X peut donc se trouver améliorée en utilisant un cristal orienté, à condition que de tels faisceaux soient disponibles et suffisamment intenses.

Actuellement, on peut extraire raisonnablement jusqu'à 10^5 ions U^{91+} par seconde de l'anneau ESR au GSI (Darmstadt), ce qui peut fournir un rendement de réactions nucléaires de 1

événement toutes les 20 secondes dans tout l'angle solide. Une expérience d'observation des rayonnements X comme horloge du temps de fission devient réalisable, à condition d'observer les X sous un grand angle solide (multidétecteur).
Quelles réactions peuvent-elles être étudiées dans ces conditions ?

- La fission de noyaux d'uranium a été étudiée par notre collaboration avec une énergie disponible de 600 MeV dans le centre de masse, avec des projectiles uranium de 24 MeV/u [Goldenbaum 99]. Nous avons vu qu'au delà de 200 MeV, seuls des temps de fission inférieurs à quelques 10^{-19} s interviennent. Abaisser cette énergie en dessous de 10 MeV/nucléon limiterait l'énergie disponible à moins de 250 MeV, et optimiserait donc le taux de fission à faible énergie d'excitation. Ces mesures seraient complémentaires des mesures de blocage cristallin, car les temps longs accessibles sont plus grands (quelques 10^{-17}s à 10^{-15}s), et le rôle des neutrons retardés serait inexistant, alors qu'il a été estimé de façon assez grossière dans l'analyse de notre expérience de blocage.
- Des réactions de type fusion – fission semblent plus difficiles à envisager en raison de la petitesse des sections efficaces (quelques dizaines de mbarn). De plus, l'existence de temps de fission longs résulte de l'existence d'une barrière de fission comparable à l'énergie d'excitation résiduelle après émission de neutrons par le noyau composé. Il est donc nécessaire de partir de la plus faible énergie d'excitation possible, avec un projectile lourd à une énergie juste au dessus de la barrière coulombienne.

3 Photoionisation par création de paires

Ce chapitre est en marge de mon activité liée à l'interaction ion-cristal. Durant mon séjour au Lawrence Berkeley National Laboratory, j'ai rejoint le groupe de physique atomique à haute énergie. Ce groupe est spécialisé dans l'étude ses processus d'électrodynamique en champs forts, pour laquelle il bénéficie d'un important support et de collaborations théoriques. Nous avons travaillé sur la photoproduction de paires e+e-, couplée à l'ionisation d'un atome. En effet, Ionescu et al. ont montré que, pour des photons aux énergies relativistes, le processus le plus probable conduisant à la photoionisation d'un atome est la création de paire sur cet atome [Ionescu 98]. La figure 25 ci-dessous illustre ce propos. Elle montre à la fois les sections efficaces d'absorption de photons par un atome d'or en fonction de l'énergie, et les sections efficaces conduisant à l'ionisation de la couche K de cet atome. Au-delà de quelques centaines de MeV, c'est la photoionisation par création de paire (PCP) qui est le processus dominant, même s'il est inférieur de trois ordres de grandeur au processus de création de paire seule. Ce dernier processus ne conduit pas à l'ionisation de l'atome cible, contrairement à l'effet photoélectrique et à l'effet Compton.

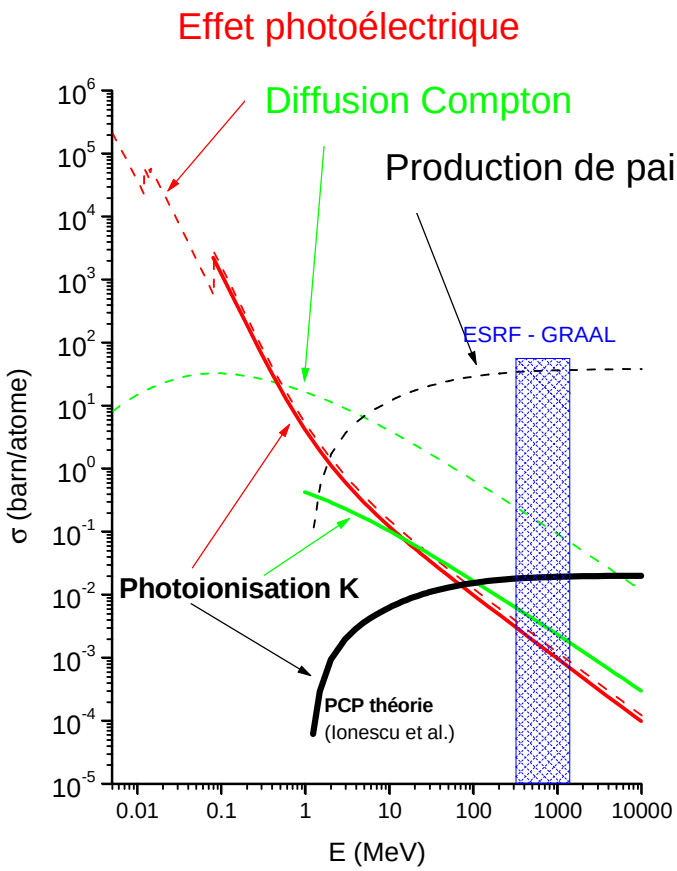

Figure 25 : Sections efficaces d'absorption de photons par un atome d'or, en fonction de l'énergie des photons. Les sections efficaces des processus conduisant à l'ionisation K de l'atome sont indiquées (courbes continues). Le domaine d'énergie de photons accessibles sur la ligne GRAAL de l'ESRF est colorisé.

Deux mécanismes ont été proposés pour l'ionisation par création de paire :

- La paire e+e- est créée dans le champ du noyau de la cible. L'électron ou le positon ainsi matérialisé peut entrer en collision avec un électron lié du même atome. Ce premier mécanisme est un processus du second ordre. La section efficace σ_1 de ce mécanisme croît avec le numéro atomique de la cible, car la section efficace de création de paire sur le noyau est proportionnelle à Z^2. Elle est pratiquement indépendante de la couche atomique.
- la paire est créée directement sur un électron lié, et le recul de ce dernier peut être suffisant pour que l'atome soit ionisé ; pour une couche atomique donnée, la section efficace de ce processus décroît faiblement lorsque le numéro atomique de la cible augmente, car le transfert d'énergie nécessaire à l'ionisation de l'atome cible augmente. Au premier ordre, la section efficace est proportionnelle au nombre d'électrons sur la couche atomique.

La figure 26 ci-dessous montre la variation des sections efficaces des deux mécanismes en fonction du numéro atomique.

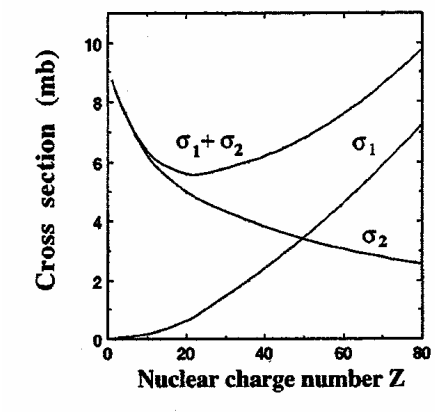

***Figure 26** : sections efficaces de photoionisation par création de paires e+e- en fonction du numéro atomique de la cible (voir texte). D'après [Ionescu 99].*

Notons que seul le premier mécanisme est nouveau, au sens où il n'avait jamais été proposé ni observé. La création de paire sur un électron est connue, même si on ne la conçoit pas comme un processus de photoionisation en général.
L'étude en fonction du numéro atomique de la cible, ainsi qu'en fonction du numéro de couche pour un même atome, doit donc aider à distinguer entre ces deux processus. Nous avons donc réalisé une série d'expériences entre 1999 et 2004. Ces expériences ont été réalisées sur la ligne de photons rétrodiffusés GRAAL à l'ESRF de Grenoble.
La publication suivante, *"Measurement of Vacuum-Assisted Photoionization at 1 GeV for Au and Ag Targets"* [Dauvergne 03B] correspond aux expériences réalisées jusqu'en 2002.

Measurement of Vacuum-Assisted Photoionization at 1 GeV for Au and Ag Targets

D. Dauvergne,[1] A. Belkacem,[2] F. Barrué,[1] J. P. Bocquet,[3] M. Chevallier,[1] B. Feinberg,[2] R. Kirsch,[1] J. C. Poizat,[1] C. Ray,[1] and D. Rebreyend[3]

[1]*Institut de Physique Nucléaire, CNRS/IN2P3, Université Claude Bernard, Lyon I, 4 rue E. Fermi, F-69622 Villeurbanne cedex, France*

[2]*Lawrence Berkeley National Laboratory, Berkeley, California 94720*

[3]*Laboratoire de Physique subatomique et de Cosmologie, CNRS/IN2P3, Université Joseph Fourier, 53 avenue des Martyrs, F-38026 Grenoble cedex, France*

(Received 30 September 2002; published 15 April 2003)

We report a measurement of photon impact ionization of *K* and *L* shell of Au and *K* shell of Ag targets in the 1-GeV energy range. We show that the cross section is dominated by a contribution from a new channel called vacuum-assisted photoionization. In this process the energy-momentum balance associated with the removal of the innershell electron is obtained by conversion of a high-energy photon into an electron-positron pair. This measurement is consistent with the theoretical prediction that vacuum-assisted photoionization is the most probable ionization mechanism at very high energies.

DOI: 10.1103/PhysRevLett.90.153002 PACS numbers: 32.80.Fb

Innershell photoionization of an atom, molecule, or ion, is one of the most basic processes in atomic collisions. With several very high energy and high intensity synchrotron x-ray sources existing or being built around the world, the physics of innershell photoionization has undergone a significant rebirth in the last two decades [1–3]. Detailed studies of single and double ionization mechanisms, electron correlation effects, and post-collision interaction effects have resulted in major advances of our understanding of photoionization mechanisms in the soft and hard x-ray regime. Ionization may proceed through the photoelectric effect or Compton scattering and, in the limit of high energies, the cross section associated with both processes decreases nearly linearly with increasing photon energy [4,5].

The situation is quite different at relativistic energies. When the photon energy exceeds twice the rest mass of the electron, the negative-energy continuum will play an additional important role. Photoionization can now proceed through a new channel in which the excess energy is taken by one of the negative-energy continuum electrons [6,7]. The final result is the creation of an innershell vacancy (*K, L, M,* ...) along with the creation of an electron-positron pair on the same atom. The recent theoretical work by Ionescu *et al.* [6] predicted that this new mechanism called vacuum-assisted photoionization (VAP) will become the most probable ionization mechanism for photon energies beyond a few hundreds of MeV. Various mechanisms contribute to the VAP cross section and a detailed discussion of each mechanism can be found in Ref. [6]. One of the mechanisms that contribute to the total cross section is the well-known triplet production [8]. This latter process is usually calculated as the incoherent part of the pair production process that, in addition to ionization, includes major contributions in which the atom is left in an excited state.

The aim of this Letter is to report the first measurement of vacuum-assisted photoionization in the GeV energy range for Au and Ag targets and its comparison to theory. The experimental work is carried out at the European Synchrotron Radiation Facility (ESRF) in Grenoble, France. High-energy photons are produced by Compton backscattering of laser photons from the 6 GeV electron beam (GRAAL beam line [9]). The ring is run in 16-bunch mode, leading to a pulsed photon beam. A sketch of the layout is shown in Fig. 1. Each backscattered photon is tagged in energy and time by the detection of the scattered electron after deflection inside a bending magnet. The tagging setup consists of an array of plastic scintillators that divide the energy range of the scattered electrons into 15 intervals. The energy of the backscattered high-energy photon is given as a difference between the initial energy of the electron in the ring and the detected energy of the scattered electron. The "tagged" photon energy distribution ranges from 0.7 to 1.5 GeV

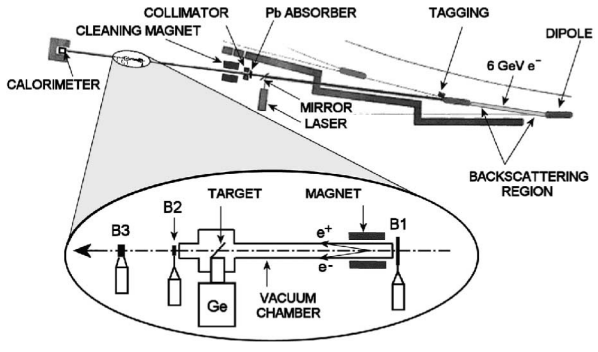

FIG. 1. Experimental setup at the high-energy photon-GRAAL beam line of ESRF. The inset shows details of the target area. B1 to B3 are plastic scintillators, Ge a germanium detector (see text).

with the lower limit of the range given by a geometrical detection cutoff of the tagging system and the higher photon energy limit corresponding to the Compton edge.

A two-slit collimator defines a photon beam spot of 19 mm (horizontal) and 15 mm (vertical) at the target location. A 2-mm thick lead absorber set at the collimator location prevents synchrotron radiation produced in the ring from reaching the target area and creating unwanted background. The lead absorber and the collimation result in an attenuation of about 40% of the Compton backscattered high-energy photon beam. Further cleaning of the high-energy photon beam is achieved by a strong dipole magnet that removes all charged particles created upstream or in the ring.

The expanded inset in Fig. 1 shows some details of the target and detection area. The 2-m target area is kept under primary vacuum of 10^{-3} Torr. A large area thin scintillator (B1) set 1.8 m upstream from the target is used as a veto of any event that involves a charged particle impinging directly on the target. A second magnet further sweeps out of the beam any charged particle created downstream of B1. This combination of cleaning magnets, shielding, and veto counters ensures that only photons in the selected energy range impinge on the target. The photon beam intensity is always kept below 3×10^5 photons/second to avoid fortuitous events caused by multiple incoming photons per pulse.

The high-energy photon beam has a fraction of less than a percent probability to convert into an electron-positron pair in the thin Au and Ag foils. The created high-energy electron and positron fly downstream along the same direction as the initial photon and will deviate by at most a few mrad from the beam direction. Electron-positron pairs created in the target are detected by a thin scintillator B2. B2 is used to validate the trigger of the pair production in all the measurements presented here and its thickness is chosen in a way to bring the detection efficiency of a charged particle close to unity while keeping the probability of triggering by a high-energy photon to a fraction of a percent. To further discriminate against false triggers by the incident photon beam a thicker (5 mm) plastic scintillator B3 is used to sign the pair creation. At relativistic energies electrons or positrons are minimum ionizing particles and will deposit about 1 MeV in B3 independently of their energy. Two charged particles will lose twice that amount of energy. An amplitude analysis of the response of detector B3 allows the selection of events in which two simultaneous charged particles (e^+ and e^-) go through it. A calorimeter (B4) made of entangled lead and scintillating fibers with a total absorption length of several radiation lengths is used to collect the total energy deposited by produced e^+ and e^- particles giving an additional measurement of the incident photon energy.

Electron-positron pair production was extensively studied for the last several decades and a good understanding of the process and agreement for total and partial cross sections with theoretical calculations are achieved. As a check of our experimental technique we first measured electron-positron pair production total cross section in the Au and Ag targets by selecting the two-particle events in B3. Figure 2 shows the measured absolute e^+-e^- pair production probabilities for Au and Ag atoms as a function of target foil thickness. Linear fits of the data provide a measured cross section of 35.1 and 14.2 b for Au and Ag, respectively. Fluctuations of the data around the mean probabilities are very small. These values are in very good agreement with the theoretical values 36.6 and 14.7 b, respectively [8] when the experimental photon incident energy range is folded in the calculations.

A signature of VAP is given by a simultaneous detection of a K- or L-vacancy in coincidence with the production of an electron-positron pair. Note that, unlike the case of the produced pair, the energy of the ionized-target electron is generally too low [6] to be detected by our experimental setup. The innershell vacancy is detected through its characteristic fluorescence K_α or K_β lines when the vacancy is filled. A large area germanium detector (Ge) is used to detect x rays emitted at the target. We used two methods to calibrate the x-ray detection efficiency of our system. In the first method the x-ray detection efficiency is calculated using x-ray absorption probabilities along the path to the detector, including autoabsorption in the target, fluorescence yields, response efficiency, and geometrical efficiency of the Ge detector. In the second method we used Pb foils upstream of the target to produce well-known amounts of electron-positron pairs. We measured innershell ionization generated by these pairs in the Au and Ag targets and used tabulated electron impact ionization cross sections [10] to deduce the detection efficiency. The two methods give consistent detection efficiencies for the set up. Figure 3(a) shows a typical x-ray spectrum for a Ag target. The corresponding energy spectrum of the particle detector B3 is shown

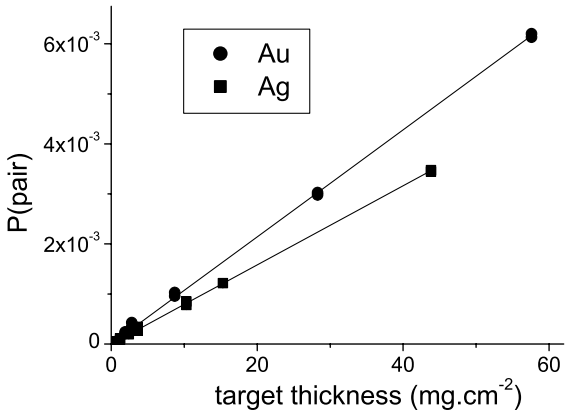

FIG. 2. Pair creation probability in silver and gold targets.

in Fig. 3(b) and exhibits well separated peaks for one- and two-particle contributions. Note that the B3 spectrum includes in it the condition that the Ge detector sees a photon as shown in Fig. 3(a) (fluorescence peaks and background). When we require the creation of an innershell vacancy in the target by setting a cut on the fluorescence Ag-$K_{\alpha,\beta}$ x rays the one-electron peak in the B3 spectrum almost vanishes and the spectrum is almost entirely dominated by a two-particle peak (see the dark area in Fig. 3) corresponding to the creation of an electron-positron pair. The one-electron peak in B3 is correlated mostly to the background seen by the Ge detector and is likely due to Compton scattering in all the surrounding material, including B2, which is much thicker than the target. In contrast the detection of an innershell vacancy selects events that took place inside the target. This is a clear signature that innershell photoionization is strongly correlated with the creation of an electron-positron pair. Two cases are likely to have happened: (i) The innershell vacancy and the pair creation take place on the same target atom; (ii) the innershell vacancy and the pair conversion take place on two separate atoms of the target. First the pair is produced in the field of one atom and then the electron or the positron interacts with a different atom resulting in the creation of an innershell vacancy. This constitutes a background to our measurement that we will call a two-step process.

The interest here is to extract the contribution of VAP that is the process in which both innershell vacancy and pair creation take place on the same atom. In order to do this, we measure, as a function of the target thickness, the probability of creating an innershell vacancy (K_α and K_β, for example) in coincidence with the creation of an electron-positron pair (two-particle peak in B3 spectrum). The probability for VAP varies linearly with target thickness while the two-step process varies as the square of the target thickness.

Figure 4 shows the variation of the absolute probabilities for innershell vacancy production in coincidence with pair creation for Au (K and L shells) and Ag (K shell), as a function of target thickness. The two-step process dominates for the very thick targets. The measured probabilities are reproduced to better than 5% by theoretical values calculated using tabulated electron-positron cross sections [8] folded with tabulated electron impact ionization cross sections [10]. This provides a further check of the experimental setup. We observe a clear departure from the quadratic dependence shown as dashed lines for all the studied systems. The finite linear term of the fit gives a measure of VAP. We summarize in Table I the cross sections extracted from the fits. We also include the pair production cross sections discussed earlier in this Letter and the comparison of both processes with theoretical predictions. These experimental results constitute the first absolute measurement of VAP cross section. These values are a factor of 5 to 10 larger than contributions from Compton scattering and photoelectric effect taken from the literature. These measurements are consistent with the prediction that VAP dominates

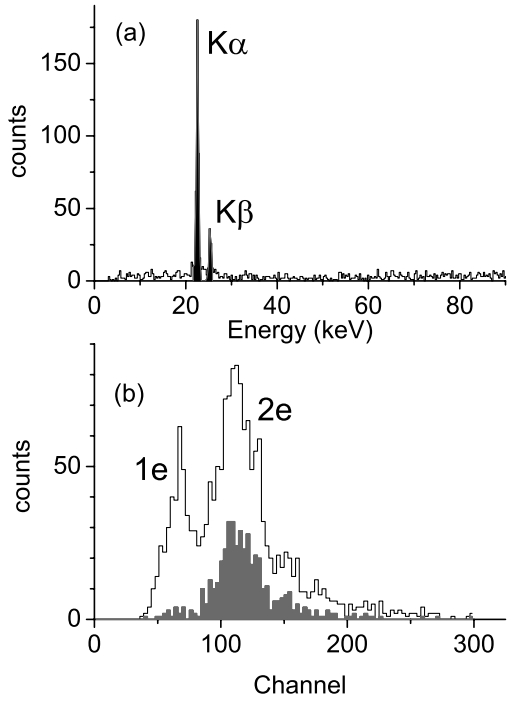

FIG. 3. (a) Energy spectrum of x rays detected in coincidence with a charged particle for a 15.3 mg · cm^{-2} thick Ag target. (b) corresponding amplitude spectrum in the thick scintillator B3. The gray zones of both spectra correspond to the selection of events containing only $K_{\alpha,\beta}$ photons detected by the Ge detector.

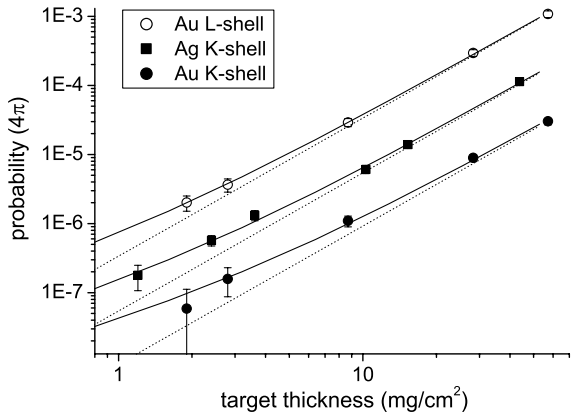

FIG. 4. Probabilities for K- or L-shell vacancy production in coincidence with pair creation in gold and silver targets. Error bars correspond to statistical and absolute dose determination uncertainties. Solid lines are fits using the sum of a linear and a quadratic function. Dashed lines are the corresponding quadratic functions.

TABLE I. Cross sections per target atom for pair creation and per target shell for vacuum assisted photoionization (VAP). Uncertainties are due to statistics and fitting procedure. An additional 20% systematic error bar has to be accounted for experimental VAP cross sections. Theoretical cross sections are taken from Ref. [6]. Compton scattering (CS) and photoelectric effect (Photo) cross sections are taken from Ref. [8].

	Pair creation (barns)	Pair creation theory [8] (barns)	VAP (mbarns)	VAP theory [6] (mbarns)	CS and Photo (mbarns)
Au K shell	35.1	36.6	8.3 ± 6.2	19.4	2.3
Au L shell			116 ± 76	42.2	9.3
Ag K shell	14.2	14.7	18 ± 6	13.2	2.3

photoionization cross sections at high energies. The theoretical values of VAP shown in Table I are deduced from VAP calculations for hydrogenic Ag and Au ions [6]. They include contributions from both the process in which the pair is created on the target electron as well as the process in which the pair is created on the nucleus. These two contributions to VAP are discussed in Ref. [6]. In particular it is expected that the contribution to VAP cross section for tightly bound Au K shell comes mainly from the mechanism that involves pair creation on the nucleus. The experimental value of VAP appears to be slightly smaller than theory for Au K shell and in agreement or slightly larger than theory for Au L shell and Ag K shell. This may be an indication that the contribution from VAP that involves pair creation on the nucleus is smaller than predicted by theory. This could be due to e^+/e^- mutual screening at the Au K-shell orbital scale. However the error bars of our measurement are large and further experimental studies are needed to draw any definitive conclusion on the relative contributions of the two VAP mechanisms.

We gratefully thank the GRAAL Collaboration for granting us access to the high-energy photon beam. This work is supported by a France-Berkeley grant, by the French CNRS/IN2P3, and by the Office of Science, Office of Basic Energy Sciences, Chemical Sciences Division of the U.S. Department of Energy (DOE) under Contract No. DE-AC-03-76SF00098.

[1] J. C. Levin *et al.*, Phys. Rev. Lett. **76**, 1220 (1996).
[2] *Atomic, Molecular and Optical Physics Handbook*, edited by G.W. Drake (AIP, Woodbury, NY, 1996); see section written by Bernd Crasemann, p. 701.
[3] Special issue on *X-Ray and Innershell Processes*, edited by P. Lagarde, J. F. Wuilleumier, and J. P. Briand [J. Phys. (Paris), Colloq. **48**, C9-48 (1987)].
[4] W. Heitler, *The Quantum Theory of Radiation* (Dover, New York, 1984).
[5] R. H. Pratt, A. Ron, and H. K. Tseng, Rev. Mod. Phys. **45**, 273 (1973).
[6] D. C. Ionescu, A. H. Sorensen, and A. Belkacem, Phys. Rev. A **59**, 3527 (1999).
[7] A. Belkacem, D. Dauvergne, B. Feinberg, H. Gould, D. C. Ionescu, and J. Maddi, in *X-Ray and Innershell Processes*, edited by R.W. Dunford, D. S. Gemmell, E. P. Kanter, B. Krassig, S. H. Southworth, and L. Young (AIP, Melville, New York, 2000), p. 153, ISBN 1-56396-713-8.
[8] J. H. Hubbell, H. A. Gimm, and I. Overbo, J. Phys. Chem. Ref. Data **9**, 1023 (1980).
[9] J. -P. Bocquet, Nucl. Phys. **A622**, 124c (1997).
[10] J. H. Scofield, Phys. Rev. A **18**, 963c (1978).

Le tableau suivant complète les résultats donnés dans l'article, en les comparant aux valeurs théoriques des deux mécanismes cités plus haut :

Sections efficaces (mbarn)	**expérience**	Théorie ([Ionescu 99].) σ1	σ2
Au couche K	**11±6**	14.2	5.2
Au couche L	**133±70**	14.2	28
Ag couche K	**18±6**	6.2	7

Depuis, nous avons effectué deux nouvelles prises de données: l'une en 2003, en utilisant un détecteur X Si-Li afin d'avoir une meilleure efficacité à basse énergie et une sensibilité aux photons gamma de haute énergie la plus faible possible. Malheureusement, un défaut de réparation du détecteur ne nous a pas permis d'obtenir une bonne efficacité géométrique. Au mieux nous avons pu vérifier que l'ordre de grandeur obtenu en 2001 pour la photoionisation en couche L de l'or était bon. Nous n'avons pas pu mettre en évidence ce processus avec des cibles de cuivre. La dernière expérience, réalisée en 2004, a permis d'affiner quelque peu les résultats précédents avec des cibles d'or et d'argent. Les résultats sont reportés sur la figure 27 ci-dessous. Nous avons un problème d'efficacité relative entre les mesures avec les cibles d'or et les cibles d'argent. Cependant on peut renormaliser les résultats pour les cibles d'argent, et la variation relative entre les deux points aux épaisseurs de 3,6 et 43 mg/cm^2 reproduit parfaitement nos mesures antérieures. Pour les cibles d'or les résultats en couche K reproduisent également nos mesures publiées en 2003. En particulier le point à l'épaisseur 2,8 est inférieur à la valeur mesurée avec la même cible, tout en étant compatible statistiquement. Ce fait renforce l'idée que le processus du deuxième ordre (création de paire dans le champ du noyau et ionisation de l'électron K par impact de l'électron ou du positon), calculé comme prépondérant pour la photoionisation K de l'or, est très inférieur aux estimations faites par un calcul un peu « avec les mains » d'Allan Sorensen dans la référence [Ionescu 99]. Quant à l'ionisation en couche L de l'or, l'ordre de grandeur de la section efficace est confirmé.

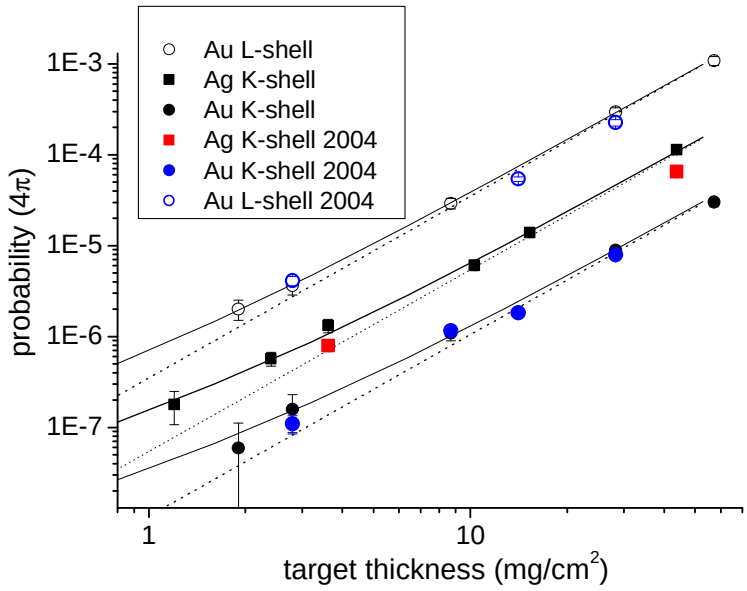

Figure 27 : mesure de la probabilité d'ioniser un atome et de créer une paire en fonction de l'épaisseur de cible, pour des cibles d'or (ionisation en couche K et L) et d'argent (ionisation en couche K). Les mesures extraites de la référence [Dauvergne 03B] sont en noir et blanc, les mesures faites en 2004 sont en couleur.

Pour conclure ce chapitre, nous avons mis en évidence la photoionisation par création de paire à haute énergie. Ce processus, bien qu'il ait une faible section efficace (quelques dizaines de barns) peut jouer un rôle important dans l'endommagement de couches minces. En effet, le taux d'ionisation en couche interne sur des atomes même légers est en grande partie responsable de l'endommagement de ces couches minces sous irradiation par des rayonnements gamma de très haute énergie. Ce type de rayonnement est présent dans le milieu interstellaire, mais aussi dans les détecteurs auprès des accélérateurs de très haute énergie comme le LHC.
Le processus du second ordre amène à se poser une question fondamentale. Lorsqu'une paire e+e- est créée (dans un volume dont le diamètre est typiquement égal à la longueur d'onde de Compton), après quelle distance parcourue par les constituants peut-on considérer que l'électron et le positon ne s'écrantent plus mutuellement ? La taille des orbitales K d'un atome d'or est typiquement du même ordre de grandeur que la longueur d'onde de Compton (à moins qu'un facteur 2 près). La très faible valeur obtenue pour le processus 1 peut suggérer qu'à cette échelle, l'écrantage est très fort et inhibe l'ionisation par impact du positon ou de l'électron.
Mon esprit étant perverti par l'intérêt d'utiliser des cibles cristallines alignées, on pourrait imaginer une expérience cherchant à mesurer cette distance pendant laquelle l'écrantage existe. Le processus en deux étapes (création de paire et EII sur deux atomes distincts), responsable de la forte contribution quadratique aux cibles épaisses, peut être étudiée à l'aide d'un cristal : ce processus doit être fortement augmenté lorsque le faisceau de photons est aligné le long d'une direction d'axe cristallin, car les atomes utiles pour l'ionisation en couche interne sont dans la trajectoire des constituants de la paire, créée sur un noyau d'une rangée d'atomes (l'angle d'émission entre l'électron et le positon est de $1/\gamma$, γ étant le facteur de Lorentz). L'écrantage entre l'électron et le positon doit contrecarrer cet accroissement dans la direction de l'axe. Une mesure en fonction de l'angle d'incidence pourrait permettre de mesurer cette longueur pendant laquelle l'écrantage est efficace.

Conclusion

Au travers des expériences décrites dans ce manuscrit, j'ai pu faire le point sur une quinzaine d'années de recherche au sein du groupe CAS de l'IPNL. De nombreux programmes ont été menés en parallèle, ce qui est inhérent aux expériences de relativement courte durée menées sur les grands accélérateurs. On a pu nous reprocher de ne pas nous concentrer sur un seul programme et une seule thématique, mais nous n'aurions pas pu vivre notre vie scientifique avec une expérience tous les trois ans.
Certaines expériences sont très abouties, d'autres nous laissent un peu sur notre faim :

- la capture NEEC, telle que nous avons essayé de la mettre en évidence au GANIL, est à portée de main ; comme je l'ai déjà précisé, c'est une question de volontés qui ne dépendent pas de nous ; à mon avis l'expérience vaut d'être vécue…
- les expériences de blocage cristallin ont montré leurs limites, imposées à la fois par la statistique disponible avec des expériences d'une à deux semaines de faisceau, et par la qualité des cristaux disponibles pour faire ces expériences ; nous étudierons toutefois la possibilité d'effectuer de nouvelles expériences de ce type avec des noyaux exotiques disponibles à SPIRAL 2 ;
- au GSI, nous n'avons pas pu atteindre la limite inférieure de l'énergie cinétique pour laquelle un faisceau d'uranium ou de plomb hydrogénoïde peut encore voyager dans un cristal sans capturer d'électrons ; toutefois les expériences avec les faisceaux extraits sont tellement difficiles à réaliser qu'il est difficile d'aller plus avant dans ce programme.

Nous nous sommes lancés depuis deux ans dans une nouvelle expérience, qui est la suite logique des expériences associées à l'effet de superdensité. Nous voulons mettre à profit les très forts dépôts d'énergie associés aux collisions rasante d'un ion lourd le long d'une rangée pour étudier l'endommagement en surface d'un cristal. En effet, lorsqu'un ion pénètre un cristal en rasant une rangée, chaque atome de cette rangée peut recevoir une dizaine de keV par ionisation de la plupart de ses électrons. L'explosion coulombienne éventuelle de cette rangée, si le temps de recombinaison des atomes est suffisamment long (à l'échelle de quelques dizaines de femtosecondes), doit conduire à une importante émission ionique en surface du cristal. Ce programme est initié au GANIL, nous attendons de réaliser la première expérience, au cours de laquelle nous mesurerons en coïncidence les ions secondaires par temps de vol, avec les ions transmis à travers le cristal, en fonction de leur état de charge et de leur perte d'énergie, donc de leur énergie transverse. Cette première expérience devrait justifier la continuation de ce programme dans des conditions de surfaces très propres sous ultra-vide. C'est à mon avis une thématique tout à fait originale et novatrice dans le domaine de l'interaction ion-matière, et les informations qu'on en tirera seront fondamentales pour la compréhension de la dynamique de l'endommagement de la matière sous irradiation intense.

Si la politique actuelle et future de nos établissements de recherche publique nous en laisse la possibilité, encore bien des sujets liés à l'interaction de particules chargées avec des cristaux peuvent être traités.
En premier lieu, l'excitation résonnante cohérente nucléaire. Ces études figuraient déjà dans mon projet de recherche pour rentrer au CNRS en 1994… Les priorités en cours ont toujours différé ce programme, que nous pourrions reprendre, soit au GANIL avec des faisceaux métastables ayant une faible énergie d'excitation, soit au GSI, auprès du futur accélérateur FAIR, avec lequel des transitions de quelques dizaines de keV pourraient être étudiées sur des noyaux stables.

Nous sommes également sollicités par une collaboration japonaise pour contribuer à des études de faisabilité d'utiliser des cristaux pour produire des positons. Ceci fait suite aux expériences menées au CERN sur cette thématique, auxquelles je n'ai participé que de façon très marginale jusqu'à présent. Nous utilisons le renforcement du taux de création de paires lorsqu'une particule relativiste est canalisée dans un cristal. Ce renforcement est dû à la somme cohérente des probabilités sur les atomes individuels.
Notre groupe s'engage actuellement dans un programme très alimentaire de mesures de sections efficaces de fragmentation d'ions carbone pour la hadronthérapie. J'aimerais profiter de notre participation à une telle thématique pour étudier la faisabilité d'utiliser un cristal courbe pour dévier des faisceaux d'ions carbone de quelques centaines de MeV/u. Cela peut paraître irréaliste, mais il n'est pas impossible qu'on puisse courber, même en faible proportion, des faisceaux jusqu'à des angles de plusieurs dizaines de degrés dans un cristal de moins d'un centimètre d'épaisseur. Cela vaut la peine d'être tenté, lorsqu'on connaît le coût et la difficulté de mettre en place des systèmes de faisceau orientables avec des têtes isocentriques. La figure ci-dessous est une simulation de trajectoires d'ions carbone de 400 MeV/u dans le plan (110) d'un cristal de silicium pour plusieurs courbures perpendiculaires à ce plan. Avec une déflexion angulaire de 5.10^{-8} radian par unité de longueur $d_{(110)}$, une courbure de 30° serait atteinte avec une longueur de cristal de 4 mm. Certes la diffusion multiple sur les électrons n'est pas prise en compte dans cette simulation, et sera sans doutes la principale limitation physique pour la déflexion des particules chargées.

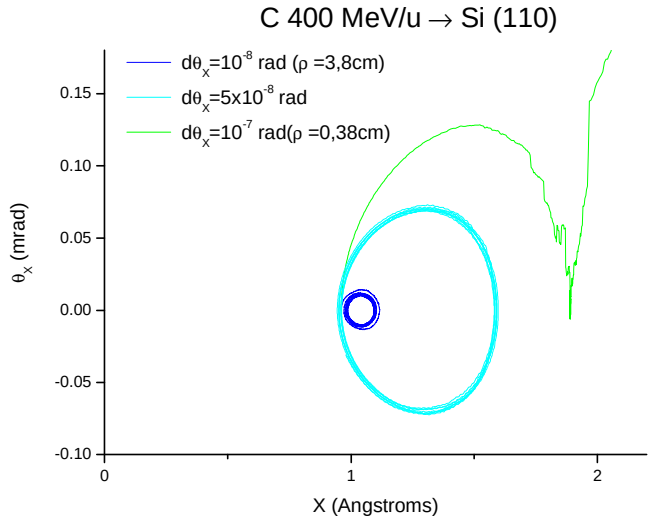

***Figure 26** : Simulations de trajectoires dans l'espace (x,θ_x) d'ions C^{12+} de 400 MeV/u canalisés dans le plan (110) d'un cristal de silicium. Les valeurs $d\theta_x$ correspondent à la variation angulaire du plan du cristal par unité de longueur $d_{(110)}$=3,84Å. Les valeurs de ρ sont les rayons de courbure correspondant.*

Enfin, il me faut rendre hommage à mes collaborateurs sans qui ces travaux n'auraient pas pu être réalisés. J'ai eu la chance de pouvoir m'insérer dans ces programmes expérimentaux, menés par des équipes pluridisciplinaires de taille humaine. La curiosité et l'intérêt scientifique sans cesse renouvelé a permis à ce petit groupe de travailler ensemble pendant des années, bien avant que je le rejoigne. La confiance mutuelle a – presque – toujours été le ciment de notre motivation à travailler ensemble. N'étant spécialiste de rien, les échanges avec les physiciens de la matière condensée, les physiciens atomistes et les physiciens nucléaires que j'ai côtoyés au cours de ces années m'ont énormément apporté.
J'espère que je pourrai en faire autant à mon tour.

Bibliographie

[Andersen 96] J.U.Andersen, J. Chevallier, G.C. Ball, W.G. Davies, J.S. Forster, J.S. Geiger, J.A. Davies, H. Geissel, E.P. Kanter, Physical Review A **54** (1996) 624.
[Andriamonje 87] S. Andriamonje, M. Chevallier, C. Cohen, J. Dural, M.J. Gaillard, R. Genre, M. Hage-Ali, R. Kirsch, A. l'Hoir, B. Mazuy, J. Mory, J. Moulin, J.-C. Poizat, Y. Quéré, J. Remillieux, D. Schmaus et M. Toulemonde, Physical Review Letters 59 (1987) 2271.
[Andriamonje 92] S. Andriamonje, M. Chevallier, C. Cohen, N. Cue, D. Dauvergne, J. Dural, R. Genre, Y. Girard, R. Kirsch, A. l'Hoir, J.-C. Poizat, Y. Quéré, J. Remillieux, D. Schmaus et M. Toulemonde, Physics Letters A164 (1992) 184.
[Andriamonje 96] S. Andriamonje, M. Chevallier, C. Cohen, N. Cue, D. Dauvergne, J. Dural, F. Fujimoto, R. Kirsch, A. l'Hoir, J.-C. Poizat, Y. Quéré, J. Remillieux, C. Röhl, H. Rothard, J.-P. Rozet, D. Schmaus, M. Toulemonde et D. Vernhet, Physical Review A54 (1996) 1404.
[Andriamonje 96B] S. Andriamonje, M. Chevallier, C. Cohen, N. Cue, D. Dauvergne, J. Dural, F. Fujimoto, R. Kirsch, A. l'Hoir, J.-C. Poizat, Y. Quéré, J. Remillieux, C. Röhl, H. Rothard, J.-P. Rozet, D. Schmaus, M. Toulemonde et D. Vernhet, Nuclear Instruments and Methods in Physics Research B107 (1996) 1.
[Andriamonje 97] S. Andriamonje, K. Beckert, M. Chevallier, C. Cohen, D. Dauvergne, J. Dural, H. Eickhoff, B. Franzke, H. Geissel, R. Kirsch, A. l'Hoir, P. H. Mokler, R. Moshammer, F. Nickel, F. Nolden, J.-C. Poizat, H.-T. Prinz, H. Reich, J. Remillieux, F. Sanuy, C. Scheidenberger, D. Schmaus, M. Steck, Th. Stöhlker et M. Toulemonde, Journal of Physics B **30** (1997) 5099.
[Azuma 99] T. Azuma, T. Ito, K. Komaki, Y. Yamazaki, M. Sano, M. Torikoshi, A. Kitagawa, E. Takada et T. Murakami, Physical Review Letters **83** (1999) 528.
[Balashov 06] V.V. Balashov et I.V. Bodrenko, Nuclear Instruments and Methods **B 245** (2006) 52.
[Barrué 02] F. Barrué, S. Basnary, A. Chbihi, M. Chevallier, C. Cohen, D. Dauvergne, H. Ellmer, J. Frankland, D. Jacquet, R. Kirsch, P. Lautesse, A. l'Hoir, M. Morjean, J.-C. Poizat, C. Ray et M. Toulemonde, Nuclear Instruments and Methods in Physics Research **B 193**, (2002) 852.
[Barrué 02B] F. Barrué, Thèse, Université Lyon 1 (2002) Prprint LYCEN T-2002-36.
[Barrué 04] F. Barrué, M. Chevallier, D. Dauvergne, R. Kirsch, J.-C. Poizat C. Ray, L. Adoui, A. Cassimi, H. Rothard, M. Toulemonde, C. Cohen, A. l'Hoir, D. Vernhet, C.Demonchy, L. Giot, W. Mittig, S. Pita, P. Roussel-Chomaz, et A. Billebaud, Physical Review A **70**, 032902 (2004).
[Basnary 02] S. Basnary, Thèse, Université de Caen (2002). Preprint GANIL T-02-02.
[Belkacem 90] A. Belkacem, E.P. Kanter, K.E.Rehm, E.M. Bernstein, M.W. Clark, S.M. Fergusson, J.A. Tanis, K.H. Berkner et D. schneider, Physical Review Letters 64 (1990) 380.
[Belkacem 97] A. Belkacem, H. Gould, B. Feinberg, R. Bossingham et W. E. Meyerhof, Physical Review A **56** (1997) 2806.
[Bethe 57] H. A. Bethe et E. E. Salpeter, *Quantum Mechanics of One- and Two-Electron Atoms*, Springer Verlag (Berlin) 1957.
[Betz 70] H.D. Betz et L. Grodzins, Physical Review Letters **25** (1970) 211.
[Bräuning 01] H. Bräuning, P. H. Mokler, D. Liesen, F. Bosch, B. Franzke, A. Krämer, C. Kozhuharov, T. Ludziejewski, X. Ma, F. Nolden, M. Steck, Th. Stöhlker, R. W. Dunford, E. P. Kanter, G. Bednarz, A. Warczak, Z. Stachura, L. Tribedi, T. Kambara, D. Dauvergne, R. Kirsch et C. Cohen, Physical Review Letters 86 (2001) 991.

[Chevallier 00] M. Chevallier, C. Cohen, N. Cue, D. Dauvergne, J. Dural, P. Gangnan, R. Kirsch, A. l'Hoir, D. Lelièvre, J.-F. Libin, P. H. Mokler, J.-C. Poizat, H. T. Prinz, J.-M. Ramillon, J. Remillieux, P. Roussel-Chomaz, J.-P. Rozet, F. Sanuy, D. Schmaus, C. Stephan, M. Toulemonde, D. Vernhet et A. Warczak, Physical Review A.61 (2000) 022724.
[Claytor 88] N. Claytor, B. Feinberg, H. Gould, C.E. Bemis, J. Gomez Del Campo, C.A. Ludemann, et C. R. Vane, Phys. Rev. Lett. **61** (1988) 2081.
[Cohen 04] C. Cohen et D. Dauvergne, Nuclear Instruments and Methods in Physics Research **B225** (2004) 40.
[Crawford 79] O.H. Crawford et R.H. Ritchie, Physical Review A**20** (1979) 1848.
[Cue 89] N. Cue, J. C. Poizat et J. Remilleux, Europhys. Lett. **8**, 19 (1989).

[Datz 95] S. Datz, P.F. Dittner, H.F. Krause, C.R. Vane, O.H. Crawford, J.S. Forster, G.S. Ball, W.G. Davies et J.S. Geiger, Nuclear Instruments and Methods in Physics Research **B100** (1995) 272 et références incluses.
[Dauvergne 93] D. Dauvergne, Thèse, université Lyon 1, n° 69-93.
[Dauvergne 99] D. Dauvergne, C. Scheidenberger, A. l'Hoir, J.-U. Andersen, S. Andriamonje, C. Böckstiegel, M. Chevallier, C. Cohen, N. Cue, S. Czajkowski, J. S. Forster, H. Geissel, H. Irnich, T. Kandler, R. Kirsch, A. Magel, P. H. Mokler, G. Münzenberg, F. Nickel, YU. L. Pivovarov, J.-C. Poizat, M.-F. Politis, J. Remillieux, D. Schmaus, Th. Stöhlker, T. Suzuki et M. Toulemonde, Physical Review A 59 (1999) 2813.
[Dauvergne 03] D. Dauvergne, A. Bräuning-Demian, F. Bosch, H. Bräuning, M. Chevallier, C. Cohen, A. Gumberidze, R. Kirsch, C. Kozhuharov, A. l'Hoir, D. Liesen, P. H. Mokler, J.-C. Poizat, C. Ray, Th. Stöhlker, M. Tarisien, E. Testa, S. Toleikis et M. Toulemonde, Nuclear Instruments and Methods B 205 (2003) 773.
[Dauvergne 03B] D. Dauvergne, A. Belkacem, F. Barrué, J-P. Bocquet, M. Chevallier, B. Feinberg, R. Kirsch, J.-C. Poizat, C. Ray et D. Rebreyend, Physical Review Letters 90 (2003) 153002.
[Dauvergne 06] D. Dauvergne, M. Chevallier, J.-C. Poizat, C. Ray, E. Testa, A. Bräuning-Demian, F. Bosch, S. Hagmann, C. Kozhuharov, D. Liesen, P.H. Mokler, Th. Stöhlker, M. Tarisien, P. Verma, C. Cohen, A. L'Hoir, J.-P. Rozet, D. Vernhet, H. Bräuning, et M. Toulemonde, XXIV International Conference on the Photonic, Electronic and Atomic Collisions, (Rosario, Argentine, 20-26 Juillet 2005), à paraître. Preprint Lycen 2005-38.
[Drouart 06] A. Drouart, J. L. Charvet, R. Dayras, L. Nalpas, C. Volant, A. Chbihi, C. Escano Rodriguez, J. D. Frankland, M. Morjean, C. Stodel, M. Chevallier, D. Dauvergne, R. Kirsch, P. Lautesse, C. Ray, E. Testa, C. Cohen, A. L'Hoir, D. Jacquet, M. Laget, Proceedings of the International. Symposium on Exotic Nuclei, Peterhof, July 5-12 2004, World Scientific, p192-197.
[Echenique 79] P.M. Echenique, R.H. Ritchie, W. Brandt, Physical Review B **20** (1979) 2567.
[Gemmell 02] D. S. Gemmell, Proceedings of the 19th International Conference on X-rays and Inner-shell Processes (X2002), Rome, 24-28 July 2002.
[Goldanskii 76] V. I. Goldanskii et V. A. Namiot, Phys. Lett. **62B**, 393 (1976).

[Goldenbaum 99] F. Goldenbaum, M. Morjean, J. Galin, E. Liénard, B. Lott, A. Péghaire, Y. Périer, M. Chevallier, D. Dauvergne, R. Kirsch, J.-C. Poizat, J. Remillieux, C. Cohen, A. L'Hoir, B. Prévost, D. Schmaus, J. Dural, M. Toulemonde et D. Jacquet, Physical Review Letters 82 (1999) 5012.

[Indelicato 03] Paul Indelicato, communication privée.

[Ionescu 99] D.C. ionescu, A.H. Sorensen et A. Belkacem, Physical Review A 59 (1999) 3527.

[Kandler 95] T. Kandler, P.H. Mokler, Th. Stöhlker, H. Geissel, H. Irnich, C. Kozhuharov, A. Kriessbach, M. Kucharski, G. Münzenberg, F. Nickel, P.Rymuza, C. Scheidenberger, Z. Stachura, T. Suzuki, A. Warczak, D. Dauvergne, R.W. Dunford, Physics Letters A **204** (1995) 274.

[Kimball 91] J. C. Kimball, D. Bittle et N. Cue, Phys. Lett. **152**, 367 (1991).

[Lamour 06] E. Lamour, B. Gervais, J. P. Rozet et D. Vernhet, Physical Review A **73** (2006) 042715.

[L'Hoir 90] A. l'Hoir, S. Andriamonje, R. Anne, N.V. De Castro Faria, M. Chevallier, C. Cohen, J. Dural, M.J. Gaillard, R. Genre, M. Hage-Ali, R. Kirsch, B. Farizon-Mazuy, J. Mory, J. Moulin, J.-C. Poizat, Y. Quéré, J. Remillieux, D. Schmaus et M. Toulemonde, Nuclear Instruments and Methods in Physics Research **B48** (1990) 45.

[L'Hoir 06] A. l'Hoir, L. Adoui, F. Barrué, A. Billebaud, F. Bosch, A. Bräuning-Demian, H. Bräuning, A. Cassimi, M. Chevallier, C. Cohen, D. Dauvergne, C. E. Demonchy, L. Giot, A. Gumberidze, R. Kirsch, C. Kozhuharov, D. Liesen, W. Mittig, P. H. Mokler, S. Pita, J.-C. Poizat, C. Ray, P. Roussel-Chomaz, H. Rothard, J.-P. Rozet, Th. Stöhlker, M. Tarisien, E. Testa, S. Toleikis, M. Toulemonde et P. Verma, Nuclear Instruments and Methods **B245** (2006)1.

[Massa 82] I. Massa et G. Vannini, Nuovo Cimento **5** (1982) 1.

[Meyerhof 85] W.E. Meyerhof et J.-F. Chemin, Advances in Atomic And Molecular Physics **20** (1985) 173.

[Molitoris 93] J.D. Molitoris et al., Phys. Rev. Lett. **70** (1993) 537.

[Morjean 98] M. Morjean, M. Chevallier, C. Cohen, D. Dauvergne, J. Dural, J. Galin, F. Goldenbaum, D. Jacquet, R. Kirsch, E. Lienard, B. Lott, A. Peghaire, Y. Perier, J.-C. Poizat, B. Prévost, J. Remillieux, D. Schmaus, M. Toulemonde, Nuclear Physics A 630 (1998) 200c

[Prinz 97] H.-Th. Prinz, D. Dauvergne, S. Andriamonje, K. Beckert, M. Chevallier, C. Cohen, J. Dural, H. Eickhoff, B. Franzke, H. Geissel, R. Kirsch, A. l'Hoir, P. H. Mokler, R. Moshammer, F. Nickel, F. Nolden, J.-C. Poizat, H. Reich, J. Remillieux, F. Sanuy, C. Scheidenberger, D. Schmaus, M. Steck, Th. Stöhlker et M. Toulemonde, Hyperfine Interactions 108 (1997) 325.

[Okorokov 65] V.V. Okorokov, Yad. Fiz. **2** (1965) 1009; Pis'ma Zh. Eksp. Teor. Fiz. **2** (1965) 175.

[Rozet 99] J. P. Rozet, C. Stephan, I. Despiney-Bailly, C. Fourment et L. Dubé, Journal of Physics B **32** (1999) 4677.

[Salin 98] A. Salin, A. Arnau et P.M. Echenique, Physical Review A **57** (1998) 2772.

[Schnell 03] M. Schnell, G. Gwinner, N.R. Badnell, M.E. Bannister, S. Böhm, J. Colgan, S. Kieslich, S.D. Loch, D. Mitnik, A. Müller, M.S. Pindzola, S. Schippers, D. Schwalm, W. Shi, A. Wolf et S.-G. Zhou, Physical Review Letters **91** (2003) 043001.

[Stöhlker 95] Th. Stöhlker, C. Kozhuharov, P. H. Mokler, A. Warczak, F. Bosch, H. Geissel, R. Moshammer, C. Scheidenberger, J. Eichler, A. Ichihara et al., Phys. Rev. A 51 (1995) 2098.

[Stöhlker 98] Th. Stöhlker, T. Ludziejewski, H. Reich, F. Bosch, R. W. Dunford, J. Eichler, B. Franzke, C. Kozhuharov, G. Menzel, P. H. Mokler, F. Nolden, P. Rymuza, Z. Stachura, M. Steck, P. Zwiat, A. Warczak et T. Winkler, Physical Review **A 58** (1998) 2043.

[Testa 05] Etienne Testa, Thèse, Université Lyon 1, 2005. Preprint LYCEN T-2005-34.

[Testa 06] E. Testa, D. Dauvergne, A. Bräuning-Demian, F. Bosch, H. Bräuning, M. Chevallier, C. Cohen, A. Gumberidze, S. Hagmann, R. Kirsch, C. Kozhuharov, A. l'Hoir, D. Liesen, P. H. Mokler, J.-C. Poizat, C. Ray, J.-P. Rozet, Th. Stöhlker, S. Toleikis, M. Toulemonde et P. Verma, Nuclear Instruments and Methods **B 245** (2006) 47.

[Tribedi 95] L.C. Tribedi, V. Nanal, M.B. Kurup, K.C. Prasad, P.M. Tandon, Physical Review **A 51** (1995) 1312.

[Vickridge 90] I. Vickridge, A. L'Hoir, J. Gylai, C. Cohen et F. Abel, Europhysics Letters **13** (1990) 635.

[Wilschut 04] H.W. Wilschut et V.L. Kravchuk, Nucl. Phys. A **734**(2004) 156.